# Experimental Investigations of Near-Wall Processes in an Optically Accessible Spark-Ignition Engine

Vom Fachbereich Maschinenbau
an der Technischen Universität Darmstadt

zur Erlangung des akademischen Grades eines
Doktors der Ingenieurwissenschaften (Dr.-Ing.)
genehmigte

**Dissertation**

von

**Marius Schmidt, M.Sc.**

aus Gießen

| | |
|---|---|
| Berichterstatter: | Prof. Dr. rer. nat. A. Dreizler |
| Mitberichterstatter: | Prof. Dr.-Ing. L. Zigan |
| Tag der Einreichung: | 30.05.2023 |
| Tag der mündlichen Prüfung: | 27.07.2023 |

Darmstadt 2023

**Schmidt, Marius:**
"Experimental Investigations of Near-Wall Processes in an Optically Accessible Spark-Ignition Engine"

Darmstadt, Technische Universität Darmstadt,
Jahr der Veröffentlichung der Dissertation auf TUprints: 2024
Tag der mündlichen Prüfung: 27.07.2023

URN: urn:nbn:de:tuda-tuprints-266204
URL: https://tuprints.ulb.tu-darmstadt.de/id/eprint/26620

*The nitrogen in our DNA, the calcium in our teeth,*
*the iron in our blood, the carbon in our apple pies*
*were made in the interiors of collapsing stars.*
*We are made of starstuff.*

Carl Sagan

# Erklärung

Die Dissertation ist von mir mit einem Verzeichnis aller benutzten Quellen versehen. Ich erkläre, dass ich die vorliegende Dissertation selbstständig verfasst und keine anderen als die von mir angegebenen Hilfsmittel verwendet habe. Ich erkläre außerdem, dass ich bisher noch keinen Promotionsversuch unternommen habe.

Marius Schmidt

Darmstadt, 23.05.2023

# Danksagung

Mit dem Schreiben dieser Dissertationsschrift geht eine vielfältige und spannende Zeit als Doktorand am Fachgebiet RSM vorbei. Natürlich ist Forschung und die wissenschaftliche und lehrende Tätigkeit an einer Universität ein kooperativer Prozess, daher möchte ich für die Unterstützung und Zusammenarbeit bei einer Vielzahl von Leuten bedanken.

An erster Stelle gilt mein Dank meinem Doktorvater Prof. Dr. Andreas Dreizler. Zum einen für die Möglichkeit der Promotion, zum anderen für den Aufbau eines Fachgebiets mit spannenden Fragestellungen und einer motivierenden, konstruktiven und menschlichen Atmosphäre. Deine Begeisterung für die Sache, lieber Andreas, dein offenes Ohr für inhaltliche Diskussionen und deine von fachlicher Kompetenz und Vertrauen geprägte Führung ist mir in vielerlei Hinsicht ein Vorbild.

Weiterhin möchte ich mich bei Prof. Dr.-Ing. Lars Zigan für die Übernahme des Koreferats und das Interesse an meiner Dissertation bedanken. Da Sie über die Jahre immer wieder an für meine Arbeit relevanten Publikationen beteiligt waren, freue ich mich auf die Diskussion über Ergebnisse und Methoden.

Einen herzlichen Dank möchte ich an Dr.-Ing. Benjamin Böhm richten, der mich als Arbeitsgruppenleiter vom ersten Kontakt in der Bewerbung, über die gesamte Arbeitszeit stets unterstützt hat, mit geschätztem Rat und Tat zur Seite stand und Abschlussberichte, Finanzen und Laborequipment immer im Blick hatte.

Vielen Dank auch an meine aktuellen und früheren Kollegen: an Rene Honza und Dr.-Ing. Carl-Philipp Ding, der zu Beginn sein Wissen mit mir geteilt hat und dessen Herangehensweise beim wissenschaftlichen Arbeiten im Labor und in der Datenanalyse für mich eine Inspiration war. Gerne erinnere ich mich an viele persönliche Gespräche. Es freut mich auch, über viele Jahre immer wieder Kontakt mit Dr. Brian Peterson zu haben. Weiterhin ein Danke an Cooper Welch, der mit mir viele lange und abwechslungsreiche Stunden im Labor und Büro verbracht hat, fachliche und private Perspektiven eröffnet hat und nicht zuletzt jede (gemeinsame) Publikation im Lektorat geschärft hat. Danke ebenso an Lars Illmann, für die gemeinsame Zeit in der Motorgruppe und viele kurzweilige und zielführenden Diskussionen in Labor und Büro.

Ein wesentlicher Punkt ist die gute kollegiale Atmosphäre, die von der Zusammenarbeit vieler Kollegen lebt. Daher möchte ich mich für viele hilfreiche Diskussionen, Anregungen, Hilfestellungen und privaten Gespräche bei Dr.-Ing. Lukas Becker, Dr.-Ing. Andreas Preusche, Dr.-Ing. Johannes Emmert, Dr.-Ing. Florian Zentgraf, Dr.-Ing. Max Greifenstein, Dr.-Ing. Tao Li, Wibke Leudesdorff, Christopher Geschwindner, Dr.-Ing. Anna von der Heyden, Pascal Johe, Dr.-Ing. Steven Wagner, Henrik Schneider, Johannes Trabold, Ariane Auernhammer, Steffen Walther, Matthias Bonarens, Jannick Erhard, Thomas Krenn, Pedro Ye und Sandra Schary bedanken. Ferner beim aktuellen und früheren IT-Team, mit Hardy Hamel, Henrik Matero, Janik Hebel und Robin Schultheis, welches großartige Arbeit geleistet hat.

Mein Dank gilt auch der angenehmen Zusammenarbeit mit dem STFS, wo ich an dieser Stelle stellvertretend Prof. Dr.-Ing. Christian Hasse, Dr.-Ing. Arne Scholtissek, Matthias Steinhausen und Dr.-Ing. Andrea Pati nennen möchte und allen Kolleginnen und Kollegen im TRR 150.

Zu einer universitären Arbeit gehören auch viele Studierenden, für deren Beitrag ich mich an dieser Stelle bedanken möchte. Die Laborarbeit wäre nicht möglich ohne das Team in der feinmechanischen Werkstatt des RSM. Vielen Dank an Roland Berntheisel und Dirk Feldmann sowie Sebastian Feuerbach und Mathias Felter für die kompetente und hilfsbereite Unterstützung. Weiterhin an Andreas Ludwig und Gabriele Goet, die hier viele Systeme am Laufen halten, sowie das Sekretariatsteam, Marion Müller, Angela Berger und Patricia John, die durch nichts zu ersetzen sind.

Abschließend möchte ich mich bei Freunden und Familie bedanken. Zunächst meinen Eltern Heike Stieglitz-Schmidt und Joachim Schmidt, ohne die ich nicht an diesem Punkt wäre. Ihr habt die Grundlage für vieles in meinem Lebensweg gelegt und mich in allen Aspekten stets unterstützt. Dafür danke ich euch von Herzen. Ein Danke an meinen geschätzten Freundeskreis, der für die Würze im Leben sorgt, und nicht zuletzt an meine Freundin Magdalena, die in den letzten Jahren und gerade in der letzten, nervenaufreibenden Phase eine große Unterstützung war.

Darmstadt, Mai 2023 Marius Schmidt

# Abstract

Within this dissertation, near-wall processes in an optically accessible direct-injection spark-ignition engine are investigated experimentally. These processes affect the thermodynamic efficiency and pollutant emission, specifically through heat transfer, fuel wall film formation, turbulent transport and mixing, flame-wall interaction, and pollutant formation. Because reducing greenhouse gas and pollutant emissions is imperative in the context of climate change mitigation and compliance with future regulations, a comprehensive understanding of these interacting processes is required.

In this work, experimental investigations are performed using a combination of minimally invasive optical diagnostics in a well-characterized engine test bench. Thermographic phosphors are applied at several locations in the combustion chamber to measure wall temperatures for motored and fired operation. During fired operation, temperatures increase steadily, with the greatest rise occurring in the first 50 cycles. The flame-wall interaction in the crevice, into which the flame is pushed during combustion, is investigated for the first time. Furthermore, heat fluxes are estimated from the time-resolved surface temperatures. Peak heat fluxes during fired operation are up to $15\,\mathrm{MW\,m^{-2}}$ on the metallic piston side and approximately $1\,\mathrm{MW\,m^{-2}}$ on the piston and cylinder glass.

The velocity boundary layer above the piston is resolved down to the viscous sublayer with high-resolution particle tracking velocimetry. At an engine speed of 2500 rpm, the viscous sublayer is as thin as 30 µm. Furthermore, there is a strong overlap of the inner and outer layer and velocity profiles do not adhere to the logarithmic law. However, in both velocity magnitude and fluctuations, similarities to impinging wall jets are observed. Conditional averaging reveals that the degree of boundary layer development depends on the horizontal location and instantaneous flow mode.

Emission formation in the context of wall films is studied with simultaneous diagnostics combining velocimetry, laser-induced fluorescence of acetone, and flame as well as soot visualizations. Therefore, a fuel wall film is deliberately created by a late single-hole injection of acetone. The resulting soot luminosity above the piston (commonly called *pool fire*) is characterized and attributed to flame-free pyrolysis of fuel-rich zones in the hot burnt gas. A strong sensitivity of vaporization and consequently soot formation processes to the wall temperature is observed. Measured acetone mole fractions in the bulk flow are on average below 2 %, which indicates that soot formation is limited to sufficiently high fuel-air ratios in the direct wall vicinity. Thereby, cycle-to-cycle variations of soot luminosity are high. Strong correlations between the velocity and mixing field, and soot luminosity are found. Conditional statistics reveal the influence of the flow on the flame propagation. It is hypothesized that combustion-induced convection of soot nests along the colder temperature boundary layer is responsible for reduced soot luminosity in some cycles.

The presented results provide novel insights into relevant near-wall phenomena in an engine and extend the data available for validation and the boundary conditions for numerical simulations.

# Kurzfassung

In dieser Dissertation werden wandnahe Prozesse in einem optisch zugänglichen Ottomotor mit Direkteinspritzung experimentell untersucht. Diese Prozesse wirken sich auf den thermodynamischen Wirkungsgrad und die Schadstoffemissionen aus, insbesondere durch Wärmeübertragung, Bildung von Kraftstoffwandfilmen, turbulenten Transport und Vermischung, Flamme-Wand-Wechselwirkung und Schadstoffbildung. Da die Verringerung der Treibhausgas- und Schadstoffemissionen von technischen Verbrennungsprozessen im Zusammenhang mit der Bekämpfung des Klimawandels und der Einhaltung künftiger Abgasregularien unerlässlich ist, ist ein umfassendes Verständnis dieser interagierenden Prozesse erforderlich.

In dieser Arbeit werden experimentelle Untersuchungen mit einer Kombination aus minimalinvasiver optischer Diagnostik in einem umfangreich charakterisierten Motorprüfstand durchgeführt. Thermografische Phosphore werden an mehreren Stellen im Brennraum angebracht, um die Wandtemperaturen im geschleppten und gefeuerten Betrieb zu messen. Zum ersten Mal liegen Temperaturmessungen im Kolbenspalt vor, die einen vertikalen Temperaturgradienten am Kolben aufzeigen. Im gefeuerten Betrieb steigen die Temperaturen stetig an, wobei der stärkste Anstieg in den ersten 50 Zyklen zu verzeichnen ist. Die Flamme-Wand-Wechselwirkung im Kolbenspalt, in den die Flamme während der Verbrennung hineingedrückt wird, wird zum ersten Mal untersucht. Außerdem werden aus den zeitlich aufgelösten Oberflächentemperaturen Wandwärmeströme abgeschätzt. Diese betragen im gefeuerten Betrieb bis zu $15\,\mathrm{MW\,m^{-2}}$ auf der metallischen Kolbenflanke und etwa $1\,\mathrm{MW\,m^{-2}}$ auf dem Kolben- und Zylinderglas.

Die Geschwindigkeitsgrenzschicht über dem Kolben wird mit hochauflösender Particle-Tracking-Velocimetry aufgelöst. Bei einer Motordrehzahl von 2500 U/Min ist die viskose Unterschicht 30 µm dick. Außerdem überlappen sich die innere und die äußere Schicht stark, und die Geschwindigkeitsprofile folgen dem logarithmischen Wandgesetz nicht. Sowohl in der Geschwindigkeitsmagnitude als auch bei den Fluktuationen sind jedoch Ähnlichkeiten mit Prallströmungen zu beobachten. Konditionierte Mittelwerte zeigen, dass der Grad der Grenzschichtentwicklung von der horizontalen Position und dem instantanen Strömungsmodus abhängt.

Die Emissionsbildung im Zusammenhang mit Kraftstoffwandfilmen wird mithilfe von simultanen Messungen mit PIV, laserinduzierter Fluoreszenz von Aceton sowie Flammen- und Rußvisualisierungen untersucht. Dazu wurde durch späte Injektion von Aceton mit einem Einlochinjektor gezielt ein Kraftstofffilm erzeugt. Das im Verlauf resultierende Rußleuchten oberhalb des Kolbens (häufig als “Pool Fire” bezeichnet) wird charakterisiert und auf Pyrolyse von kraftstoffreichen Zonen im heißen Abgas zurückgeführt. Es wird eine starke Sensitivität der Verdampfungs- und folglich Rußbildungsprozesse gegenüber der Wandtemperatur beobachtet. Die gemessenen Aceton-Molenbrüche der Hauptströmung liegen im Durchschnitt unter 2 %, was darauf hindeutet, dass die Rußbildung auf Regionen in unmittelbarer Wandnähe mit hohem Kraftstoff-Luft-Verhältnissen beschränkt ist. Zudem werden starke Schwankungen des Rußeigenleuchtens von Zyklus zu Zyklus beobachtet. Signifikante Korrelationswerte werden zwischen den Geschwindigkeits- und Mischungsfeldern und dem Rußleuchten berechnet. Konditionierte Statistiken zeigen den Einfluss der Strömung auf die Flammenausbreitung. Es wird die Hypothese aufgestellt, dass die verbrennungsbedingte Konvektion von initialen Rußpartikeln entlang der kälteren Temperaturgrenzschicht für das geringere Rußleuchten in einigen Zyklen verantwortlich ist.

Die vorgestellten Ergebnisse bieten neue Einblicke in relevante wandnahe motorische Phänomene und erweitern den Datensatz der für die Verifikation sowie die Randbedingungen von numerischen Simulationen zur Verfügung steht.

# Contents

# List of Tables

# List of Figures

# Nomenclature

| Lower-case Latin letters | | Unit |
|---|---|---|
| $\dot{m}$ | Mass flow rate | $\mathrm{kg\,s^{-1}}$ |
| $c_p$ | Heat capacity at constant pressure | $\mathrm{J\,kg^{-1}\,K}$ |
| $h$ | Specific enthalpy | $\mathrm{J\,kg^{-1}}$ |
| $k$ | Thermal conductivity | $\mathrm{W\,m^{-1}\,K^{-1}}$ |
| $l$ | Characteristic length | m |
| $m$ | Mass | kg |
| $n$ | Engine speed | rpm |
| $p$ | Pressure | bar |
| $q$ | Heat flux | $\mathrm{W\,m^{-2}}$ |
| $r$ | Pearson correlation coefficient | - |
| $t$ | Rate (of emission/deactivation processes) | $\mathrm{s^{-1}}$ |
| $t$ | Time | s |
| $U$ | Velocity | $\mathrm{m\,s^{-1}}$ |
| $u$ | Velocity fluctuation | $\mathrm{m\,s^{-1}}$ |
| $V$ | Velocity | $\mathrm{m\,s^{-1}}$ |
| $x$ | Mole fraction | - |
| $x, y, z$ | Spatial coordinates | m |

| Upper-case Latin letters | | Unit |
|---|---|---|
| Bi | Biot number | - |
| Fo | Fourier number | - |
| $A$ | Area | - |
| $E$ | Laser energy | mJ |
| $H$ | Shape factor | - |
| $M_k$ | Molar mass of species $k$ | $\mathrm{g\,mol^{-1}}$ |
| $n_k$ | Number density of species $k$ | $\mathrm{cm^{-3}}$ |
| $Q$ | Heat release | $\mathrm{kJ\,m^{-3}\,°CA^{-1}}$ |
| $S$ | Signal | - |
| $T$ | Temperature | K |
| Re | Reynolds number | - |

| Lower-case Greek letters | | Unit |
|---|---|---|
| $\alpha$ | Thermal diffusivity | $m^2\,s^{-1}$ |
| $\delta^*_{1/2}$ | Momentum/ displacement thickness | - |
| $\eta$ | Detection efficiency | - |
| $\eta$ | Dynamic viscosity | $kg\,m^{-1}\,s^{-1}$ |
| $\gamma$ | Surface tension | $mN\,m^{-1}$ |
| $\lambda$ | Air-fuel equivalence ratio | - |
| $\nu$ | Kinematic viscosity | $m^2\,s^{-1}$ |
| $\nu_L$ | Laser center frequency | nm |
| $\phi$ | Relative humidity | - |
| $\rho$ | Density | $kg\,m^{-3}$ |
| $\sigma_{abs}$ | Absorption cross section | - |
| $\tau$ | Decay time | s |

| Upper-case Greek letters | | Unit |
|---|---|---|
| $\Phi$ | Fuel-air equivalence ratio | - |
| $\Phi_f$ | Fluorescence quantum yield | - |
| $\Theta$ | Crank angle | °CA |

| Indices and Superscripts | |
|---|---|
| $'$ | Fluctuation |
| $'$ | Relative coordinate/variable |
| abs | Absorption |
| ac | Acetone |
| cyl | Cylinder |
| eDI | Electronic injection duration |
| eSOI | Electronic start of injection |
| f | Fluorescence |
| hEOI | Hydraulic end of injection |
| pf | Poolfire |
| ref | Reference |
| SI | Spark ignition |
| sv | Sideview (camera) |
| * | Per unit number density |

| | |
|---|---|
| $^*$ | Semi-locally scaled |
| $^+$ | Per unit mole fraction |
| $^+$ | Wall-scaled |
| $i, j, k$ | Integer index |
| $m$ | Magnitude |
| $n$ | Piston speed normalized |
| $x, y, z$ | Vector components |

### Operators and Mathematical symbols

| | |
|---|---|
| $\langle \ \rangle$ | Expected value |
| $\langle \ \rangle$ | Phase-average |
| $\sigma(\ )$ | Standard deviation |

| **Physical constants** | | **Value** |
|---|---|---|
| $c$ | Speed of light | $299\,792\,458\,\mathrm{m\,s^{-1}}$ |
| $h$ | Planck's constant | $6.626 \times 10^{-34}\,\mathrm{J\,s}$ |
| $R$ | Ideal gas constant | $8.3145\,\mathrm{J\,mol^{-1}\,K}$ |

### Abbreviations

| | |
|---|---|
| 2D2C | two-dimensional, two-component |
| BDC | bottom dead center |
| BL | boundary layer |
| CAD | crank angle degree |
| CCD | charge-coupled device |
| CCV | cycle-to-cycle variations |
| CMOS | complementary metal-oxide-semiconductor |
| CR | compression ratio |
| CTF | contrast transfer function |
| DI | direct injection |
| DNS | direct numerical simulation |
| EV | electric vehicles |
| ICE | internal combustion engine |
| ISC | inter-system crossing |
| ECN | Engine Combustion Network |
| EGR | exhaust gas recirculation |
| ETU | engine timing unit |
| FAR | fuel-air ratio |

| | |
|---|---|
| FoV | field of view |
| FPGA | field programmable gate array |
| FQY | fluorescence quantum yield |
| FWHM | full width at half maximum |
| GHG | greenhouse gas |
| HS | high-speed |
| IRO | intensified relay optic |
| IMEP | indicated mean effective pressure |
| IW | interrogation window |
| MFC | mass flow controller |
| OP | operating point |
| PAH | polycyclic aromatic hydrocarbon |
| PDF | probability density function |
| PFI | port fuel injection |
| PIV | particle image velocimetry |
| PTV | particle tracking velocimetry |
| RANS | Reynolds-averaged Navier-Stokes |
| RIM | refractive index matching |
| RoI | region of interest |
| LES | large-eddy simulation |
| LIF | laser-induced flourescence |
| LII | laser-induced incandescence |
| LRS | linear regression of the sum |
| LPF | large pool fire (area) |
| SNR | signal-to-noise ratio |
| SPF | small pool fire (area) |
| TDC | top dead center |
| TP | thermographic phosphor |
| TUDa | Technische Universität Darmstadt |
| UHC | unburnt hydrocarbon |
| UV | ultra violet |
| VR | vibrational relaxation |

# Chapter 1

# Introduction

Anthropogenic climate change is one of the greatest challenges of modern times. It is caused by the accumulated emission of greenhouse gases (GHG) from human activities over the last century [105, p. 5]. Even though these circumstances are unequivocally recognized in science and increasingly so in politics, society, and economy, global greenhouse gas (GHG) emissions have continued to rise from 2010 to 2019 [106, p. 7]. The reduction in emissions due to the COVID-19 pandemic and accompanying travel and supply chain restrictions has only been temporary, with 2022 reaching a new all-time high [102]. The transport sector contributed 15 % (8.7 $GtCO_2$-*eq.*) of direct emissions in 2019, with road transport accounting for 10 % globally [106, p. 237]. Of the road transportation sector, light- and heavy-duty vehicles are responsible for approximately 2/3 and 1/3 of emissions, respectively [101]. Driven by economic and population growth in regions starting from low motorization rates, these emissions are increasing. In addition, vehicle size and engine power have increased due to consumer preferences [106, p. 1056]. With current policies, it is likely that global warming[1] will exceed 1.5 °C during the 21st century [106, p. 14]. Therefore, a rapid acceleration of mitigation efforts is needed in order to limit warming below 2 °C [106, p. 14].

A number of countries have enacted increasingly stringent regulations to reduce vehicle emissions, such as the European Union's *European emission standard*, with *Euro 7* being set to take effect in 2025 [57]. Stricter regulations have succeeded in reducing both toxic and climate-affecting tailpipe emissions significantly [115]. However, the goal of reaching net zero GHG emissions demands far-reaching changes, with the deployment of low- or zero-emission technologies and changes in infrastructure as well as sociocultural and behavioral changes [107]. In addition, air pollution needs to be continuously reduced, since, for example, the current average exposure to fine particulates is four times higher than the guideline value recommended by the World Health Organization (WHO), with disproportionately higher effect on less developed communities [115].

Electrification of light-duty vehicles has large potential to reduce GHG emissions on a life cycle basis [107]. Driven by government incentives in China, Europe, and North America, the sale of electric vehicles (EV) has increased exponentially, with a market share of 14 %

[1] *Global warming* refers to the global (mean) surface temperature relative to the average between 1850 and 1900.

of all new cars sold in 2022 [103, p. 8]. In scenario projections[2], EVs account for 10 to 16 % of the road vehicle fleet by 2030 [103, p. 109]. Effective bans on the sale of internal combustion engines (ICEs), for example in the European Union[3] [32], California, and Canada by 2035 [106], will contribute to radically increasing the proportion of EVs in the road fleet, starting from a share of 1 % in 2020 [106, p. 258]. However, the still-dominant share of vehicles with ICEs emphasizes that multiple mitigation strategies are needed to rapidly reduce GHG emissions. Over the next 30 years, a large number of light-duty vehicles is likely to operate ICEs in conventional and hybrid configurations. This is particularly true in the heavy-duty vehicle and marine shipping sector, where higher power requirements are challenging to meet with the lower energy density of electrochemical storage compared to liquid fuels [106, p. 1065].

In consequence, the decarbonization of ICEs has to first be pursued by improving the thermodynamic efficiency through advanced engine concepts, electrification of sub-systems, and the use of low-carbon fuels. A promising example of low- and zero-carbon fuels is ammonia produced using low-carbon hydrogen for the shipping sector. For the use of ammonia as a fuel, there is the need for further development of combustion and storage technology [106, p. 1095]. Likewise, for both shipping and road transport, biofuels are of interest, if produced sustainably and in accordance with other climate change mitigation strategies. An important advantage of biofuels is that they can be used with existing technology and infrastructure, which offers short- and mid-term mitigation opportunities, particularly in developing countries [106, p. 1065]. On the other hand, biofuels remain more expensive than pursuing other strategies, such as improving fuel efficiency, electrification, and investing in alternative means of transportation [106, Fig. SPM.7].

A number of technology pathways is being explored to reduce fuel consumption and emissions (here with focus on light-duty gasoline vehicles): cylinder deactivation, primarily stoichiometric operation, variable turbine geometries, Miller cycle with early intake valve closing, mild hybridization (brake regeneration, actuated cam phaser), prechamber ignition, three-way catalyst and gasoline particulate filter, direct injection at 350 bar with multiple injections to reduce wall wetting and particle emissions in cold start and low speed situations, higher compression ratios, and downsizing with optimized turbocharging [106, 116].

Successful implementation of new technologies requires an understanding of the underlying physical processes, for example through a combination of experiments and simulations. These approaches are complementary, as high-resolution experiments can be used to investigate a number of different operating conditions for thousands of cycles and provide validation data for detailed simulations, which can consider fewer cycles but offer the full description of the physical state.

Engine downsizing and higher compression ratios increase the surface-to-volume ratio. Consequently, a higher fuel fraction is burnt in the vicinity of walls, which has implica-

[2]The *Stated Policies Scenario* (STEPS), which reflects existing measures and stated targets; and the currently more ambitious *Net Zero ($CO_2$) Emissions by 2050* (NZE) scenario, which is likely to limit warming to 1.5 °C [103, 107].

[3]Currently excluding engines burning $CO_2$-neutral fuels.

tions on heat losses and efficiency. Flame quenching, partial burning, and fuel wall films can lead to the emission of unburnt hydrocarbons (UHCs) and particulates. Since these processes are not comprehensively understood, further research is necessary.

## 1.1 Current State of Research

This section summarizes the current state of research concerning numerical and experimental studies of engine processes with the focus on the near-wall region and the topics wall temperature and heat flux, BLs, and wall film evaporation and emission formation. Parts of this section are taken from a previous publication and are reproduced with permission [E214].

### 1.1.1 Boundary Layers and Wall Heat Flux

Since the current trend of downsizing increases the surface-to-volume ratio, near-wall processes are growing in importance. Heat losses to the walls directly influence engine efficiency and pollutant emissions (e.g., unburnt hydrocarbons and CO formation [6]) as well as the thermal load of components. In spark-ignition (SI) engines, forced convection is regarded as the primary mechanism of near-wall heat transfer [97].

Near-wall heat transfer is governed by the highly turbulent bulk flow and its interaction with the mass and energy transfer processes in the BLs at combustion chamber walls. However, these transport processes in engines are still not well-understood. The near-wall flow in engines is unsteady as temperature, pressure, and velocity change continuously, meaning BLs vary spatially and are not fully developed compared to established, but idealized canonical flows [213].

**Hydrodynamic boundary layers** In numerical investigations like Reynolds-averaged Navier-Stokes (RANS) simulations and large-eddy simulations (LES), prohibitive computational costs typically prevent the resolution of BLs; instead, wall models are commonly used to predict transfer processes [193, 200, 209]. Recent studies, however, report significant deviations between engine BLs and idealized theories behind many of these wall models, namely, the law-of-the-wall [111, 161, 204, 216, 223].

Due to constraints in the optical access and the unsteady nature of engine flows, measurements of BLs inside engines are challenging. Early studies employed laser Doppler anemometry (LDA) near the cylinder head wall [64, 85, 192] and showed the small scale of engine BL, but were limited to single point measurements. With the advance of particle image velocimetry (PIV) and particle tracking velocimetry (PTV), two-dimensional flow gradients could be better resolved. Alharbi and Sick [4] achieved a resolution of 45 µm and observed sub-millimeter vortices moving through the outer BL. Jainski et al. [111] reported the absence of a logarithmic layer, a result which was replicated in further configurations by different authors [80, 204, 223]. Greene [81] conducted measurements at both the cylinder head and piston surface. Renaud et al. [204] further increased the

wall-normal resolution and Shimura et al. [223] and Yokoyama et al. [260] claimed an increasing resemblance to the laminar Blasius solution towards top dead center (TDC), by using the flat-plate coordinate $x$ as a fitting parameter. MacDonald et al. [161] investigated turbulent fluctuations in the BL and the contributions from the core flow and wall shear, and proposed a two-point correlation method to estimate the BL thickness.

Using the data from [80, 111], Ma et al. [159, 160] developed and evaluated wall models and reported significant advantages of models taking non-equilibrium effects into account. In recent times, high-fidelity simulations of engine-like configurations have been made possible [216, 217]. Schmitt et al. [216] found correlations between the local temperature field and heat flux, with fluctuations which were driven by wall-perpendicular flows. First studies used the resulting data to develop new, predictive wall models [21, 125]. Giannakopoulos et al. [79] achieved the first direct numerical simulation (DNS) of a single compression stroke in an optical engine. Boundary layers were found to deviate from ideal scenarios due to impinging flows and streamwise pressure gradients as well as anisotropic turbulence generation.

While previous studies provide an improved understanding to near-wall flows in engines, there are still open questions regarding the behavior of engine BL at higher, technically more relevant engine speeds and corresponding Reynolds numbers, and their temporal and spatial variation. In addition to experiments, future scale-resolving simulations will allow the study of these processes in all dimensions, but will require detailed data for validation and will still be limited in the attainable number of cycles. Using the Reynolds analogy, insights from velocity BLs can also be applied to thermal BLs, which are otherwise challenging to measure inside an engine.

**Wall temperatures and heat flux** Wall temperatures have been measured in engines as early as in 1969 [148]. Studies used thermocouples and derived wall heat fluxes by solving one-dimensional heat conduction equations, often on the basis of a Fourier series representation. Temperatures were found to increase by approximately 1 to 15 K during combustion, depending on the measurement location, before returning to the initial level during the expansion and exhaust stroke. Derived wall heat fluxes were in the order of 1 to 5 $\mathrm{MW\,m^{-2}}$. Nijeweme et al. [176] utilized fast response thermocouples at different positions and found a phase shift between the heat flux and the delta in bulk gas and wall temperature, which was explained by unsteady effects in the thermal BL. Other studies used thin-film temperature probes with improved response times on the piston and cylinder head [36]. Yokoyama et al. [260] combined this technique with high resolution PIV to measure in the velocity BL and found correlations between the wall-normal velocity and the heat flux. With the advent of optical diagnostics and phosphor thermometry, two-dimensional time-resolved surface temperature measurements became possible [72, 74, 226]. This was applied in investigations of flame-wall interactions by Ding et al. [42], where thermographic phosphors were combined with OH-LIF, which captured the flame development and allowed crank-angle-resolved observation of flame impingement and wall temperature rise. In [41, E215], thermographic phosphors, PTV, and $SO_2$-LIF were used to resolve the velocity BL, flame development, and wall temperatures in the engine of this work. The near-wall flow was observed to accelerate or decelerate depending on

the relative direction of the flame development. The temperature increase due to flame impingement was found to be highly consistent, with minor variation (<8 %) depending on the maximum cylinder pressure.

Ojo et al. [56, 178–180] used a constant volume chamber with artificial crevice to study the thermal BL and wall temperatures during flame-wall interaction. Using this chamber, [56, 179] employed fs/ps coherent anti-Stokes Raman spectroscopy (CARS) to resolve the thermal BL development during compression, flame-wall interaction, and gas expansion. Ojo, Escofet-Martin, and Peterson [180] combined $CH^*$ imaging with a highly sensitive thermographic phosphor and resolved cusps in the flame during propagation in the crevice. Wall temperatures in these regions of negative flame curvature were found to be consistently lower. Furthermore, wall heat fluxes were calculated based on the time-resolved temperature measurements.

Wall temperatures are an important boundary condition for numerical simulations. Since the optical engine in this work is simulated in a number of numerical investigations, an accurate knowledge of the temperature distribution is advantageous. Motored wall temperatures are currently not known, since measurements by [41] focused on the piston top in fired operation. In addition, temperatures in different locations such as the cylinder head and in the crevice are of interest. The same applies to the transient temperature evolution over hundreds of cycles to evaluate the effects of measurement start times and to facilitate comparison between numerical and experimental work. Finally, studying flame-wall interactions inside the crevice (the gap between piston and cylinder liner) would offer insight into heat transfer and quenching processes.

### 1.1.2 Fuel Wall Films and Soot

Wall films are known to be a source of hydrocarbon and particle emissions in spark-ignited direct-injection engines [48]. They originate from spray impingement on the valves, spark plug, and most importantly, on the cylinder liner and piston [31, 183]. The impinging fuel can mix with oil lubricant, which alters its properties and can act as a fuel source for later cycles [181, 182]. During vaporization of the film, fuel rich regions develop, which promote soot formation. The remaining residue and locally rich combustion can lead to permanent fouling of in-cylinder surfaces and reduce thermodynamic efficiency [231]. Early studies found emissions to be higher during cold-start conditions, when wall temperatures are lower [27, 259]. Song et al. [227] visualized fuel-rich pockets above the wall film with spectra infrared imaging and found ongoing oxidation in the expansion and exhaust stroke.

Fuel wall films are often accompanied by luminous regions of orange color, which were characterized as diffusion flames, leading to the naming *pool fire* [33, 140, 231, 263]. Stevens and Steeper [231] used LIF of gasoline to investigate fuel film formation on an optical piston and found it to correlate with pool fire. Kim et al. [130] visualized film formation on the cylinder liner. More detailed measurements by Stojkovic et al. [232] combined time-resolved $OH^*$-imaging and soot temperature as well as extinction diagnostics. Two sources of soot production were apparent for stratified charge operation:

First, partially premixed, rich zones in which the produced soot was rapidly oxidated further. Second, pool fires above the piston, lasting into the expansion stroke.

Koegl et al. [140, 141] measured soot using a volumetric extinction method and compared soot formation of fuels with varying ethanol content in combination with varying exhaust gas recirculation (EGR). They found that the high evaporation enthalpy of ethanol limits evaporation rates of fuel wall films, leading to fuel-richer zones and pool fire. Wall wetting mostly occurred during intake-stroke injections, while late injections during compression had a higher tendency for incomplete mixing and soot production in the gas phase. In contrast, higher ethanol content reduced soot production at higher EGR levels, showing the benefit of oxygenated fuels under low oxygen conditions. The high sensitivity of ethanol blends and soot production to the wall temperature was also seen in studies using refractive index matching (RIM) to measure wall films [43, 44, 94]. In a combined numerical and experimental investigation, Dahlander et al. [33] emphasized the need for realistic wall temperatures and materials as well as fuel blends. They found particle emissions to decrease rapidly for injection timings with reduced wall wetting and saw an influence of spray-flow interactions on the mixing quality.

A different interpretation of pool fires in stoichiometric conditions was proposed by Ketterer and Cheng [126, 127]. They concluded that pool fire cannot be a diffusion flame phenomenon because it occurs in oxygen-depleted burnt-gas regions. Instead, soot particles are formed due to high temperature pyrolysis in fuel rich regions during and after the combustion[4]. These soot particles are then visible due to their temperature radiation in the hot burnt gas.

Other experiments with endoscopic access in metallic engines were done by Shahbaz et al. [222], who showed that gasoline wall films survived approximately an order of magnitude longer than isooctane-toluene blends. Their data indicated that vaporization rates were not affected by flame-film interactions and that wall temperatures were the primary influencing factor. Furthermore, soot incandescence was found preferentially downstream of the fuel film and was delayed compared to the main combustion. The influence of transient operation was studied by Fach et al. [59, 60] in an endoscopic engine. Changes in the spray shape during dynamic load variations led to wall films and pool fires, which correlated with the velocity field below the spark plug.

More generic configurations allow the use of more advanced diagnostic combinations. Roque et al. [207, 208] employed diffuse back-illumination (DBI), Schlieren, RIM, natural luminosity imaging, and fuel component LIF in a constant volume chamber with an impinging spray and a laminar flame. The multi-component fuel was observed to undergo distillation processes, which affected soot formation. This was also true for entrainment flows above the film after combustion. Extinction measurements were considered a better approach to visualize soot than luminosity imaging. Jüngst and Kaiser [118, 119] studied pool fire in a constant flow facility with tracer and polycyclic aromatic hydrocarbon (PAH) LIF to characterize the wall film and gas phase, respectively, combined with soot laser-induced incandescence (LII) and a complementary DNS. They showed

[4]The term *pool fire* - albeit potentially misleading - is further used in the remainder to follow popular convention and refers to visible soot formation above a wall film.

that PAHs form in post-combustion regions adjacent to the film, with soot emerging in adjacent regions further away from the wall. Vaporization rates were approximately constant, which indicates a constant film temperature. Compared to the wall temperature, combustion had a minor effect on vaporization.

In summary, the importance of wall films for emission formation in direct-injection spark-ignition engines has been recognized in the past and important relationships between wall temperature, fuel composition, combustion, and fuel pyrolysis have been identified, though not comprehensively understood. Recent studies employed multi-parameter diagnostics in generic configurations and engines, highlighting the need to understand cause-and-effect chains. Against the background of stringent goals on pollutant emission and alternative fuels, a more detailed understanding of involved processes is necessary. Among others, this concerns the effect of the mixture field above the film on the combustion dynamics and the interaction between the flow, film vaporization, and soot formation processes.

## 1.2 Aim and Structure of this Work

The aim of this thesis is to address several open scientific questions about near-wall processes in engines, as described in their context in the previous section. Thereby, the approach is two-fold: Detailed experimental investigations expand the physical understanding of underlying processes, aiding in future research and technology development. In addition, data are needed for both informed model creation in numerical simulations and validation of predictive numerical tools, especially since the engine in this work is simulated by a number of other researchers in the context of the *Darmstadt Engine Workshop*. For this purpose, minimally invasive advanced laser diagnostics are used in an optically accessible engine to measure variables with high resolution in time and space.

In the context of heat transfer, a more comprehensive characterization of wall temperatures is of interest, since they are an important boundary condition for numerical simulations and experimental data synthesis. Therefore, wall temperatures were measured using thermographic phosphors in different locations inside the engine. Flame-wall interactions inside the crevice between cylinder liner and piston are studied and heat fluxes estimated.

Previous studies on velocity boundary layers showed that assumptions used in common wall models do not hold true in the non-equilibrium, turbulent engine flow. These studies were limited to lower engine speeds, such that an extension to more realistic speeds and therefore Reynolds numbers is of interest. A more detailed description of boundary layer characteristics beyond single locations and phase averages is needed. Furthermore, findings may be transferred to temperature boundary layers using the Reynolds assumption, as their direct probing in an engine environment is challenging. Therefore, high-resolution particle tracking velocimetry (PTV) was used to measure the velocity boundary layer on top of the piston and the high number of acquired cycles was used to analyze conditional statistics.

Near-wall convection and mixing processes affect the vaporization of fuel wall films, which are responsible for particle and UHC emissions. The development of so-called *pool fires* was investigated by combining simultaneous acetone LIF to measure the mixture field, luminosity visualizations, PIV, and flame detection. Thereby, multi-parameter relationships such as the interaction of flow, mixing field, and soot formation are analyzed.

To this end, Chapter 2 introduces relevant fundamentals concerning physical processes and diagnostics. Next, the engine test bench is described in Chapter 3. Subsequently, Chapter 4 gives an overview of the macroscopic flow field inside the engine. Chapter 5 presents thermographic phosphor measurements and results. In Chapter 6, the investigation on velocity boundary layers is presented. Finally, Chapter 7 discusses engine wall films and pool fires, before Chapter 8 summarizes the results and presents an outline for further research.

# Chapter 2

# Fundamentals

## 2.1 Research Object

### 2.1.1 Engine Processes

In this section, some relevant relations in the engine context are given. For a comprehensive book on engine fundamentals, the reader is referred to Heywood [97].

#### 2.1.1.1 Geometric Parameters

The piston position is defined through the kinematic geometry of the crank shaft and connecting rod. The lowest and highest piston position are called bottom dead center (BDC) and top dead center (TDC), respectively. Thereby, the current crank angle (CA) $\Theta$ is given in crank angle degree (CAD). In this work, this angle is counted from $-360\,°\mathrm{CA}$, the beginning of the intake stroke, over $0\,°\mathrm{CA}$, which is ignition TDC, to $360\,°\mathrm{CA}$, which marks the end of a cycle. The geometric compression ratio

$$r_\mathrm{c} = \frac{V_\mathrm{d} + V_\mathrm{c}}{V_\mathrm{c}}, \tag{2.1}$$

is the ratio of the combustion chamber volume at BDC to the clearance volume $V_\mathrm{c}$, whereby $V_\mathrm{d}$ denotes the displacement or swept volume. A useful metric for scaling of engine processes is the average piston velocity

$$v_\mathrm{p} = 2 l_\mathrm{p} n, \tag{2.2}$$

with the piston stroke $l_\mathrm{p}$ and the engine speed $n$.

#### 2.1.1.2 Thermodynamic

Work is produced in the cylinder as the increasing gas pressure during combustion pushes the piston downwards during the expansion stroke. The *indicated work per cycle* is obtained by integrating the pressure-volume work

$$W = \int p_\mathrm{cyl} \,\mathrm{d}V, \tag{2.3}$$

with the cylinder pressure $p_{\mathrm{cyl}}$ and change in cylinder volume $\mathrm{d}V$. In a four-stroke cycle, two definitions are commonly used: The *gross* indicated work per cycle is the work delivered to the piston over the compression and expansion stroke only. In contrast, the *net* indicated work per cycle includes all four strokes, with the intake and exhaust phase. For comparison inbetween engines, the indicated work is usually normalized to the displaced volume

$$\mathrm{IMEP} = \frac{W}{V_{\mathrm{d}}}, \tag{2.4}$$

which is called indicated mean effective pressure (IMEP) and has the units of a pressure.

A certain mixture of fuel and air is needed for combustion. The ratio of oxygen to fuel molecules for stoichiometric combustion depends on the fuel composition. Therefore, the *air-fuel equivalence ratio*

$$\lambda = \frac{m_{\mathrm{air}}}{m_{\mathrm{fuel}}} \Bigg/ \left(\frac{m_{\mathrm{air}}}{m_{\mathrm{fuel}}}\right)_{\mathrm{stoichiometric}} \tag{2.5}$$

is a useful normalized value, which indicates rich ($\lambda < 1$) and lean ($\lambda > 1$) operation.

Due to the piston movement during the compression stroke, the in-cylinder gas is compressed, which increases temperature and pressure. With the assumption of an isentropic process[5], thermodynamic properties of the in-cylinder content can be calculated:

$$\left(\frac{T_2}{T_1}\right)^{\frac{1}{\gamma-1}} = \left(\frac{p_2}{p_1}\right)^{\frac{1}{\gamma}} = \frac{V_1}{V_2} = \frac{\rho_2}{\rho_1}, \tag{2.6}$$

with the isentropic coefficient (heat capacity ratio) $\gamma$, pressure $p$, temperature $T$, volume $V$, and density $\rho$. The polytropic process can be described with

$$\frac{T_2}{T_1} = \frac{p_2}{p_1} \cdot \frac{V_2}{V_1}. \tag{2.7}$$

### 2.1.2 Heat Transfer

Approximately 20 to 30 % of the fuel energy input of an engine is lost to the coolant [97]. This obviously affects the overall thermodynamic efficiency, though only a fraction of these losses, namely the heat loss during combustion and expansion, could be theoretically utilized. In addition to the effect on the fuel consumption, a sophisticated thermal load management is needed to ensure the system's lifetime. Depending on the engine phase and the condition of the in-cylinder gas, the heat is transferred from the cylinder walls to the in-cylinder gas or vice versa. The near-wall region, which is colder than the gas during combustion, and crevice volumes in particular are a major source of emissions [6].

[5]Measurements by Bürkle et al. [26] show that this assumption is valid for the global temperature throughout most of the compression stroke.

According to Fourier's law for a solid, stationary body in the one-dimensional case:

$$\dot{q}_n = -k \cdot \frac{\mathrm{d}T}{\mathrm{d}n}, \tag{2.8}$$

the heat flux in wall normal direction $\dot{q}_n$ can be described by the thermal conductivity $k$ and the temperature gradient $\mathrm{d}T/\mathrm{d}n$ [19]. After generalizing to three dimensions and transforming this equation to represent unsteady heat conduction, one arrives at the heat equation:

$$\frac{\mathrm{d}T}{\mathrm{d}t} = \alpha \cdot \nabla^2 T \quad \text{with} \quad \alpha = \frac{k}{\rho \cdot c_\mathrm{p}}. \tag{2.9}$$

Here, the temporal change in temperature is only dependent on the temperature's curvature and the thermal diffusivity $\alpha$, which is the ratio of thermal conductivity $k$ and the volumetric heat capacity, the product of density $\rho$ and specific heat capacity $c_\mathrm{p}$ [19]. In a substance with a high thermal diffusivity, such as gases and metals, temperature gradients are equalized more rapidly. For three-dimensional problems, Equation 2.9 can usually only be solved numerically. In the case of one-dimensional, unsteady heat flux through a half body with known, time-dependent surface temperature, solutions in the form of Fourier series [5] and Duhamel's integrals [235] can be calculated. The latter will be applied in Chapter 5 (Equation 5.2).

So far only stationary bodies were discussed. In a fluid flow, heat is transferred by both heat conduction (diffusion) and convection (fluid motion). Typically, no analytical solution is available for these problems. In the case of heat transfer in a boundary layer, the definition of Equation 2.8 can be used:

$$\dot{q} = h(T_{wall} - T_{\mathrm{flow},\infty}). \tag{2.10}$$

Thereby, the thermal conductivity is replaced by the heat transfer coefficient $h$ [19]. This heat transfer coefficient is typically calculated based on empirical formulas and dimensionless numbers, like the Nusselt and Prandtl number. Ding [41] estimated an average value of $\alpha = 1000\,\mathrm{W\,m^{-2}\,K^{-1}}$ at in-cylinder surfaces in the engine of this work.

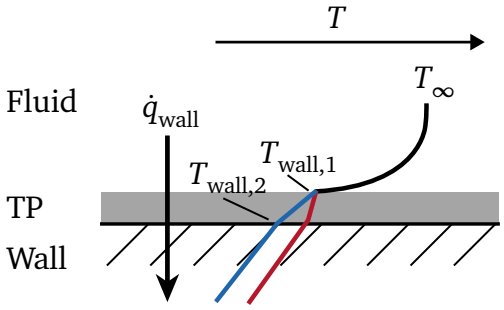


Figure 2.1: Heat transfer at a wall with TP coating. Two different temperature profiles resulting from two different thermal conductivities of the TP layer are shown.

The Biot number:

$$\mathrm{Bi} = \frac{h}{k} L, \tag{2.11}$$

with the characteristic length $L$, is a dimensionless heat transfer quantity. It is the ratio of thermal resistance for conduction inside a body to the resistance for heat transfer in the fluid. A Biot number much smaller than 1 indicates a nearly uniform temperature field inside the body compared to the fluid.

The Fourier number:

$$\mathrm{Fo} = \alpha \frac{t}{L^2} = \frac{t}{t_\mathrm{d}}, \tag{2.12}$$

is a dimensionless time. It represents the ratio of the time of a process $t$ to the time scale for heat diffusion $t_\mathrm{d} = L^2/\alpha$. If the Fourier number is much bigger than one, enough time has passed for a body which has one side heated to a certain temperature to approach a constant temperature throughout the body.

The importance of these relations is shown in Figure 2.1. In the case of a thermographic phosphor (TP) coating on a wall, the coating's thickness and material properties have to be designed such that the temperature gradient in the coating is small, in order to measure accurate wall temperatures. If the thermal diffusivity $\alpha$ of the coating is high compared to that of the wall and/or the fluid boundary layer, the coating will follow temperature changes of the system quickly. Furthermore, temperature gradients inside the coating are small if the thermal conductivity $k$ is high and the thickness of the coating small.

### 2.1.3 Vaporization

In this section, a brief overview of vaporization regimes is given. A liquid film on a surface below the saturation temperature $T_\mathrm{S}$, also called boiling point, will be subject to *evaporation*. In this process, molecules on the liquid-gas interface transition from the liquid into the vapor phase. This continues, until the vapor (partial) pressure reaches the equilibrium vapor pressure, where condensation and evaporation are in equilibrium. In the case of an open environment, the liquid volume could fully evaporate. Liquids with high vapor pressure are called *volatile*. Vaporization is a endothermic process, the system looses energy in the amount of the enthalpy of vaporization $\Delta H_\mathrm{vap}$ at the current temperature.

*Boiling* occurs if the wall temperature $T_\mathrm{W}$ exceeds the saturation temperature $T_\mathrm{S}$. First, the heat is transported by convection to the surface, where the liquid vaporizes. At higher temperatures, vapor bubbles form at the wall-liquid interface, a regime called nucleate boiling (see Fig. 2.2). With further increase of the wall temperature, the *Leidenfrost* point is reached. Here, the heat flux at the wall surface is high enough for a continuous vapor layer to exist. This vapor layer insulates the liquid against the wall. Consequently, the heat flux decreases and the time for full vaporization of the liquid volume $t_\mathrm{vap}$ increases. The shown processes are a function of the system pressure, since, for example, the sat-

uration temperature and the height of the vapor layer in the Leidenfrost regime change with pressure.

## 2.1.4 Boundary Layer Flow

Technical flows are often bounded by walls, such is the case in an engine. Due to the *no-slip* condition[6], the flow is slowing down near the wall in a region of high gradients perpendicular to the wall, which is called boundary layer. In this section, parameters for the description of boundary layers are first presented. Then, the universal law of the wall is described.

### 2.1.4.1 Boundary Layer Parameters

A common parameter to describe BL is the boundary layer thickness

$$\delta_c = y' \big|_{u=c\cdot u_\infty}, \tag{2.13}$$

where $y'$ denotes the wall distance at which the velocity first reached a fraction $c$ of the wall-parallel bulk velocity $u_\infty$. Typically, for $c$ a value of 0.99 is used, though it must be noted that it's experimental derivation is susceptible to noise. More robust measures to

[6]Though the no-slip condition has been found to be valid under many circumstances and is often considered "textbook knowledge", the concept of fluid slip at the wall was already discussed in times of Navier and Stokes. Advances in experimental methods led to *slip* being verified for microscopic flows in confined geometries, such as sealing gaps, defined by a *slip length* [175].

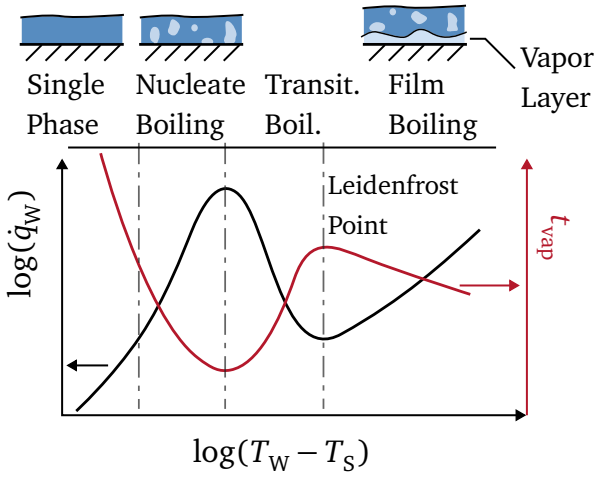


Figure 2.2: Nukiyama curve showing vaporization regimes for pool boiling. Adapted from [14, 230].

characterize the BL are:

$$\delta_1^* = \int_0^\delta \left(1 - \frac{\rho(y)u(y)}{\rho_\infty u_\infty}\right) \mathrm{d}y \qquad \text{displacement thickness,} \tag{2.14}$$

$$\delta_2^* = \int_0^\delta \frac{\rho(y)u(y)}{\rho_\infty u_\infty}\left(1 - \frac{\rho(y)u(y)}{\rho_\infty u_\infty}\right) \mathrm{d}y \qquad \text{momentum thickness,} \tag{2.15}$$

which consider location-dependent densities due to thermal gradients. The displacement thickness $\delta_1$ represents the distance by which "the inviscid outer flow is displaced outwards by the drop in velocity in the boundary layer" [213]. In a similar manner, the momentum thickness $\delta_2^*$ can be understood as the distance by which a hypothetical inviscid flow at a wall is displaced, such that the same momentum flow rate occurs as in the real fluid.

A Reynolds-number can be defined from the momentum thickness:

$$\mathrm{Re}_{\delta_2^*} = \frac{u_\infty \delta_2^*}{\nu}, \tag{2.16}$$

with the kinematic viscosity $\nu$. It can be used to predict the BL's transition from laminar to turbulent. Of similar use is the shape factor

$$H = \frac{\delta_1^*}{\delta_2^*}, \tag{2.17}$$

as a ratio of displacement and momentum thickness. It was found to transition from 2.59 in the laminar region to 1.4 in the turbulent region of a flat plate boundary layer [213, p. 423].

#### 2.1.4.2 The Law of the Wall

A historically important and often used model to describe turbulent boundary layers is the *law of the wall*. It was derived for idealized channel flows and flows over a flat plate [194, 195]. The following section is based upon the derivation in [194, p. 269]. For more detailed information, the reader is referred to [194, 213].

A flow along the $x$-direction with the wall-perpendicular coordinate $y$ is considered. The total shear stress $\tau(y) = \rho\nu\,\mathrm{d}\langle U\rangle/\,\mathrm{d}y - \rho\langle uv\rangle$, is the sum of the viscous stress (with the density $\rho$, kinematic viscosity $\nu$ and derivative of the mean flow in $x$-direction $\langle U\rangle$ with respect to $y$ ) and the Reynolds stress (with the fluctuating velocity components $u$ and $v$ in $x$- and $y$-direction, respectively). Due to the the no-slip condition at the wall, the wall shear stress

$$\tau_\mathrm{w} \equiv \rho\nu \left(\frac{\mathrm{d}\,\langle U\rangle}{\mathrm{d}y}\right)_{y=0}, \tag{2.18}$$

is solely defined by the viscous contribution, in stark contrast to the bulk flow. Due to this importance of viscous parameters close to a wall, viscous scales will be defined. The

*friction velocity*

$$u_\tau \equiv \sqrt{\frac{\tau_w}{\rho}} \tag{2.19}$$

and the *viscous lengthscale*

$$\delta_\nu \equiv \nu \sqrt{\frac{\rho}{\tau_w}} = \frac{\nu}{u_\tau}. \tag{2.20}$$

Based on this, the wall distance can be measured in viscous lengths or *wall units*

$$y^+ \equiv \frac{y}{\delta_\nu} = \frac{u_\tau y}{\nu}, \tag{2.21}$$

which is similar to a local Reynolds number, indicating the relative importance of viscous and turbulent forces, which changes throughout the boundary layer. The scaled velocity can be defined as

$$u^+ \equiv \frac{\langle U \rangle}{u_\tau}. \tag{2.22}$$

From a dimensional analysis, one can conclude that the velocity gradient depends on just two non-dimensional parameters

$$\frac{\mathrm{d}\langle U \rangle}{\mathrm{d}y} = \frac{u_\tau}{y} \Phi \left( \frac{y}{\delta_\nu}, \frac{y}{\delta} \right), \tag{2.23}$$

with the boundary layer thickness $\delta$ and an unknown function $\Phi$. Thereby, both the inner, viscous scales as well as the outer scales are incorporated by $\delta_\nu$ and $\delta$, respectively. One can now postulate that there is a *inner layer* close to the wall ($y/\delta \ll 1$), where just the viscous scales play a role and the flow is independent of outer layer scales like $\delta$ and $U_\infty$, and arrive after some transformations at

$$u^+ = f_w(y^+), \tag{2.24}$$

the *law of the wall*. It is apparent that in this region, $u^+$ depends solely on the wall distance $y^+$.

After considering the boundary conditions at the wall and series expansion, the equation for the *viscous sublayer* is derived

$$u^+ = f_w(y^+) = y^+ + \mathcal{O}(y^{+4}). \tag{2.25}$$

For a wide range of flows, the departure from the linear relation $u^+ = y^+$ is negligible in the viscous sublayer ($y^+ < 5$).

In the outer parts of the inner layer, viscosity's influence is diminishing. After transformation of Eq. 2.23, one arrives at

$$u^+ = \frac{1}{\kappa} \ln(y^+) + C, \tag{2.26}$$

which is often called *log law*, although Schlichting and Gersten [213, p. 524] make the case that *logarithmic overlap law* is a more suitable term[7]. Hereby, $C$ and $\kappa$ are constants, which are not universal, but determined by numerous experiments to be

$$\kappa = 0.41, \qquad C = 5.0\text{-}5.2, \tag{2.27}$$

whereby in this work $B = 5.0$ is adopted, unless specified otherwise.

This description is valid for a wide range of parameters, however, some important limitations are relevant. The flow is assumed to be in equilibrium, fully developed and to have zero-pressure gradients. Figure 2.3 shows wall-scaled mean velocity profiles from numerical simulations and the theoretical law of the wall. First focusing on the case without pressure gradients (blue), the boundary layer adheres well to the logarithmic law. It is important to note that sufficiently high Reynolds numbers $\mathrm{Re}_{\delta_2^*}$ (here 1800) are needed for a logarithmic layer to appear. At lower $\mathrm{Re}_{\delta_2^*}$, e.g. $\mathrm{Re}_{\delta_2^*} = 300$, the outer and inner layer overlap (not shown). In effect, the outer layer starts before a log layer can form [204]. In technical configurations with higher free stream turbulence, a developed turbulent boundary layer with a log region can exist down to $\mathrm{Re}_{\delta_2^*} \approx 100$ [233], which is relevant for the engine flows of this work.

Focusing again on Fig. 2.3 another influence of non-idealized flows can be observed: In flows with adverse pressure gradients (positive gradients in flow direction, red), the flow decelerates, with the velocity profile lying below the log law before overshooting in the outer layer. For a favorable pressure gradient ($\mathrm{d}p/\mathrm{d}x < 0$, yellow), the flow accelerates and overshoots in the log layer. In a different type of flow, namely impinging wall jets, the boundary layer can be observed to develop with increasing distance from the stagnation point (green). Far from the wall, velocities drop to zero due to the recirculation beyond the jet. Idealized channel flows are often the basis for wall models in numerical simulations. Therefore, it is of interest how engine boundary layers with transient fluid properties, pressure gradients, surface roughness and a turbulent bulk flow deviate from them.

#### 2.1.4.3 Semi-local Scaling

As discussed, the law of the wall was derived for constant fluid properties throughout the flow. Inside an engine, the gas density, pressure, and temperature change continuously during compression (and of course combustion). Therefore, temperature gradients at the wall need to be taken into account. Since the temperature profile is not known, the Reynolds analogy was applied, which equates the temperature profile to the qualitative shape of the velocity profile. This analogy holds, if both the Prandtl number and the turbulent Prandtl number are unity. The Prandtl number in air is a function of temperature and close to 0.7. The turbulent Prandtl number is likely closer to unity [123]. However, in chapter 6 (Fig. 6.7), the Reynolds analogy was found to be a valid estimation of the real temperature profile.

[7] Next to the log law, also *power laws* models are applicable to describe this region [194].

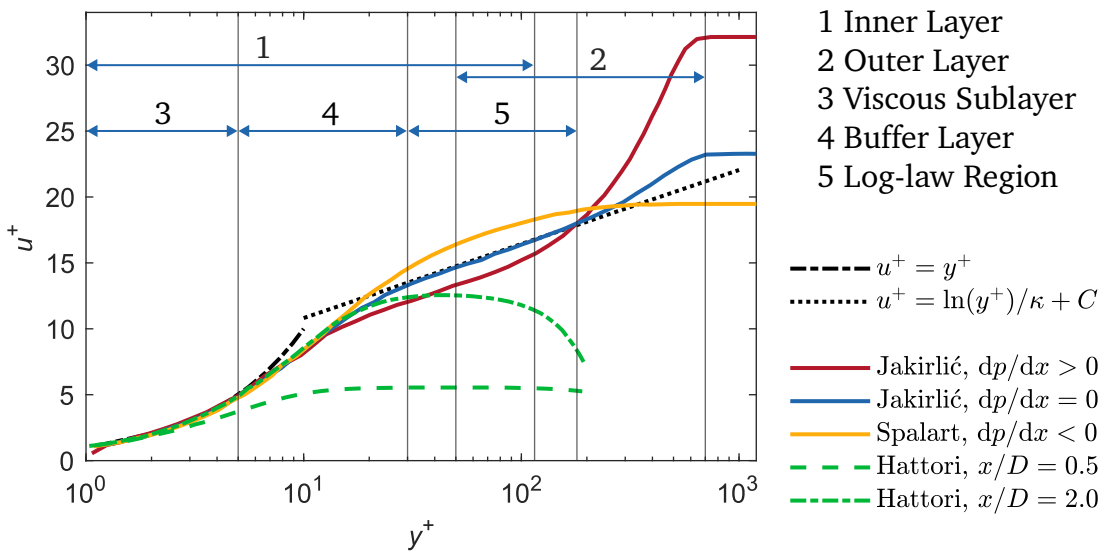


Figure 2.3: Mean velocity profiles of different flows in wall-scaled coordinates. Data labeled Jakirlić and Spalart represent flat-plate boundary layers subjected to different pressure gradients (digitized and adapted from [204]). $\mathrm{Re}(\delta_2^*)$ decreases from 3350 (red) to 1800 (blue) and 379 (yellow). Jakirlić employed a RANS simulation with a near-wall Reynolds stress model [112], Spalart [228] conducted a DNS. The description of regions 1-5 relates to the zero-pressure gradient curve (blue). Hattori and Nagano [91] performed a DNS of an impinging wall jet. $x/D$ corresponds to a dimensionless distance from the stagnation point. A value of $C = 5.2$ is used in the log law. Data are digitized from publications using [206].

Wall temperatures were measured in Chapter 5 and are mostly constant throughout a motored cycle. Bulk gas temperatures were calculated with an isentropic relation (Eq. 2.6, see also Fig. 5.8). The density $\rho(y)$ was calculated with the ideal gas law. Together with the dynamic viscosity $\mu(y)$ from the Sutherland law [234], the kinematic viscosity $\nu(y)$ was derived. To calculate $\mathrm{Re}_{\delta_2^*}$, the kinematic viscosity $\nu_\mathrm{f}$ based on the film temperature, that is the average of wall and bulk temperature, is used.

With the friction velocity

$$u_\tau^* = \sqrt{\frac{\tau_\mathrm{w}}{\rho(y)}}, \tag{2.28}$$

using the wall shear stress from Eq. 2.18, one arrives at the semi-local scaling [216]:

$$u^* = \frac{\langle U \rangle}{u_\tau^*} \tag{2.29}$$

$$y^* = \frac{y u_\tau^*}{\nu(y)}. \tag{2.30}$$

### 2.1.5 Soot

The formation of soot in a combustion environment is a multi-step process, which is covered in the following section. Thereby, hydrocarbon fuel molecules containing a few carbon atoms transition from the gas phase to a solid phase with millions of carbon atoms [164]. This process can occur both simultaneously or separately to combustion processes. A schematic of the process is shown in Fig. 2.4. The following description is based on Tree and Svensson [241] and Mansurov [164], additional information can be found e.g. in [169, 205].

**Fuel Pyrolysis** During pyrolysis reactions, the molecular structure of hydrocarbons is altered without significant oxidation. Pyrolysis is often - but not always - endothermic and therefore highly temperature dependent. The resulting species are precursors for soot, such as acetylene $C_2H_2$, ethylene $C_2H_4$, and benzene $C_6H_6$. Through the addition of alkyl groups, the size of molecules increases and PAH are formed. This precursor formation is in competition with precursor oxidation by hydroxyl radicals, OH. Since the rate of oxidation increases faster with temperature than the rate of pyrolysis, higher temperatures lead to less soot in premixed flames and more soot in diffusion flames. Correspondingly, oxygenated fuels like acetone reduce the soot tendency [203], because the additional oxygen inhibits the formation of soot precursors [132].

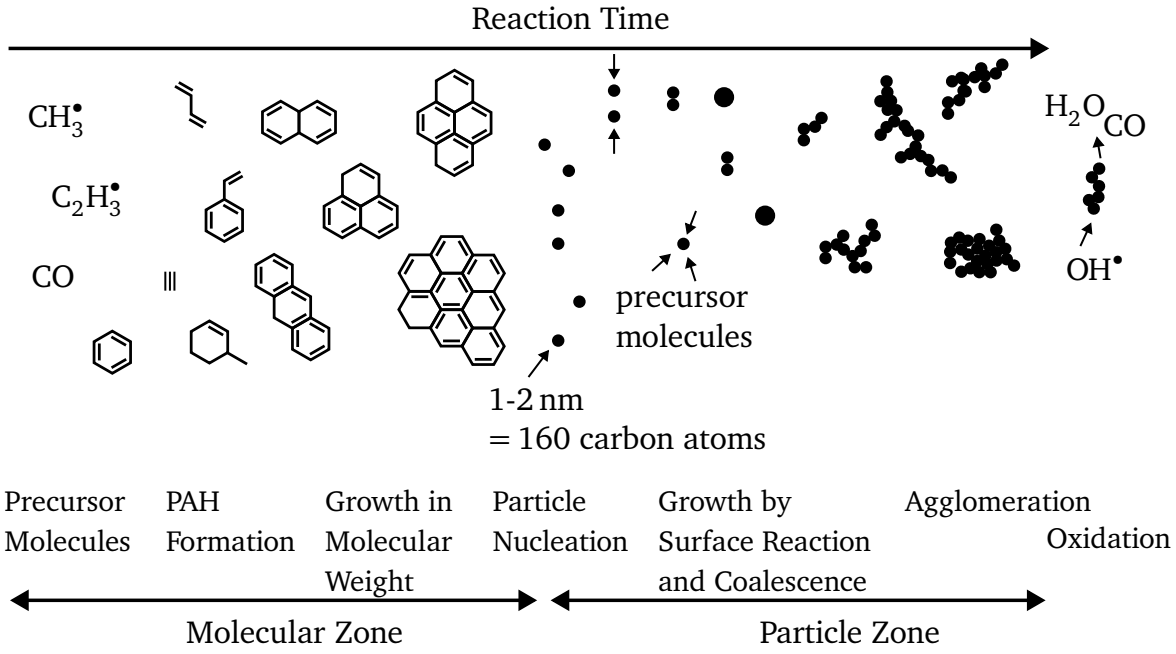


Figure 2.4: Soot formation processes from the gas phase to solid, agglomerated particles. Adapted from [114].

**Nucleation** Through continuous growth in molecular size, nucleation is the transition from the gas phase to first detectable particles with a size in the order of 1.5 to 2 nm. These particle nuclei represent a minor contribution to the total soot mass, but provide sites for surface growth. A number of mechanisms describing the growth of PAH have been proposed [205]. The initial nucleation in flames is typically restricted to the primary reaction zone, with the highest temperature and radical concentration.

**Surface Growth** In this process, the nucleated soot particles grow by gaining mass. The hot reactive surface accepts gas-phase hydrocarbons such as acetylen or PAH-radicals. In consequence, the total soot mass increases at a constant number of particles, reaching a size of up to 50 nm. Due to a higher number of reactive sites, small particles show higher growth rates than larger particles. This process may continue in cooler regions outside the primary reaction zone (in case of a flame), where initial nucleation of particles is not possible anymore.

**Coalescence and Agglomeration** If primary particles collide and coalesce, the number of particles decreases, while the total mass stays constant. Two approximately spherical particles thereby form a single larger particle, which is spherically shaped. In contrast, during agglomeration, primary particles stick together to form large, fractal clusters of primary particles, while maintaining their shape. Depending on the conditions, chain-like or clumped particles may develop. In the case of Diesel engines, this process continues even after combustion, reaching sizes from 0.1 to 2 µm.

**Other Influences** Soot components may be oxidized by OH and $O_2$, a process which may take place any time during the soot formation. If a carbon atom has been partially oxidized to CO, it will no longer participate in soot formation.

Temperature is the most influential factor on the sooting process, as it determines soot formation and oxidation rates. Minimum temperatures for soot inception are around 1400 K. Due to increasing rates of collision, higher pressures increase soot formation rates, with dependencies of up to $p^2$ being reported. Another important factor is the equivalence ratio. Increased oxygen content typically suppresses soot formation. Since partial oxidization to CO is sufficient to remove carbon from soot formation reactions, equivalence ratios above 2-3 are needed for soot formation [122, 132], whereby the exact fuel composition plays a role.

## 2.2 Optical Diagnostics

### 2.2.1 Photophysics of Excitation and Emission

In the following section, a brief introduction to the photophysics of fluorescence and phosphorescence is given. For a comprehensive discussion, the reader is referred to text-

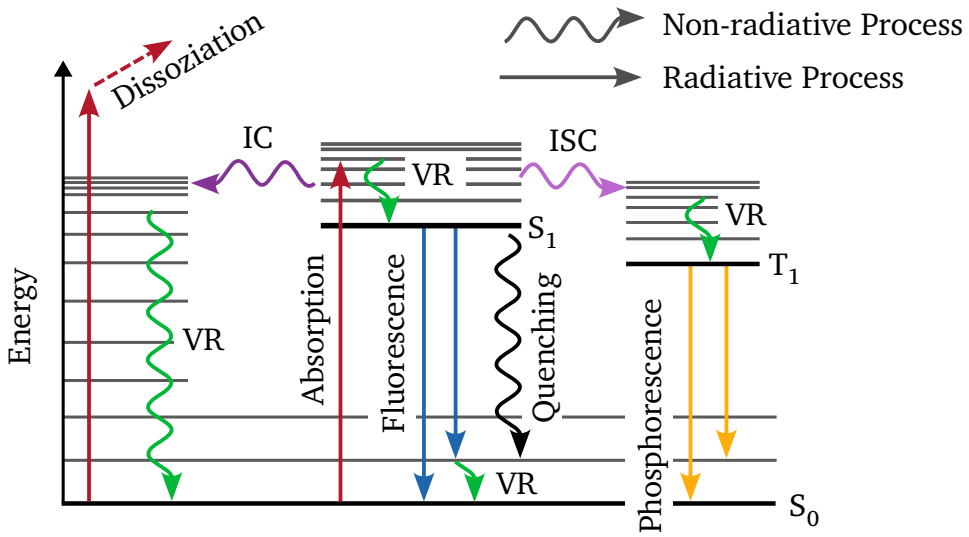


Figure 2.5: Jabłoński diagram for fluorescence and phosphorescence, following [145, 219, 265].

books and publications such as [88, 219], on which the following text is based, or [52, 145].

The change of internal energy in matter may be separated into rotational, vibrational, and electronic energy changes. Each of these modes have different magnitudes. Electronic transitions, which generally are accompanied by additional changes in vibrational and rotational energy, correspond to the energy range of visible and ultra-violet (UV) photons. *Planck's Law* gives the energy of a photon

$$\Delta E = h\nu = hc/\lambda, \tag{2.31}$$

with the wavelength $\lambda$, the frequency $\nu$, and Planck's constant $h = 6.63 \times 10^{-34}$ Js. Figure 2.5 shows the energy transfer processes for a molecule or atom after absorption of a photon.

Three discrete electronic energy states, the ground state $S_0$ and excited states $S_1$ and $T_1$ are visible, together with corresponding vibrational modes in thinner gray lines. A photon is absorbed with a certain probability, which can be expressed as the *absorption cross section* $\sigma_A$. After absorption, different radiative and non-radiative energy depopulation pathways are possible. The molecule dissociates if excitation exceeds bonding forces. Lower energies result in an excited electronic state, such as $S_1$, often with additional vibrational excitation. Collisions with surrounding molecules transfer the molecule to lower vibrational levels within the excited electronic state, which is called vibrational relaxation (VR). This process is very fast ($10^{-14}$ to $10^{-12}$ s) and typically brings the molecule to the lowest vibrational level. However, since it happens through inter-molecular collisions, the rate depends on the phase state (liquid or gaseous) and pressure.

The $S_1 \rightarrow S_0$ transition due to spontaneous emission of a *fluorescence* photon is fast and usually occurs in an interval of 1-100 ns. Due to the vibrational relaxation, the fluorescence photon has less energy than the excitation photon, which is called *Stokes*- or red-shift. This - in the context of laser diagnostics sometimes desired - process competes with other radiating and non-radiating loss paths. First, internal conversion (IC) denotes the spin-allowed transition between states, where the energy of the electronically excited state is given off to vibrational modes, thus converting the excitation energy into heat. Internal conversion needs an overlap in singlet energy states, such that it is less relevant for typical fluorescence species with a large gap between $S_1$ and $S_0$. Second, in non-radiative, spin-forbidden inter-system crossing (ISC) the molecule transitions between states of different spin multiplicity $S_1$ (anti-parallel spins; singlet) $\rightarrow T_1$ (parallel spins, triplet). For ketones, this process is three orders of magnitude faster than spontaneous $S_1 \rightarrow S_0$ emission. Furthermore, it is the prerequisite for the spontaneous emission of a *phosphorescence* photon. As the transition $T_1 \rightarrow S_0$ is spin-forbidden, meaning there is a transition in spin-multiplicity, angular momentum is not conserved. Therefore, an additional interaction is needed, for example in the form of a collision with another molecule. Consequently, triplet lifetimes are significantly longer than singlet lifetimes, leading to phosphorescence emission in the order of microseconds to seconds (and hours).

The probability of a fluorescence photon emission is called fluorescence quantum yield (FQY):

$$\Phi_\mathrm{f} = \frac{\tilde{k}_\mathrm{fl}[M^*]}{\tilde{k}_\mathrm{abs}[M][h\nu]}, \tag{2.32}$$

where the concentration of excited molecules $[M^*]$, which decay with the fluorescence rate coefficient $\tilde{k}_\mathrm{fl}$, is compared to the absorption rate $\tilde{k}_\mathrm{abs}[M][h\nu]$ with $[h\nu]$ being the photon density. The FQY can also be understood as the ratio of rate coefficients of fluorescence and total depopulation processes. A similar expression is valid for phosphorescence.

Another deactivation mechanism of excited molecules is collisional *quenching*. Thereby, an electronically excited molecule can transfer its electronic energy to a neighboring molecule. Especially $O_2$, which in the ground state is a triplet, is a strong quenching partner of some fluorescence species, as it facilitates the transition into triplet states. Aromatic molecules are strongly quenched by oxygen, whereas ketones are less affected. As with every collision-dependent process, ambient conditions like pressure, temperature and collision partner concentrations determines the quenching probability (and thus the FQY). Longer lifetimes of excited states, such as triplet states during phosphorescence, are more likely to be quenched before a radiative transition occurs.

### 2.2.2 Thermographic Phosphor Thermometry (TPT)

The phosphorescence emission mentioned in the previous section can be utilized for optical surface temperature measurements. Thereby, a thin layer of so-called thermographic phosphors (TPs) is applied to the respective surface. These TPs are solid, often powdery materials consisting of a ceramic host material doped with rare-earth ions, called

activators [3]. In this work, laser radiation is used to excite the TP, where typically the activator material absorbs the excitation energy. Since most of the activator ions in the crystalline host matrix are isolated from each other, non-radiative deactivation is less likely and radiative emission in form of phosphorescence is the dominating deactivation pathway [3].

Characteristics of this emission depend on the TP's temperature. Two major thermometry approaches are possible [24]: First, a time-integrated method that evaluates the intensity of a single spectral band or the ratio of two spectral bands. Second, time-resolved methods evaluate the luminescence characteristics in the time or frequency domain. In the frequency domain, the temperature-dependent phase shift between a modulated excitation and the resulting emission is measured. On the other hand, measurements in the time domain evaluate the temperature-dependent decay of the luminescence intensity. This approach is typically the most robust and achieves the highest accuracy and precision [24, 70]. Consequently, a decay-time measurement approach is chosen in this work. The following section will focus on relevant aspects.

The time-dependent luminescence intensity $I(t)$ can be modeled as

$$I(t) = I_0 \exp\left(-t/\tau(T)\right), \tag{2.33}$$

where $I_0$ is the initial intensity, $t$ is the time after end of excitation, and $\tau(T)$ is the temperature-dependent decay time (lifetime) [24]. The time-dependent population of the excited state $N^*(t)$ follows the differential equation

$$\frac{\mathrm{d}N^*(t)}{\mathrm{d}t} = -(R_\mathrm{R} + R_\mathrm{NR})N^*(t), \tag{2.34}$$

with the rate of radiative and non-radiative deactivation processes ($R_\mathrm{R}$ and $R_\mathrm{NR}$, respectively. One solution to this equation is

$$N^*(t) = N_0^* \exp\left(-t\left(R_\mathrm{R} + R_\mathrm{NR}\right)\right), \tag{2.35}$$

with $N_0^*$ denoting the population at $t = 0$ [24]. As the luminescence intensity is proportional to population of the excited state, one finds

$$\tau = 1/(R_\mathrm{R} + R_\mathrm{NR}). \tag{2.36}$$

Since the rate of non-radiative deactivation processes depends on the temperature, the temperature can be determined by measuring the decaying intensity and deriving the decay time $\tau$ according to Equation 2.33. Typically, a calibration is performed to characterize the decrease in decay time with increasing temperatures. Not all TP exhibit a strictly mono-exponential decay. In those cases, Equation 2.33 may be expanded with additional (exponential) terms.

A number of TP materials with different properties is known, and corresponding comparisons can be found in review publications [1, 3, 7, 24, 28, 128]. The most important property is the decay time's order of magnitude, which ranges from $10^{-2}$ to $10^{-9}$ seconds for different commonly used TP materials. Thereby, the decay time should be smaller

than characteristic heat transfer time scales of the investigated physical problem. In the engine, these are in the order of $10^{-4}$ s. Furthermore, for an accurate measurement, the detection system should acquire at least 4-6 samples during the duration of one decay time. This typically necessitates the use of high-speed cameras or photo multiplier tubes (PMT). In addition, the temperature sensitivity of the decay time should be sufficient over the temperature range of the process. Finally, excitation and emission spectra must be in appropriate ranges, with high emission intensities being preferable. For further details, the reader is referred to comprehensive descriptions in the literature, for example [3, 16, 24, 128]. Additional information about sources of uncertainty and processing approaches can be found in Chapter 5.

For in-cylinder measurements at intermediate temperatures with high repetition rates, Chromium activated Gadolinum Gallium Garnet ($Gd_3Ga_5O_{12}$:Cr) was found suitable [72]. However, it has a significant afterglow, which can be reduced by co-doping with a small amount of Cerium ($Gd_3Ga_5O_{12}$:Cr, Ce) [17, 73]. Its emission spectrum after excitation with 266 nm is in the range of 650 nm to at least 850 nm [73] and therefore accessible with standard high-speed cameras. It features a high intensity emission and mostly mono-exponential decay with a decay time between $2 \times 10^{-4}$ to $2 \times 10^{-6}$ s for 300 to 800 K, which is sufficient for context of this work. At significantly higher temperatures, black body radiation has to be taken into account [73]. The application of this TP is described in Chapter 5.

### 2.2.3 Laser-Induced Fluorescence (LIF)

The following section is largely based on [219, 265]. Fluorescence as described in Section 2.2.1 can be utilized for diagnostic purposes by (selectively) exciting certain species and measuring the resulting emission. This enables a non-intrusive measurement of quantities like fuel concentration, fuel-air ratio, temperature, fuel composition, and residual gas concentration. The selected species either occurs naturally in the process (e.g. radical species in a flame or fuel component) or is added as an artificial tracer.

The recorded LIF signal intensity can be written as

$$S_\mathrm{f} = \frac{E_\mathrm{L}}{h\nu_\mathrm{L}} \cdot V \cdot n_\mathrm{f} \cdot \sigma_\mathrm{abs}(\lambda_\mathrm{L}, T) \cdot \Phi_\mathrm{f}(\lambda_\mathrm{L}, T, p, x_i) \cdot \frac{\Omega}{4\pi} \eta_\mathrm{opt}, \tag{2.37}$$

with the laser photon number $E_\mathrm{L}/h\nu_\mathrm{L}$, probed volume $V$, number density of the fluorescing molecule $n_\mathrm{f}$, absorption cross section $\sigma_\mathrm{abs}$, and observation angle $\Omega/4\pi$ with the detector efficiency $\eta_\mathrm{opt}$. Thereby, laser wavelength $\lambda_\mathrm{L}$, temperature $T$, pressure $p$ and ambient gas composition $x_i$ are relevant parameters influencing the absorption cross section and FQY. Due to the large number of variables, typically a calibration is necessary. Furthermore, depending on the tracer (fluorescing molecule) and desired quantities, a number of principal approaches is possible. First of all, the fluorescence signal can either be represented in terms of number density (per molecule) or mole fraction (per volume):

$$S_\mathrm{f}^* \propto n_\mathrm{f} \cdot \sigma_\mathrm{abs} \Phi_\mathrm{f} \tag{2.38}$$

$$S_\mathrm{f}^+ \propto x_\mathrm{f} p/T \cdot \sigma_\mathrm{abs} \Phi_\mathrm{f}, \tag{2.39}$$

which are related to each other through the equation of state. As only the latter takes into account density changes, the choice of representation affects the final pressure and temperature sensitivity. A single-line excitation and single-color detection strategy can be used to determine one variable, such as tracer concentration, when the other variables are constant or known with respect to a reference.

More parameters are accessible in two-line excitation or two-color detection LIF. In two-line LIF, two excitation wavelengths are used and the emission is captured with a single detection system. For suitable species, for example ketones such as acetone and 3-pentanone, the intensity of each emission changes with pressure, temperature and/or oxygen concentration, while the spectral content is rather constant. A signal ratio is then formed, which cancels out the tracer number density from Eq. 2.37. Suitable wavelengths and species have to be selected to ensure a high sensitivity with regards to the second desired variable, which is often the temperature [51, 151, 154, 238, 244]. In a similar manner, two-color detection (but single-line excitation) strategies utilize the red-shift of the fluorescence signal with increasing temperature, as VR in the excited states gets more efficient and the population of higher vibrational modes in the $S_0$ state increases. For this, the LIF signal after single-line excitation is split into two suitable spectral ranges, which are detected individually. Again, a signal ratio is formed and next to the tracer concentration, inhomogeneities in the laser sheet cancel out, though the image matching of the two detection channels is more complex compared to two-line excitation approaches. [8, 157, 190]

Another strategy makes use of oxygen quenching to determine the fuel-air equivalence ratio. $\Phi$. If quenching dominates over the other intra-molecular deactivation pathways, the fluorescence signal is proportional to the ratio of tracer to oxygen number density, which scales with the fuel-air equivalence ratio $\Phi$.

In all presented approaches, the tracer needs to be well characterized in the given thermodynamic conditions (temperature, pressure, bath gas composition). Contamination of the signal from other sources, such as PIV tracer particles and fuel components need to be ruled out. While isooctane as a model for gasoline fuel does not fluoresce, prolonged storage in fuel tanks and being subjected to increased pressure and heat can lead to creation of or contamination by unwanted products. Further information can be found in [219, 265].

#### 2.2.3.1 Tracer Choice

In Chapter 7 of the current work, the fuel mole fraction above a wall film is the variable of interest, such that suitable single- and two-line excitation strategies in the engine context are explored there. An overview of suitable tracers is given in this section.

Molecules used as tracers can be grouped in different categories. The following categorization and information is based on the work of [219, 265].

- Atomic tracers feature a large absorption cross section and strong fluorescence signals, which enables low seeding levels. However, processes of high temperature

are needed to for atomized material to be present. Due to low saturation limits, this class of species is considered not suitable for engine conditions.

- Small inorganic molecules exist as radicals in flame fronts (OH, CH). In mixing studies, other species such as NO, $SO_2$ or $I_2$ have been used. Their spectroscopic properties are well studied. However, they are toxic and/or corrosive and typically gaseous at atmospheric conditions, meaning they cannot be mixed with liquid fuels. An inverse tracing of the air is possible but reduces the sensitivity, due to low fuel-air ratios.
- Organic dyes are well known for their use as laser dyes or tracers in the liquid phase. The wide variety of molecules allows tailored selection of spectroscopic and thermodynamic properties, however, they are not applicable for measurements in the gas phase.
- Poly-atomic organic molecules are chemically close to or actually present in commercial fuels. Due to a high density of states, absorption and emission are broad band, which allows for a variety of excitation approaches. Furthermore, they often exhibit similar thermodynamic properties (such as vapor pressure and boiling point) as common engine fuel components, though preferential evaporation needs to be considered [34, 86]. These substances can be further subdivided into ketones and aromatics, which will be discussed in more detail below, with the focus on their use in gasoline engines. An overview of photophysical and thermodynamic properties is given in Table 2.1.

**Aromatic hydrocarbons** are present in commercial fuels, for example benzene and toluene in gasoline fuel. They have a high FQYs (toluene $\Phi_f = 0.17$, benzene $\Phi_f = 0.22$, [219]) and come in a wide variety of molecular sizes and therefore boiling points. However, they are strongly quenched by oxygen, which limits applicability in fired engine experiments, but may be exploited for fuel-air ratio (FAR) LIF. Their emission is typically in the (near) ultra violet (UV) and ranges from 260 to 360 nm.

*Toluene* has been well characterized as a tracer [134, 135, 219]. It is often used in gas-phase temperature measurements [8, 121, 158, 190] (two-color detection approach), though its strong quenching by oxygen limits the application in engines to nitrogen atmospheres. Utilizing this effect for fuel-air ratio LIF needs careful correction of the temperature dependency. Toluene is less toxic than some other aromatics like benzene and not considered carcinogenic.

*p-xylene* has been used for gas phase temperature and concentration measurements [248]. It is a natural component of gasoline with a medium-range volatility. It was characterized for LIF applications by [249], who also utilized a two-color detection for temperature measurements [248]. Furthermore, the combination acetone and p-xylene was used to investigate fuel evaporation [264]. However, the influence of oxygen quenching and the behavior at higher pressures is not documented.

*Anisole* shows a significantly higher fluorescence signal (due to higher absorption cross section and FQY) than toluene [61]. Spectroscopic data exists in a wide range of pressures and temperatures [13, 61, 240]. It has been used to measure temperatures in two-color LIF studies [142, 143, 221, 239] and in a single-color approach to measure

the fuel-air ratio by utilizing temperature-insensitive spectral emission range [144]. Furthermore, it is considered non-toxic and non-carcinogenic.

**Aliphatic compounds** such as ketones are an often used class of fluorescent tracers [219]. Compared to aromatic compounds, their FQY is low (acetone $\Phi_f = 0.002$ [87]), however, oxygen quenching is far less pronounced, which results in comparable signals in air. Faust et al. [62] compared the signal of selected organic tracers in air at room temperature. They found that the fluorescence signal per molecule of anisole is about 35 times stronger than that of toluene, whose signal in turn is 10 times stronger than that of acetone. To some extent, this is compensated by higher vapor pressures of ketones, which allow higher tracer concentrations, though a low concentration is often preferred to be as non-intrusive as possible.

*Acetone* is often used as a gas tracer and well characterized [138, 237]. According to the model of Thurber et al. [237], the rate of ISC is several orders of magnitude above the rate of fluorescence. The resulting long-lived phosphorescence is effectively quenched by small oxygen concentrations, such that emission can be assumed to be fluorescence only, when studied in air [156]. Acetone has been used in mixing studies [98, 156, 210, 251]. Since the absorption cross section increases with the temperature for excitation above 266 nm, a two-line excitation approach can be used to (additionally) measure temperatures [154, 238, 244] and was also applied in multi-tracer studies [131, 139, 150, 166, 258, 265].

*3-pentanone* is structurally and photophysically similar to acetone, with a slightly larger absorption cross section and FQY [265]. Its boiling point is close to that of isooctane, which qualifies it as a fuel tracer in a number of engine-related studies [30, 51, 66, 134, 137, 138, 150, 170, 187, 243] concerning liquid sprays, mixing, temperature and exhaust gas processes.

*Biacetyl*'s FQY of approximately 0.25 % is similar to that of acetone. Its boiling point of 88 °C is lower than that of typical fuels but too high to allow high tracer gas concentrations at room temperature. Probably also due to its strong odor, it has been less often used for LIF applications than ketones [219]. Due to photodissociation in the UV it is best excited at relatively high wavelengths, for example with frequency-tripled Nd:YAG lasers. Biacetyl shows strong phosphorescence in the absence of oxygen. At engine relevant conditions, the fluorescence signal is sensitive to changes in pressure and temperature, such that a suitable reference or correction needs to be applied [189, 225]. Further information can be found in [110, 156, 219, 256]

*Triethylamine* (TEA) is a tracer with strong fluorescence signal even at low concentrations [265], with sufficient signal-to-noise ratio (SNR) being reported at just 0.25 % TEA in weight in isooctane [18, 265]. It is suitable for FAR-LIF, due to the strong dependence of its fluorescence on the oxygen concentration at excitation with 248 nm [265]. In contrast, the pressure and temperature dependence at engine-relevant conditions is low [18, 108, 265]. Most calibration data is based on excitation at 248 nm using excimer lasers, such as studies by [150, 151], who combined acetone and 3-pentanone with TEA to investigate the FAR, gas temperature, and exhaust gas fraction. [69, 186] used TEA in

a laser-induced exciplex fluorescence (LIEF) approach to visualize a liquid spray. Only limited data is available of excitation at 266 nm [68].

**Conclusion** In Chapter 7, the vaporization of a wall film is investigated with tracer LIF. A negative tracer approach is ruled out due to the expected low vapor mole fraction above the wall and correspondingly lower sensitivities of this approach. As discussed above, aromatic tracers are similar to isooctane in terms of thermodynamic properties but are strongly quenched by oxygen. While this can be exploited for FAR-LIF, this method measures the tracer concentration only indirectly. For a quantitative analysis, the oxygen concentration has to be known. This is especially problematic in the presence of exhaust gas, which cannot be assumed to be homogeneously distributed throughout the combustion chamber. Therefore, ketones were considered as (fuel) tracers. Specifically, acetone and 3-pentanone were chosen as suitable tracers because their photophysical properties under engine-relevant conditions are well documented for mixture and/or temperature measurements, which is less the case for biacetyl.

### 2.2.4 Velocimetry

One of the most widely used methods for flow field measurements is particle image velocimetry (PIV). An overview in the context of engine measurements is given here, while a comprehensive description can be found in for example [2, 198, 242]. In PIV, the fluid motion is visualized by adding particles to the flow. Size and density of the particles are chosen such that they track the fluid motion well. These particles are then illuminated by two short light pulses with a time delay $\Delta t$ and the scattered light is recorded with a camera, typically in two distinct frames. With a known magnification or spatial calibration, the particle shift $\Delta x$ is determined and the velocity $U = \Delta x / \Delta t$ derived. A schematic of the principle for two-dimensional, two-component (2D2C) PIV is shown in Fig. 2.6

The seeding particles are usually solid or liquid, though for very large probe volumes also helium filled soap bubbles have been used [212]. Solid particles, like titanium dioxide or alumina powder, have the advantage to survive the combustion and non-abrasive types

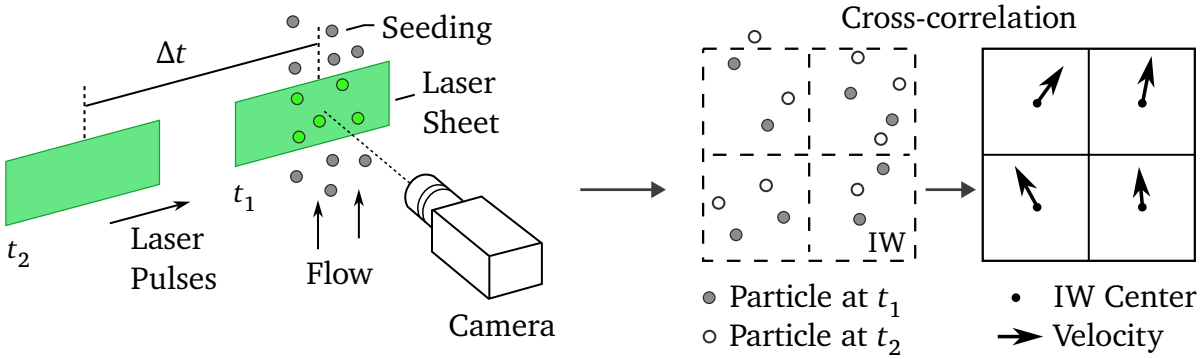


Figure 2.6: Schematic of a PIV setup and data evaluation. Adapted from [198, 262].

Table 2.1: Photophysical and thermodynamic properties of frequently used organic tracer molecules in comparison to isooctane. Parameters are given for approximately room temperature, if applicable. Values are taken from [104] if not specified otherwise. The emission peak is given in parenthesis. $\rho$ denotes the liquid density, $\gamma$ the surface tension, $\nu$ the kinematic viscosity, $\Delta H_{vap}$ the enthalpy of vaporization, $T_{BP}$ the boiling point, and $T_{ign}$ the auto-ignition temperature.

| Tracer | Absorption nm | Emission nm | $\sigma_{abs}$ [a] $\times 10^{20}$ cm$^2$ molecule$^{-1}$ | $\Phi_f$ % | $\rho$ g cm$^{-3}$ | $\gamma$ mN m$^{-1}$ | $\nu$ µm s$^{-2}$ | $\Delta H_{vap}$ kJ kg$^{-1}$ | $T_{BP}$ °C | $T_{ign}$ °C |
|---|---|---|---|---|---|---|---|---|---|---|
| Isooctane ($C_8H_{18}$) | - | - | - | - | 0.69 | 18.3[f] | 0.66[f] | 307[e] | 99 | 410 |
| Toluene ($C_6H_5CH_3$) | 240-270[k] | 260-340 (280)[k] | 19[k] | 19[m] | 0.87 | 28.5[f] | 0.69[g] | 402[e] | 111 | 535 |
| p-xylene ($C_6H_4(CH_3)_2$) | 230-285[j] | 270-340 (295)[j] | 34[j] | - | 0.86 | 28 | 0.76 | 399[j] | 138 | 540 |
| Anisole ($C_7H_8O$) | 245-285[q] | 270-350 (295)[p] | 350[q] | 36[p] | 0.99 | - | 0.81[g] | 433[g] | 154 | 475 |
| Acetone ($(CH_3)_2CO$) | 225-328[n] | 300-500 (395)[b] | 4.4[o] | 0.2[b] | 0.79 | 24.0[f] | 0.41[g] | 516[g] | 56 | 528 |
| 3-pentanone ($C_5H_{10}O$) | 225-325[d] | 310-550 (420)[d] | 4.5[c] | 0.8[d] | 0.81 | 24.7[f] | 0.55[g] | 258[e] | 102 | 455 |
| Biacetyl ($(CH_3CO)_2$) | 340-470[h] | 420-520 (485)[h] | 8 (417 nm)[h] | 0.25[h] | 0.99 | - | 0.45[e] | 450[e] | 88 | 345 |
| TEA ($N(CH_2CH_3)_3$) | 210-280[i] | 260-350 (280)[i] | - | - | 0.73 | 20.7[f] | 0.48[g] | 344[g] | 89 | 215 |

[a] For excitation at 266 nm
[b] Schulz and Sick [219]
[c] Koch and Hanson [137]
[d] Koch [138]
[e] Linstrom [152]
[f] Zigan [265]
[g] National Center for Biotechnology Information [174]
[h] Lozano, Yip, and Hanson [156]
[i] Lind et al. [150]
[j] Wang et al. [249]
[k] Koban et al. [136]
[m] Cheung [29]
[n] Hansen and Lee [87]
[o] Thurber et al. [237]
[p] Faust, Dreier, and Schulz [61]
[q] Benzler [13]

can be used in engines. However, ensuring a constant seeding rate is challenging and optical surfaces tend to get soiled faster than with liquid particles. A common liquid seeding is Di-Ethyl-Hexyl-Sebacat (DEHS), which is not suited for measurements during the compression stroke because of its low boiling point of about 250 °C. In this work a silicon oil is used instead and atomized with aerosol generators.

In order to follow the flow as close as possible, small particles with low density are advantageous. For low particle Reynolds numbers, the characteristic time for a particle to react to a change in the flow can be derived as:

$$\tau_\mathrm{p} = \frac{2r_\mathrm{p}^2(\rho_\mathrm{p} - \rho_\mathrm{f})}{9\eta_\mathrm{f}}, \tag{2.40}$$

with the particle radius $r_\mathrm{p}$, the particle and fluid density $\rho_\mathrm{p}$ and $\rho_\mathrm{f}$, and the dynamic viscosity of the flow $\eta_\mathrm{f}$ [242, p. 164].

Particle illumination is usually achieved with lasers, due to their good focusability into appropriately thin light sheets, short pulse durations which reduces motion blur, and high fluence, though also high-power LEDs can be used. The incident light is scattered, a process which can be described with Maxwell's equations. Thereby, the scattered intensity increases with increasing particle diameter. Depending on the Mie parameter

$$x_\mathrm{M} = \frac{\pi d_\mathrm{p}}{\lambda}, \tag{2.41}$$

which compares the particle diameter $d_\mathrm{p}$ to the wavelength of the incident light $\lambda$, different scattering regimes can be identified:

$$I(x_\mathrm{M}) \propto \begin{cases} (d_\mathrm{p}/\lambda)^6 & \text{if } d_\mathrm{p}/\lambda \ll 1 \\ (d_\mathrm{p}/\lambda)^2 & \text{if } d_\mathrm{p}/\lambda \gg 1. \end{cases} \tag{2.42}$$

The first regime with particle diameters smaller than the wavelength of the light is called Rayleigh scattering. Typical PIV particles in this work are in the order of 1 µm, which corresponds to the second regime, called Mie scattering [198, 242]. Accordingly, there is a conflict of objectives: Small particles follow the flow better but scatter less light. Mie scattering is anisotropic and varies in the spatial directions, with alternating minima and maxima. Most of the light is scattered in forward direction, some in backwards directions, and even less in the other directions, with the ratio between forward and sidewards scattering being approximately $10^4$ [198].

The particle images are detected by a camera system, typically a high-speed complementary metal-oxide-semiconductor (CMOS) camera. The two laser pulses are timed for the end of the first and beginning of the second frame, whereby the particle's exposure is mostly determined by the duration of the laser pulse and not the frame exposure. With a suitable combination of objective, working distance, and aperture, the field of view (FoV) and depth of field are determined. In an engine context, the curved cylinder glass typically introduces strong astigmatism, which needs to be corrected for high-resolution measurements. For this purpose, a cylindrical correction lens can be used [202].

A spatial calibration is needed to transform the pixel coordinates of a camera image into real world coordinates. Pinhole models are able to correct typical spherical abberations of objectives. In the case of distortion due to additional influences like the cylinder glass, a polynomial fit is better suited. For both options, target plates with known patterns have to be placed in the measurement plane.

Finally, the two-dimensional velocity information is calculated from the particle images. Therefore, the image is subdivided into square regions, so called interrogation window (IW) with a edge length of 8 to 96 pxl. For each IW, the cross-correlation between the first and the translated second frame is calculated. The result is a correlation map that shows the correlation value between the two frames for all possible two-dimensional pixel shifts. The correlation value is maximum at the position of the actual particle shift (see Fig. 2.6). To improve the velocity resolution to sub-pixel accuracy, a two-dimensional Gaussian is fitted to this correlation peak. The calculated pixel shift (and velocity) is filtered both spatially, by taking into account the particle ensemble of one full IW, as well as temporally, by computing the velocity from information at $t_1$ and $t_2$ only. In common PIV software implementations, the cross-correlation is actually calculated in frequency space for improved performance. Furthermore, multi-pass PIV calculations are standard, with iterative velocity estimations at decreasing IW sizes and adaptive IW shapes.

The presented PIV approach is robust in terms of seeding density and particle shift, though the maximum viable particle shift is limited by the out-of-plane velocity component and laser sheet thickness as well as in-plane velocity and IW size. Significant particle-loss, that is particle movement out of the IW, decreases the SNR. In the presence of strong gradients relative to pixel and IW sizes, a hybrid PIV+PTV can be employed. Thereby, after an initial PIV estimation step, individual particles are separated using an intensity threshold. For each detected particle, a cross-correlation with an IW of just a few pixel is calculated. This maintains the PIV subpixel accuracy and increases the spatial resolution dramatically, especially in the sense of reduced spatial filtering. Such a PTV approach needs lower particle densities than PIV and a good overlap of both laser sheet profiles. However, it is especially suited for strong gradients close to walls and multi-phase flows.

### 2.2.5 Temperature Radiation

Every physical body emits electromagnetic radiation due to its non-zero temperature. In the idealization of a *black body*, which in thermal equilibrium has an emissivity $\epsilon = 1$, the emitted spectral radiance at a wavelength $\lambda$ and temperature $T$ is given by

$$B_\lambda(\lambda, T) = \frac{8\pi hc}{\lambda^5} \frac{1}{\exp\left(hc/(\lambda k_\mathrm{B} T)\right) - 1}, \tag{2.43}$$

with the Boltzmann constant $k_\mathrm{B}$, Planck constant $h$, and speed of light $c$ [37]. The wavelength of maximum radiance at a given temperature is

$$\lambda_\mathrm{max} = \frac{2.897 \times 10^{-3}\,\mathrm{m\,K}}{T}. \tag{2.44}$$

In reality, most materials have a emissivity $\epsilon$ that is smaller than unity

$$\epsilon_{\text{real}} = \frac{B(\lambda, T)\big|_{\text{real}}}{B(\lambda, T)}, \tag{2.45}$$

which indicates that some fraction of incoming radiation is transmitted or reflected, in contrast to a black body, where all incoming radiation is absorbed.

Therefore, soot particles inside an engine will emit radiation according to their temperature, which is sometimes called natural luminosity (NL) [96]. According to Equations 2.43, this radiation is dominated by hotter soot and increases significantly at longer wavelengths.

# Chapter 3

# Engine Test Bench

The engine test bench used in this work is a single-cylinder optically accessible research engine, which has been first thoroughly described by Baum et al. [10] and has been subject of many experimental (e.g. [11, 41, 188, E214, E252]) and numerical (e.g. [25, 45, 79, E184]) studies in the past decade. It was designed to offer consistent boundary and operating conditions at unchanging geometrical parameters, such that each study increases the set of available data. Notable changes include the switch from a wall-guided to a spray-guided cylinder head configuration [65], whereby this work focuses solely on the latter. Furthermore, next to premixed combustion with port fuel injection (PFI), operation with direct injection (DI) using a Spray-G injector from the Engine Combustion Network (ECN) was expanded [E78, E253].

In this chapter, first the test bench periphery and instrumentation is described. Then, the engine itself and relevant OPs are presented.

## 3.1 Instrumentation and Test Bench Environment

Figure 3.1 shows the engine test bench and peripheral instrumentation. Inlet and outlet manifolds (inner diameter 56 mm) are connected to plenums, which dampen pressure fluctuations induced by the periodic intake and exhaust process (more on this in Section 3.3). A gas mixture system supplies the engine with a defined mix of dried air (relative humidity $\leq 1.8\,\%$ at $4\,°C$), $N_2$, and $CO_2$, which are fed by mass flow controllers (MFCs) into a pressure plenum (P1). Normally, only air is used in engine operation. If required, the latter two gas supplies enable simulation of exhaust gas content or tracer quenching studies. The test bench is pressure regulated, therefore a pneumatic control valve (Samson) controls the flow of the gas mixture into plenum P2.

A rotary piston meter (Zc 038.05, Aerzen) equipped with pressure (PAA-33X, Keller) and temperature sensors (PT100, TMH; signal converter: WK109PTH, Wachendorf) is used to measure the intake mass flow (standard uncertainty of 1.5 %). In addition, the intake temperature can be varied by a flow heater (Schniewindt, $P_{el} = 4.5\,kW$). At the start of the straight intake pipe with a length of approximately 25 $D$, additional gases can be added, for example particle tracer for PIV or fluorescing tracer gases for LIF.

Thermodynamic parameters in the intake manifold are measured with two absolute pressure sensors ($p_{in}$, PAA-H8cool HB, Keller; accuracy ±1 mbar) and two thermocouples ($T_{in}$, type K, tip diameter 0.5 mm, TMH; signal converter: Wachendorff WK109TC0; accuracy ±1.5 °C). In-between, two port fuel injectors (Bosch) can be used to atomize isooctane ($C_8H_{18}$) and liquid tracers (such as acetone) at an injection pressure of 4 bar. This allows engine operation with homogeneously premixed combustion and reduced

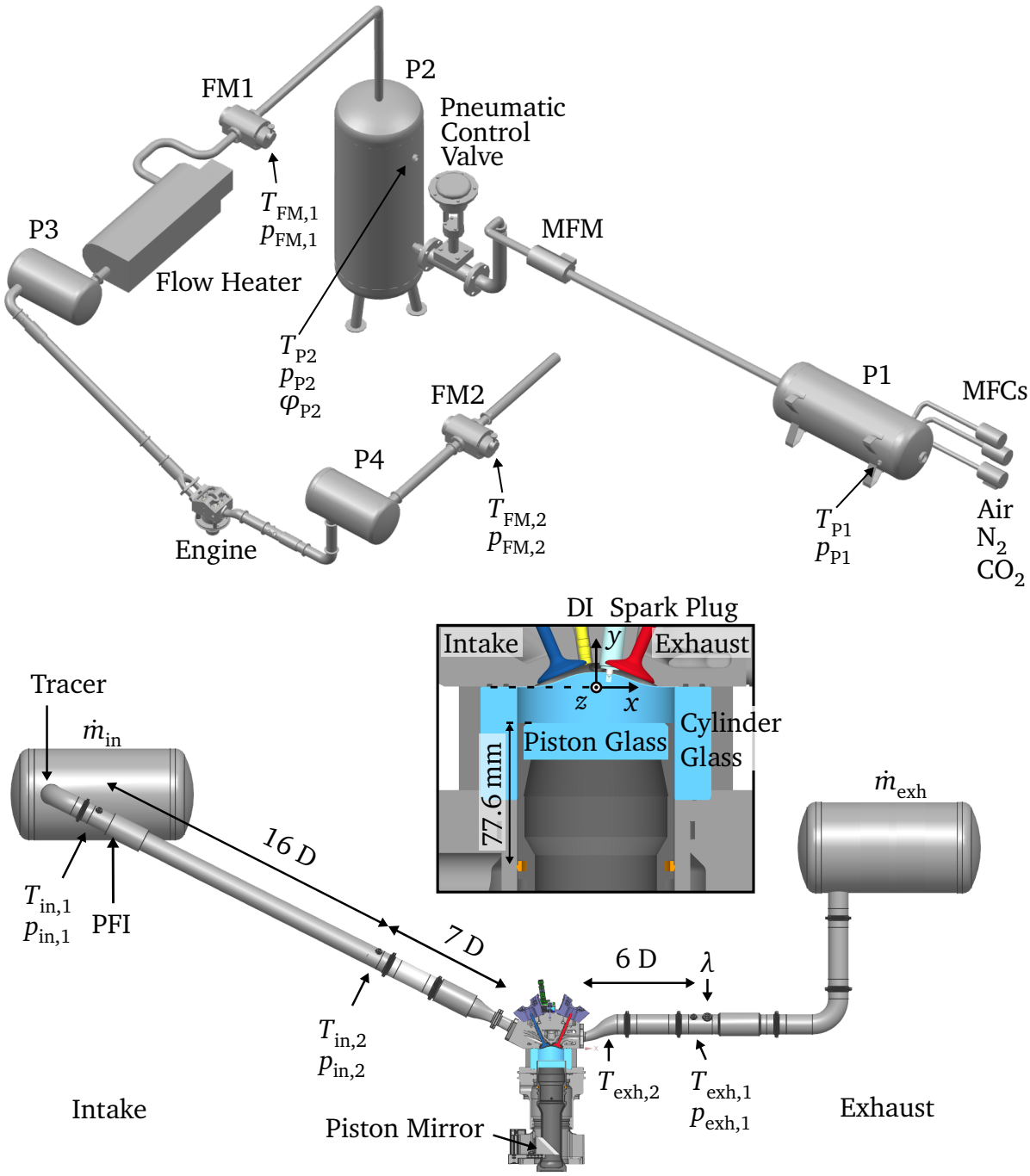


Figure 3.1: Schematic of engine test bench with sensor positions and intake and exhaust manifolds.

complexity compared to direct injection. To prevent the formation of wall films, a heating sleeve is positioned at the PFI location to heat up the walls above the boiling point. Additionally, three thermocouples of type K (tip diameter 1.5 mm, TMH; signal converter: NI 9213, National Instruments) are mounted flush with the inner pipe wall to acquire wall temperatures.

The cylinder pressure $p_{\mathrm{cyl}}$ is measured with a piezoelectric pressure sensor (GU22C, AVL) and a piezoelectric charge amplifier for signal conversion (MicroIFEM, AVL), with a combined standard uncertainty of 0.3 %[8]. In order to compensate for inevitable drift of this sensor architecture, the pressure is referenced to the intake pressure $p_{\mathrm{in,2}}$ at BDC. According to the specifications, the remaining drift due to the cyclic change in temperature and the thermal shock of combustion is $\leq \pm 0.4\,\mathrm{bar}$ and $\leq \pm 0.2\,\mathrm{bar}$, respectively.

In the exhaust manifold, the gas temperature is measured with thermocouples at two positions ($T_{\mathrm{exh}}$, type K, tip diameter 0.5 mm, TMH; signal converter: Wachendorff WK109TC0; accuracy $\pm 1.5\,°\mathrm{C}$), next to another absolute pressure sensor ($p_{\mathrm{exh}}$, PAA-H8cool HB, Keller; accuracy $\pm 1\,\mathrm{mbar}$). The air-fuel equivalence ratio ($\lambda$) is measured with a wide-band lambda probe (LSU 4.9, Bosch) operated with a lambda meter (LA4, ETAS) with a total estimated accuracy of 2 % corresponding to a standard uncertainty of 1.2 %[9]. This probe allows the measurement of air-fuel equivalence ratios from 0.65 to $\infty$ by measuring the amount of unburnt hydrocarbons or residual oxygen for rich and lean mixtures, respectively. Due to the sensor principle, oscillations in the absolute exhaust gas pressure or partial pressure of oxygen lead to oscillations in the measured $\lambda$ [173], which are removed by averaging.

The mentioned analogue signals from the instrumentation are digitally acquired in the *indicating* system on a time or crank angle basis (X-ion 1HU, AVL). It is equipped with analog-digital converters (U4H2 and U4S2, AVL), which offer a sample rate of up to 2 and 1 Mega Samples/s with an accuracy better than $\pm 0.07\,\%$. Thereby, the crank angle decoder (365C, AVL) and engine timing unit (ETU) (427, AVL) provide the current crank angle and allow for a synchronized triggering of injection, ignition, and measurement systems. In addition, an FPGA (cRIO-9049, National Instruments) is used for further triggering and is equipped with a general purpose injector driver module (NI 9751, National Instruments) to control the DI.

## 3.2 Optically Accessible Engine

The engine unit is a single-cylinder research engine (AVL). Optical access is given by a quartz glass liner (Corning 7980) with a thickness of 20 mm, which allows a FoV of up to 75 mm × 55 mm (width × height) plus an additional height of 8 mm in the pent-roof head. In addition, the Bowditch extension and piston mirror allow access through the quartz glass window (Corning 7980) recessed into the piston crown.

[8] Taking the uncertainty of the sensor sensitivity and the amplifier uncertainty according to calibration sheets into account.

[9] with the assumption of a rectangular distribution.

The pentroof cylinder head houses two intake and exhaust valves (diameter 29 mm), the pressure sensor, and the spark plug (NGK) as well as the injector in central location at an angle of 7 and 8°, respectively. Due to the symmetric intake manifold geometry and valve angle of 23°, the engine exhibits a tumble flow without swirl. Further geometric parameters can be found in Table 3.1. Figure 3.2 shows the kinematics of valves and piston.

In comparison to metallic, *thermodynamic* engines, this optically accessible engine features a significantly larger crevice volume, that is volume between the piston and cylinder liner. This is due to the low position of the piston sealing ring, which should not make contact with the cylinder glass (see Fig. 3.1). At a crevice height of approximately 77 mm and width of 0.5 mm, the crevice volume amounts to approximately 10 $cm^3$. As a consequence, up to 16 % of the clearance volume is located inside the crevice. Even more mass is pushed into the crevice during combustion as the in-cylinder gas expands [41]. During the expansion stroke, crevice gases expand again and out-gas into the main combustion chamber, where they combust if temperatures are high enough. This phenomena is discussed in more detail in Chapter 5 and 7.

Furthermore, the piston is not lubricated and cooled with oil. Instead, a cooling air jet is positioned inside the piston crown. Contrary to metallic piston rings of thermodynamic engines, the single hydraulic sealing ring operates dry and features a comparably high impermeability. Accordingly, the blow-by mass flow rate is small, as measurements in the crank and mirror housing case indicate an influence on the cylinder pressure of $< 0.1$ bar.

Table 3.1: Geometric parameters of the single-cylinder engine.

| Parameter | Value |
|---|---|
| Stroke/ Bore | 86 / 86 mm |
| Connecting Rod Length | 148 mm |
| Displacement Volume | 499 $cm^2$ |
| Clearance Volume | 64.9 $cm^2$ |
| Compression Ratio | 8.7 |
| Valve Lift | 9.5 mm |
| Intake Valve Opening (IVO) | 325 °CA |
| Intake Valve Closing (IVC) | −125 °CA |
| Exhaust Valve Opening (EVO) | 105 °CA |
| Exhaust Valve Opening (EVC) | −345 °CA |

The conditioning system (AVL) provides oil and coolant at a temperature of 60 °C. An asynchronous motor (AVL, torque 120 nm, power 38 kW) and a flywheel are used to control the engine speed to a constant value. At 0.95 bar intake pressure and fired operation, maximum variations in speed throughout a cycle are ±6 % and ±2 % for 800 and 1500 rpm, respectively, with 2500 rpm lying in-between. During motored operation, speed variations are in the range of 1 to 2 %. Having a low level of vibrations is indispensable for the application of optical diagnostics on the engine rig. Due to dynamic mass balances, typical vibrations throughout the cycle are in the order of 0.25 mm.

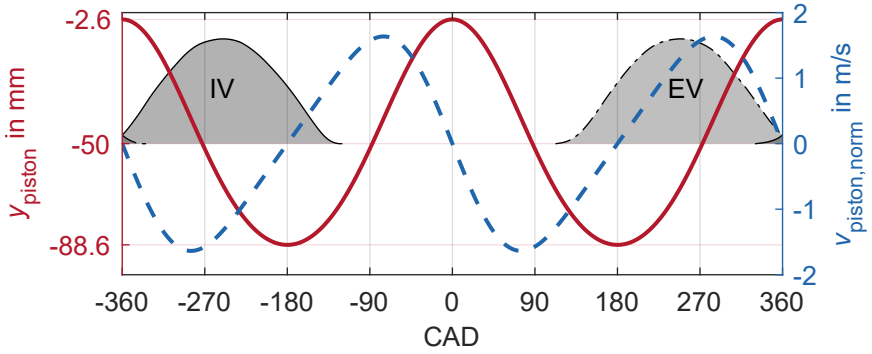


Figure 3.2: Piston position and piston speed normalized to the cycle average with respect to the crank angle. Intake valve (IV) and exhaust valve (EV) lift indicated by gray shaded areas.

## 3.3 Operating Conditions

Four operating points (OPs) are commonly used at this engine rig, labeled A-D, with a variation in engine speed (800 and 1500 rpm) and intake pressure (0.95 and 0.4 bar). In this work, these were extended to higher engine speeds of 2500 rpm, labeled E and F. Table 3.2 and 3.3 present relevant parameters and boundary conditions of the fired and motored operating conditions, respectively. Unless otherwise specified, isooctane was used as fuel during fired operation. The timing of spark ignition ($\theta_{SI}$) is optimized for an angle of the maximum cylinder pressure $\theta_{pcyl,max}$ between 5 to 10 °CA.

As apparent in Table 3.3 and 3.2, the air intake mass flow $m_{air}$ does not scale linearly with the intake pressure. The reason for this is a backflow from the cylinder into the intake manifold for the low pressure/load cases. After the exhaust stroke, the cylinder pressure is approximately at ambient level, which is higher than the pressure in the intake manifold. When the intake valves open, a backflow occurs, which increases the exhaust gas content for these cases. Consequently, the fresh gas mass flow rate and the IMEP are reduced disproportionately.

In a similar manner, the pressure levels are responsible for the significantly higher exhaust gas temperatures of the motored, low-load cases compared to the high load cases. When the exhaust valves open, there is a backflow from the exhaust manifold into the cylinder, and the pressure increases from approximately 0.4 bar to 1 bar. This effective compression leads to higher exhaust gas temperatures. Because the engine is not operated in thermal equilibrium, the exhaust gas temperatures for fired OPs are transient and therefore not given in Table 3.3. The number of consecutive fired cycles is limited to about 200-400, due to the thermal expansion of piston and cylinder liner, which are not water-cooled.

Finally, the varying importance of heat losses to the cylinder walls can be observed based on $\theta_{pcyl,max}$ of the motored OPs. At lower engine speeds and lower intake pressures, the cylinder pressure peak occurs earlier, indicating higher heat losses relative to the trapped cylinder mass. This corresponds the *thermodynamic loss angle*.

Table 3.2: Definition of *motored* OPs and corresponding indicating data.

| Parameter | A | B | C | D | E | F | Unit |
|---|---|---|---|---|---|---|---|
| $n$ | 800 | 800 | 1500 | 1500 | 2500 | 2500 | rpm |
| $p_{\mathrm{in,2}}$ | 0.950 | 0.400 | 0.950 | 0.400 | 0.950 | 0.400 | bar |
| $\bar{V}_{piston}$ | 2.93 | 2.93 | 4.30 | 4.30 | 7.17 | 7.17 | $\mathrm{m\,s^{-1}}$ |
| $T_{\mathrm{in,2}}$ | 33.4 | 43.3 | 35.0 | 37.8 | 33.5 | 35.2 | °C |
| $T_{\mathrm{exh,2}}$ | 37.1 | 96.3 | 42.0 | 104.6 | 44.2 | 111.6 | °C |
| $\dot{m}_{\mathrm{air}}$ | 11.4 | 3.5 | 21.8 | 7.4 | 41.0 | 15.3 | $\mathrm{kg\,h^{-1}}$ |
| $p_{\mathrm{cyl,max}}$ | 13.3 | 5.3 | 14.5 | 6.0 | 17.1 | 6.9 | bar |
| $\theta_{p\mathrm{cyl,max}}$ | -2.1 | -2.6 | -1.8 | -2.4 | -1.7 | -2.3 | °CA |

Table 3.3: Definition of *fired* operating points (OPs) and corresponding indicating data. Averages of 200-400 cycles. Isooctane was port-fuel injected for stoichiometric conditions, besides for OP E and F, where data were acquired with methane as fuel.

| Parameter | A | B | C | D | E | F | Unit |
|---|---|---|---|---|---|---|---|
| $n$ | 800 | 800 | 1500 | 1500 | 2500 | 2500 | rpm |
| $p_{\mathrm{in,2}}$ | 0.95 | 0.40 | 0.95 | 0.40 | 0.95 | 0.40 | bar |
| $\theta_{\mathrm{SI}}$ | -14.2 | -22.2 | -22.2 | -27.2 | -32.8 | -45 | °CA |
| $T_{\mathrm{in,2}}$ | 35.5 | 41.3 | 33.0 | 38.8 | 38.4 | 43.1 | °C |
| $\dot{m}_{\mathrm{air}}$ | 10.3 | 3.6 | 20.0 | 7.5 | 35.1 | 12.7 | $\mathrm{kg\,h^{-1}}$ |
| $p_{\mathrm{cyl,max}}$ | 31.3 | 9.6 | 34.3 | 12.1 | 34.2 | 13.1 | bar |
| $\mathrm{CoV}(p_{\mathrm{cyl,max}})$ | 3.7 | 6.7 | 4.3 | 5.3 | 5.5 | 5.3 | % |
| $\theta_{p\mathrm{cyl,max}}$ | 9.7 | 15.6 | 8.6 | 10.4 | 9.1 | 7.1 | °CA |
| $\mathrm{IMEP}_{\mathrm{gross}}$ | 4.8 | 2.0 | 5.9 | 2.2 | 6.3 | 2.0 | bar |

Figure 3.3 shows intake, exhaust, and cylinder pressure traces for OP A-F. Focusing first on the manifold pressures, the oscillations excited by the periodic intake and exhaust process can be clearly seen. Their frequency is constant, since natural resonances of the manifolds are excited. Consequently, fewer periods per cycle occur as engine speed increases, with amplitudes increasing due to the higher momentum of the gas column. The interaction between these oscillations and the intake flow will be briefly discussed in Chapter 4 and was analyzed in [E255].

As mentioned, cylinder pressures increase with increasing engine speed for both fired and motored cases. The lower load cases (bottom row) exhibit higher relative cycle-to-cycle variations (CCV) of the cylinder pressure compared to the high load cases, as indicated by the envelope. This is due the backflow-induced higher exhaust gas content, which leads to a lower flame speed. An estimation of respective flame speeds and thicknesses of OP A-D can be found in [41].

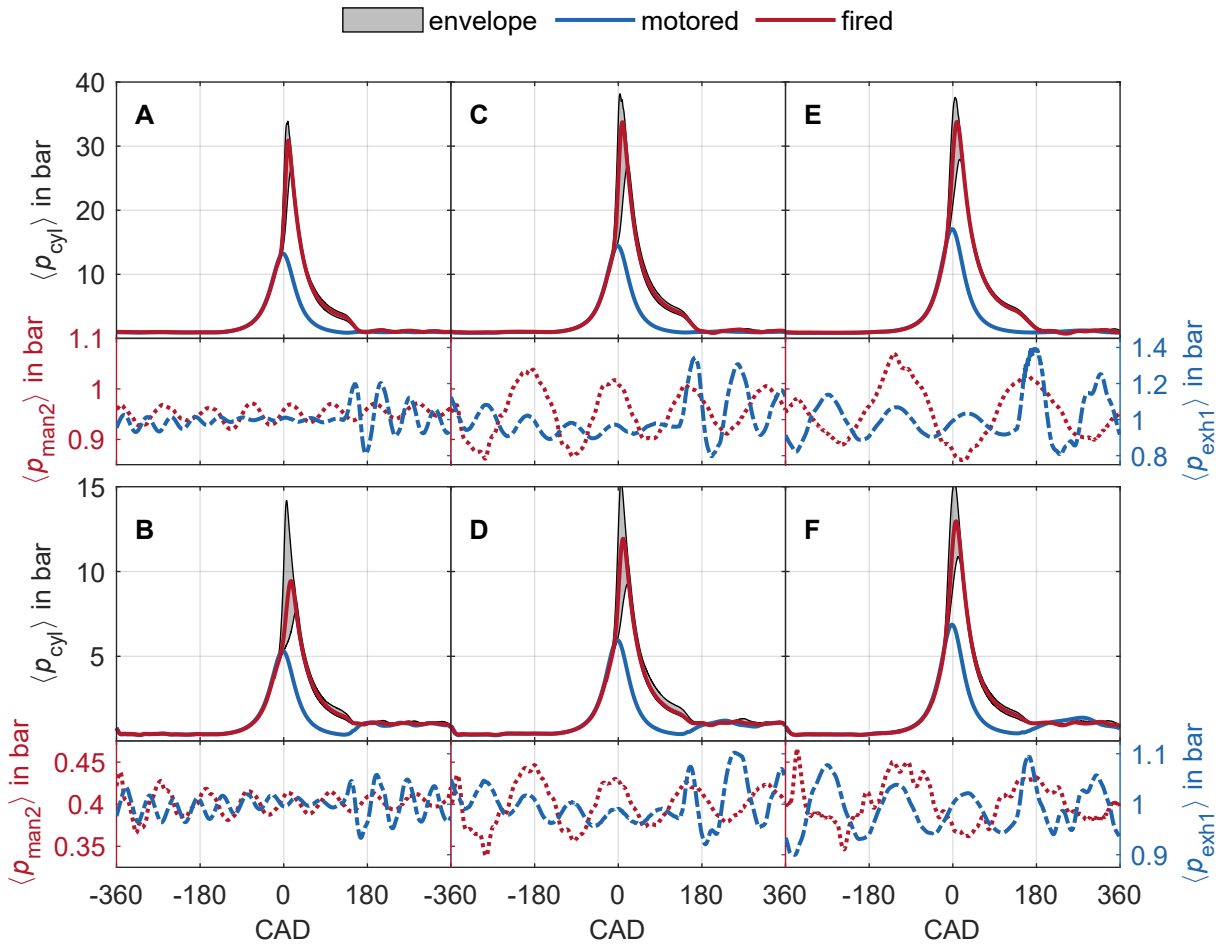


Figure 3.3: Phase averaged intake, exhaust, and cylinder pressure traces for OP A-F. Next to the motored cylinder pressure (blue), the fired pressure trace (red) and the pressure envelope (min, max; gray) are shown.

# Chapter 4

# Macroscopic Velocity Field

In this chapter, an introduction to the macroscopic flow field of this engine is given. For this purpose, PIV results in the vertical tumble plane are shown and differences between the operating points, with focus on OP E and F, are examined. A detailed description of the experimental setup is not given here, and instead reference is made to comparable setups in the other chapters.

The investigated engine features a characteristic tumble generated by the angled intake flow and subsequent asymmetric flow over the valves. Operating points at different engine speeds can be compared if the flow velocity is scaled by the mean piston velocity. This scaling of mean flow and turbulence is one fundamental reason engines are able to operate in a wide range of engine speeds [22]. In Fig. 4.1, the engine-speed-scaled, phase-averaged velocity in the tumble plane of OP A, E, and F is shown. A similar structure can be seen: during the intake phase, the flows of both valves combine and are redirected to the bottom right in a region of high velocity magnitude, which is guided by the cylinder walls towards the piston. In the valve plane an intake jet forms, with a recirculation zone below the valve [E252, E255]. When the intake valves close, intake velocities decrease and the clockwise tumble structure begins to emerge. In this plane and FoV higher velocities begin to appear again, when the piston moves upwards during compression. It is evident that the tumble does not act like a rigid-body vortex centered in the cylinder, but arises from a complex three-dimensional interaction of different high velocity flow regions moving through the cylinder volume [41, 45].

The described intake flow is driven by the pressure difference between intake manifold and cylinder, which is induced by the piston movement and valve opening. In addition, pressure oscillations in the manifold can also play a role. These were analyzed for OP C and D in [E255] and can be ascribed to two effects: lower frequency oscillations are induced by the periodic intake flow, while a backflow from the cylinder into the manifold is responsible for higher frequency oscillations. The latter are the reason for a significant spike in the intake velocity at part-load operation. Since the frequency of the pressure oscillation depends on the intake geometry (and fluid properties), it is constant for different engine speeds, with only the phase relation between oscillation and intake flow changing. Figure 4.2 shows the intake velocity and valve lift. For OP D, the superposition of pressure oscillation and intake flow leads to a doubling of the intake velocity at −255 °CA. This effect can also be observed at 2500 rpm: In addition to a slightly delayed

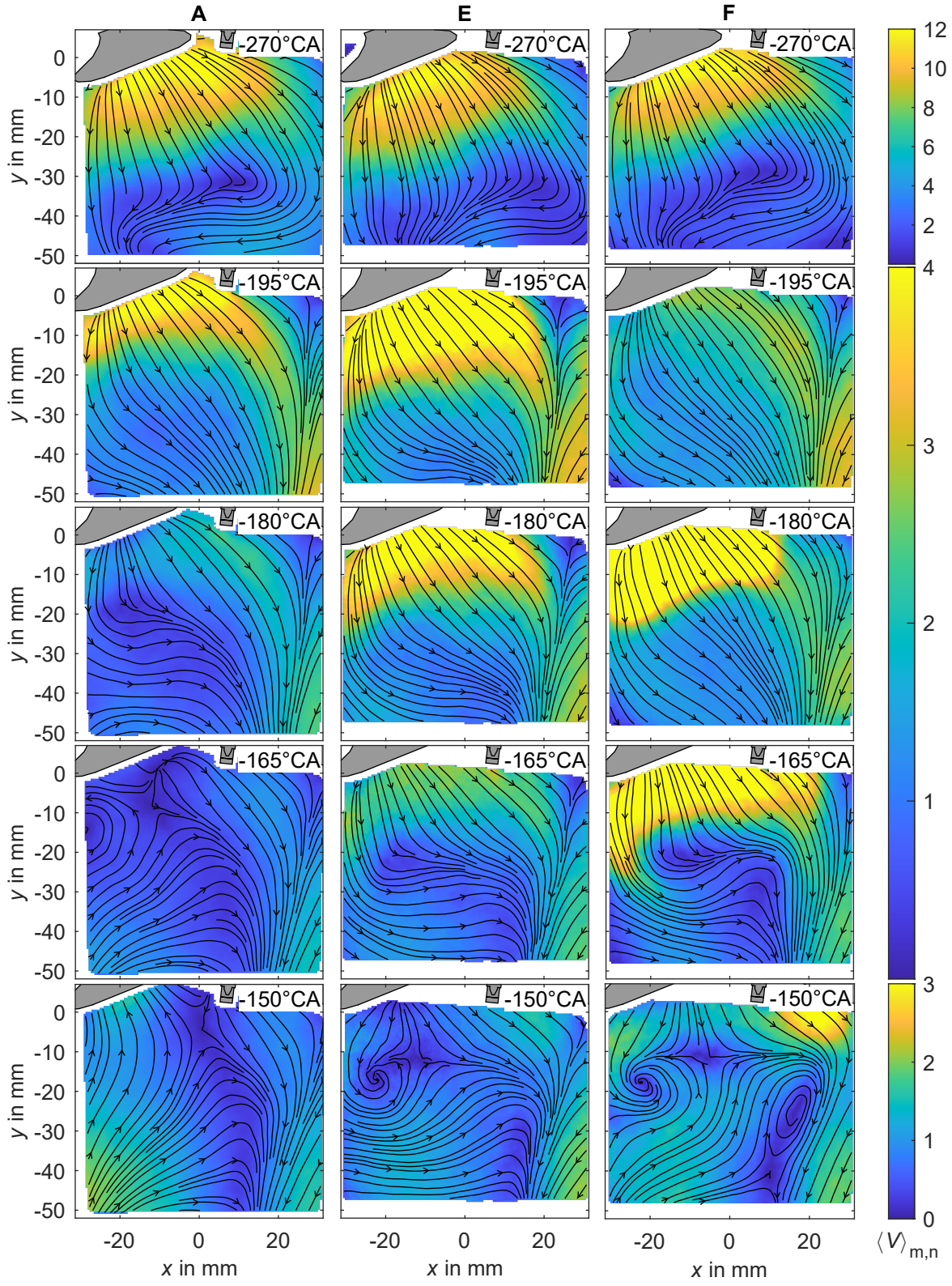


Figure 4.1: Comparison of macroscopic flow fields in the tumble plane during the intake and early compression stroke. The velocity magnitude (normalized to the piston speed) and direction are represented by the colormap and streamlines, respectively.

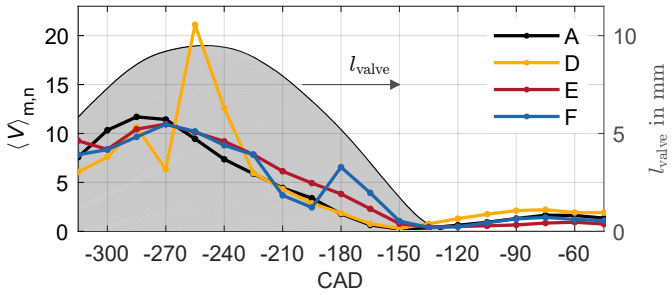


Figure 4.2: Intake velocity variations in the tumble plane. Phase average of the velocity magnitude below the intake valves normalized to the piston speed. The velocity is spatially averaged in the area $-6\,\text{mm} \leq x \leq 6\,\text{mm}$ and $-10\,\text{mm} \leq y \leq -2.5\,\text{mm}$. The intake valve lift $l_{\text{valve}}$ is indicated by the gray-shaded area.

intake flow of OP E and F compared to OP A, a spike in the intake velocity can be seen at $-180\,°\text{CA}$ for the part-load case F.

To further analyze these phenomena, Fig. 4.3 shows a direct comparison of intake manifold and cylinder pressure traces during the intake phase. It is evident that the cylinder pressure follows the intake pressure closely, but phase-shifted, which is especially obvious in the higher frequency oscillation. The phase shift is 20 and 30 °CA for OP D and F, respectively, which corresponds to a time delay of 2.1 ms. At a distance of 0.6 m between the two pressure sensors, this is approximately equal to the speed of sound. An increase in engine speed means that fewer oscillation periods occur during the shorter intake duration. Furthermore, the momentum of the moving air column in the intake increases, which increases the pressure oscillation's amplitude. For OP D, the low-frequency peak in intake pressure at $-180\,°\text{CA}$ leads to a 0.05 bar higher cylinder pressure compared to OP B. In addition, there is a high-frequency minimum of the intake pressure at $-290\,°\text{CA}$ leading to a deficit in the cylinder filling. The following rebound in intake pressure at maximum valve lift leads to a steep rise of the cylinder pressure at $-250\,°\text{CA}$, which explains the strong increase of the velocity in Fig. 4.2 [E255]. Similarly, OP F features such a steep cylinder pressure increase at -180°CA, which corresponds to its (smaller) velocity peak in Fig. 4.2, and is induced by the high-frequency minimum of the intake pressure

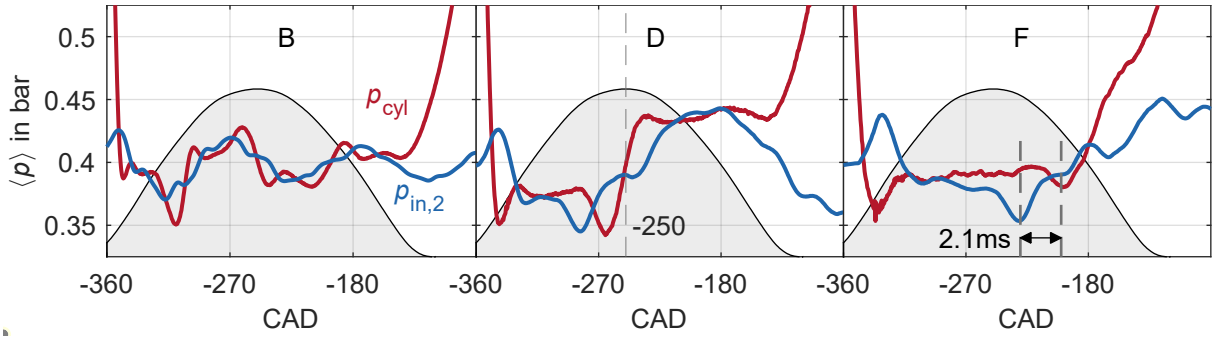


Figure 4.3: Comparison of the phase-averaged in-cylinder pressure (red) and manifold pressure (blue) of OP B, D, and F (part load operation) during the intake phase. The qualitative intake valve lift is indicated by the gray-shaded curve.

at −235 °CA. In addition to this, the low-frequency pressure oscillation and momentum of the intake air column results in rising cylinder pressures after BDC, even though the piston movement and therefore intake process reverses. After intake valve closing at −125 °CA, all three cylinder pressures rise steeply due to the advancing compression.

To summarize, as the engine speed increases, cylinder pressures at intake valve closing increase due to the pressure wave action[10], leading to a potentially higher maximum cylinder pressure even without considering the reduced wall heat loss at higher engine speeds. Furthermore, intake velocity fluctuations are present also in OP F, albeit smaller and at a later timing compared to OP D.

[10]This effect is purposefully utilized in *tuned* intake systems [97, p. 215]

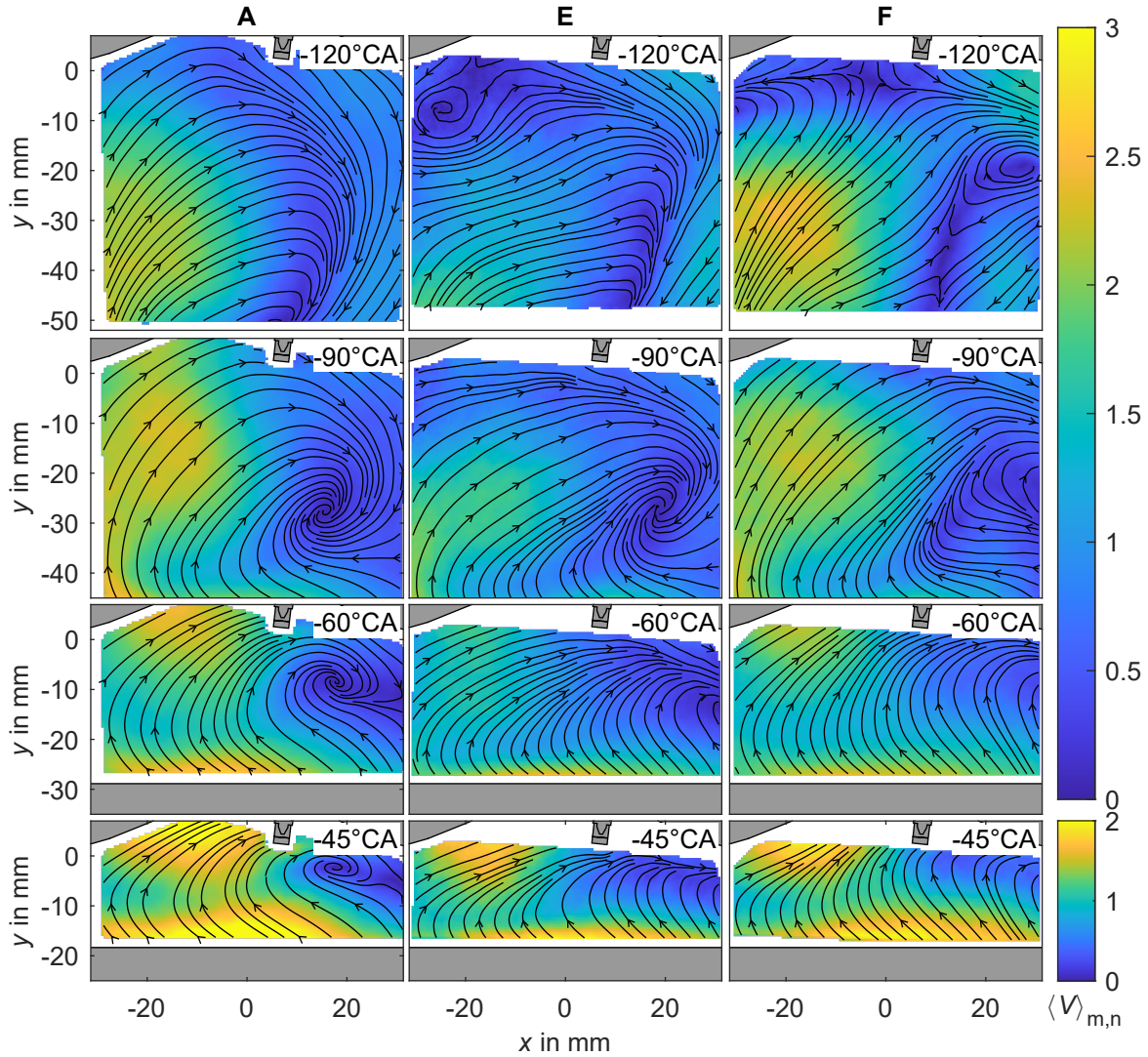


Figure 4.4: Comparison of macroscopic flow fields in the tumble plane during the compression stroke. The velocity magnitude (normalized to the piston speed) and direction are represented by the colormap and streamlines, respectively.

Changes in the momentum distribution during the intake phase can introduce valve jet flapping [12, E255] and affect the tumble development. The phase-averaged flow field during compression is shown in Fig. 4.4. For OP A to D (only A shown here), the overall picture is similar: a region of high velocities on the left side and a distinct tumble center at $x \approx 20\,\mathrm{mm}$. Due to the discussed intake flow fluctuations, OP D (not shown) features higher velocities and slightly different flow angles, which was found to affect the near-wall and boundary layer flow [E40, E215]. However, larger differences can be observed for OP E and F. The upwards, high-velocity region appears later and scaled velocities are lower for OP E. For both, the typical vortical tumble shape is deformed and no clear tumble center can be defined in the FoV from $-60\,°\mathrm{CA}$. It could be that the tumble center is outside of the FoV, in the remaining 15 mm of the cylinder radius. Another possibility is a strongly three-dimensional flow, where the characteristic tumble in this plane is no longer present. In the context of such a *tumble breakdown* [22], LESs of this engine geometry by Ding [45] suggest that the tumble motion can degenerate into two separate swirl vortices. They found that cycles with a weaker upwards flow were more likely to exhibit this flow mode, which is induced by the elliptical instability of the tumble motion. Possibly OP E and F are more susceptible to this flow mode, due to the slight differences in intake flow timing and fluctuations discussed before. Further investigations, e.g. in a horizontal plane, are needed to confirm this hypothesis.

The formation of a tumble vortex is a deliberate goal of the intake manifold design to preserve kinetic energy that can be used later in the cycle for mixing and combustion processes. Continuous dissipation transports this energy to smaller scales, where it affects e.g. the turbulent flame speed. Larger scales still play a role in convecting e.g. the spark, the early flame kernel, and combustion products. For the initial flame development, the flow around the spark plug is of great importance. In [E254] it was found that slow and fast combustion cycles correlate with the instantaneous velocity around the spark plug for OP D with artificial EGR.

In comparison, the different OPs show similar flow fields at $-45\,°\mathrm{CA}$, with a right-up directed flow around the spark plug. Due to the high sensitivity to the exact flow situation, considerable differences in combustion behavior can nevertheless occur and cannot be concluded from such phase-averaged velocity fields. An example of the severe CCV that can occur is shown in Fig. 4.5 with two manually selected cycles at $-60\,°\mathrm{CA}$ of OP E. Cycle 48 is mostly dominated by the upwards piston movement, lacks most of the tumble structure, and velocity magnitudes are low. In contrast, cycle 84 features a strong vortical motion on the left side of the cylinder. These differences persist over more than 90°CA. Cycle-to-cycle variations are an intrinsic characteristic of engine processes. Classical correlation analysis, conditioned statistics, and machine-learning models can aid in interpreting acquired data.

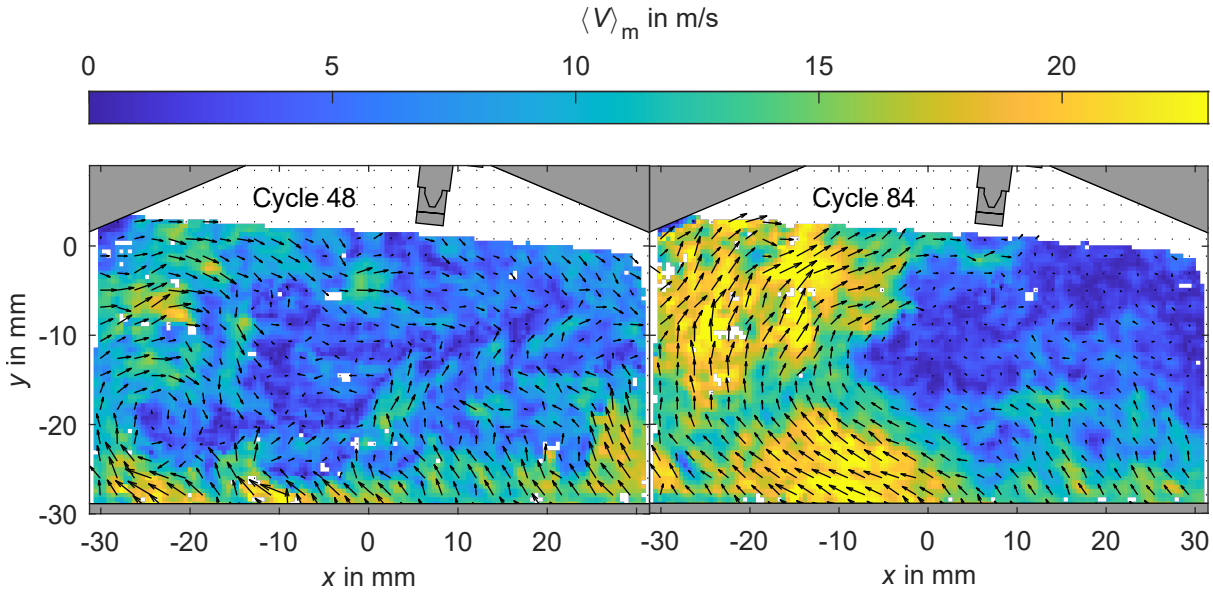


Figure 4.5: Two exemplary instantaneous flow fields of OP E at -60°CA. The velocity magnitude and direction are represented by the colormap and arrows, respectively. Every fourth vector is shown.

# Chapter 5

# Wall Temperatures

## 5.1 Aim

In this chapter, in-cylinder wall temperatures are investigated. This is achieved by coating the piston window, the cylinder liner, and the cylinder roof with thermographic phosphors (TPs) and exciting them with a UV laser. Experiments are carried out in both motored and fired operation to define thermal boundary conditions and to gain insights into the influence of the flame, especially in the piston crevice.

## 5.2 Method

### 5.2.1 Thermographic Phosphor Thermometry

Based on previous measurements at the institute in the flame-wall interaction [262] and engine context [41, 42, 71, 73], the phosphor $Gd_3Ga_5O_{12}:Cr^{3+},Ce^{3+}$ (GGG:Cr,Ce) was used with a phosphorescence decay-time approach. It was synthesized by the Solid State and Materials Chemistry Lab at Technische Universität Darmstadt (TUDa). In order to apply as thin and homogeneous a layer as possible, the phosphor powder was first suspended in a binder solution (ZYP Coatings Inc., HPC-Binder, >98 % volatiles, active ingredients $MgO-SiO_2$) and then air-brushed onto the respective surface (Badger Air-Brush Co., Badger 150, 3 bar pressure). Thereby a mixture of 0.8 g phosphor in 5 mL binder was used. The resulting coating was dryed using a heat gun, to remove the volatile water content. Heat treatment is also known to increase mechanical stability of the coating, an aspect which the cylinder roof coating was later found to be lacking.

An exemplary coating[11] was analyzed using a 3D confocal microscope (Alicona, InfiniteFocus). The average thickness was determined to be 11 µm, with high relative roughness values of $R_z = 30\,\mu m$[12] and $R_a = 5\,\mu m$[13]. The surface is strongly inhomogeneous and granular in character. This fact, together with varying grades of porosity, increases the uncertainty in determined material properties, such as density and thermal conductivity.

[11] Coating on the heated copper block used for calibration; similar surface parameters were measured for a piston glass coating by [43].

[12] Five-point mean roughness (maximum peak to valley height)

[13] Arithmetical mean roughness

Table 5.1 lists the properties required to calculate the Biot number (see 2.1.2) from two sources.

To accurately capture the wall temperature, the thermal resistance introduced by the TP, and thus the internal temperature gradient, should be small compared to the gradients of the system. Together with an assumed heat transfer coefficient of $\alpha = 1000\,\mathrm{W\,m^{-2}\,K^{-1}}$ [42], the Biot number is estimated to be on the order of Bi = 0.0014 to 0.014. Based on this, the thermal resistance of the TP layer is much lower than the resistance in the convective boundary layer. Consequently, temperature gradients in the TP layer are small compared to the gradients in the gas phase. Another aspect is the temporal response of the TP layer. The diffusion time scale, that is, the characteristic time for heat to diffuse through the layer, is estimated to be $t_\mathrm{d}$ = 25 to 250 µs, which is on the order of the duration of one crank angle (111 µs for 1500 rpm) and sufficiently small for the dynamic processes investigated.

Table 5.1: Material properties of GGG:Cr,Ce and the fused silica piston window. Density $\rho$, specific heat capacity $c_\mathrm{p}$, and thermal conductivity $k$ are given for a temperature range $T$.

| | $\rho$ kg/m$^3$ | $c_\mathrm{p}$ J/(kg K) | $k$ W/(m K) | at $T$ K |
|---|---|---|---|---|
| $Gd_3Ga_5O_{12}$:$Cr^{3+}$, $Ce^{3+}$ [41] | 7300 | 500 | 7.8 | unspecified |
| $Gd_3Ga_5O_{12}$:$Cr^{3+}$, $Ce^{3+}$ [42] | 2800 | 470 - 880 | 1.2 - 0.77 | 309-472 |
| Fused silica [95] | 2200 | 960 | 1.38-1.84 (1.6) | 293-673 (avg) |
| Piston ($AlSi_{18}CuMgNi$) [246] | 2680 | 960 | 140 | 293-570 |

Even in the case of such small estimated Biot numbers, small TP layer thicknesses are paramount if accurate wall temperatures are to be measured. Knappe et al. [133] showed that temperature gradients inside the TP layer in an engine increased significantly for thicknesses above 20 µm. For a layer of 40 µm thickness, the differences between wall- and gas-side temperature amounted to up to 20 K after flame impingement, whereas at 20 µm no difference was detected. To conclude the discussion of thermal properties, the TP application in the current work, with a thickness of approximately 11 µm, is considered appropriate for wall temperature measurements.

### 5.2.2 Experimental Setup

The experimental setup is shown in Fig. 5.1. A high-speed Nd:YAG laser (Edgewave, pulse energy 0.7 mJ, estimated 0.35 mJ inside the engine) was formed into a sheet (250 µm FWHM at about 8 mm width, piston top; 600 µm FWHM at about 10 mm width, crevice) and guided through the piston mirror to excite the TP on the piston window (①) and cylinder roof (②). The phosphorescence decay was imaged by a high-speed camera (SA-X2, Photron, 12 bit, 20 µm pixel pitch) with a 105 mm objective (Sigma Macro f/2.8) through a beamsplitter and a band-pass filter to block the excitation wavelength and chemiluminescence of the combustion. The laser was triggered on demand either

33 or 44 times per cycle every 45 °CA apart, with a refinement to every 5 °CA during late compression and early expansion. Shortly before each laser trigger, the camera started a burst of 140 frames at 400 kHz with an exposure time of 1/996 923 s, whereby the first 21 frames where used to gather background images. The aperture was set to $f/4$ for measurements on the cylinder roof (②) and in the crevice (③). During the measurements on top of the moving piston, the aperture was mistakenly set to $f/2.8$, which reduced the spatial resolution due to blurriness at extremes of the piston stroke. The camera's resolution was set to $128 \times 48$ pxl, resulting in a spatial discretization of 110 µm pxl$^{-1}$ (①, piston glass at −45 °CA), 116 µm pxl$^{-1}$ (②), and 133 µm pxl$^{-1}$ (③). For experiment ③ in the crevice, both the camera's view and the laser were guided through the glass liner at a slight angle to each other (not shown in Fig. 5.1). Motored measurements were conducted after the engine achieved stable boundary conditions especially indicated by stable exhaust temperatures. For fired operation, isooctane was injected in the intake manifold and the ignition timing from Table 3.2 was used. The engine was pre-heated using a work-rest scheme, whereby only during work cycles ignition was active. After 200 work - 300 rest - 200 work - 300 rest cycles, up to 400 work cycles followed with measurements starting in the second fired cycle.

An in-situ calibration was performed to derive temperatures from measured decay times. Therefore, after measurements on the piston top, the cylinder head was removed and a heated copper block was placed on top of the piston glass with the TP layer and heated up to 730 K. In a second configuration, the TP was applied directly to the copper block and mounted with an air gap above the piston to resemble measurements at the cylinder head roof. To determine the temperature of the surface, two PT100 temperature probes

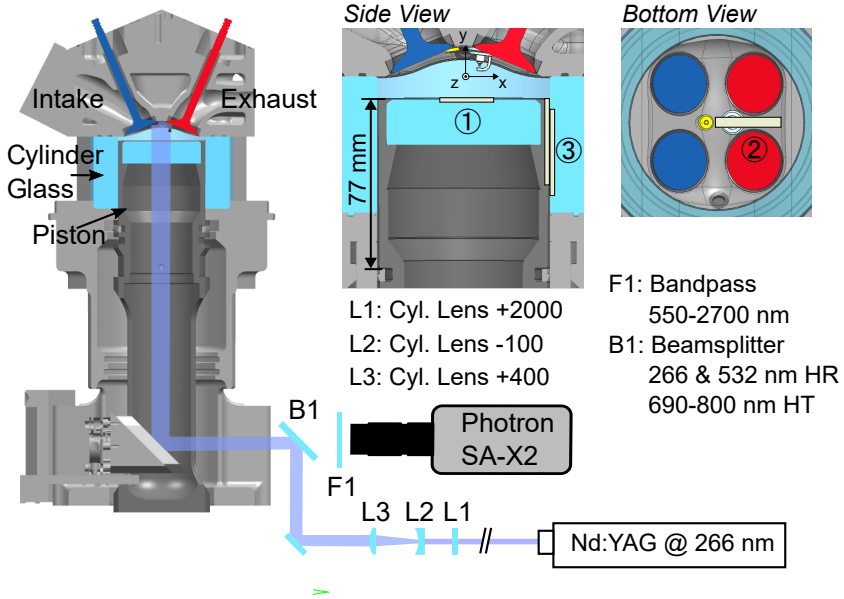


Figure 5.1: Experimental setup of the wall temperature measurements. Thermographic phosphor was applied to three locations and excited by a UV laser. In experiment ③ (crevice wall temperatures), the laser was guided through the cylinder liner at the same height as and at an angle to the camera (not shown).

(class A) were located 20 mm apart in the copper block. Decay time measurements were taken every 10 K during passive cooling of the stationary assembly. Comparability to engine measurements was ensured by using the same trigger scheme of 33 triggers per cycle. For each temperature step, 3 virtual cycles at simulated 800 rpm with a total of 99 decay times were recorded.

Figure 5.2 shows three exemplary temperature steps of this calibration. During the first measurements (red curve), from simulated −360 to −270 °CA, a slight initial temperature increase can be observed at the 520 and 320 K steps. A similar effect is seen around simulated TDC, in the region of increased measurement frequency. The reason for both phenomena could be laser-induced heating of the TP layer. At higher temperatures the effect is weakened, likely due to the increasing specific heat capacity (see Table 5.1). In terms of precision, the spatial standard deviations are on the order of a few K.

The resulting calibration curves are shown in Fig. 5.3. A detailed description of the processing is presented in the next section. Here, each calibration point's decay time is calculated by taking the median of decay times in space and then averaging in the time dimension. In comparison, the piston top (red) and cylinder head (blue) configuration vary only slightly, with deviations of maximum 10 K for the same decay time at higher temperatures. This is likely due to the different boundary conditions at the heating block surface, with natural convection of air in the case of the cylinder head and direct contact with the piston glass in the piston top configuration. Both are quantitatively and qualitatively close to the work of Ding [41] and Meißner et al. [167], who used the same batch of GGG:Cr,Ce phosphor as this work, but different experimental setups. This shows the robustness of the decay time approach with respect to excitation energies and detection efficiencies. Finally, the temperature $T = f(\log_{10}(\tau))$ is fitted with *PCHIP*[14] splines as a function of the decay time $\tau$. For the remainder of this work, the *piston top* calibration is applied to aid comparability.

Since the TP's sensitivity cannot be easily assessed in Fig. 5.3 due to the logarithmic scale, Fig. 5.4 shows the sensitivity $\mathrm{d}\tau / \mathrm{d}T$ and the relative spatial standard deviation of derived temperatures with respect to the temperature. It is apparent that the sensitivity is highest for temperatures below 400 K. The standard deviation increases and sensitivity decreases at intermediate temperatures. Even though the sensitivity is minimum at temperatures above 600 K, spatial standard deviations stay low. Additional analysis on the precision is discussed in section 5.2.4.

### 5.2.3 Processing

Several processing steps are necessary to derive temperatures from the recorded image data:

1. In order to reduce noise, the intensity-corrected images are averaged in a sliding window of size $3 \times 3$ pxl.

[14] Piecewise Cubic Hermite Interpolating Polynomial (PCHIP) [165]

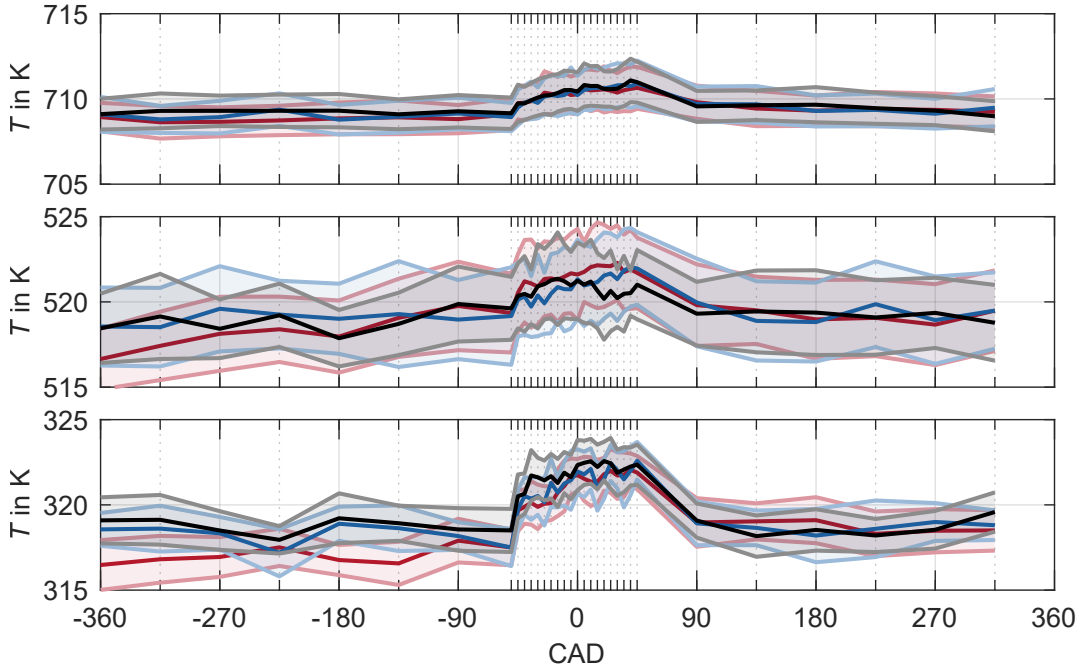


Figure 5.2: Three exemplary temperature steps of the TPT calibration (piston top). For each step, three virtual cycles with 33 measurements each were recorded. The spatial average is indicated by bold, the spatial standard deviation by shaded lines. Each laser excitation is emphasized by the minor and major tick lines.

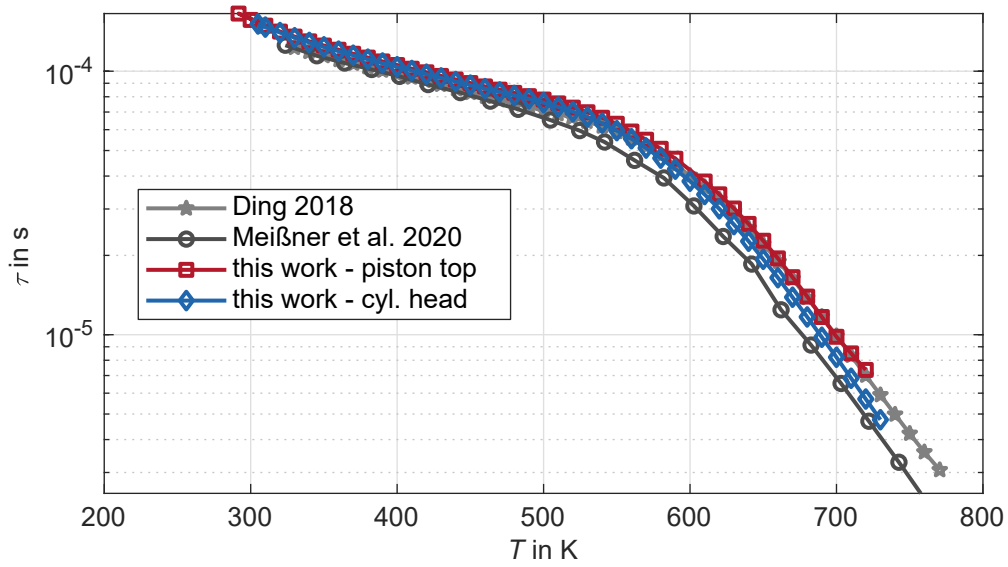


Figure 5.3: Comparison of decay time calibrations. Next to literature data (gray) [41, 167], the calibration on the piston top (red) and the cylinder head calibration (blue) of this work are shown with respect to the sensor temperature.

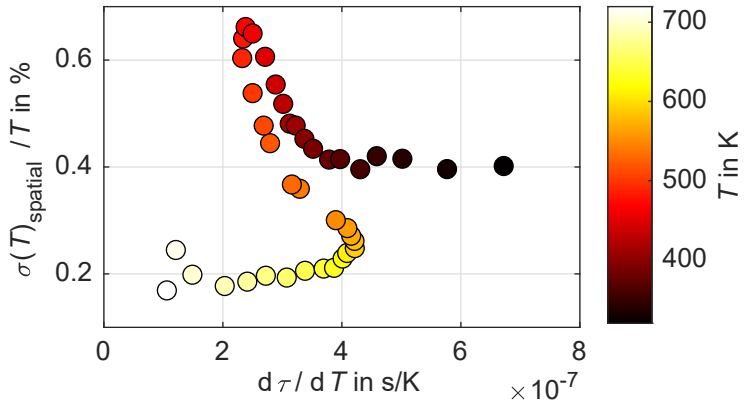


Figure 5.4: Sensitivity and precision of the TPT calibration. For different temperatures (color), the sensitivity $\mathrm{d}\tau/\mathrm{d}T$ and relative spatial standard deviation of the TPT calibration are presented.

2. The background is corrected by subtracting a median image of the background frames acquired before each laser excitation. Between −30 to +45 °CA, the background's intensity evolution over time is fitted with splines, to account for changes in the flame's luminosity during the exponential decay (see Fig. 5.5). This approach was altered for measurements in the crevice, since high initial intensities and low temperatures led to remaining decaying signals for triggers with 5 °CA separation. In this case, one median image per measurement run was calculated from background frames of unaffected triggers.

3. To calculate the decay time, the 2-parameter[15] linear regression of the sum (LRS) approach described by Fuhrmann, Brübach, and Dreizler [71, 75, 76], who implemented and evaluated the procedure from Everest and Atkinson [58], was adapted. In the employed iterative approach, the fitting window depends on the calculated decay time itself and starts at 0.8 $\tau$ and ends at 3.75 $\tau$ after excitation. In this way, the influence of multi-exponential processes at the beginning of the decay is minimized.

4. Finally, temperatures are calculated from the derived decay times. The 2D temperature field is post-processed by checking for minimum intensity levels and calibration temperature bounds. Furthermore, outliers are detected in an iterative approach.

### 5.2.4 Uncertainty

An indication of the sensitivity and precision of the employed TP was already given in Fig. 5.2 and 5.4. To assess the contribution of the decay time calculation algorithm to the precision, a Monte Carlo simulation was conducted. Ideal signal traces $I(t)$ with a decay time of $\tau$ were created. After adding Poisson shot noise and camera noise sim-

[15]The initial intensity $I_0$ and decay time $\tau$.

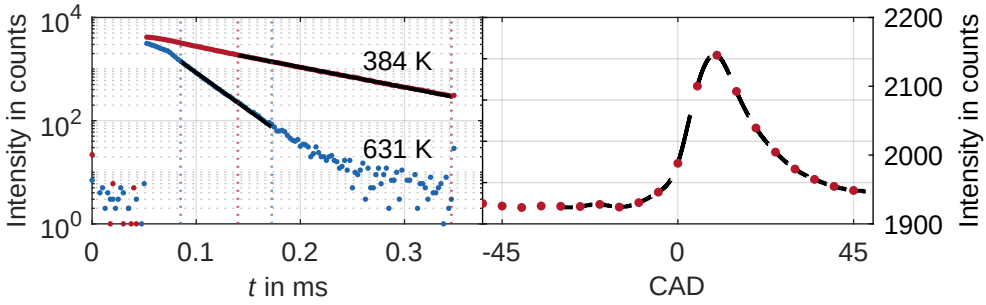


Figure 5.5: TPT processing. Left: Exemplary decaying signal with the calculated fit (black line) in the fitting window (dashed vertical lines). Right: Background luminosity of the combustion is corrected by a spline fit (background frames as red dots, interpolated background during decay in black).

ulated by Gaussian noise, the decay time $\tau_{\mathrm{calc}}$ was calculated. No systematic deviation $\tau_{\mathrm{calc}} - \tau$ was found. The standard deviation of this difference is shown in the left panel of Fig. 5.6. A nearly linear relationship to the decay time itself can be observed. After applying the temperature calibration (right panel), the simulated temperature standard deviation (red) and experimentally acquired standard deviation during the calibration (blue) show similar characteristics. This indicates that most of the fluctuations can be explained by Poisson shot noise, as the contribution of camera noise was found to be neglectable. The peak around 470 K is emphasized in the 80th percentile of the absolute temperature fluctuations around the mean (black line). Since neither the TP sensitivity nor the decay time calculation change significantly around this temperature, it is likely

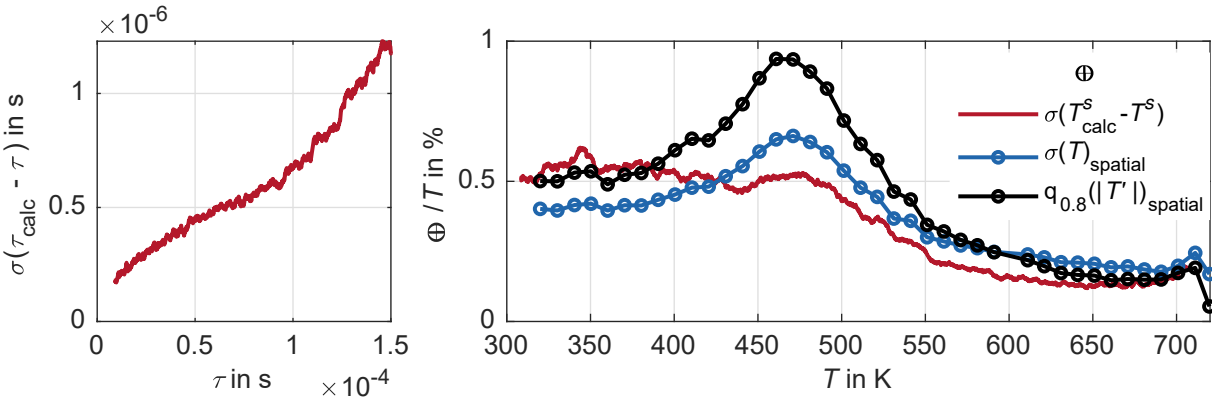


Figure 5.6: Analysis of TPT precision. Left: Influence of noise on the decay time calculation. Shown is the moving average of the difference between Monte-Carlo-simulated signals and the analytical solution, with respect to the analytical solution. Right: Measure of temperature precision. Shown are the standard deviation of the temperature calculation error obtained by Monte-Carlo-simulated signals (red), the spatial standard deviation of the calibration measurements (blue), and the 0.8-percentile of the measurement's absolute spatial fluctuation around the mean (black), with respect to the temperature.

that photophysical changes in the emission process, which also introduce the change in slope of the calibration curve, are responsible for these higher fluctuations.

Assessing the accuracy is less straight forward. Changes in the TP's photophysical properties could be induced by chemical reactions and interaction with the surrounding gas or wall material. However, Fuhrmann [76] found no influencing factors in an engine environment. Another important contribution is the optical detection of the decaying signal. The employed camera characterization minimizes non-linearities in the transfer function of each pixel. Moving objects, such as the piston wall in the crevice, introduce additional uncertainty due to the spatial discretization, remaining pixel-to-pixel variations, and changes in the optical efficiency throughout the FoV. Therefore, phosphor thermometry on fast moving particles typically employs an intensity ratio approach [24, 63, 117]. In this study, measurements on the cylinder head and liner are stationary, while the movement of the piston top towards the camera is negligible in its effect. On the side piston wall, the movement is a maximum of 15 pxl and negative influences were minimized by binning 4 pixels in the movement's direction.

Additional sources of uncertainty are the algorithm for isolating the decaying signal and calculating the decay time as well as the application of the calibration. Here, the proven LRS algorithm with low systematic errors [71] was used. The calibration was fitted with a spline and consists of adequately spaced temperature steps, which are measured with a PT100 and have an absolute error of 1.6 K. The pre-processing of the decaying signal, that is the background correction and the selection of a fitting window, has the greatest impact. In exemplary calculations, a remaining offset of 5 % or 200 counts of the initial signal amounts to an error of approximately 5 % in the decay time and 4 % in the temperature, which would correspond to 15 K. The employed background correction, as described in section 5.2.3, proved to be suitable for the presented measurements during manual inspection.

Deviations between the wall and TP temperature were already discussed in section 5.2.1 and are considered negligible in the context of convective heat transfer. However, another potentially important contribution is heating due to the laser excitation. Based on experiences in the literature [41, 42] and the temporal stability of the calibration results (see Fig. 5.2), a negligible impact of laser heating was expected. However, results from engine measurements showed a phenomenon that could be related to laser heating: Motored measurements from the piston top exhibit a temperature gradient in the z-direction, perpendicular to the laser sheet, which cannot be explained by engine processes. Figure 5.7 shows the gradient in temperature over z (red) for three CAD symmetric about TDC. The laser sheet position is indicated by the phosphorescence luminosity (black), whereby previous excitations are shown in fading gray lines.

The temperature slope can be seen to alternate during the cycle, with high temperatures appearing at positive and negative z for compression and expansion, respectively. Around TDC, temperatures are homogeneously distributed at a slightly greater mean. There is a correlation with the slight movement of the laser sheet in z-direction due to the vertical piston movement. Thereby, the temperature maximum lags behind the sheet movement, which may indicate that the deposited energy from previous laser shots plays a role.

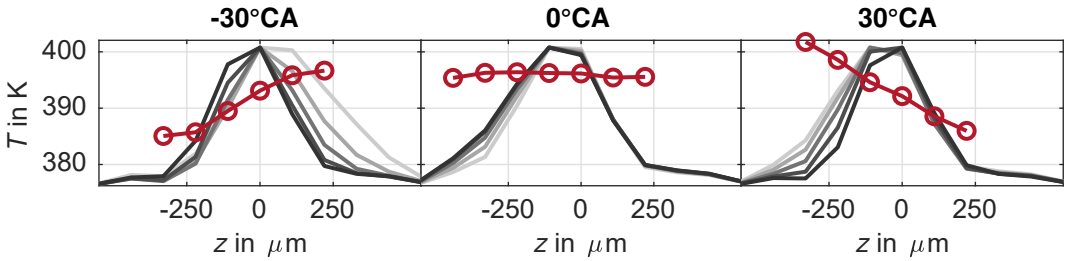


Figure 5.7: Influence of the laser position history. Wall temperatures of motored OP A on the piston top (red) and the qualitative phosphorescence luminosity as a measure of the incident laser energy of the current CAD (black) and previous ones (fading grayscale), both with respect to $z$, the sheet perpendicular coordinate.

Estimating the possible temperature increase using the thermodynamic parameters from Table 5.1 and parameters of the laser sheet, values between 5 to 20 K are reasonable. The heat would be conducted through both the phosphor and the glass until equilibrium is reached. However, it is questionable whether such temperature gradients would last long enough on a 0.5 mm scale. To some extent, heating effects are included in the calibration, where the PT100 sensors cannot detect such a localized and instantaneous temperature rise. Most likely, the large thermal mass and orders of magnitude higher conductivity of the copper block equalize temperature differences faster than the piston glass. Overall, local temperature differences in the z-direction can be as high as 20 K and 40 K for OP A and C, respectively. Interestingly, they cease to appear during fired operation, which could indicate an additional quantum mechanical effect next to the thermal effect of the laser fluence. Measurements in the crevice do not show such a temperature gradient perpendicular to the laser for two reasons: First, it's laser sheet position is stationary; second, the laser fluence is lower due to a less focused laser sheet. Nevertheless, temperatures in the vertical y-direction along the sheet width differ by about 5 to 10 K.

All in all, the observed "laser heating" phenomenon is not fully understood. To correct its effect on the temperature measurement, reported spatially averaged temperatures of motored operation are calculated by averaging for each $z$ along $x$, in the example of the piston top (see Fig. 5.1 and 5.7), and then taking the minimum temperature $z$. For the crevice, it is done by averaging along $y$ and taking the minimum in the circumferential direction. While this correction makes for a better estimate of the true wall temperature, temperatures might be overestimated by 5 to 15 K, especially at TDC.

## 5.3 Results

First, averaged results from motored operation are discussed. After startup and an initial stabilization period, the engine runs in a steady state, with constant pressures and exhaust temperatures. Wall temperatures acquired by TPT are constant over cycles too (not shown). They are furthermore largely constant throughout a cycle, only around TDC an

increase can be observed. This can be attributed to both increasing gas temperatures due to the compression and laser heating effects during the 5 °CA trigger spacing. From the acquired data it is estimated that the wall heat flux due to the compression leads to a wall temperature increase below 10 K.

These results of quasi-constant temperatures are in line with previous insights: Bürkle et al. [26] measured gas temperatures inside this engine for motored OP A with laser absorption spectroscopy and found a line-of-sight-averaged temperature increase of 350 K during compression, reaching approximately 400 °C in total (see Fig. 5.8). Gas temperatures followed the isentropic process closely until TDC, which indicates an overall marginal heat flux from the gas to the walls. This can be explained by the low temperatures of the process compared to fired operation and the ratio of densities and specific heat capacities of wall and gas: if hot compressed air at 400 °C and 10 bar in the boundary layer up to 1 mm away from a quartz glass wall would be subject to heat transfer resulting in a temperature change of 200 K, the wall would heat up by just 5 K in a depth of up to 0.1 mm. Further discussion of temperature profiles during a cycle is presented in section 5.3.1 and 5.3.2.

Fig. 5.9 shows wall temperatures averaged in space and over four crank angles of motored operation for OP A-D at the four different locations. To minimize the influence of laser heating, the minimum temperature perpendicular to the laser sheet is used, as discussed before. Furthermore, four representative CAD during the intake and compression are selected. In addition to the cycle-averaged spatial standard deviation (errorbars), the dashed line denotes the conditioning temperature of coolant and oil. As expected, all temperatures are above the nominal conditioning temperature. Higher engine speeds translate into higher wall temperatures, as can be seen for OP C and D, which correlates with increased IMEPs and mass flow rates. The cylinder head, which incorporates several coolant channels, is at lower temperatures than the piston glass, which is cooled only via an air jet from the mirror casing. Inside the crevice at about the same vertical position, wall temperatures are similar. The differences between the piston crown made from an aluminium alloy and the quartz glass cylinder liner are approximately 5 K. This is noteworthy, since contrary to the piston, the liner is not actively cooled. On the other hand, the crevice gap of 0.5 mm in the cold engine is so small that no major radial temperature gradients are to be expected.

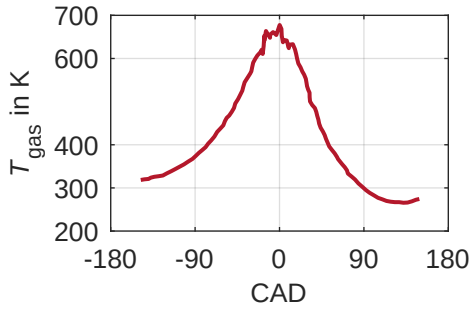


Figure 5.8: In-cylinder gas temperature as measured by Bürkle et al. [26] using laser absorption spectroscopy for motored OP A and an intake temperature of 20 °C.

At TDC, the crevice of this engine represents 15 % of the in-cylinder volume. Combined with a high surface-to-volume ratio, heat fluxes in the crevice have a major impact on achieved peak pressures. During fired operation, the flame is being pushed into the crevice, where it quenches. Outgoing, unburnt gases are being combusted during the expansion. Therefore, a more detailed investigation of temporally and spatially resolved crevice temperatures is of interest.

### 5.3.1 Crevice Temperatures

Figure 5.10 shows the intra-cycle evolution of piston wall temperatures in the crevice for OP A and C. Each 2D measurement, binned down to 1D in circumferential direction to reduce artifacts from the moving piston, is shown at its vertical position relative to the piston top $y'$ with respect to the crank angle. Due to the piston movement in front of the camera, the imaged region depends on the current piston position. As can be seen, at TDC a region −35 to −52 mm below the piston top is accessible, which is in the lower half of the 77 mm deep crevice. For motored operation, phase-averaged temperatures are shown, while for fired operation one instantaneous cycle was selected about 130 cycles after the first fired cycle, since in the fired case wall temperatures are not steady and flame-crevice interactions intermittent, as will be discussed later.

Several observations can be made: Even in motored operation, a clear gradient from top to bottom is visible, which is in line with higher average temperatures seen for the piston glass in Fig. 5.9. Furthermore, the temporal variation throughout the cycle is low, and OP C features higher temperatures than OP A. During fired operation, overall temperatures are higher. A clear temperature increase is visible shortly after TDC. This indicates that the flame or at least hot, burnt gases are occasionally being pushed inside the crevice

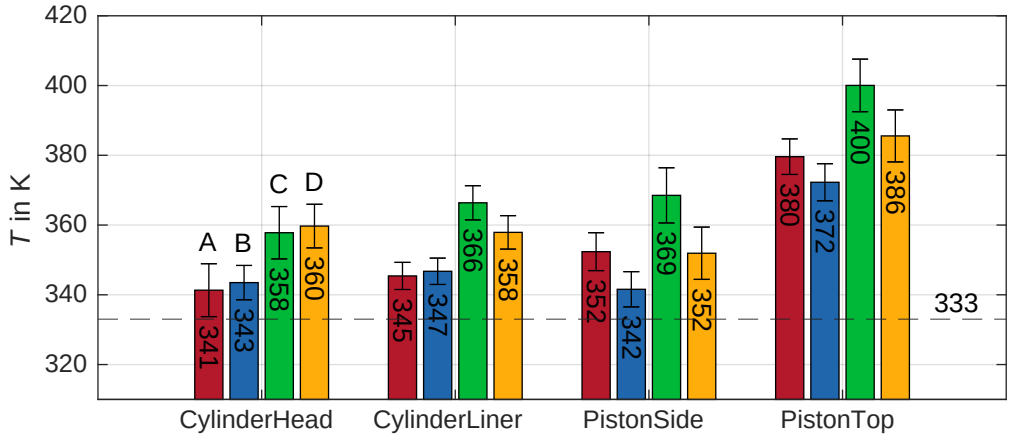


Figure 5.9: Wall temperatures during motored operation. Spatially and temporally (−360, −315, −50 and −45 °CA) averaged temperatures are shown for OP A-D at four different locations. Errorbars denote the cycle-averaged spatial standard deviation. Measured temperatures lie above the conditioning temperature (dashed line).

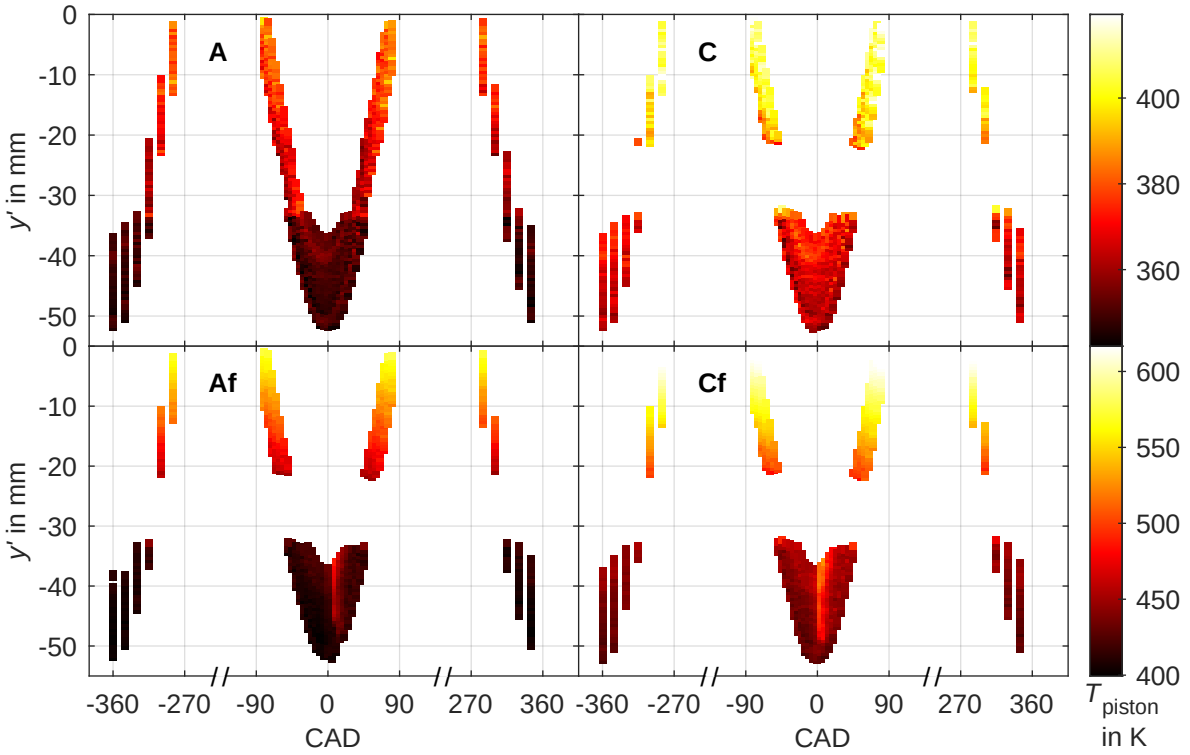


Figure 5.10: Evolution of the piston wall temperature in the crevice. For OP A and C, wall temperatures from motored (top) and fired operation (bottom) are shown at their piston-top-relative position $y'$ with respect to the crank angle. For motored operation the phase average temperature and for fired operation the temperature of an exemplary cycle is given. Gaps around $y' = -25\,\mathrm{mm}$ are due to detaching phosphor areas.

at a depth of up to 50 mm. This phenomenon will be discussed in more detail later. Temperature differences between top and bottom get as high as 40 and 150 K for OP C in motored and fired operation, respectively.

The opposite side of the crevice is shown in Fig. 5.11, where cylinder liner wall temperatures are presented in a similar way as described previously, except that the glass is stationary. From −40 to −55 mm, no clear gradient in the vertical $y$-direction can be discerned, aside from a pattern, which could be stemming from laser heating or inhomogenieties in the TP. Only minor changes are present during one cycle's evolution. Overall, temperatures are lower than on the metallic piston side. During fired operation, there is again a distinct temperature increase due to the flame reaching deep into the crevice. This temperature jump weakens over the crevice depth. As indicated earlier, these events do not occur in every cycle at the measurement location.

To analyze this further, Fig. 5.12 shows the cycle-resolved rise in temperature after ignition for the cylinder liner and piston wall at $y$ and $y'$ between −38 to −43 mm, called *L1* further on. The temperature differences in the crevice are relatively stable for hundreds of cycles, a result which was found by [41, 42] also for the piston top. This is despite the fact that overall temperatures rise significantly during fired measurements, as the

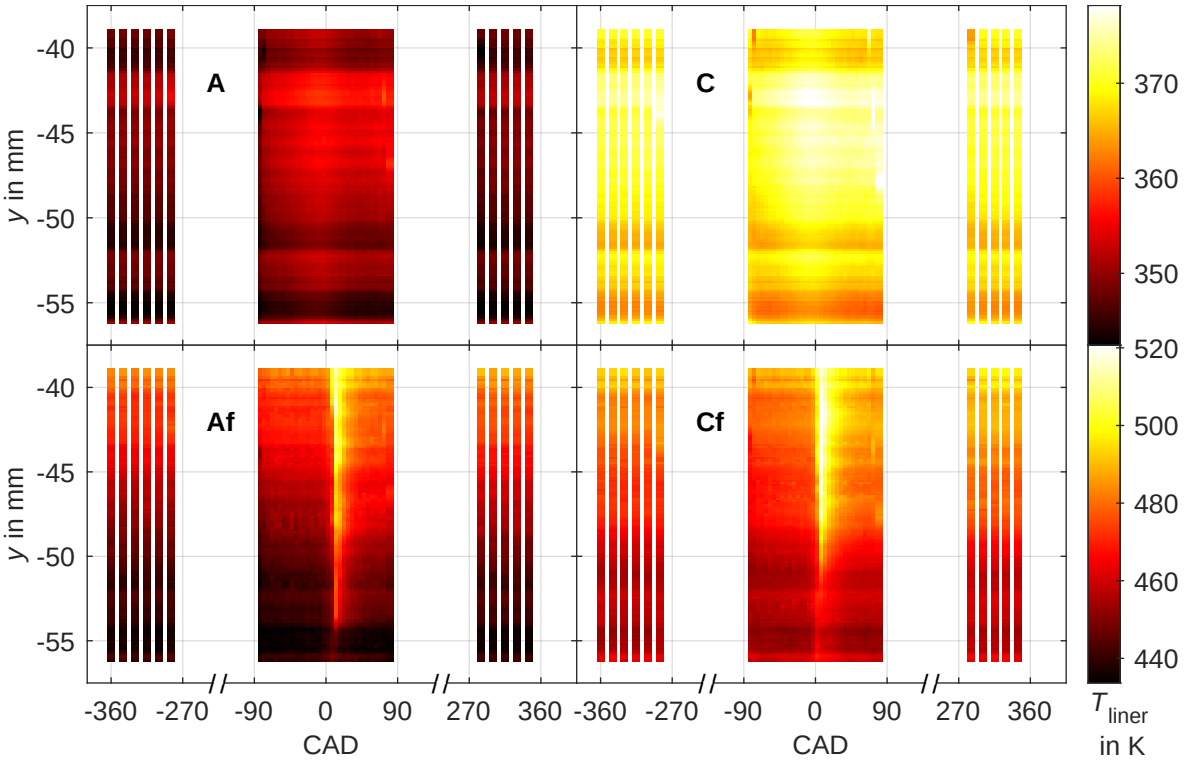


Figure 5.11: Evolution of the wall temperature of the cylinder liner glass in the crevice. For OP A and C, temperatures from motored and fired operation are shown at their global engine position $y$ with respect to the crank angle. For motored operation the phase average temperature and for fired operation the temperature of an exemplary cycle is given.

engine is not in thermal equilibrium, which will be discussed later. For OP A and C (red and black), a distinct pattern emerges: there is a minimum temperature increase of 10 and 20 K, respectively, which is caused by the temperature increase due to compression and combustion, and potentially laser heating effects. For some cycles the temperature increase is in the range of 20 to 40 K, which indicates the presence of a flame or hot gas at the measurement location.

The intermittent nature of this phenomena can be explained with Fig. 5.13, where high-speed visualizations of the flames' propagation into the crevice are shown. Two frames with a separation of 10 °CA from two typical cycles of OP A are selected. About 25 °CA after ignition, the flame propagates into the crevice. Widespread, blue chemiluminescence indicates that reactions are still ongoing. The flame fronts appear wrinkled, with a cusp-like morphology, similar to crevice flames observed by [113] in an engine and [180] in a generic crevice chamber. However, the extensive chemiluminescence disappears quickly, either due to a lack of fuel and oxygen or flame extinction from heat loss. 5 °CA later, only the foremost flame tip is visible. The maximum extent of the flame is typically reached early on, as subsequent frames show a stagnating flame front, indicating a low flame speed and quenching inside the crevice. Only a few "gulfs" can be seen to

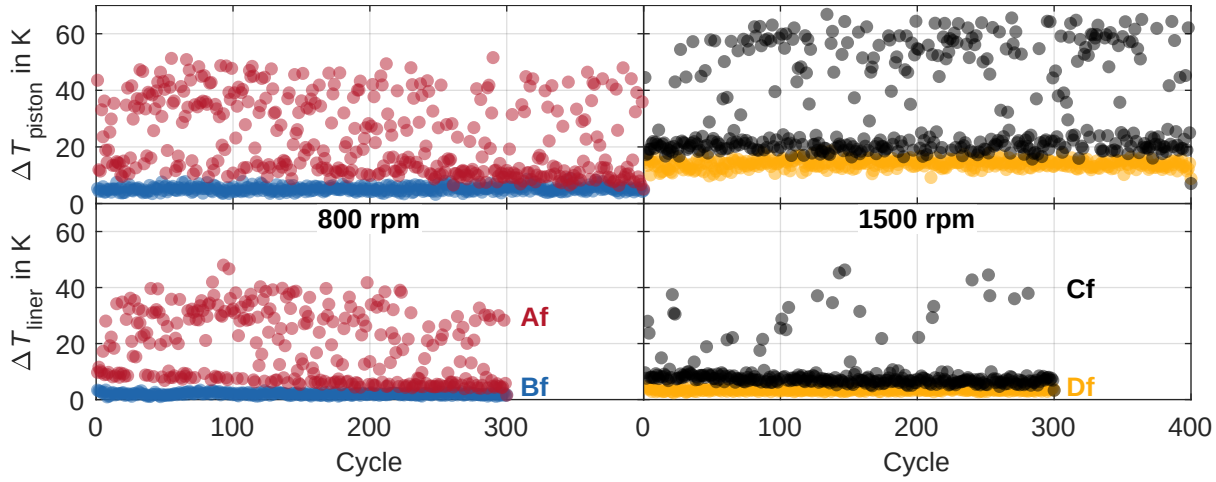


Figure 5.12: Temperature rise at the crevice walls for $y$ and $y'$ in the interval $(-43, -38)$mm. For fired OP A-D, the difference between the maximum temperature and the temperature at $-35\,°$CA is shown for each cycle, for the piston wall (top) and cylinder glass liner wall (bottom).

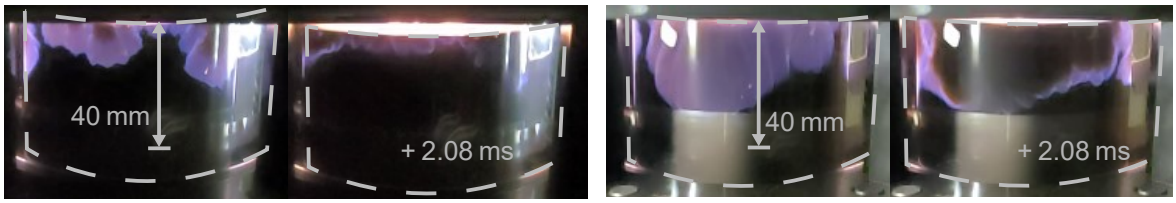


Figure 5.13: High-speed visualization of the flame in the crevice at OP A viewed through the glass cylinder liner. Two frames being 10 °CA (2.08 ms) apart, are shown for two cycles. The piston shape is implied by dashed gray lines.

disappear. Therefore, the main propagation mechanism seems to be advection or rather gas expansion due to the heat release by the main combustion.

The realized crevice temperature increase and thereby penetration depth could be related to the combustion speed, but an analysis of $\Delta T$ and the respective maximum cylinder pressure showed no correlation. In conclusion, the cycle-to-cycle variations in the temperature increase inside the crevice can be attributed to variations in the flame shape. Even though a penetration depth of up to 40 mm into the crevice can be reached, it varies from cycle to cycle and in circumferential direction. Interestingly, for OP C the number of flame events varies between the cylinder liner and piston side measurements, even though indicating data such as maximum cylinder pressures vary in a typical range, which could imply other unknown run-to-run influences.

For OP B and D (Fig. 5.12, blue), no intermittent temperature increase can be observed, which implies that the flame does not reach the TP inside the crevice. A number of parameters change when going to part load: next to pressure, the amount of internal EGR, the spark timing and altogether the flame speed and thickness. Empirical relations for the extinction width of a two-wall channel, that is the channel width at which flame propagation stops, have been derived in the past. Friedman and Johnston [67] proposed

for the channel width $W_C$ in mm:

$$W_C = K_1 P_{max}^{-0.9} T_W^{-0.5}, \tag{5.1}$$

where the maximum cylinder pressure $P_{max}$ in MPa, the wall temperature $T_W$ in K and a constant $K_1$ appears. Ishizawa [109] found a value of $K_1 = 14.8$ in a gasoline engine without EGR and at an engine speed of 1400 rpm. With maximum cylinder pressures of 25, 7.3, 29.2 and 10.4 bar (OP A-D) and an average crevice temperature of 400 K, extinction channel widths of 0.32 and 0.28 mm for OP A and C, and 0.98 and 0.71 mm for OP B and D are obtained. Even though the applicability of this empirical relation can be questioned, it is interesting to note that extinction distances increase by a factor of 3 when going to part-load. Since the crevice width is 0.5 mm, it is possible that all OP and in particular the part-load cases are subject to extinction in the crevice, meaning the flame is not self-sustaining. Indeed, high-speed visualizations indicate fewer, less deep advances of the flame into the crevice for OP B. Further investigations are needed to examine this phenomena in more detail.

To take a closer look at the heat transfer in the crevice, Fig. 5.14 depicts the change in wall temperatures around TDC. An increase of 5 to 10 K is measured during motored operation at the piston wall. This does not appear to be related to laser heating, as temperatures drop even though the trigger spacing remains constant, nor to piston movement, which is symmetrical about TDC. Remarkably, the maximum is reached around −10 °CA, which is earlier than the onset of maximum cylinder pressure at −2 °CA.

For fired operation, temperatures in the late compression tend to increase slightly slower, which is conclusive in the context of higher overall wall temperatures and subsequent

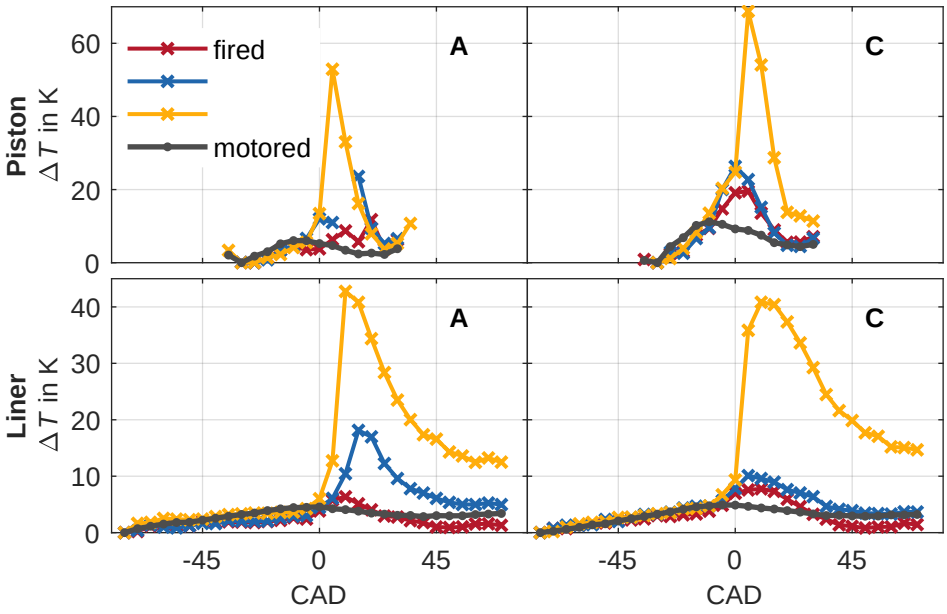


Figure 5.14: Crevice wall temperature evolution at *L1*. The temperature difference $T_{max} - T_{min}$ is shown as phase-average for motored operation. For fired operation three instantaneous cycles with low, median, and high $\Delta T$ are selected.

reduced heat transfer. As was discussed before, the jump in temperature varies between cycles depending on the flame's progression into the crevice. However, even for cycles with just a modest jump in temperature, the maximum is higher and later compared to motored operation, corresponding with the global in-cylinder pressure and therefore temperature rise during combustion. On the aluminum piston wall, temperatures revert to their pre-flame level in just 5 ms (24 °CA).

Similar observations can be made for the cylinder liner. Due to the stationary measurement location, temperatures are available in a wider range of crank angles. Peak temperature increases are smaller and cooling down is slower than on the piston wall, which is in line with the significantly lower heat conductivity of the quartz liner. Remarkably, motored temperatures plateau at a higher than initial level after about 45 °CA. During the course of expansion, the walls are supposed to be hotter than the bulk gas and should subsequently be cooled. Even at earlier timings, when the bulk gas temperature is still above the wall temperature, studies found a negative heat flux, meaning gas being heated by the walls [147, 176]. It was hypothesized that unsteady effects are the reason: due to the sustained heat loss, regions in the boundary layer can become colder than both the wall and bulk gas when expanded [147]. Another mechanism of a sudden change in heat transfer after 45 °CA could be mixing and convection phenomena. However, hotter in-cylinder gases, which where not subject to the intense heat loss in the crevice, do not enter the crevice during expansion. Instead, crevice gases escape into the combustion chamber during the expansion stroke (see e.g. [190]), where they burn during fired operation. One explanation of the plateauing wall temperatures could be superimposed laser heating.

From the time-resolved temperature evolution, the wall heat flux can be determined, if a semi-infinite body with one-dimensional heat conduction is assumed. As given by [235, p. 519], the heat flux at the wall surface can be written as

$$q_\mathrm{w}(t) \equiv \dot{q}_\mathrm{w}(t) = \sqrt{\frac{\rho c_\mathrm{p} k}{\pi}} \int_0^t \frac{\mathrm{d}T_\mathrm{w}(\tau)}{\mathrm{d}\tau} \frac{1}{\sqrt{t-\tau}} \mathrm{d}\tau, \tag{5.2}$$

with the density $\rho$, heat capacity $c_\mathrm{p}$, and thermal conductivity $k$ of the wall (see Table 5.1) , the time $t$ and integration variable $\tau$, as well as the measured temperatures $T_\mathrm{w}$.

Figure 5.15 shows calculated wall heat fluxes in the crevice walls for OP A and C. Heat flux and temperature follow each other closely in the motored and fired cases (left column). Furthermore, heat fluxes differ by one order of magnitude between liner and piston, which is due to the much higher thermal conductivity of the piston metal (see Table 5.1). This observation is supported by the analysis of all cycles (right column). For fired OP C, maximum heat fluxes on the piston wall are up to $15\,\mathrm{MW\,m^{-2}}$, while just $1\,\mathrm{MW\,m^{-2}}$ are measured on the liner. The corresponding heat fluxes of OP A are about half as large, matching the scaling in engine speed. This can be understood with the following reasoning: Based on the maximum cylinder pressure, total heat losses in OP C are similar to, but slightly lower than those in OP A. However, since the time available for heat transfer nearly halves, heat fluxes have to increase proportionally. This is likely an effect of thinner boundary layers and increased mixing in the near-wall region. Interest-

ingly, the ratio of peak heat fluxes in fired operation with flame and motored operation is consistently about eight.

To judge the results, a comparison with similar investigations in the literature is helpful. An overview is shown in Table 5.2 and 5.3. Measurements typically employ TPT, surface thermocouples or thin film resistance thermometers and derive heat fluxes by numerically or analytically solving the Fourier law. [5, 176, 260] measured wall heat fluxes at different locations inside an engine in the range of 0.2 to 0.8 $\mathrm{MW\,m^{-2}}$ for motored operation, while in numerical simulations of [79, 125] with isothermic temperature boundary conditions just 0.06 to 0.3 $\mathrm{MW\,m^{-2}}$ were calculated. The presented results in Fig. 5.15 are higher, with 1 and 2.5 $\mathrm{MW\,m^{-2}}$ for OP A and C on the metallic piston side. On the cylinder glass 0.08 and 0.12 $\mathrm{MW\,m^{-2}}$ are measured, respectively. One commonality stands out: the heat transfer is happening during mostly ±30 °CA around TDC, when the gas temperature has risen significantly above the wall temperature and the maximum is reached before TDC.

For fired operation, maximum heat fluxes measured by [5, 176] increase to 1 to 5 $\mathrm{MW\,m^{-2}}$. Dejima and Nakabeppu [35] found significant differences between phase-averaged and instantaneous heat fluxes, the latter being in the range of 2 to 7 $\mathrm{MW\,m^{-2}}$. In the current work, similar values are reached on the glass liner (0.5 to 1 $\mathrm{MW\,m^{-2}}$). Fired heat fluxes on the piston are higher, with a range of 8 to 15 $\mathrm{MW\,m^{-2}}$. Ojo, Escofet-Martin, and Peterson [180] investigated flame dynamics in a generic crevice setup by applying a highly sensitive phosphor to the steel wall. Heat fluxes from 0.4 to 4.5 $\mathrm{MW\,m^{-2}}$

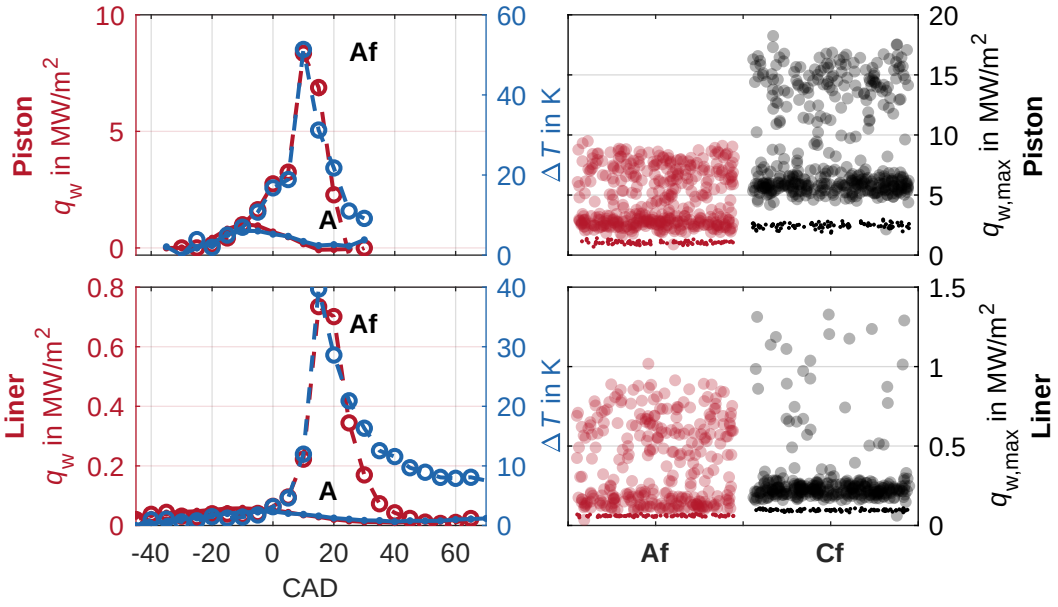


Figure 5.15: Crevice wall heat fluxes in fired operation at *L1*. Left column: Wall heat flux $q_w$ (red) and temperature (blue) of OP A shown as a phase average for motored and as an exemplary cycle for fired operation on the piston (top) and liner (bottom). Right column: Scatter plot of maximum wall heat fluxes for OP A and C. Open circles represent fired, small dots motored operation.

were found to vary with the morphology of the flame around the measurement location and the final height of extinction. The pressure of up to 2 bar before ignition was lower, the crevice thickness of 1.2 mm higher than the presented engine conditions with about 14 bar and 0.5 mm, respectively.

To the author's knowledge, these are the first measurements of flame-wall interaction in an engine crevice. In the next section, the temperature evolution throughout the cylinder will be compared for fired operation.

### 5.3.2 Global Temperature Evolution under Fired Operation

The optical engine cannot be continuously operated under fired condition. Unlike in a thermodynamic (metallic) engine, the piston is not cooled via oil but with an air jet only. Prolonged fired operation runs the risk of significant heat expansion and subsequent contact between the piston and the glass liner. Therefore, the engine does not reach a thermally steady-state. In a typical measurement procedure, the engine is fired for a few hundred cycles followed by a few hundred cycles of motored operation. This procedure is repeated, such that temperature levels are elevated for the final measurement sequence, where data acquisition typically starts around cycle 50 to 100, to avoid initial steep temperature gradients.

To evaluate this approach, Fig. 5.16 shows spatially averaged temperatures[16] of fired operation at the piston top and in the crevice. Averages are obtained before ignition, beginning with the second fired cycle of the final fired set. The TP on the cylinder head began to detach during fired measurements and is therefore excluded. In line with motored results, temperatures of part load operation are lower than under full load operation. The influence of the load is stronger than the influence of the engine speed, since the gas density affects the fuel mass and heat release as well as thickness of and heat conduction in the boundary layer. First concentrating on the piston wall, a slight, linear temperature increase can be seen over the cycles. The respective[17] cylinder liner temperatures start at a similar level, but experience a stronger, non-linear rise during the first 100 cycles. This effect is amplified on the piston top, where temperatures rise by up to 150 K during the first 100 cycles. For comparison, the exhaust temperature $T_{\mathrm{EX2}}$ of OP C, measured with a 0.5 mm tip diameter thermocouple is shown.

As it was found for the crevice, the temperature increase due to flame impingement on the piston top is expected to be independent from the absolute temperature. The left panel of Fig. 5.17 shows the temperature trace of two consecutive cycles for each OP. High heating rates are reached during flame impingement, which is followed by a slow cooling until the late compression and ignition of the next cycle. Maximum heat fluxes calculated with Equation 5.2 amount to 1 and 1.3 $\mathrm{MW\,m^{-2}}$ for OP A and C, and 0.5 and 0.8 $\mathrm{MW\,m^{-2}}$ for OP B and D (see Table 5.3). These values are a bit higher than on the

[16] Different to to the motored operation, gradients perpendicular to the laser sheet on the piston top disappeared during fired operation, such that there no laser heating correction was applied.

[17] Averaging the temperature field shortly before ignition leads to similar measuring positions in the crevice for piston and cylinder wall.

Table 5.2: Comparison of *motored* engine wall heat flux measurements in the literature.

| Source | Location | $q_{w,max}$ in $MW\,m^{-2}$ | CR[a] | Load[b] (IMEP) in bar | Speed in rpm | $\alpha_{wall} = k/(\rho c_p)$ in $m^2\,s^{-1}$ | Method |
|---|---|---|---|---|---|---|---|
| [5] | cylinder roof | 0.2-0.4 | 8.56 | not specified | 1500 | $5.4 \times 10^{-5}$[c] | duplex thermocouple; Fourier coeff. solution |
| [176] | roof, liner, piston top | $0.2 - 0.7$ | 10 | 0.4, 1 | 700-2000 | $7.49 \times 10^{-5}$ | duplex thermocouple; FEM of Fourier law |
| [260] | metallic piston top | $0.4 - 0.8$ | 13 | not specified | 2000 | $5.4 \times 10^{-5}$[d] | Thin film sensor; heat conduction model |
| [79] | piston (top, crevice) | 0.06 | 8.7 | 0.4 | 800 | - | DNS, isothermal walls |
| [125] | piston (top, crevice) | 0.3 | 8.7 | 0.95 | 2500 | - | wall-resolved LES, isothermal walls |
| this work | piston side (crevice) | 1-2.5 | 8.7 | 0.95 | 800, 1500 | $5.4 \times 10^{-5}$ | TPT, Eq. 5.2 |
| this work | cylinder liner (crevice) | 0.08-0.12 | 8.7 | 0.95 | 800, 1500 | $7.6 \times 10^{-7}$ | TPT, Eq. 5.2 |

[a] compression ratio
[b] intake pressure
[c] unspecified: "the probe bodies were manufactured from the same material used in making the cylinder head" [5]; aluminum was assumed, thermal diffusivity $\alpha$ derived from properties in Table 5.1.
[d] used the same sensor as [36]; probe body specified as $AlSi_{12}CuNiMg$, which has similar properties as $AlSi_{18}CuMgNi$ [246]; thermal diffusivity $\alpha$ derived from properties in Table 5.1.

Table 5.3: Comparison of *fired* engine wall heat flux measurements in the literature.

| Source | Location | $q_{w,max}$ in $MW\,m^{-2}$ | CR[a] | Load[b] (IMEP) in bar | Speed in rpm | $\alpha_{wall} = k/(\rho c_p)$ $m^2\,s^{-1}$ | Method |
|---|---|---|---|---|---|---|---|
| [5] | cylinder roof | 1-3.5 | 8.56 | not specified | 1000-2000 | $5.4 \times 10^{-5}$[c] | duplex thermocouple; Fourier coeff. solution |
| [176] | roof, liner, piston top | $1-5$ | 10 | 0.56, 0.7 | 1000, 2000 | $7.49 \times 10^{-5}$ | duplex thermocouple; FEM of Fourier law |
| [35] | cylinder roof | 2-7 | 15 | (8) | 2000 | $5.4 \times 10^{-5}$[d] | Thin film sensor; heat conduction model |
| [180] | generic crevice chamber, steel wall | $0.4-4.5$ | 1 | 2 | 0 | $0.4 \times 10^{-5}$[e] | TPT, Eq. 5.2 |
| this work | piston side (crevice) | 9, 15 | 8.7 | 0.95 (4.8, 5.8)[f] | 800, 1500 | $5.4 \times 10^{-5}$ | TPT, Eq. 5.2 |
| this work | cylinder liner (crevice) | 0.75, 1 | 8.7 | 0.95 (4.8, 5.8)[f] | 800, 1500 | $7.6 \times 10^{-7}$ | TPT, Eq. 5.2 |
| this work | piston glass | 0.5-1.3 | 8.7 | 0.4, 0.95 (2-5.8)[f] | 800, 1500 | $7.6 \times 10^{-7}$ | TPT, Eq. 5.2 |

[a] compression ratio
[b] intake pressure
[c] unspecified: "the probe bodies were manufactured from the same material used in making the cylinder head" [5]; aluminum was assumed, thermal diffusivity $\alpha$ derived from properties in Table 5.1.
[d] used the same sensor as [36]; probe body specified as $AlSi_{12}CuNiMg$, which has similar properties as $AlSi_{18}CuMgNi$ [246]; thermal diffusivity $\alpha$ derived from properties in Table 5.1.
[e] material stated as stainless steel; thermal diffusivity $\alpha$ calculated from typical manufacturer values at 100 °C.
[f] $IMEP_g$, only compression and expansion stroke.

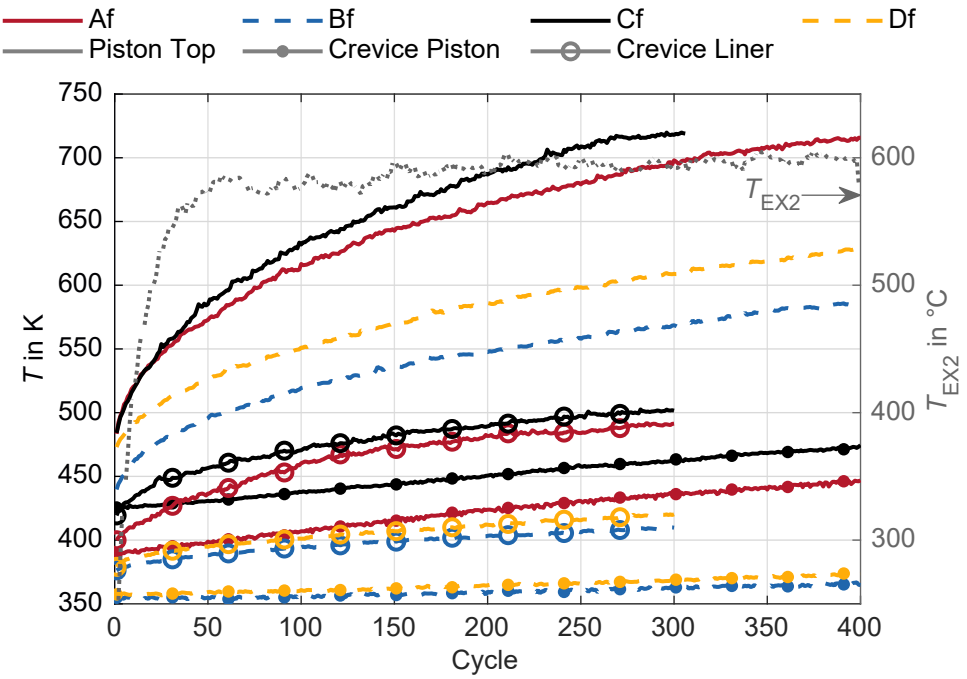


Figure 5.16: Evolution of wall temperatures during fired operation. For OP A-D the spatial averages of the temperature field at −40 to −30 °CA are shown with respect to the cycle number (after the second fired cycle). Dashed lines denote part-load OP B and D. Markers indicate the measurement location. For comparison, the exhaust temperature $T_{EX2}$ of OP C is shown as a gray, dashed line.

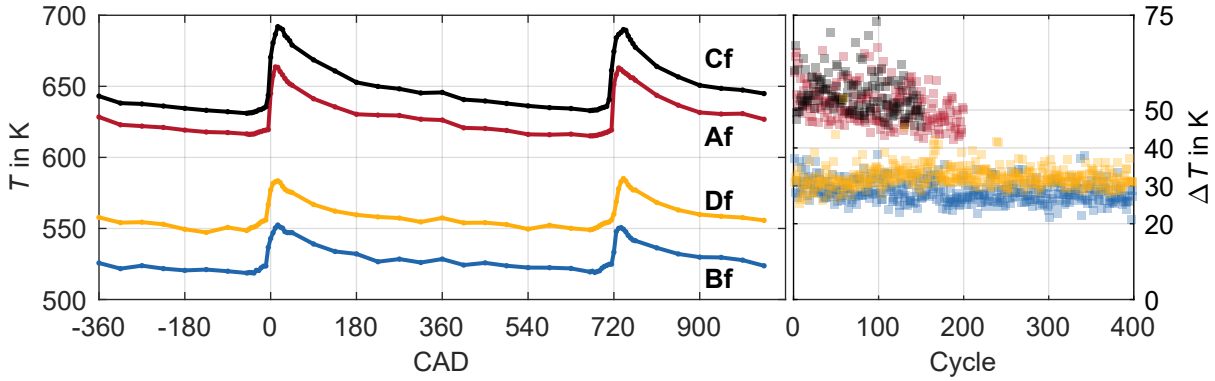


Figure 5.17: Spatially averaged wall temperatures of the piston top during fired operation. Left: Cycle 100 and 101 are shown for OP A-D. Right: Difference between average temperatures at −40 to −30 °CA and the maximum temperature of each cycle.

crevice liner, which is to be expected, due to the more prevalent side-wall quenching in the crevice as well as heat lost to the upper crevice regions.

The isolated temperature differences (right panel) are only shown for the first 150 and 200 cycles for OP C and A, respectively. This is because peak temperatures of later cycles lie outside the calibrated temperature range. Besides that, constant differences of 30 and 50 K independent of absolute temperature are observed for part- and full-load cases, which replicates the findings of Ding [41] in the same configuration and location, with an offset of 5 to 10 K, which could stem from laser heating and other unaccounted effects.

The results show that the temperature history of the engine has to be considered for detailed comparison of data, be it experimental or numerical. Fired measurements should be used earliest from cycle 50 on to avoid the initial wall temperature gradient.

## 5.4 Summary

This chapter presented an investigation of wall temperatures at three locations: the piston top, the cylinder head and in the crevice. The aim was to define the thermal boundary conditions more accurately, to describe the transient temperature evolution during fired operation, and to investigate flame-crevice interactions. Therefore, a thin layer of TP (GGG:Cr,Ce) was applied to the surfaces and excited with a UV laser. The decay-time approach was used to derive 2D temperatures.

An in-situ calibration on the piston top was employed. Comparison with other studies showed the robustness of this method with respect to the optical setup. A laser-heating like effect was observed, the origin of which is not fully clarified, though a correction was devised for measurements on the piston top.

Wall temperatures during motored operation were found to be steady over cycles, with inter-cycle variations in the range of 5 to 10 K due to increasing temperatures during compression. Wall temperatures on the cylinder head and in the crevice on the cylinder liner and piston side were found to be approximately 10 to 20 K above the conditioning temperature of 333 K. On the piston side, a vertical gradient of about $1\,\mathrm{K\,mm^{-1}}$ was observed. Consequently, the piston glass was hotter, at approximately 380 K, due to the lower thermal conductivity and exposed location inside the combustion chamber. In addition, higher engine speeds result in higher wall temperatures.

During fired operation, temperatures increase steadily with each fired cycle, since the engine is not in thermal equilibrium. The increase is greatest on the piston top, with the steepest rise in the first 50 cycles. After 100 cycles, temperatures of 625 and 550 K are reached for full- and part-load operation, respectively. In the crevice, temperatures on the cylinder liner are higher than on the metallic piston side.

High-speed visualizations showed that the flame propagated into the crevice, though mostly due to advection and expansion of cylinder gasses. This was concluded from a low rate of change on the flame front and extinction after a certain depth. Furthermore, it was supported by empirical formulations indicating extinction in channels of the size

of the crevice. Furthermore, the maximum progress of the flame differs depending on the circumferential position. Correspondingly, cycle-intermittent sudden increases in the wall temperatures of the crevice could be detected for OP A and C, which amounted to 40 K in a depth of up to 55 mm. No increase was found for part-load OP B and D, indicating faster extinction.

Wall heat fluxes were calculated from the time-resolved temperature evolution by assuming one-dimensional heat conduction. Under fired operation, peak heat fluxes on the cylinder and piston glass were in the order of 0.5 to 1.3 $\mathrm{MW\,m^{-2}}$, while on the metallic piston side 15 $\mathrm{MW\,m^{-2}}$ was measured.

# Chapter 6

# Near-Wall Flow

## 6.1 Aim

Following on from the last chapter on wall temperatures and heat transfer, in this chapter, near-wall flow dynamics and the hydrodynamic boundary layer (BL) above the piston surface are investigated by applying PIV and PTV. Conclusions from previous studies ([41, 204, E215]) are extended to higher Reynolds numbers and engine speeds. A large number of acquired engine cycles enables the novel analysis of conditioned statistics. Several contents of Chapter 6 were published in Schmidt et al. [E214], and are reproduced here, in modified and expanded form, with permission from Elsevier (see Appendix A.1.1).

## 6.2 Method

### 6.2.1 Particle Image and Tracking Velocimetry

Velocity fields were measured with a combined 2D2C-PIV and -PTV approach. Fundamentals to these techniques are presented in section 2.2.4. While PIV is an established diagnostic [199], adding PTV can improve the applicability to flows with low particle image density. Volumetric seeding of the engine volume with typical PIV particle densities, combined with high magnifications of the detection system can lead to significant loss of SNR due to multiscattering. In addition, window-correlation techniques can be biased close to a wall and in the instantaneous velocity calculation when flow gradients or inhomogeneous seeding exist [120]. In the applied combined approach, a low resolution estimate of the velocity field is first generated using PIV. Subsequently, individual particles are tracked, resulting in a scattered velocity field. Since flow gradients appear predominantly perpendicular to the wall, applying an averaging grid with high aspect ratio results in high-resolution flow measurements.

### 6.2.2 Experimental Setup

The optical setup is shown in Fig. 6.1. As fluid tracers, silicone oil (Dow Corning 510, 50 cSt) was atomized by Palas AGF 10.1 and Palas UGF 2000 seeders into droplets with

an average size of 0.5 µm and introduced in the intake manifold. A high-speed Nd:$YVO_4$ laser (Edgewave IS4II-DE, 532 nm) was guided through the cylinder liner and formed into a sheet in the central tumble plane (sheet thickness FWHM: 90 µm; $1/e^2$: 220 µm). While introducing the laser through the piston glass allows for a better view into the cylinder roof and is not affected by the piston position, coupling the laser sideways results in less reflections at the wall surface and allows for metallic piston inserts (which are not presented in this work).

The Mie scattering of droplets was imaged by a Phantom v2640 high-speed camera, equipped with a 180 mm Sigma objective and distance rings. To reduce vignetting because of the piston geometry and increase the signal close to the wall, the detection system was angled by $\alpha = 5°$ towards the piston surface. Additionally, a Scheimpflug angle of $\beta = 9°$ was set between camera and objective. Two different magnifications were employed, as summarized in Table 6.1. The astigmatism introduced by the curved cylinder glass was corrected with a $f = 2000$ mm cylindrical correction lens placed about 140 mm away from the tumble plane. A high-resolution calibration target (1 mm dot distance, LaVision) was used to transform pixel into world coordinates by polynomial dewarping.

Table 6.1: Optical setups for boundary layer measurements.

| Setup | Pixel Resolution | FoV | Distance rings |
|---|---|---|---|
| I | 7.8 µm pxl$^{-1}$ | 15.2 × 16 mm | 165 µm |
| II | 2.3 µm pxl$^{-1}$ | 4.5 × 4.7 mm | 400 µm |

Measurements were performed at different piston and camera positions corresponding to −60, −45 and 30 °CA, each with a high-speed PIV resolution of 5 °CA. Between 700 and 1200 cycles (−60 and −45 °CA), and 560 cycles (−30 °CA) were acquired. The engine was operated at 800 and 2500 rpm, as detailed in Table 6.2.

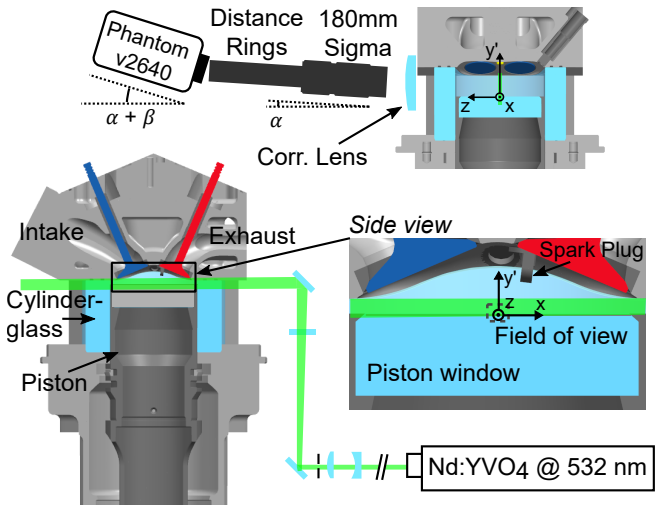


Figure 6.1: Experimental setup for high-resolution near-wall velocity measurements. Figure adapted from [E215] with permission from Elsevier.

Table 6.2: Operating points used in the boundary layer measurements.

| Name | A | B | E | F |
|---|---|---|---|---|
| Intake pressure $p_{\mathrm{in},2}$ in bar | 0.95 | 0.4 | 0.95 | 0.4 |
| Engine speed $n$ in rpm | 800 | 800 | 2500 | 2500 |

### 6.2.3 Processing

The data was first processed in DaVis 10.1.2 (LaVision), where after the spatial dewarping, a multi-pass PIV step was performed, with a final interrogation window size of $24^2$ and $48^2$ pxl for setup I and II, respectively. Using the PIV velocity field, a PIV+PTV step in Davis 10.0.5 calculated the velocity of individual particles, using a particle size threshold of 1 to 6 pxl, an intensity threshold of 45 (I) and 55(II) counts, a final interrogation window size of $6^2$ pxl, and a maximum shift of 3 pxl relative to the reference velocity as parameters. An additional outlier detection was found to be not necessary.

The resulting high-resolution and scattered vector data was processed further in Matlab (MathWorks). Each vector's position was redefined as the average of the particle's position in the PIV frames. Since flow-wall interactions are of interest, the data needs to be transformed onto a piston-relative coordinate system. Due to the small scales of the boundary layer (BL) encountered in engines, the wall position cannot be derived just from a priori knowledge using the target position and engine geometry. Instead it must be determined on a run-to-run basis. In a first step, the position was derived from phase-averaged image data: stationary particles and residue on the piston surface lead to a peak in signal intensity, which were taken as the preliminary piston position.

In order to facilitate statistical analysis, the scattered and sparse vector data was then restructured on a regular grid. Since gradients of the average flow in wall-parallel direction are small compared the wall-perpendicular ones and the wall-perpendicular velocity profile $V_x = f(y)$ are of primary interest to describe the BL, it is valid to resample the data in a rectangular grid with a high-aspect ratio and therefore anisotropic resolution. For investigation of the BL, the width of each grid cell was set to 1500 µm and the wall-perpendicular height to 15.6 and 5 µm for setup I and II, respectively. This corresponds to about 2 camera pixel per grid cell. To reduce noise, the cell height was increased beyond 500 µm from the wall, where velocity gradients in y-direction are smaller. These dimensions were chosen such that on average at least one particle/vector was expected per cell. For an overview of the bulk flow region a square grid of $(120\,\mu\mathrm{m})^2$ and $(75\,\mu\mathrm{m})^2$ was used. In all configurations, the edge of the first cell was positioned on the wall surface estimation of step one. For all data shown in this chapter, this piston-relative $x$-$y'$-coordinate system is used (see Fig. 6.1). Then, an average vector was calculated for each cell of the instantaneous flow field. In the next step, phase averages were derived from this structured velocity field.

The wall position was further fine-tuned by exploiting a symmetry in the acquired velocity profiles. Since the glass piston wall is reflective, virtual particle images and therefore vectors appear beyond the determined wall position. An example of the wall-parallel $V_x$

component's profile is shown in Fig. 6.2. Next to the real profile on the right, the virtual one stemming from reflected particle images can be seen on the left. Since full symmetry of the real and virtual profiles can be assumed in a small region near the wall, the wall position was adjusted such that symmetry is reached. This offset was determined by fitting a polynomial of 6$^{th}$ order to the data and calculating the position of its maximum. For setup I, the correction is typically in the range of 10 to 40 µm or 0.6 to 2.5 pxl. Figure 6.2 shows shifted velocity profiles, with $y'$ being the final distance from the wall. The non-zero velocity at the wall is discussed in the next section.

In a further step, the velocity gradient at the wall $\mathrm{d}Vx/\mathrm{d}y'$ is estimated by a linear fit (black lines), which is forced to go through the origin (0,0). Progressively, vectors farther from the wall are added until a maximum in the $R^2$-value is reached. This is repeated for the virtual data points. Finally, the average of both slopes is taken as the wall gradient.

It should be emphasized that a meaningful interpretation of the high resolution BL data is only possible by resampling on a rectangular grid together with phase averaging over several cycles. While there are on average 2-4 and 0.7-1.3 near-wall vectors per cell for setup I and II, respectively, the seeding particle density, which is low at these scales, limits the applicability for instantaneous cycles. The chosen seeding density is a compromise between enough particle separation for the PTV algorithm's tracking, multiple scattering and soiling of windows reducing the signal strength, and a dense vector field.

### 6.2.4 Uncertainty

Due to the angled detection system and the non-zero thickness of the laser sheet, the velocity information acquired at each pixel actually represents a spatial average in the wall-normal $y'$ and wall-parallel $z$-direction. This is depicted in Fig. 6.3 (ray B). In effect, this corresponds to averaging the $V_x$-$y'$ profile (see Fig. 6.3) in sliding windows of $\Delta y' = \sin(\alpha) \cdot t \approx 19\,\mu\mathrm{m}$, with the sheet thickness $t$. this does not introduce a significant bias for most of the near-wall flow. However, closer than $\Delta y'/2 \approx 10\,\mu\mathrm{m}$ to the wall, another effect has to be considered. As discussed in the previous section, the reflective piston

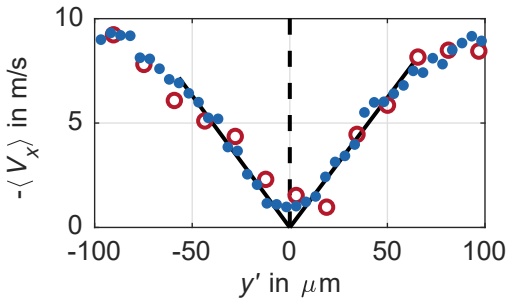


Figure 6.2: Exemplary near-wall phase-averaged $V_x$ profiles of OP E after final wall position correction, setup I (red), and II (small blue). Linear fit of the wall-gradient (black lines fitted to red data points). Figure adapted from [E215] with permission from Elsevier.

glass[18] leads to virtual particle images, beyond the determined wall position (ray A in Fig. 6.3). This progressively biases the spatial average of the velocity to higher values, if the wall distance $y'$ gets smaller that $\Delta y'/2$. Ultimately, this leads to non-zero velocities being measured directly at the wall, in ostensible contradiction to the no-slip condition. However, the influence on derived quantities and results in this work is considered small.

Another source of uncertainty is the spatial calibration. It's expanded uncertainty ($k = 2$) of the phase-average velocity magnitude and wall distance is calculated to be 2.3 %. The accuracy of individual vectors, however, is limited by the uncertainty in the particle shift detection, which can be as low as 0.02 pxl for relatively large particle image diameters between 3 and 15 pxl [120]. Particle image diameters encountered in this work are typically in the range of 2 to 5 pxl. As a more conservative approach, a value of 0.1 to 0.2 pxl uncertainty in the pixel shift [242] is assumed. This corresponds to a statistical uncertainty (precision) of 4 %, which is significantly reduced when phase-averaged on a grid. Furthermore, the uncertainty in the wall distance determination is estimated to be mostly smaller than 10 µm. In addition, the instantaneous piston position varies by about ±4 µm compared to the phase-average, caused by jitter in the timing and engine vibrations. Due to the near-wall bias and limited resolution of the viscous sublayer at higher engine speeds, the wall gradient is most likely underestimated.

Additional systematic error sources are the discussed near-wall bias and regular fluctuations in some averaged velocity profiles, which have been observed for regions of very high gradients. These fluctuations could stem from laser sheet inhomogeneities in combination with the angled detection system (ray C in Fig. 6.3). Finally, interpolation effects due to the spatial dewarping as well as aliasing effects due to the resampling on a regular grid are considered negligible.

[18] Machined aluminum was found to be reflective enough, too.

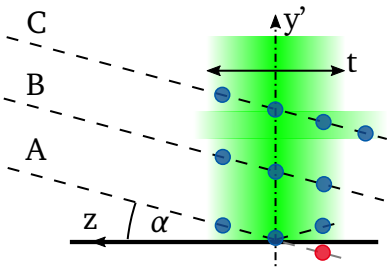


Figure 6.3: Effects of the detection angle and laser sheet thickness. Figure taken from [E215] with permission from Elsevier.

## 6.3 Results

As discussed in chapter 4, the global flow inside the engine is driven by the piston motion and momentum of the intake flow, which creates the typical tumble vortex during compression. Since the flow is highly turbulent and unsteady by nature, individual cycles typically differ significantly in large scale flow structures, a phenomena known as CCV. Figure 6.4 shows two exemplary cycles of motored OP E during the compression. Above the scattered PTV vectors, spatially averaged, gridded streamlines emphasize the flow's direction and the piston position is denoted with a dashed gray line. Both cycles feature distinctly different velocity fields: in the top panel, the flow is predominantly wall parallel and shows a high velocity magnitude. In the bottom panel, the impinging component is more dominant and the near-wall flow detaches at $x = 0\,\text{mm}$. Furthermore, flow structures persist over the depicted 10 °CA.

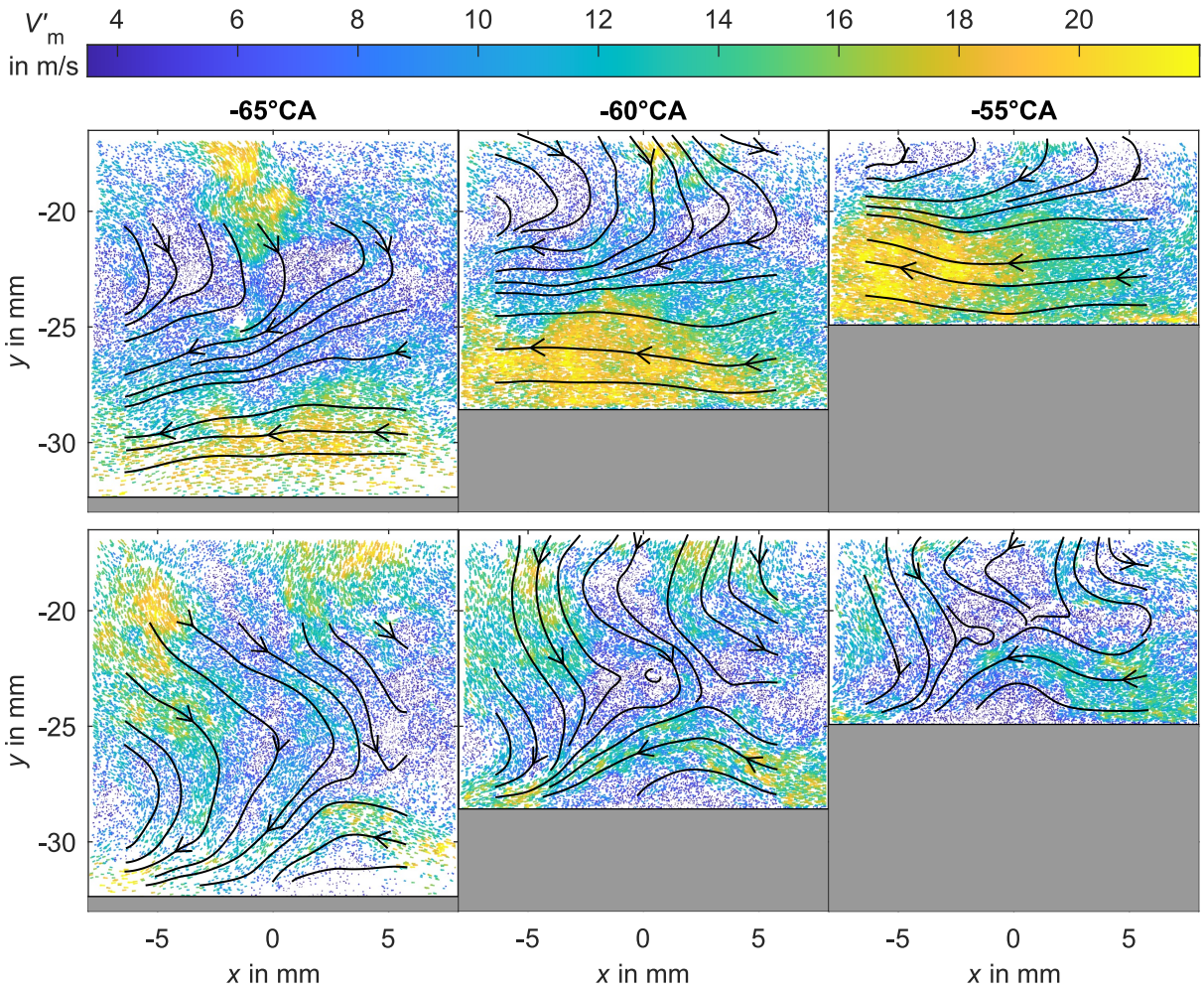


Figure 6.4: Exemplary instantaneous flow fields of OP E. Two different cycles (top, bottom) are shown. The flow is given as high-resolution, scattered PTV vectors in the background and colored according to the piston-relative velocity magnitude. Black streamlines represent the data after averaging on a $(120\,\mu\text{m})^2$ grid.

After phase-averaging, a repeatable average flow field emerges. During the compression, there is a superposition of the large scale tumble motion and the motion induced by the upwards piston movement. In the tumble plane, the flow is quasi-two-dimensional, the out-of-plane component $V_z$ is on average zero in a region a few mm around the tumble plane [41].

If observed in a piston-relative frame, that is by subtracting the instantaneous piston velocity, the flow resembles an impinging wall jet (Fig. 6.5). Depending on the $x$-position, different flow modes arise: the average clockwise tumble flow impinges on the wall an proceeds in a wall-parallel direction before curving upwards again. The local pressure varies in the same way. Impingement is accompanied by a strong pressure increase and subsequent deflection and deceleration [204]. Typically, velocities increase in the wall-parallel region, where a favorable pressure gradient can be assumed. Before the flow reaches the opposite cylinder wall, the local pressure increases, leading to a deceleration and upwards deflection. This spatial and temporal variety is less prominent in phase-averaged data, on which the following discussion will focus first.

### 6.3.1 Unscaled boundary layer profiles

Figure 6.6 shows velocity profiles at $x = 0\,\text{mm}$, obtained by the high-resolution grid resampling (15.6 µm in wall-normal $y'$ for setup I, colored lines; 5 µm for setup II, black dotted line). All values are normalized by the mean piston speed of a cycle. Measurements at −60 °CA of both setups agree very well, which indicates a good repeatability of both the diagnostics even at different magnifications and the engine operation. Several further observations can be made: First, for all four OPs, close to the wall a region of high gradients with nearly linear growth is apparent, before reaching a maximum. Second, contrary to a channel flow, the velocity far away from the wall decreases due to the tumble vortex (see Fig. 6.5). This is less apparent for OP A and B, as it happens beyond the axis limits of Fig. 6.6. Additionally, velocities decrease during compression, as the kinetic

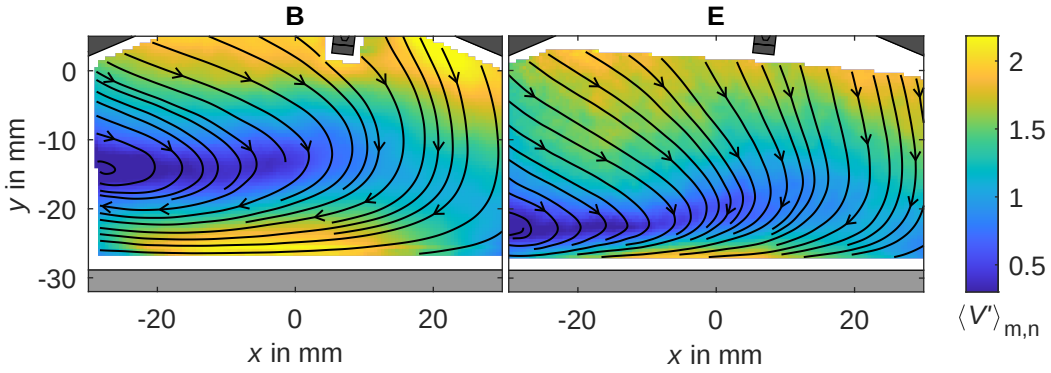


Figure 6.5: Phase-averaged flow field in a piston-relative frame, with the flow magnitude normalized by the mean piston speed. OP B and E are shown for −60 °CA. The cylinder head geometry is conveyed in black and the piston in gray. Figure adapted from [E215] with permission from Elsevier.

energy of the bulk flow is dissipated. However, wall gradients stay constant. Third, as expected the BL thickness scales inversely with the Reynolds number and therefore engine speed and intake load. This can be deduced from graphical results but also quantitatively from Table 6.3, which will be discussed later.

Nearly identical for all shown CADs is the standard deviation of the wall-normal $V_y$ and wall-parallel $V_x$ velocity component, normalized by the mean piston speed. Fluctuations in $x$ are greater for OP E and in a similar range for OP A, B and F. Note that the change in resampling cell size (as mentioned in section 6.2.3) is visible in a slight dent at 500 µm from the wall. Fluctuations do not vanish at the wall, which can be attributed to the near-wall bias discussed in section 6.2.4 and noise. The fluctuation component $\sigma_x$ rises faster and peaks earlier than the velocity itself and than $\sigma_y$, which behaves approximately linear in this scaling. Notably, different CADs collapse onto a single line, resulting in an increased turbulence intensity for later CADs. A similar shape is found for channel flows [194, p. 284] and impinging wall jets [91], though a more thorough comparison can be done in non-dimensional coordinates.

### 6.3.2 Scaled boundary layer profiles

Canonical turbulent BL of sufficiently high Reynolds number exhibit a typical structure, described by the law of the wall (see Section 2.1.4.2). They consist of a viscous sublayer, buffer layer, and logarithmic layer. Furthermore, profiles exhibit self-similarity if normal-

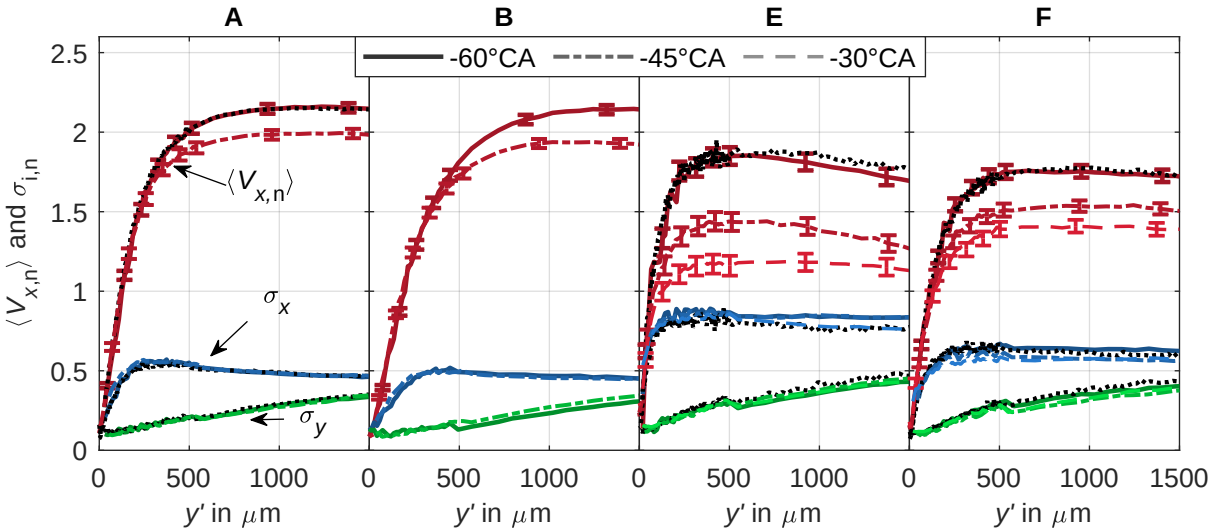


Figure 6.6: Boundary layer profiles and fluctuations. The piston-parallel velocity component $V_x$ at $x = 0$ (red colors) and the standard deviation of $V_x$ (blue) and $V_y$ (green) are normalized by the mean piston speed and shown with respect to the wall distance $y'$ at different CADs. For each 6$^{\text{th}}$ vector the 95 % confidence interval of the mean is implied by the error bar. Colored lines correspond to setup I, the black dotted line to setup II at −60 °CA. Figure adapted from [E215] with permission from Elsevier.

ized with wall units ($u^+$ and $y^+$, see Eq. 2.22). Since the gas temperature changes significantly during an engine cycle, temperature gradients at the wall need to be taken into account. Therefore, another meaningful scaling uses semi-local fluid properties, where density and viscosity depend on the wall distance ($u^*$ and $y^*$, see Eq. 2.29). The included velocity gradient at the wall $\partial V_x/\partial y'$ is derived as described in Section 6.2.3.

Since the temperature boundary layer profile is not known, it has to be estimated by assuming the Reynolds analogy, that is, assuming the (turbulent) Prandtl number to be unity. Then, the qualitative velocity profile can be used to get the temperature profile and thereby the density and viscosity as localized properties. The needed bulk flow temperature was calculated using isentropic compression, a procedure which was found to be valid during compression [26]. On the other side, wall temperatures are needed, for which the results from Chapter 5 are used. For OP A, B, E, and F, cycle ensemble-averaged piston top wall temperatures of 387, 382, 425 and 403 K were used[19], whereby the higher engine speed cases E and F were extrapolated from existing data. Finally, viscosity and density are calculated using Sutherland's law [234] and the ideal gas equation. A sensitivity study regarding the wall und bulk gas temperature was performed. BL parameters later described in Table 6.3 vary by roughly 5 % if the wall temperature varies by the same amount. However, the qualitative shape of scaled velocity profiles stays similar, as can be seen in another sensitivity study in Fig. 6.7. Here, data from a wall-resolved LES [125] was used to vary parameters used for semi-local scaling. The Reynolds assumption appears to hold true, and variations in wall and bulk gas temperature result in minor changes relative to the reference. An overall stronger departure can be observed

[19]Due to a different processing version, these vary in a negligible amount from results in Fig. 5.9.

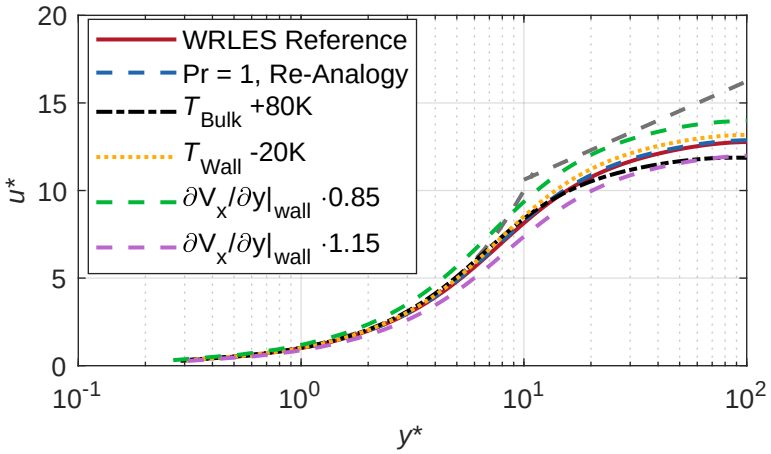


Figure 6.7: Sensitivity of BL scaling. Data from a wall-resolved LES of OP E, personal communication with Keskinen and Giannakopoulos [124], Zürich (see also [79, 125]). Scaling using the actual $V_x$ and $T$-profiles of the LES as reference in red. Reynolds analogy using the $V_x(y)$ profile shape for $T(y)$ (blue). Variation of the bulk gas and wall temperature (black and yellow). Variation of the velocity gradient at the wall, which is estimated by a linear fit (green and magenta). Law of the wall indicated as gray dashed lines.

for variations in the estimated velocity gradient at the wall, which contribute to an earlier departure of the profiles in the viscous sublayer.

**Scaled fluctuations** Figure 6.8 shows the velocity fluctuations $\sigma(V_i)$ from Fig. 6.6 scaled with wall units. Although the spatial filtering due to the averaging on a grid has to be kept in mind, the fluctuations mathematically represent scaled components of the Reynolds stress tensor $\langle u_i u_i \rangle^{1/2}/u_\tau := u_i'/u_\tau = u_i'^+$, with $u_i$ as velocity fluctuations from a Reynolds decomposition. For OP A and B, $u_x'^+$ peaks between a $y^+$ of 10-15, which is considered to be in the buffer layer [194]. Similar behavior can be seen in turbulent channel flows, for which a comparison is shown in Fig. 6.9. Turbulent channel flows were found to peak at $y^+ = 15$ with a value of $u_x'^+ \approx 2.7$ and then decrease for higher $y^+$. This was valid for a wide range of Reynolds numbers (up to $\mathrm{Re}_\infty = 40\,000$ [9, 194]) and even with varying streamwise pressure gradients [172]. Higher Reynolds numbers lead to a less rapid decay [9], while adverse pressure gradients create a second plateau [172]. The slow decrease of $u_i'^+$ in the engine resembles flows with higher Reynolds numbers or adverse pressure gradients. However, the bulk flow also plays a role, as a distinct difference from channel flows is the far-wall region. For channel flows, both $u_x'^+$ and $u_y'^+$ tend towards zero at high $y^+$. This is clearly not the case inside the engine, where high turbulence and CCV of the bulk flow lead to a increase in fluctuations far from the wall, in case of the wall-normal fluctuations $u_y'^+$ (Fig. 6.8, green) even in a monotonic manner. These results are closer to those from generic impinging wall jets [91] (not shown), which fits the flow situation on the piston surface.

Analyzing the fluctuations in Fig. 6.8 at higher engine speeds and Reynolds numbers of OP E and F, the peak value of $u_x'^+$ increases and appear at higher $y^+$. Furthermore, profiles of different CAD depart from another, due to a significant reduction in $u_\tau = \sqrt{\tau_w/\rho}$. One reason for this could be a higher uncertainty in the determination of the wall gradient at the thin BLs encountered at OP E (and F). However, setup I and II agree well at −60 °CA,

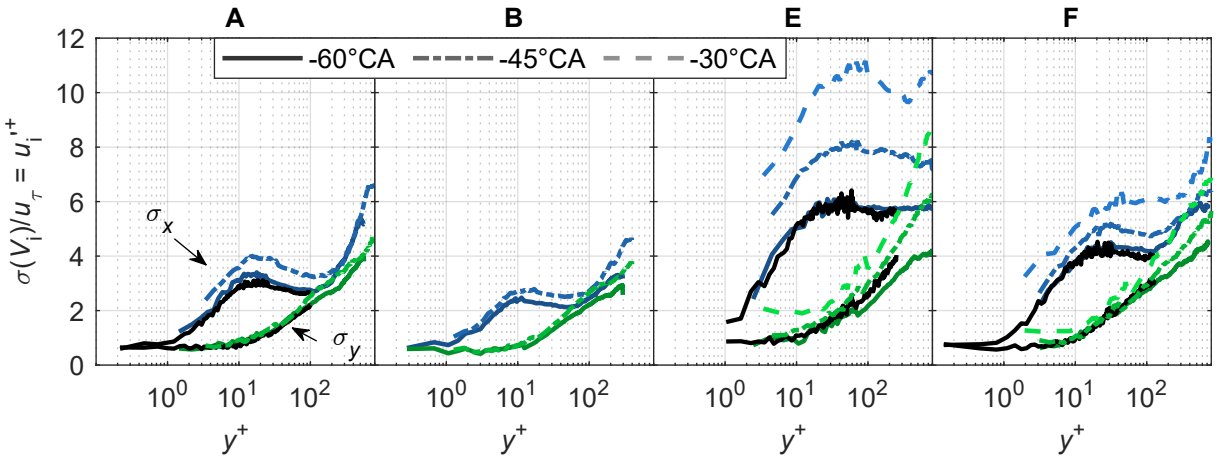


Figure 6.8: Boundary layer fluctuations of $V_x$ and $V_y$ scaled with wall units. Results from setup I are shown for −60 to −30 °CA (colored lines) and from setup II at −60 °CA (black line).

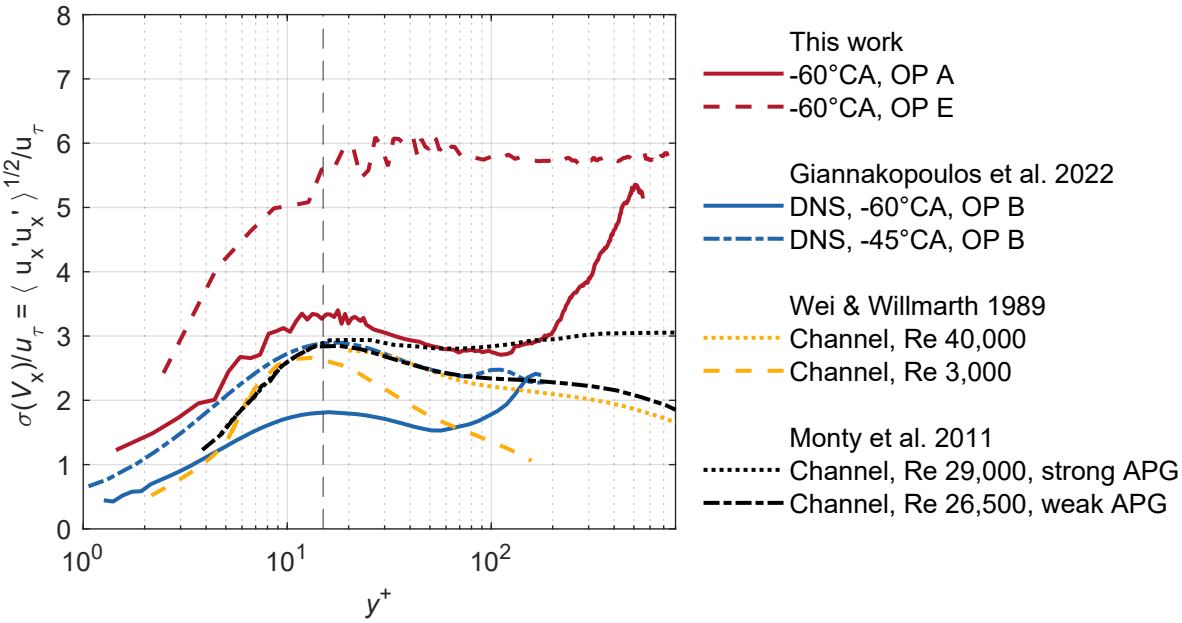


Figure 6.9: Comparison of boundary layer fluctuations of $V_x$ scaled with wall units from different studies. For this work, results from setup I are shown. Giannakopoulos et al. [79] simulated OP B of the current engine in a DNS, shown values are Favre-averaged. Experimental channel flow data from Wei and Willmarth [250] are taken from [9]. Monty, Harun, and Marusic [172] investigated channel flows with adverse pressure gradients (APG). Data are digitized from publications using [206].

which indicates a sufficient spatial resolution at least at this CAD. The velocity gradient at the wall needed for the calculation of $\tau_w$ remains fairly constant throughout compression (see Table 6.3, which is discussed later). Consequently, the rise in normalized fluctuations can be attributed to the rise in density during compression, which is highest for OP E due to lower heat losses. Giannakopoulos et al. [79] found a similar shift towards higher values at higher $y^+$ for the peak of Favre-averaged $u_x'^+$ in a DNS of this engine, albeit for OP B. Notably, they show that Reynolds stresses in the cross-tumble direction ($z$) do not increase systematically with the CAD. This indicates that flow phenomena such as pressure gradients could be responsible for the change in $u_x'^+$ during compression. Overall, features of the presented fluctuations are only found in more complex flows with higher Reynolds numbers, pressure gradients, and impinging wall jets.

**Scaled magnitudes** Figure 6.10 shows the velocity profiles scaled with semi-local and wall units ($u^+$ is offset by +5 and represented in blue). In the viscous sublayer, they collapse well for different OP and CAD, though the higher uncertainty of the wall gradient is discernible for the higher engine speeds. For OP A and B several vectors are available below $y^+ < 5$, which marks the end of the viscous sublayer. At higher engine speeds, only a few vectors lie in this region as the viscous sublayer thickness reduces to 30 µm. This illustrates the challenging demands in resolving such BLs.

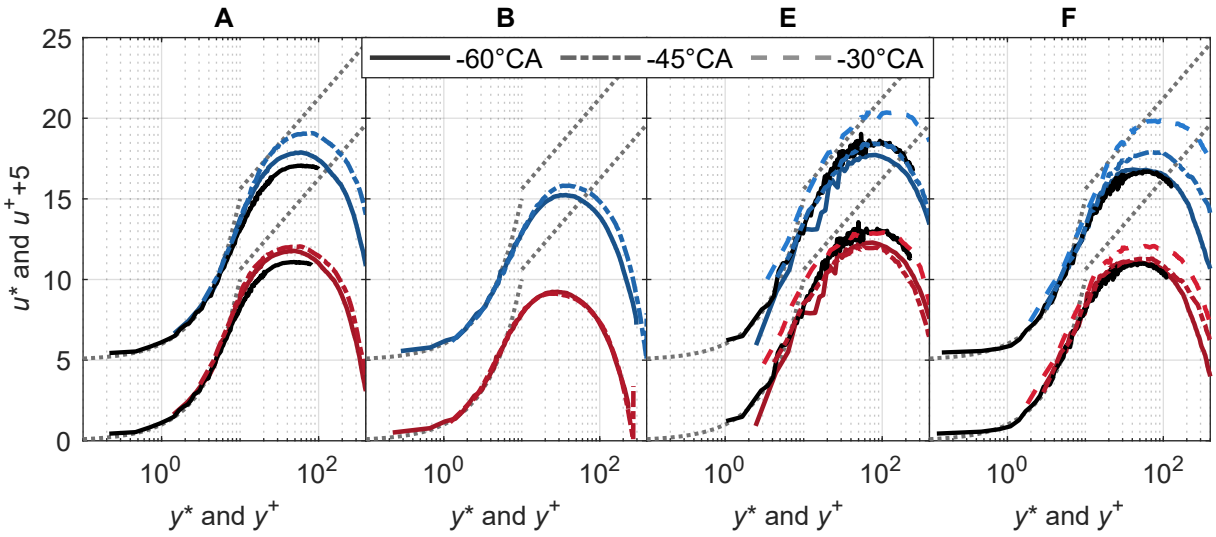


Figure 6.10: Boundary layer profiles scaled semi-locally (red) and with wall units (offset of +5, blue). Results from setup I are shown in colored lines, setup II at −60 °CA in black. The law of the wall is represented by gray dotted lines (with $u^+ = 1/0.41 \cdot \ln y^+ + 5$ in the logarithmic region). Figure adapted from [E215] with permission from Elsevier.

Beyond the viscous sublayer and buffer layer, no distinct logarithmic layer can be found, which indicates an overlap of the inner, viscosity-dominated regions, and the outer layer, and has been shown for engine flows at lower engine speed by several authors [79, 111, 161, 204, 260]. Strikingly, the observed BL are also thin in terms of the outer bulk region: The velocity peak of the bulk flow is already reached between $y^+ = 30$-$90$, which fits well with the rise in fluctuations observed in Fig. 6.8. This finding highlights the need to optimize the near-wall cell size when applying wall models in numerical simulations. Furthermore, the semi-local scaling leads to better self-similarity between different CADs compared to the scaling in wall units.

Finally, the high resolution setup II verifies the wall gradients and BL parameters derived with setup I, since both produce similar results and scaling. Even though both measurements agree well, the higher resolution is beneficial at resolving the viscous sublayer at higher engine speeds and pressures. Table 6.3 summarizes several BL parameters. The findings of Renaud et al. [204] are extended to higher engine speeds of 2500 rpm: The Reynolds number based on the momentum thickness $\delta_2^*$ is rather low compared to turbulent flat-plate flows, as is the shape factor $H$, the ratio between displacement and momentum thickness. While $\delta_{99}$ is in the range of 1.1 to 0.4 mm, the viscous sublayer already ends at 200 to 30 µm, for OP E and B, respectively.

These observations rely on phase-averaged data, which merges many different flow modes. Due to the high number of cycles acquired during the presented measurements (see Section 6.2.2), also conditioned data can be analyzed to further understand the local velocity BL of different flow modes.

Table 6.3: Boundary layer parameters for −60, −45 and −30 °CA, respectively. Values from setup II are included in brackets. BL thickness $\delta_{99}$ defined by the wall distance where 99 % of $V_{x,\max}$ has been reached. Semi-locally scaled momentum thickness $\delta_2^*$. Shape factor $H$. $\mathrm{Re}_{\delta_2^*}$ is based on the momentum thickness $\delta_2^*$, the maximum bulk velocity $V_{x,\max}$, and the viscosity at the wall. Bulk Reynolds number $\mathrm{Re}_{\mathrm{bulk}} = \overline{v}_p B/\nu$, defined with the mean piston speed $\overline{v}_p$, bore size $B$, and kinematic viscosity in the bulk flow $\nu$.

| OP | CAD | $y_{y^+=5}$ in µm | $\delta_{99}$ in mm | $\delta_2^*$ in µm | $H$ | $\mathrm{Re}_{\delta_2^*}$ | $\mathrm{Re}_{\mathrm{bulk}}$ $\times 10^3$ | $u_\tau$ in $\mathrm{m\,s^{-1}}$ | $\partial V_x/\partial y$ in $\mathrm{s^{-1}}$ $\times 10^3$ |
|---|---|---|---|---|---|---|---|---|---|
| A | -60 | 110 (100) | 0.83 (0.84) | 96 (96) | 1.9 (1.8) | 50 (44) | 18 (18) | 0.38 (0.40) | 18 (20) |
| | -45 | 82 | 0.77 | 92 | 1.6 | 57 | 22 | 0.32 | 20 |
| | -30 | - | - | - | - | - | - | - | - |
| B | | 200 (-) | 1.12 (-) | 136 (-) | 1.8 (-) | 25 (-) | 7.3 (-) | 0.47 (-) | 12 (-) |
| | | 160 | 0.99 | 126 | 1.6 | 31 | 9 | 0.40 | 13 |
| | | - | - | - | - | - | - | - | - |
| E | | 41 (40) | 0.48 (0.45) | 47 (58) | 1.9 (1.7) | 73 (96) | 69 (69) | 0.98 (0.99) | 121 (124) |
| | | 35 | 0.38 | 47 | 1.5 | 74 | 87 | 0.73 | 107 |
| | | 28 | 0.54 | 43 | 1.4 | 83 | 110 | 0.54 | 96 |
| F | | 80 (77) | 0.65 (0.63) | 72 (79) | 1.8 (1.8) | 45 (52) | 29 (30) | 1.07 (1.09) | 67 (71) |
| | | 65 | 0.71 | 79 | 1.5 | 59 | 36 | 0.84 | 64 |
| | | 50 | 0.69 | 74 | 1.4 | 73 | 46 | 0.68 | 69 |

### 6.3.3 Conditioned statistics

Instantaneous flow fields in the engine feature substantial differences due to turbulence and CCV (see Fig. 6.4). In extreme cases, for example, the horizontal flow direction can be (locally) reversed. To investigate the influence of not only different flow modes but also their evolution in time on the BL, conditional phase-averages of the flow were calculated. Two $3\,\mathrm{mm}^2 \times 1\,\mathrm{mm}^2$ regions centered at $(x, y) = (-5.5, 1)$ and $(5.5, 1)$ were considered and cycles selected that featured high instantaneous velocities in one region (higher than the 60 %-quantile). Those cycles were additionally conditioned on low velocities (lower than the 37.5 %-quantile) in the other region, resulting in a conditional averages consisting of 105 cycles (15 % of all cycles). The cycles were selected based on the flow field at $-45\,°\mathrm{CA}$ and subsequent phase-averages were calculated using the same cycle set for $-40$ and $-35\,°\mathrm{CA}$. For such conditional averages, the out-of-plane component $V_z$ is not necessarily zero, which remains a source of uncertainty.

Figure 6.11 shows two exemplary conditional averages for OP A and E, where different flow modes arise. The corresponding BL profiles were extracted at five horizontal positions. In the conditional average of OP A, a predominantly wall-parallel flow can be observed. Due to a widening upwards flow on the left and possible also out-of-plane motion, the flow decelerates from right to left. The acceleration parameter $K(x) = -\nu/V_{x,\max}^2 \cdot \partial V_{x,\max}/\partial x$ [172] gets as low as $-10 \times 10^{-11}$ (with $V_{x,\max}$ as the maximum of $V_x$ at each $x$-position). This flow structure persists during the next 10 °CA and remains stable, even though an average particle would move up to 9 mm in this time and thus well past the size of the high velocity region. Moreover, there is only a slight reduction of magnitudes over time. The corresponding BLs are rather developed as they coincide partly with the log law. There is a consistent trend: at $-45\,°\mathrm{CA}$ the profiles of $x = 3$ and 0 mm are the highest, then at $-40\,°\mathrm{CA}$ 0 and $-3$ mm and finally, at $-35\,°\mathrm{CA}$, $-3$ and $-6$ mm. This seems to be the effect of the slight shift of the high velocity region to the left and of local pressure gradients, which might be influenced by flow structures outside of the field of view.

A different flow mode is apparent for OP E, where a more perpendicularly impinging flow can be observed. The structure resembles canonical impinging wall jets: on the right side of the "stagnation point", the flow is experiencing blockage and adverse pressure gradients. The impinging flow is then redirected by the wall and undergoes strong acceleration towards the left (local $K$-values of up to $12 \times 10^{-11}$), with dense streamlines and a vortex center located just above the wall. The general structure is again persistent over the next CAD, with a slight reduction in magnitude. BL profiles of OP E show a consistent trend in the streamwise direction from the right, with low values of $u^+$ and profiles that plateau early below the log law, to the left, where the profile overlaps with the log law. Such a continuous progress is known from the developing BL of impinging wall jets [91, 146]. The profiles also depart early from the viscous sublayer. Thereby, the deviation of the first velocity data close to the wall is most likely owed to the near-wall bias discussed in Section 6.2.4, the thin BL of OP E, and the lower number of samples in the conditional averages. Farther away, however, the deviation from the viscous sublayer appears to be physical, as it was found that no variation of the wall gradient $\partial V_x/\partial y'$ can lead to an overlap. This indicates the presence of very thin viscous sublayers below

the measurement resolution and is again akin to impinging wall jets as shown in [91]. For later CAD, the BL profiles converges as velocity magnitudes decrease and the vortex center shifts to the left.

One can hypothesize about the behavior of BLs at even higher engine speeds and compression ratio (CR), though only cautious estimates can be made. Compared to OP A at the CR of 8.7, an engine with a CR of 12 would feature higher pressures and temperatures and subsequently a 20 % lower kinematic viscosity, which increases $Re_{bulk}$ by 25 %. If the higher CR is achieved by a comparatively longer piston and roof geometry, the mean piston speed would increase, resulting in an 80 unit overall increase in $Re_{bulk}$. This

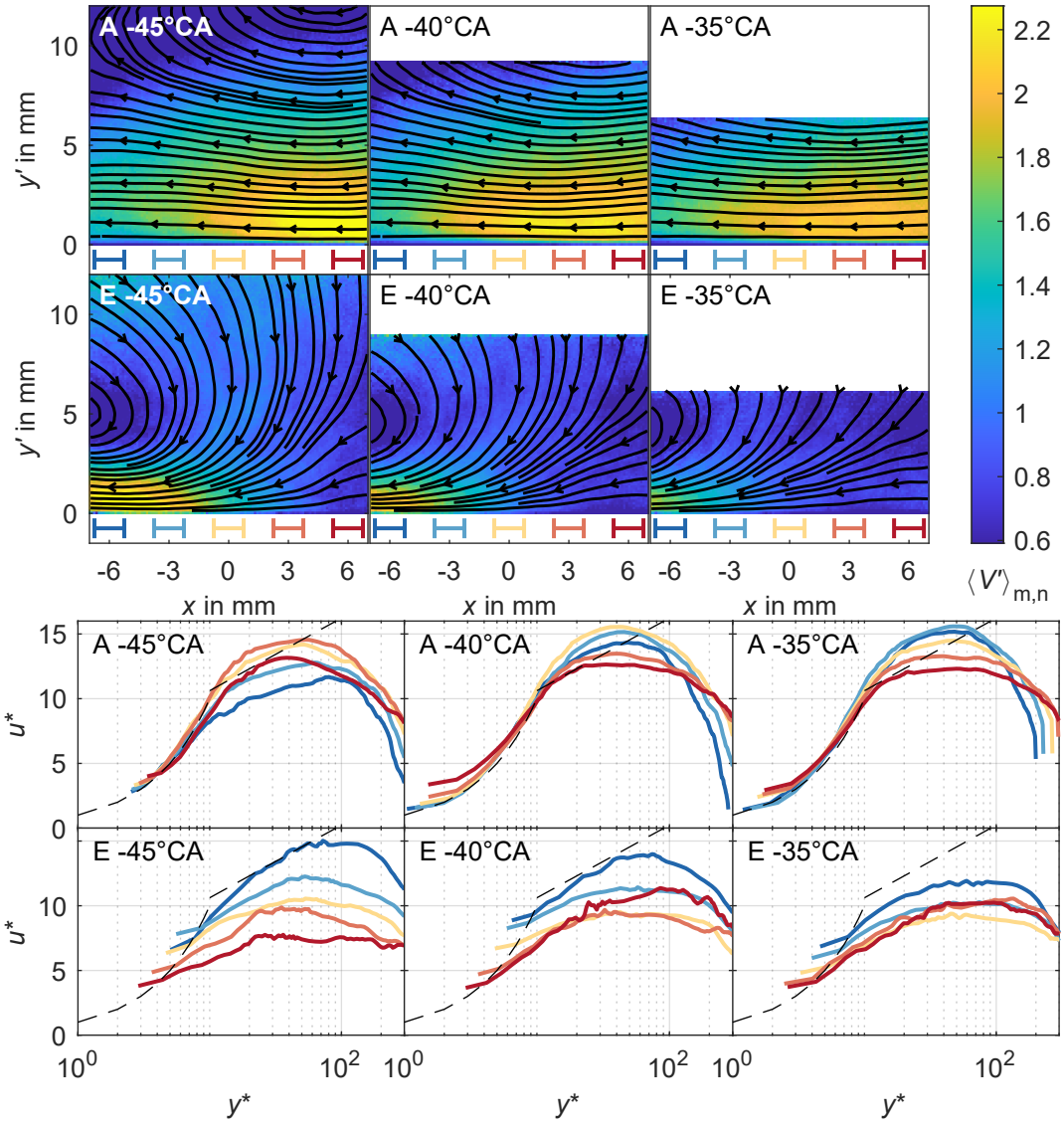


Figure 6.11: Conditioned flow fields (top) and corresponding semi-locally scaled boundary layer profiles (bottom) of OP A and E. Five horizontal positions are shown, as color-coded below the velocity fields. Figure adapted from [E215] with permission from Elsevier.

leads to thinner BL, since the thickness of the viscous sublayer scales approximately inversely with the bulk Re-number [159]. The presented data show a consistent departure from canonical, developed BL, depending on the local flow situation at bulk Re-numbers between $1 \times 10^4$ and $1 \times 10^5$. It is reasonable to assume that this is also true for higher Re numbers.

In conclusion, the conditioned analysis shows that BL inside the engine vary significantly in space and depend on the instantaneous flow situation. They depart from canonical channel flows, likely due to intense local pressure gradients as well as flow structures impinging on the wall. Numerical wall models need to take the unsteady nature of the non-equilibrium, non-zero-pressure-gradient flow into account if near-wall processes are to be predicted accurately.

## 6.4 Summary

In this study on the boundary layer flow above the piston, high-resolution PTV was applied at engine speeds of 800 and 2500 rpm. A vector resolution of maximum 5 µm allowed to resolve the phase-averaged viscous sublayer during the late compression stroke for bulk Reynolds numbers of up to 100 000. The data were conditioned on the near-wall flow to analyze the influence of different flow modes. Furthermore, uncertainties were thoroughly discussed and non-zero velocities at the wall position were traced back to the reflective piston surface and non-zero laser sheet thickness.

The results show that even at the higher, technically relevant engine speed, no logarithmic layer exists, which extends the finding of previous studies (e.g. [111, 204]). The boundary layer thickness scales inversely with the bulk Reynolds number. At 2500 rpm and 0.95 bar intake pressure, the viscous sublayer ($y^+ = 5$) gets as thin as 30 µm. Additionally the outer layer is small, as the bulk flow already starts at wall-scaled $y^+ = 30$-$90$, which has to be considered when applying wall models in numerical simulations.

Scaled velocity fluctuations were compared with canonical channel flows. In the engine, fluctuations of the far-wall region do not approach zero but increase due to the turbulence of the bulk flow. Thereby, the profiles are similar to those of impinging wall jets, with the intermediate region around $y^+ = 50$ also resembling flows with adverse pressure gradients at higher Reynolds numbers.

A conditional analysis revealed different flow modes, which differ substantially from the conventional phase-average. Even for wall-parallel flows, strong acceleration and deceleration of the flow can be observed, with the adherence of boundary layer profiles to the law of the wall depending on the horizontal position and temporal evolution. Other dominant modes include impingement on the piston, for which the degree of boundary layer development increases with the distance from the stagnation point. These findings are in notable similarity to classical channel flows with impinging wall jets.

# Chapter 7

# Fuel Wall Films and Pool Fire

## 7.1 Aim

In the previous chapters, the near-wall flow and wall temperature were characterized. During operation with direct injection (DI) in the intake or compression stroke, liquid fuel can impinge on the cylinder walls and piston. Near-wall processes play an important role in the subsequent film vaporization, mixing, combustion and production of pollutants. The following chapter describes an investigation of these processes. Thereby, a single-hole injector was used to create a localized fuel wall film during the compression stroke in combination with an otherwise homogeneous air-fuel-mixture. Simultaneous tracer LIF, PIV and visualization measurements were conducted to characterize the mixture and velocity field as well as the flame development and formation of a so-called *pool fire*.

## 7.2 Methods

### 7.2.1 Tracer Laser-Induced Fluorescence

Laser-induced flourescence was used to characterize the mixture field after DI with a single-hole injector. Since isooctane does not fluoresce, tracers have to be added, either to the in-cylinder gas or the injected fuel. Acetone and 3-pentanone have been used as gas and fuel tracers for mixing studies in engines and were selected as tracer candidates in this work. An overview of tracer candidates and their properties as well as an explanation of the selection process is given in Section 2.2.3.1. Since the fluorescence of acetone and 3-pentanone is mostly in the visible spectrum, the use of non-intensified cameras was probed. Due to compression, thermal boundary conditions during fired operation, and endothermic fuel vaporization, temperature gradients in the in-cylinder gas are unavoidable. To select a suitable diagnostic approach, the temperature sensitivity of both tracers was investigated. The options were either a two-line excitation scheme, which allows for the measurement and correction of the temperature, or a one-line excitation at a wavelength with sufficiently temperature-insensitive fluorescence.

#### 7.2.1.1 Characterization of 3-Pentanone and Acetone LIF

**Experimental setup of heated jet** A systematic investigation of the temperature dependency of both tracers was performed in an open, heated jet assembly shown in Fig. 7.1. The tracers were injected into the gas flow using a port fuel injector (4 bar pressure), which was characterized with regards to the injected mass. A mole fraction of 7.0 and 4.5 % was set for acetone and 3-pentanone, respectively. Nitrogen was supplied by a MFC as carrier gas at 150 mg s$^{-1}$. The mixture was heated up to 700 K using a heating sleeve (Horst) around a heat resistant steel pipe (outer diameter 12 mm) with a length of 0.7 m. Here, the achievable mass flow rate was limited by the maximum targeted jet temperature, which had to be reached in the given pipe length, while complying with sleeve wall temperature limits. A pipe T-junction with an inner diameter of 9 mm was used to insert a type K thermocouple and function as an exit nozzle. Additionally, a PT100 temperature sensor with a 1.5 mm tip diameter was positioned about 15 mm downstream of the nozzle exit. In order to reuse the diagnostic setup for engine experiments and enable quasi-in-situ pilot investigations, the heated jet assembly was placed on top of the mirror casing of the engine. Thereby, the cylinder head and glass cylinder were lifted off and the piston crown with the inserted piston glass removed.

On the excitation side, two different laser systems are used. A dye laser (Double Dye Laser, Sirah Lasertechnik) was pumped by two 10 Hz, frequency-doubled Nd:YAG lasers (PIV 400, Spectra Physics). The two pulses were aligned in time and reached a combined pulse energy of 430 mJ. Rhodamine 101 (also known as Rhodamine 640) dissolved in ethanol (Carl Roth) was used as dye. The laser was tuned to different wavelengths in a range of 305 to 316 nm after frequency-doubling and had a pulse energy of 9 to 12 mJ

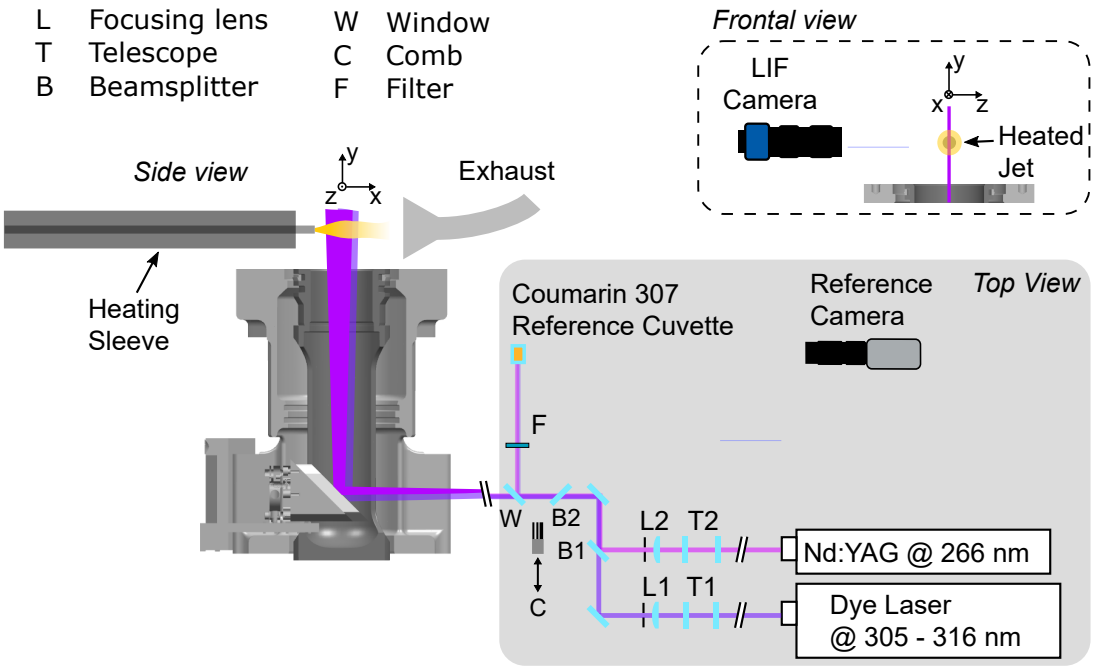


Figure 7.1: Heated jet setup for assessing the temperature sensitivity of acetone and 3-pentanone at different excitation wavelengths.

(measured with pyroelectric sensor, EnergyMax-USB J-50MB-YAG, Coherent). The second laser system consisted of a 10 Hz Nd:YAG laser (Spitlight 600 PIV, Innolas Laser), which was frequency-quadrupled to 266 nm, with a pulse energy set to approximately 15 mJ at the laser exit. Both lasers were formed into sheets by cylindrical lenses and combined with a wavelength beam splitter (ZT266rdc-UF1, Chroma Technology). A quartz glass window guided a reflection onto the reference cuvette, filled with Coumarin 307 dye and spectroscopic ethanol (Carl Roth), which was used for energy and profile correction. The lasers were then guided into the heated jet via the piston mirror, with a final sheet thickness in the FoV of 750 µm, a width of 15 mm, and effective local pulse energies of 6.5 mJ and 3 to 5.5 mJ for the 266 nm and dye lasers, respectively. Both jet and cuvette LIF signals were confirmed to be in the linear regime.

Coumarin fluorescence in the cuvette was detected with a 12 bit CCD camera (SensiCam, Excelitas PCO). Fluorescence in the jet was captured with a backside-illuminated CMOS camera (Imager CX-25, LaVision), a chip architecture which increases the sensitivity and allows for a quantum efficiency of 30 to 60 % at 325 to 400 nm in this model. It was equipped with a Canon EF 85 mm f/1.2 objective. Additionally a 160 mm achromatic collection lens (Linos) was mounted in front of the objective. The Imager CX camera features a minimum interframe time of 300 ns, such that a staggered LIF approach was used: the dye and 266 nm lasers were triggered quasi-simultaneously 4 µs apart and the respective fluorescence captured in a double frame, with one frame per emission. Phosphorescence emission of acetone (see Section 2.2.3.1) is not quenched, due to the pure $N_2$ carrier gas. This emission is mostly occurring during the second frame, which captures the signal after excitation with 266 nm. In this tracer characterization, the focus is on the excitation with 305 to 316 nm in the first frame, which is not described in the literature. Therefore, the influence of phosphorescence is considered negligible[20]. Finally, an $8 \times 8$ software binning was applied to the images.

**Processing** The resulting LIF images were post-processed in Matlab by subtracting a background image and correcting the laser sheet profile (see Fig. 7.2). To align the cuvette and jet images, a comb structure was inserted into the laser sheet (see Fig. 7.1) and the corresponding scaling and rotation parameters calculated by a Fourier-Mellin transform[21]. Then, the laser sheet profile was extracted by averaging the cuvette images in the laser direction and instantaneous profiles were normalized for each excitation wavelength to the respective laser energy measured with a pyroelectric energy sensor (J-50MB-YAG, Coherent)[22], before being applied to the jet images.

Determining the jet temperature to a high degree of accuracy proved challenging. Reynolds numbers in the pipe range between 600 and 1200, which results in a lami-

[20] In hindsight, a small amount of oxygen could have been added to the jet to effectively quench the phosphorescence while keeping out of the flammability range.

[21] Thanks to Max Greifenstein for implementing the FFT-based method described by [201, 236] in Matlab.

[22] More specifically, the instantaneous profiles were normalized to an average cuvette LIF value for each excitation wavelength and then scaled to a common energy reference of 1 mJ, thus enabling comparison of LIF values at different excitation wavelengths, even though absorption and emission characteristics of the cuvette dye change with the excitation.

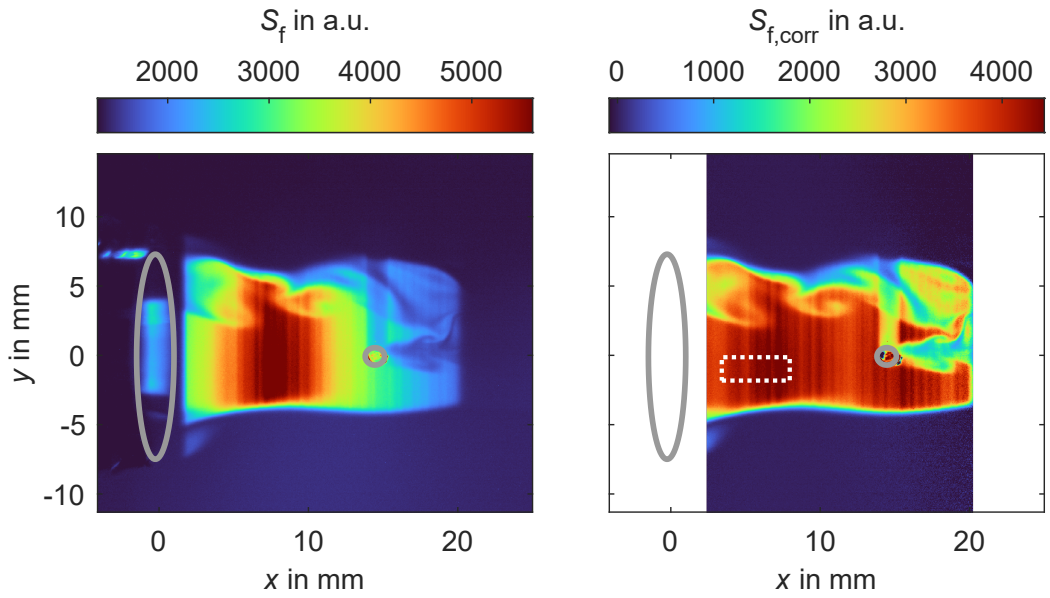


Figure 7.2: Example images of 3-pentanone-LIF in the heated jet at 25 °C. Left: Raw LIF image. Right: LIF image with corrected background and laser profile. The jet nozzle at the origin and PT100 sensor at $x = 15$ mm marked in gray, evaluation region marked with a dashed-white rectangle.

nar pipe flow. In addition to axial temperature gradients, vertical gradients appear due to natural convection in the horizontally positioned pipe. To account for axial gradients, the nozzle exit temperature was obtained in a reference measurement using a type K thermocouple with a small tip-size of 0.5 mm, in addition to the two permanently installed temperature sensors. Then, an interpolation routine based on the two permanent sensors was derived and the output defined as the jet temperature. Finally, a region of interest in the jet was determined algorithmically, by detecting the vorticity layer at the jet edges using standard deviation images. The region of interest was placed in the lower half of the jet towards the center, where the LIF signal was found to be most homogeneous (white rectangle in Fig. 7.2). This region is averaged and normalized by the tracer mole fraction to arrive at the fluorescence per unit mole fraction (see Section 2.2.3)

$$S_f^+(\lambda, T) \propto p/T \cdot \sigma_{abs}(\lambda, T) \cdot \phi_f(\lambda, T, p, x_i). \tag{7.1}$$

**Heated jet results** Figure 7.3 shows the temperature dependency of the acetone and 3-pentanone fluorescence per unit mole fraction in the heated jet. Focusing first on the absolute signal in the left panel of Fig. 7.3, the overall signal level decreases for increasing excitation wavelengths of the dye laser. This is mainly an effect of the change in absorption cross section, which decreases from about 270 nm for both tracers [265, p. 51]. Furthermore, 3-pentanone has a significantly higher fluorescence signal per unit mole fraction than acetone. This is consistent with the higher absorption cross section reported for 3-pentanone [155, 265]. Surprisingly, $S_f^+$ for 316 nm is higher than for 315 nm, which is unlikely to be physical, since the absorption cross section decreases and the FQY

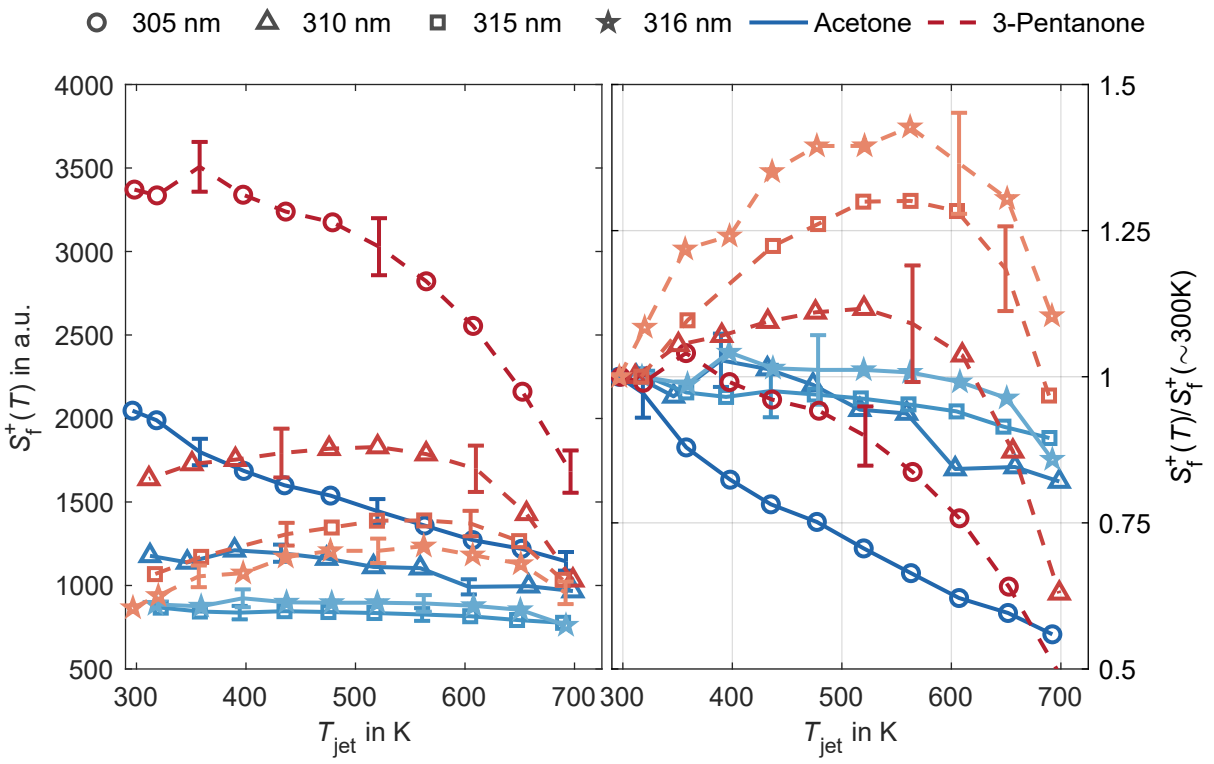


Figure 7.3: Heated jet results. Fluorescence signal per unit mole fraction as a function of temperature for the tracers acetone and 3-pentanone at different dye laser excitation wavelengths. Some markers are replaced with error bars, indicating the sample mean of the spatial standard deviation. Left: Absolute signal. Right: Signal normalized to the measurement closest to $T = 300\,\mathrm{K}$.

is nearly identical [237]. Most probably, the relative scaling of the energy, derived from reference cuvette and energy sensor data, is inaccurate at these small changes in the excitation wavelength.

To assess the temperature sensitivity in more detail, the right panel of 7.3 shows the fluorescence per unit number density normalized to the room-temperature value for each wavelength. 3-pentanone shows non-monotonic behavior at higher excitation wavelengths, as the fluorescence signal first increases then decreases with increasing temperature. Acetone's curvature is opposite-signed for 305 nm, as the signal predominantly decreases with increasing temperature. Notably, two characteristics can be observed: First, acetone excited at 305 nm shows the highest temperature sensitivity, which can be exploited for a temperature measurement. Second, excitation at 315 nm shows the opposite effect, as the normalized fluorescence per unit mole fraction is nearly constant over the investigated temperature range, decreasing to just about 0.9 at 700 K. At atmospheric pressures, this wavelength is therefore suitable for temperature-insensitive measurements of the mole fraction.

In another comparison, Fig. 7.4 shows $S_f^+$ with 266 nm-excitation. The fluorescence is significantly stronger than when excited with the dye laser, at least for lower temperatures. Due to a high temperature sensitivity, signal levels decrease rapidly for higher

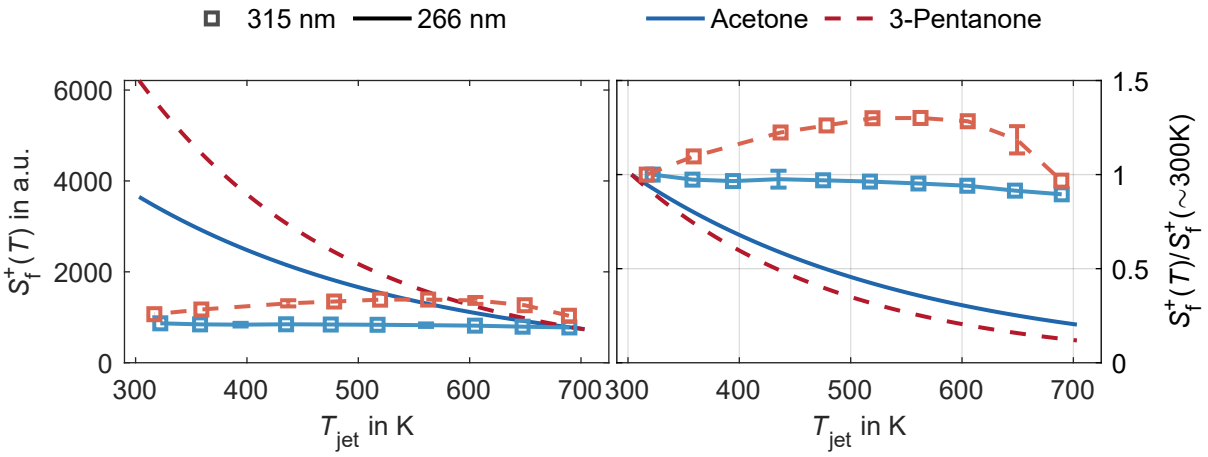


Figure 7.4: Heated jet results. Comparison of fluorescence signal of acetone and 3-pentanone per unit mole fraction between excitation at 266 and 315 nm. Data at 266 nm are presented as an exponential fit. Left: Absolute signal. Right: Signal normalized to the measurement closest to $T = 300$ K.

temperatures, where 3-pentanone exhibits a steeper slope than acetone. The results presented in Fig. 7.3 and 7.4 extend the acetone and 3-pentanone LIF data available in the literature, where besides excimer lasers (e.g. [30, 51, 84, 138, 151, 153, 154, 237, 266]) and Nd:YAG lasers (e.g. [30, 138, 170, 237, 244]), also dye lasers have been used [30, 237], but to the author's knowledge not at the wavelengths of this work. To assess the data quality and trends, a direct comparison with data from [237] and [138] is shown

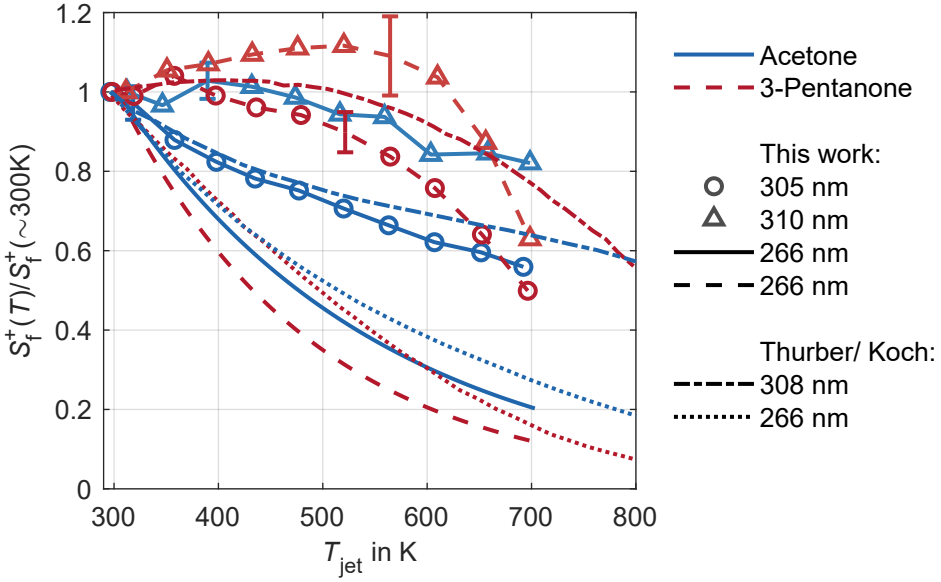


Figure 7.5: Comparison of the fluorescence signal of acetone and 3-pentanone per unit mole fraction in this work with data from Thurber et al. [237] and Koch and Hanson [137]. All data acquired in at atmospheric pressures in $N_2$. Data are digitized from publications using [206].

in Fig. 7.5. The data show good qualitative and adequate quantitative agreement and fit well with the trends between excitation wavelengths. One key difference are the slopes of 3-pentanone above 600 K, which are less steep in the data presented by [138]. Some of the deviations between the results for 266 nm are likely due to the additional phosphorescence signal captured in the second frame. Nevertheless, it is no surprise that the experimental design of the heated jet with inevitable temperature gradients at a small nozzle diameter, leads to increased uncertainties compared to experiments in constant volume chambers. For future reference, the fluorescence signal *per unit number density*, $S_f^*$, is shown in Fig. 7.6. In the current context of engine mixture measurements, the signal *per unit mole fraction* is of primary interest, since it takes into account local and global density changes.

**Conclusion and implication for engine measurements** Based on the presented data, an acetone-LIF approach with single-line excitation at 315 nm and one-color detection was chosen. Compared to two-line approaches, this reduces the experimental complexity and need for temperature calibration, while allowing the use of non-intensified cameras, as opposed to other organic tracers like anisol or triethylamine (TEA) [265]. To justify this choice, three other points have to be discussed, namely the influence of pressure on the temperature sensitivity and the signal itself, and the influence of bath gas composition.

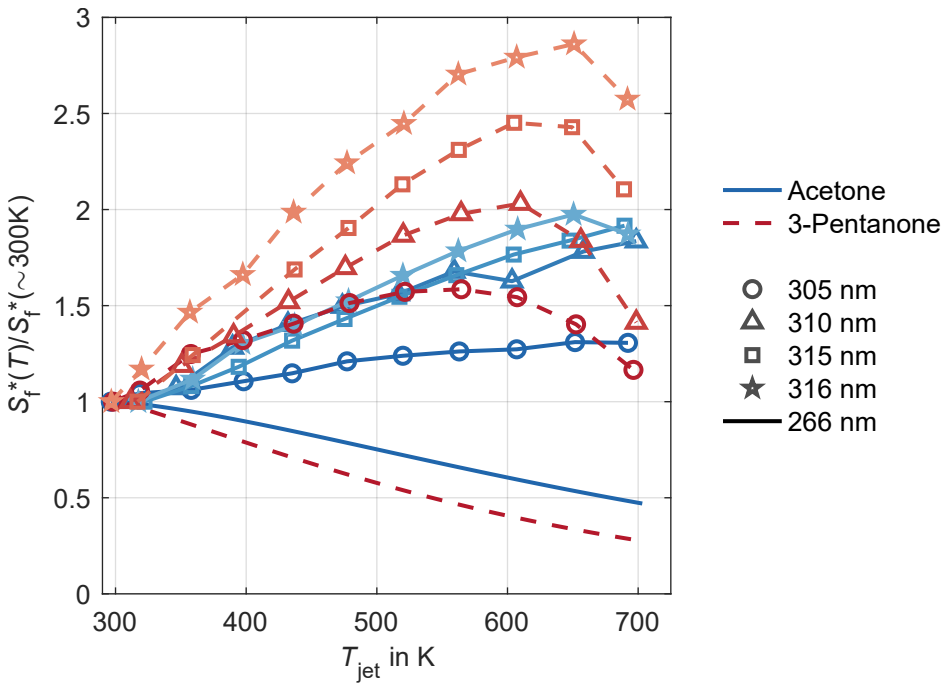


Figure 7.6: Heated jet results. Fluorescence signal per unit number density as a function of temperature for the tracers acetone and 3-pentanone, at different dye laser excitation wavelengths. Signal normalized to the measurement closest to $T = 300$ K.

Pressures in the engine prior to ignition reach up to 13 bar. From the atmospheric heated jet experiment the pressure dependency cannot be assessed. However, a model derived by Thurber et al. [237] indicates that for excitation at 308 nm and a pressure range of 1 to 10 bar the temperature sensitivity barely changes. Löffler, Beyrau, and Leipertz [154] characterized acetone at engine-relevant pressures and temperatures at the same excitation wavelength. An evaluation of their empirical fit functions reveals that the temperature sensitivity at 13 bar is only slightly increased compared to 1 bar, which supports the conclusion drawn from Thurber et al. Based on the reported trends for different excitation wavelengths, a similar result is expected for the pressure dependency at 315 nm. Thus, as shown in Fig. 7.3, the remaining temperature sensitivity between 550 to 650 K is estimated to be below ±10 % of $S_f^+$.

In contrast, the pressure dependency of the signal itself is less of a concern, since a reference image with homogeneous seeding (*white image*) can be taken at the same crank angle and therefore pressure[23]. Finally, the bath gas composition influences the signal due to quenching with $O_2$. This leads to a decrease in LIF signal with increasing $O_2$ concentration. In the current experiment, acetone serves to characterize the late injection and subsequent wall film buildup and evaporation. Consequently, regions of high fuel/acetone mole fraction contain less oxygen. To assess this factor, homogeneously seeded measurements were conducted at different nitrogen-air ratios in the engine (Fig. 7.7). As expected, signal levels increase at decreasing oxygen concentrations. However, the influence remains relatively small, as even a reduction in the oxygen concentration by 50 % changes the LIF signal by only about 10 %[24]. In summary, two effects remain uncorrected in the chosen single-line excitation, one-color detection approach: Fuel rich

[23]Below 2 bar, signal intensity at constant tracer number density strongly increases with pressure [154], as more frequent collisions limit the rate of non-radiative electronic relaxation of excited molecules and therefore increase the fluorescence yield [220, 237]. At higher pressures, however, collisional quenching with $O_2$ reduces the signal again. Represented at constant mole fraction, the signal is monotonically increasing with increasing pressures [154].

[24]At low oxygen concentrations, otherwise quenched phosphorescence might contribute to a stronger signal, too. Since the intensified relay optic (IRO) was gated only for a few hundred ns after excitation - a fraction of the phosphorescence lifetime [156] -, the influence is considered small.

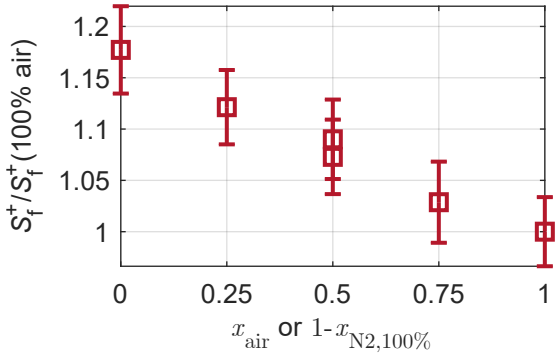


Figure 7.7: Influence of the ambient gas composition on homogeneously seeded acetone LIF in the engine at −13 °CA, with $x_{acetone} = 0.024$ and 315 nm excitation. Spatial and temporal standard deviation indicated by error bars.

regions will be at lower temperatures due to evaporative cooling and additionally will contain less oxygen. The combined effect is expected to be on the order of 5 to 15 % and is accepted as an increase in uncertainty of the measured mole fraction.

### 7.2.2 Particle Image Velocimetry and Visualizations

Velocity fields prior to combustion were measured with high-speed (HS) 2D2C PIV, capturing the $x$- and $y$-components in the tumble plane. Furthermore, flame development was captured by observing particle-void regions where the Mie-scattering PIV particles have evaporated due to the approaching flame. Thus, a visualization of the burnt-gas area in the tumble plane is possible. In addition, the PIV system captured the DI spray morphology via Mie scattering of spray droplets. Finally, natural luminosity of pool fire phenomena and soot formation during the expansion stroke were imaged by the PIV camera and an additional sideview camera.

### 7.2.3 Experimental Setup

Building upon the setup described in Section 7.2.1.1 and shown in Fig. 7.1, the diagnostics were adapted for engine measurements. A schematic is shown in Fig. 7.8. The same 10 Hz dye laser system (Double Dye Laser, Sirah Lasertechnik) with Rhodamine 101 dissolved in ethanol was tuned for 315 nm, achieving a pulse energy of 9 mJ at the laser exit (approximately 3 mJ inside the engine). Due to the one-line excitation, the 266 nm laser was not used anymore. After sheet forming optics, a reflection from a quartz glass window was guided onto the reference cuvette, filled with Coumarin 307 dye and spectroscopic ethanol. The laser sheet was set to a comparably high thickness of 1.5 mm at a width of 25 mm, to avoid laser damage on the piston mirror, glass and cylinder head. Linearity of the LIF signals was confirmed, as shown in Fig. 7.9. For velocity measurements, a HS Nd:$YVO_4$ PIV laser (Edgewave IS4II-DE, 532 nm) was added to the beam path using a beam splitter (CVI Laser Optics) and formed into a slightly converging sheet of 0.5 mm thickness (FWHM). Silicone oil (Dow Corning 510, 50 cSt) was atomized by a Palas AGF 10.1 seeder and introduced into the intake manifold as PIV tracers.

Four cameras were used in total. A 12 bit CCD camera (SensiCam, Excelitas PCO) captured the fluorescence in the reference cuvette. A HS camera (SA-X2, Photron) was equipped with a 180 mm Sigma Macro objective set to f/5.8 and a 525 nm bandpass filter (80 nm FWHM, MidOpt) to suppress the combustion luminosity. Astigmatism was corrected by a cylindrical 2000 mm lens. This system captured PIV, spray, flame and pool fire processes in the tumble plane. In addition, a low-speed CMOS camera (Imager M-lite 5M, LaVision) was positioned below the intake manifold at an angle to the piston surface to image pool fire in a global view with high depth-of-field (called *sideview camera*). The detection of LIF changed compared to the heated jet experiment of Section 7.2.1.1. With the previously used camera (Imager CX), a satisfactory SNR of 20 to 50[25] was achieved inside the engine, even though additional surfaces lead to losses in both excitation and

[25]For an acetone mole fraction of 2.5 % and excitation at 315 nm.

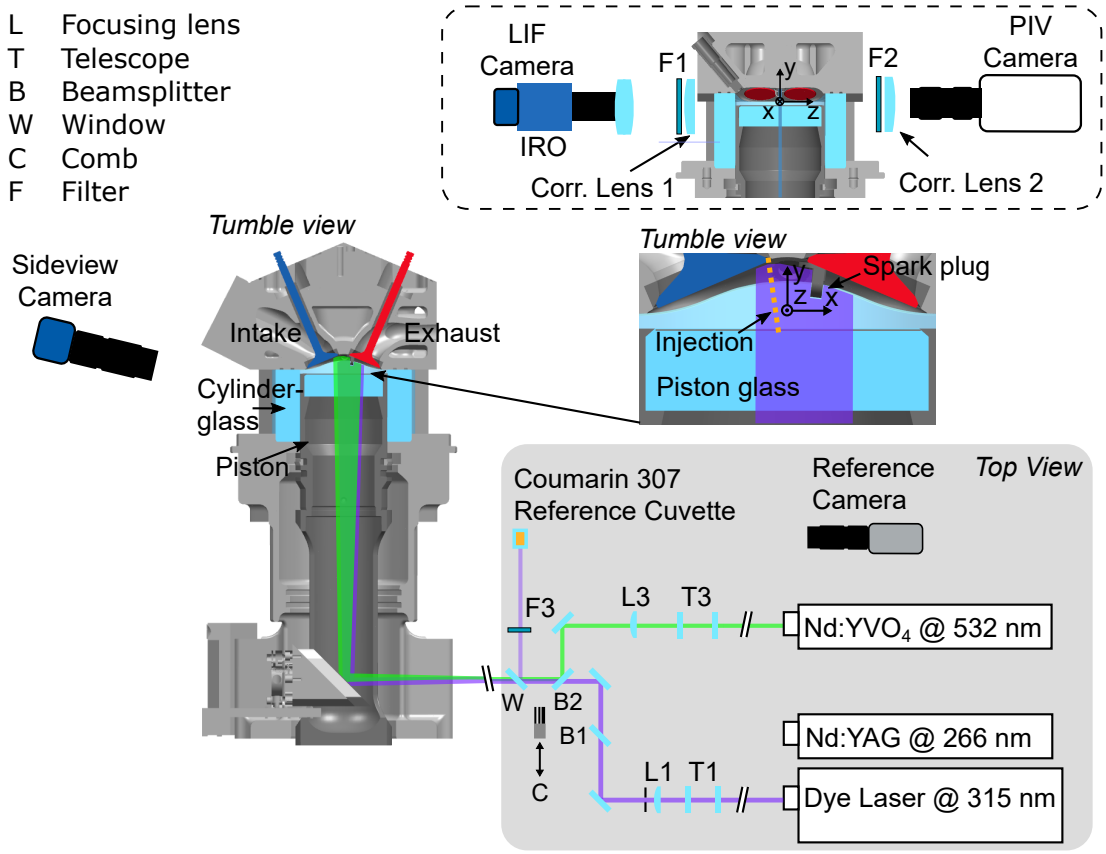


Figure 7.8: Experimental setup of the wall film and pool fire measurements.

captured emission (SNR in heated jet: 25 to 55). However, the combustion luminosity was not sufficiently blocked by the camera's electronic shutter. This manifests itself in a crosstalk of the second frame, which is saturated by the combustion, to the first frame, which contains the LIF emission and is read out at this time. Since no additional, mechanical shutter was available, an IRO (LaVision) was used to both amplify the LIF signal

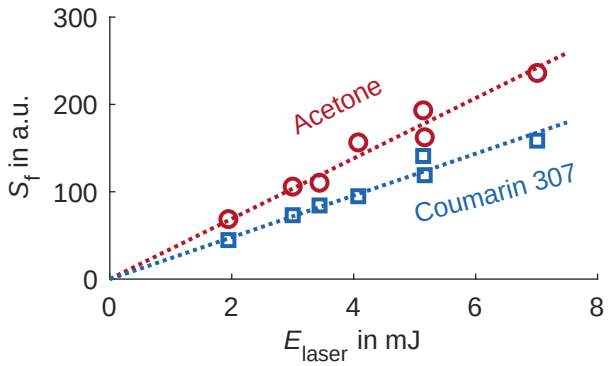


Figure 7.9: Linearity of the LIF signal after 315 nm-excitation in the engine (acetone) and reference cuvette (Coumarin 307).

and provide very short shutter times[26]. The intensified image was captured by a CMOS camera (Imager M-lite 2M, LaVision), with the IRO operating at a gain of 70 % (neutral gain 58 %) and a gate of 700 ns. It was equipped with an 85 mm Canon f/1.2 objective and a 160 mm achromatic collection lens (Linos). A cylindrical 2000 mm lens corrected the astigmatism introduced by the cylinder glass. Finally, a bandpass filter was used to suppress the dye and PIV laser (BSP01-532R-25, Semrock). The final SNR was between 25 and 35.

To evaluate the optical performance of the LIF detection system, Siemens star images were used. Evaluation was done using the YASSES script in Matlab [83]. Figure 7.10 shows calculated contrast transfer functions (CTFs) at different $z$-positions in the engine. The maximum optical resolution, defined by a CTF of 10 %, is 8.3 lp/mm or 120 µm[27]. Furthermore, the depth-of-field is sufficiently large for the chosen dye laser sheet thickness (1.5 mm), as the optical resolution is greater than 140 µm at a depth of ±0.8 mm.

The triggering scheme pulsed the dye laser at a constant frequency 10 Hz provided by a pulse-delay generator (9520 series, Quantum Composers). It was synchronized to a timing unit (PTU-X, LaVision), which triggered the LIF system every second engine cycle (800 rpm) or fifth engine cycle (1500 rpm), when the laser trigger aligned with the

[26]Since the mixture field was supposed to be captured around ignition timing, a shutter closing time on the order of 1 ms was needed. LCD shutters offer sub-ms closing times, but introduce significant optical losses as typical transmittances are below 40 %. Diaphragm shutters can be triggered on-demand, but typical closing times are on the order of 10 to 20 ms. Mechanical curtain shutters in mass-produced digital cameras close in about 2.5 ms (curtain speed of 28 $\mathrm{km\,h^{-1}}$, the exposure time itself can be as low as 1/16 000 s and is controlled by a second falling curtain), but their synchronization with the engine and a repeating trigger would need to be explored. In a similar manner, voice-coil motors in computer hard disk drives can be used to realize shutter speeds above 10 $\mathrm{mm\,ms^{-1}}$ at frequencies of up to 100 Hz [163, 218] and could enable non-intensified imaging of near-UV LIF with cooled and backside-illuminated CCD cameras like the Teledyne SOPHIA 2048B-152-VS-X in such engine contexts.

[27]Another useful metric is the FWHM of the point spread function (PSF), which was calculated to be 100 µm. The PSF is calculated from the modulation transfer function (MTF), which is directly related to the CTF [82].

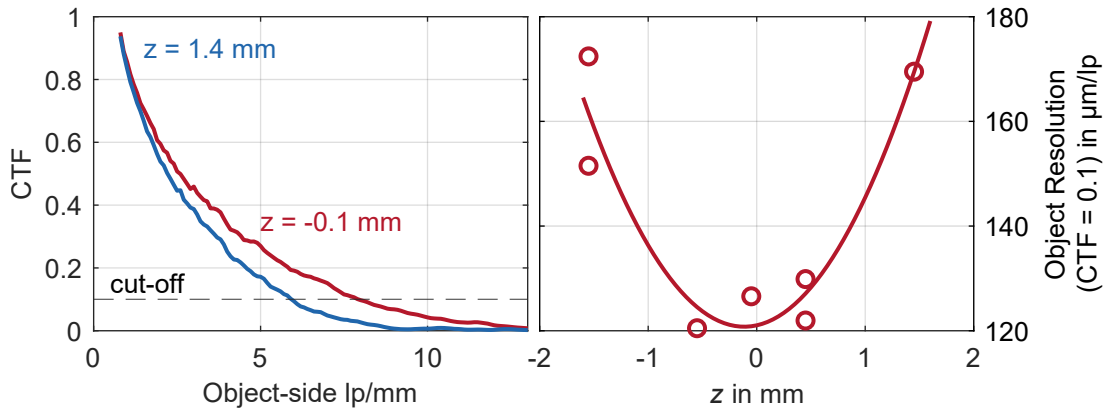


Figure 7.10: Optical performance of the LIF detection. Left: Contrast transfer function (CTF) calculated from Siemens star images with defined 10 % cut-off. Right: Depth-of-field analysis at 10 % CTF.

desired crank angle. Thereby, LIF was acquired late in the compression around ignition, while the sideview camera was triggered at 50 °CA, to visualize pool fire phenomena during expansion. In contrast, the HS PIV was acquired every cycle at a double-frame resolution of up to 1 °CA at selected crank angles during compression and expansion, with correspondingly optimized $\Delta t$ between both PIV laser pulses.

Four different operating points (OPs) were selected, which include a variation in engine speed (800 and 1500 rpm), load (0.4 and 0.95 bar), and global equivalence ratio (stoichiometric and lean). These conditions are summarized in Table 7.1. Since the goal was to study a locally confined fuel wall film and mixture inhomogeniety, most of the fuel is premixed isooctane, injected in the intake manifold. During compression, a small amount of fuel, representing less than 10 % of the equivalence ratio $\Phi$, was added with a single-hole injector, which in parts impinges on the piston surface and forms a wall film. The single-hole injector is of type Spray-G, generation 2 , provided by the Engine Combustion Network (ECN [54]) and manufactured by BorgWarner. It was operated with the Spray-G generation 1 drive scheme and a general purpose direct injection driver (NI-9751, National Instruments), at a pressure of 200 bar. Although acetone is often added as a gaseous (fuel) tracer due to its low boiling point [265], it has also been used as a liquid fuel tracer to match the characteristics of light fuel fractions [258]. Due to the difference in evaporation characteristics between isooctane and acetone it was decided to use pure acetone as fuel and tracer in the late direct injection rather than a blend. This increases the LIF signal, and even though it accelerates wall film vaporization processes due to the lower boiling point of acetone compared to isooctane (see Section 2.2.3), a monocomponent fuel prevents issues with preferential evaporation of one component. This effect is known to be a distorting factor even for tracers like 3-pentanone [34], which are closer to isooctane in terms of thermodynamic properties[28].

The measurement sequence consisted of several minutes of motored operation followed by DI and ignition (see Fig. 7.11). Due to the sensitivity of the investigated processes to thermal boundary conditions and specifically wall temperatures, measurements started at the first fired cycle and no pre-heating with additional sets of fired cycles was conducted. Three to four measurement runs with acetone DI and ignition were conducted. Each run contained 15 cycles without DI and ignition, but active lasers, during which background images were taken. After such a set, acetone was homogeneously seeded via PFI for the white image reference under motored conditions[29]. Finally, the engine was cleaned in preparation for a new measurement sequence[30]. Additionally, a comb structure was placed in the laser path to create matching images for cuvette and engine LIF.

[28]Preferential evaporation is primarily relevant for non-atomized evaporation on longer time scales.

[29]Compared to the fired LIF measurements, gas temperatures during compression are likely lower, increasing the LIF signal, while the increased oxygen content due to the absence of exhaust gas decreases it.

[30]Due to the impinging spray, the piston window is progressively soiled, which influences the laser transmission. The strongest change in transmission happens during the first cycles of the first measurement run. Therefore, taking the white image reference at the end of a set consisting of four to five runs was considered sufficient.

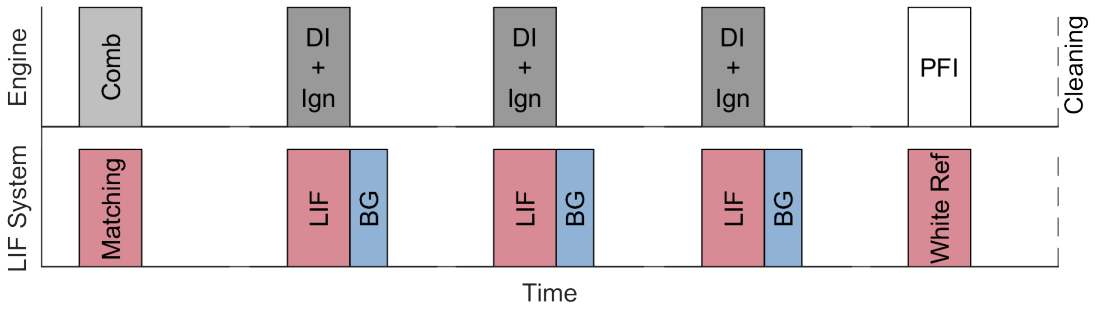


Figure 7.11: LIF measurement sequence. Comb matching images not acquired for every sequence.

## 7.2.4 Processing

### 7.2.4.1 PIV

The velocimetry data were processed in DaVis 10.2 (LaVision). After spatial dewarping, a multi-pass PIV step with interrogation window sizes of $64^2$ and $48^2$ pxl and 75 % overlap was performed. Erroneous vectors were removed below a peak ratio of 1.2 and by applying a universal outlier detection [257]. The vector data were imported in Matlab (MathWorks) and linearly interpolated on a consistent grid to facilitate comparison of different measurements.

### 7.2.4.2 Flame Detection

Burnt gas regions were detected by the absence of Mie scattering of PIV seeding droplets. These droplets evaporate in the preheat zone of the combustion and create a contrast in the image texture between burnt and unburnt regions, where the flame can be assumed to be on the boundary of this cross-section (see Fig. 7.12). In the remainder of this chapter, *flame* and *burnt-gas* are used interchangeably. To access this information, the raw Mie scattering images were binarized in Matlab. First, the spatial variance was calculated in a neighborhood of $\pm 7$ pxl for each pixel. Then, a locally smoothed threshold was determined based on the minimum and maximum of the spatial variance throughout each cycle, which takes into account differences in the reflection for images before and after the flames. Images were then binarized and an area filter applied. As apparent in the left panel of Fig. 7.12, in some runs the cylinder glass soiling or unfavorable background scattering was more intense, resulting in a low SNR. Here the algorithm was tuned to conservatively underestimate the flame's extent (as shown).

### 7.2.4.3 Pool Fire Visualization

The pool fire luminescence is captured by both the sideview and the PIV camera. To facilitate a statistical analysis, these images were also binarized. Since the sideview camera recorded after the main combustion, the image contrast was sufficient to apply a straightforward intensity threshold. For the PIV camera, a gradient-based approach was chosen

Table 7.1: Engine operating conditions for the mixture LIF measurements. The standard uncertainty of measured values is given in parenthesis (last significant digits). The $\lambda$-sensor was calibrated to isooctane. Spark timing denote by $\theta_{SI}$. Timing and electronic duration of the DI are given as $\theta_{DI}$ and $t_{eDI}$, respectively.

| Parameter | A | A lean | B | C | Unit |
|---|---|---|---|---|---|
| $p_{in,2}$ | 0.950(1) | 0.950(1) | 0.400(1) | 0.950(1) | bar |
| $n$ | 800 | 800 | 800 | 1500 | rpm |
| $\lambda$ | 1.02(1) | 1.15(1) | 1.02(1) | 1.02(1) | - |
| CoV($p_{cyl,max}$) | 3.75 | 5.9 | 24.0 | 6.1 | % |
| $x_{acetone}$ | 0.5 | 0.5 | 0.4 | 0.5 | % |
| $x_{acetone,ref}$ | 2.45(10) | 2.43(10) | 2.01(3) | 2.35(10) | % |
| $\Phi_{acetone}/\Phi_{ges}$ | 8.0 | 8.8 | 7.6 | 8.5 | % |
| $\dot{m}_{air}$ | 462(7) | 466(7) | 153(2) | 465(7) | mg/cycle |
| $\dot{m}_{acetone}$ | 4.25 | 4.25 | 1.25 | 4.25 | mg/cycle |
| $\dot{m}_{isooctane}$ | 31 | 28 | 10 | 29 | mg/cycle |
| $t_{eDI}$ | 2400 | 2400 | 630 | 2400 | µs |
| $\theta_{DI}$ | -40 | -40 | -40 | -50 | °CA |
| $\theta_{LIF}$ | -13 | -13 | -13 | -17 | °CA |
| $\theta_{SI}$ | -14.2 | -14.2 | -22.2 | -22.2 | °CA |
| $N_{cycle} \times N_{runs}$ | $34 \times 50$ | $34 \times 8$ | $34 \times 12$ | $22 \times 29$ | - |

since absolute intensities varied strongly throughout the combustion and in-between cycles. 2D image gradients were calculated after spatial median filtering and smoothed with a 2D gaussian filter, before a threshold was applied. This proved to be sufficiently robust, though, naturally geometry like the piston surface had to be masked conservatively to avoid false detections. In a binarized representation, the intensity information is obviously lost. This could introduce a bias, if the intensity also carries information about

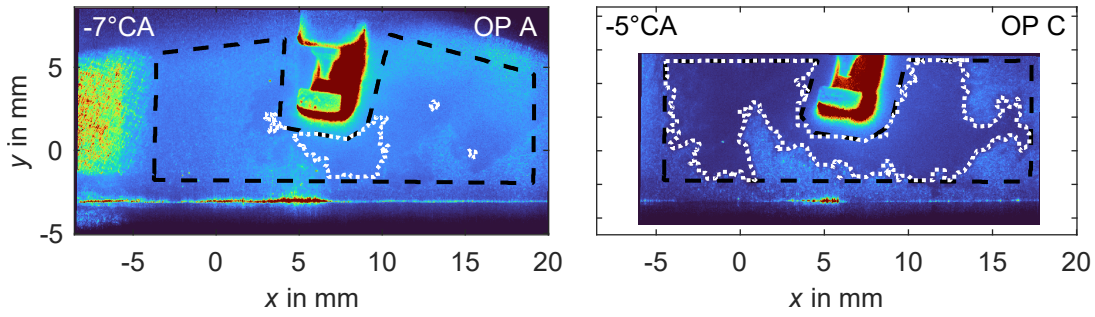


Figure 7.12: Flame detection by Mie scattering. Raw images of the PIV camera in the background. Area of interest and binarized flame boundaries marked with black and white dashed lines, respectively. For runs with low SNR, the flame is underestimated (left). At the higher engine speed of OP C, the region of interest (RoI) had to be reduced slightly to sustain the CAD-resolution.

the *amount* of soot in a certain region, in addition to the spatial extent of the binarized area. However, it shows that the summed image intensity and binarized area are strongly correlated (Pearson's $r = 0.93$), such that the use of binarized variables is justified.

#### 7.2.4.4 LIF

For a quantitative analysis of the mixture field, several processing steps are necessary:

1. LIF images were corrected by subtracting the average of 15 background images per run.
2. Cuvette and engine LIF images were matched by applying a Fourier-Mellin transform (see Section 7.2.1.1) on the comb structure images.
3. Then, instantaneous laser sheet profiles were calculated by averaging the cuvette images in the direction of the laser and applying a smoothing filter. The latter removes low amplitude, fringe-like intensity fluctuations in the cuvette LIF, which are not resolved by the IRO system with lower optical resolution.
4. Engine LIF images were normalized by the instantaneous laser sheet profiles.
5. Each instantaneous LIF image was divided by the corresponding average white image. Since both images were normalized with a laser sheet profile, also laser energy fluctuations are considered. Values now represent a fraction of the known acetone mole fraction in the white image.
6. The final acetone mole fraction is derived by multiplying with the reference run mole fraction.
7. In the end, the spatial calibration is applied by means of a 2D polynomial derived from dot-target images.

$$S_{\mathrm{r,f}} = \frac{S_{\mathrm{f}}^{+}}{S_{\mathrm{f,ref}}^{+}} = \frac{x_{\mathrm{ac}}}{x_{\mathrm{ac,ref}}} \cdot \underbrace{\frac{p}{p_{\mathrm{ref}}}}_{\sim 1} \cdot \underbrace{\frac{T_{\mathrm{ref}}}{T} \frac{\sigma_{\mathrm{abs}}(T)\phi_{\mathrm{f}}(T,p,x_{\mathrm{i}})}{\sigma_{\mathrm{abs}}(T_{\mathrm{ref}})\phi_{\mathrm{f}}(T_{\mathrm{ref}},p,x_{\mathrm{i,ref}})}}_{\sim 1 \pm 0.1 \text{ (Fig. 7.3)}} \cdot \underbrace{\frac{E}{E_{\mathrm{cuv}}} \frac{E_{\mathrm{cuv,ref}}}{E_{\mathrm{ref}}}}_{\sim 1} \cdot \underbrace{\frac{\eta_{\mathrm{opt}}}{\eta_{\mathrm{opt,ref}}}}_{\sim 1} \tag{7.2}$$

## 7.2.5 Uncertainty

In this section, factors influencing the LIF measurements and the necessary steps to derive the acetone mole fraction are discussed. One of the primary influences on the measurements is spray residue, which progressively soils the piston (see Section 7.3.1) and directly affects laser transmission. This leads to a lower signal in regions above a residue or thin film due to laser scattering and absorption[31]. More importantly, bright emissions appear at the piston surface of background images, which are not necessarily present in the measurements themselves and lead to overly aggressive background subtraction. This effect is typically localized and limited to a few regions where mole fractions are

[31]The laser could have been coupled in from the side, i.e. the cylinder glass. However, this brings disadvantages with respect to laser sheet adjustment and positioning for different piston positions. Furthermore, beam steering due to temperature gradients or, more importantly, vaporization can lead to a significant loss in signal.

biased and take unphysical values. In addition, there is soiling of the cylinder glass by the PIV seeding, so a trade-off between quantity and quality of data must be made. In order to be able to measure a large number of cycles and operating conditions, the number of sequential measurement runs before the engine was cleaned was set to a maximum of four. There are also fluctuations in the PIV seeding density and therefore in the amount of LIF emission that is multi-scattered, however, this influence is estimated to be $< 0.15$ percentage points in mole fraction only, based on measurements with and without PIV seeding. Both piston and cylinder liner soiling are responsible for the calculated negative mole fractions shown later (e.g. in Fig. 7.23). In Fig. 7.13 histograms of measured acetone mole fraction before and after engine cleaning are shown. It can be seen that unphysical negative values occur only for the clean-piston cycles, since the white images used take into account soiling of three to four runs. In addition, values around 1 % mole fraction are more common, while the peak around 0.3 % is smaller. An exact quantification of this influence is complex and strongly depends on the exact location. Still, as an estimate based on this data, the error due to soiling is reported to be locally up to $\pm 0.6$ percentage points in mole fraction.

Other factors contributing to the measurement uncertainty, are the sensitivities of the LIF regarding temperature and gas composition, as discussed in Section 7.2.1.1. Temperature inhomogeneities of the in-cylinder gas during late compression are typically small ($< 25$ K, see e.g. [190]). With DI, however, evaporative cooling will increase these inhomogeneities, so regions with a high acetone mole fraction are expected to be colder. At a bulk temperature of 650 K, a variation in temperature by $-50$ K would constitute a change in signal of just 3 % for ambient pressures (see Fig. 7.3). Even if the temperature sensitivity increases at higher pressures, the temperature influence can be considered small. The same can be said for the influence of the oxygen content: With observed acetone mole fractions below 10 %, the acetone fluorescence increases by just 1 % due to reduced quenching.

Finally, the amount of premixed acetone in the reference measurements is subject to uncertainty. Based on the characterization of the port fuel injector, the resulting standard uncertainty is calculated to be 0.1 percentage points in mole fraction. Overall, soiling, reflections and residue contribute most to measurement uncertainty.

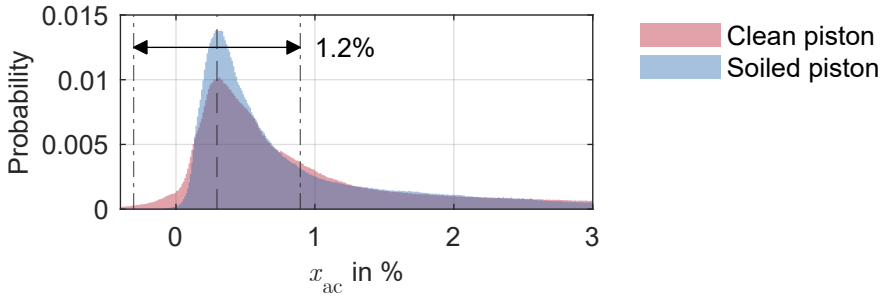


Figure 7.13: Soiling influence on the LIF measurements. Histogram of the measured acetone mole fraction in the full FoV for measurement runs directly after cleaning (clean piston) and the last runs before cleaning (soiled piston). Fired cycles 1-10 are shown, with 10 runs in each group.

Another aspect which shall be discussed is tracer stability. Compared to aromatic tracers, high laser fluences are needed for acetone LIF. It is reported that most acetone molecules dissociate into methyl ($CH_3$) and acetyl radicals ($CH_3CO$) after excitation at 266 nm [129, 177, 265]. Dissociation yields are lower for excitation at 308 nm, due to the lower photon energy and absorption cross section [162, 265]. Since an even higher wavelength of 315 nm at a lower fluence is used in this work, photo-dissociation is expected to play a minor role.

Next to photo-dissociation, thermal decomposition may be important. Pyrolysis of acetone begins at around 750 K [90] to 800 K [168] at atmospheric pressures. The onset of pyrolysis is expected to remain similar at higher pressures, in contrast to reaction rate constants, which are typically pressure dependent. With the given in-cylinder gas temperature (see Fig. 5.8), acetone is considered stable until ignition timing. A different kind of invasiveness was observed on the film: After the UV laser shot, single droplets of acetone were ejected from the film, which were recorded by the PIV camera. This could be due to local vaporization of fluid or residue but did not seem to influence the acetone mole fraction measurements. Though this creates additional seeds for soot formation, no significant difference in subsequent pool fires was found.

## 7.3 Results

During the operation with late single-hole DI, multiple characteristic processes take place. To begin the analysis, Fig. 7.14 presents key moments captured by the PIV camera. At −30 °CA, the injection is ongoing and the spray plume impacts at an angle of 9° on the piston surface. Following ignition at −14.2 °CA, the flame propagates from the spark plug, as apparent by the areas void of particles and Mie scattering. Sometimes, remaining droplets from the injection come into contact with the flame (marked with *A*) and light up after a slight time delay. The luminous signal can be observed even in the burnt gas region (*B* and *C*). Around TDC, the near-wall region close to the spray impact point also begins to emit light (*D*) as a *pool fire* forms. This signal increases in strength and area during the next CADs, when also the main combustion is visible as an intense background. During the expansion, only the pool fire remains, where its structures are being distorted and stretched due to the piston motion. In the following sections, the described processes will be discussed further.

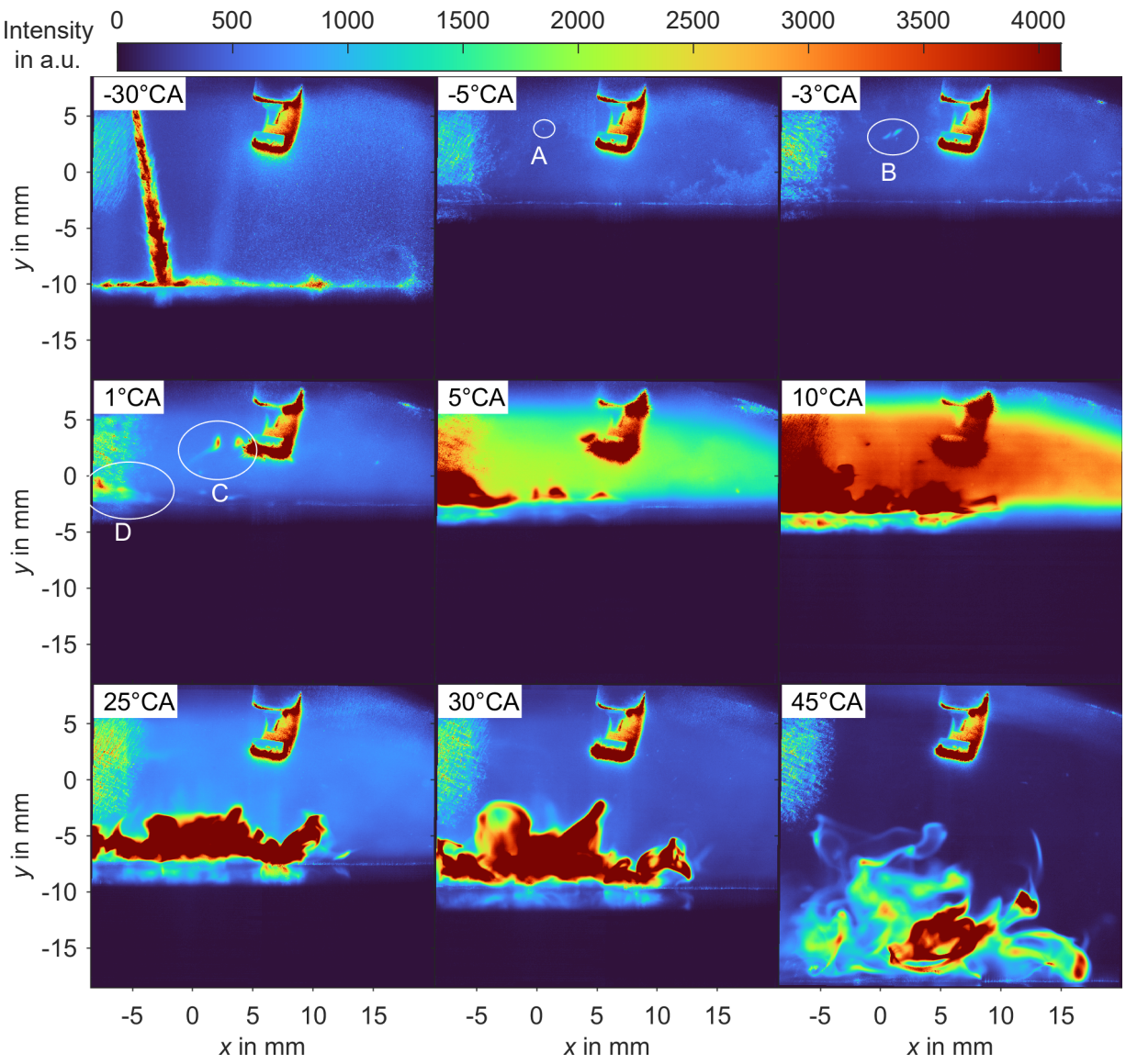


Figure 7.14: Visualization of the DI, main combustion and developing pool fire in false colors from the PIV camera. An early fired cycle of OP A is shown.

### 7.3.1 Direct Injection and Spray

Figure 7.15 shows the standard deviation of the intensity of Mie scattering images during injection as captured by the PIV camera for OP A, B and C (the DI of OP A lean and A is identical). The high intensity core of the plume saturates the camera and is represented as a plateau in the standard deviation image. Towards the edges, turbulent structures lead to fluctuations and correspondingly higher std. Several observations can be made: First, the spray plume is angled at 9°, which is slightly larger than the mounting angle of 8°. It impinges on the piston around $x = -2\,\text{mm}$ for all OPs. Second, the central plumes are approximately 1 mm wide, which is substantially smaller than the plumes produced by the Spray-G Gen1 8-hole injector at a similar injection timing. There, the

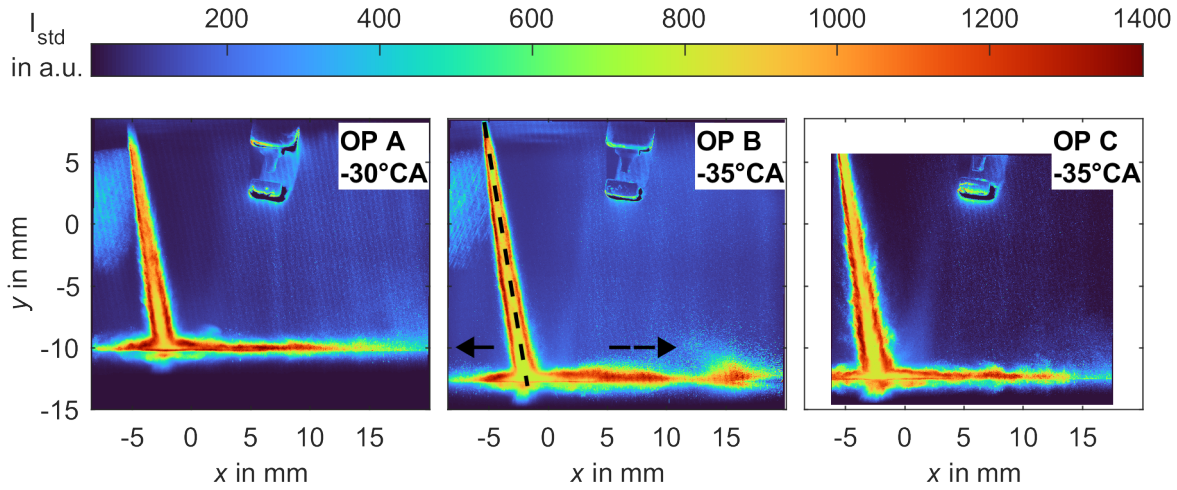


Figure 7.15: Single-hole injector spray visualized by standard deviation images of the Mie scattering in OP A, B and C. Direction of deflected droplets marked with black arrows for OP B.

plume widths were found to be on the order of 5 mm wide [E78]. The reduced atomization of the spray under these conditions is convenient, since the creation of a fuel wall film is the main objective in this investigation. Third, slight differences in the plume can be observed between OPs. OP C features higher fluctuations along the spray edge, which could be attributed to the earlier injection timing and higher turbulence levels in the surrounding flow compared to OP A. The thinnest plume occurs in OP B, which is likely related to the lower pressure and therefore density in the combustion chamber and thereby less interaction with the surrounding air, slower breakup and higher penetration of the plume core. In general, an inverse relationship between ambient gas density and spray penetration is reported for gasoline DI [171, 185]. Fourth, it can be seen that the spray droplets are preferentially deflected to the right by the piston surface and carry on a high momentum. Measured velocities of these deflected droplets are about 25 $\mathrm{m\,s^{-1}}$ (derived from manual particle tracking). This increases the overall extent of the inhomogeneous mixture layer.

Furthermore, the momentum of the spray influences the tumble structure, which is relatively weak at this stage of the compression. To examine this, Fig. 7.16 shows the velocity field around spark timing normalized to the mean piston speed for the four OPs with and without direct injection. In all four cases with DI, the velocity above the piston is significantly reduced, as the spray counteracts the tumble motion there. For both OP A cases and OP B, the tumble vortex shape is slightly deformed and a new left-downwards directed flow can be observed to the right of the spark plug. It appears that the rightwards deflected spray induces a flow, which in turn is deflected by the cylinder walls and combines with the normal tumble direction (similar to a wall-guided engine configuration). However, the velocity around the spark plug remains mostly unchanged. Stronger deviations can be seen for OP C, where without DI a wide region of high velocities can be observed above the piston. With DI, the spray induces a downward flow along the spray

axis. Furthermore, a shear layer with a wall-parallel flow emerges on the right. These seemingly greater changes can be explained with the different timing at higher engine speed, as the time-based injection is happening during a longer fraction of the compression and ignition is initiated just 390 µs after the hydraulic end of injection (see Table 7.2).

The impinging spray, wall film creation and subsequent combustion processes create a *footprint* formed by residue. A footprint of OP C after four measurement runs was analyzed with a confocal 3-D microscope (µsurf, NanoFocus). Figure 7.17 shows the true color surface texture and the height map derived with the microscope. Around a central,

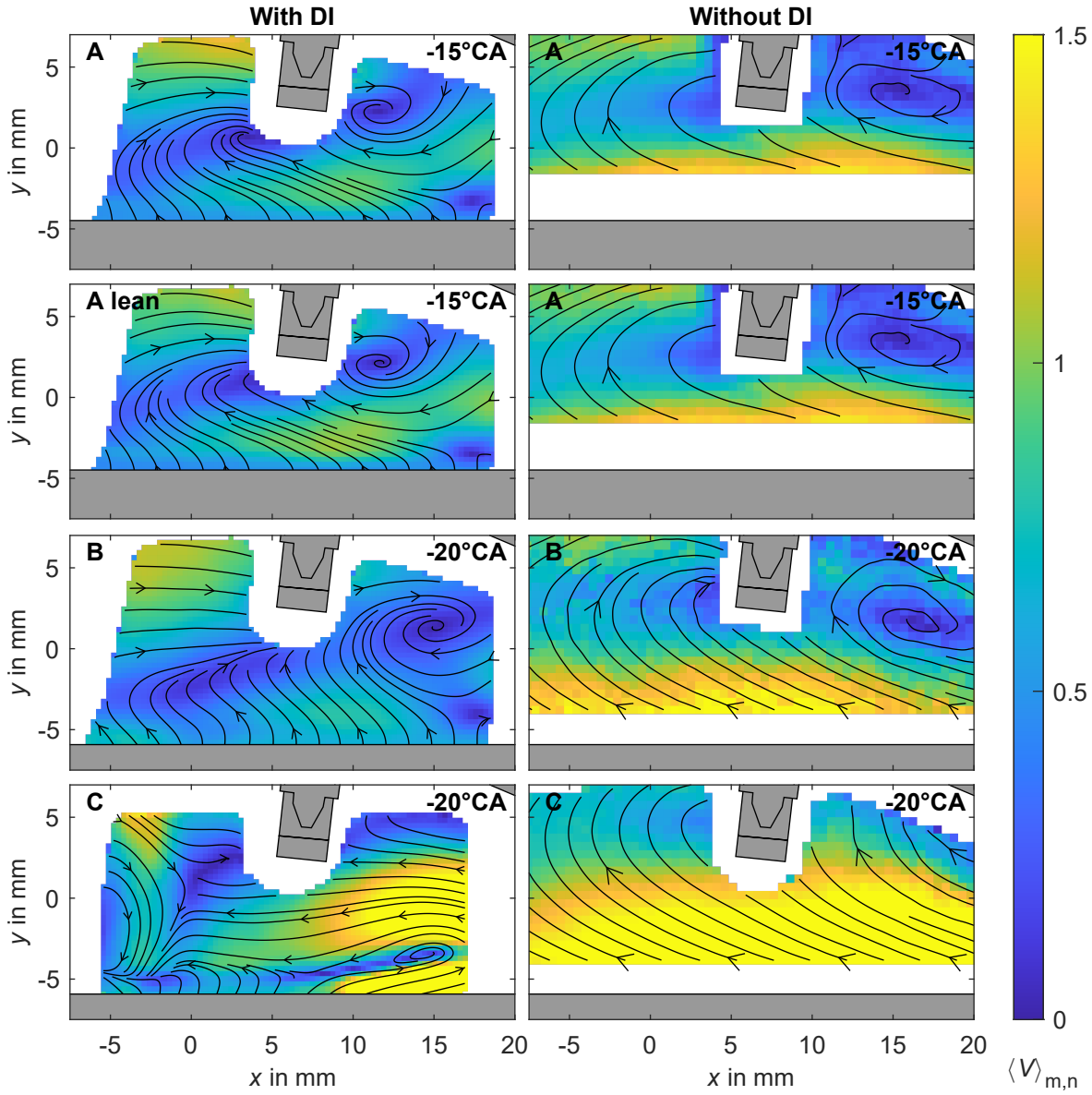


Figure 7.16: Phase-averaged velocity fields around spark timing with and without direct injection (left and right column, respectively). The velocity magnitude is normalized by the mean piston speed.

Table 7.2: Spray timing parameters. $\theta_{\mathrm{eSOI}}$ marks the electronic start of injection, $t_{\mathrm{eDI}}$ the electronic injection duration, $\theta_{\mathrm{hEOI}}$ the hydraulic end of injection, $\theta_{\mathrm{SI}}$ the spark ignition timing, $\Delta t_{\mathrm{hEOI-SI}}$ the time between hydraulic end of injection and spark ignition, and $\theta_{\mathrm{LIF}}$ the LIF timing.

| OP | $\theta_{\mathrm{eSOI}}$ in °CA | $t_{\mathrm{eDI}}$ in ms | $\theta_{\mathrm{hEOI}}$ in °CA | $\theta_{\mathrm{SI}}$ in °CA | $\Delta t_{\mathrm{hEOI-SI}}$ in ms | $\theta_{\mathrm{LIF}}$ in °CA |
|---|---|---|---|---|---|---|
| A | -40 | 2.40 | -27 | -14.2 | 2.66 | -13 |
| A lean | -40 | 2.40 | -27 | -14.2 | 2.66 | -13 |
| B | -40 | 0.630 | -35.5 | -22.2 | 2.77 | -13 |
| C | -50 | 2.40 | -25.7 | -22.2 | 0.390 | -17 |

oval shape, a nearly circular ring of spattered material with a diameter of approximately 30 mm can be seen. Though the original orientation inside the engine is not known, it is likely that the $y$-coordinate in this figure corresponds to the $x$-direction inside the engine, due to the oval shape of the central impinging point and the angle of the injector. The height of the outer ring is on the order of only 3 µm. It consists of a sticky, oil-like substance of unknown composition. Since acetone would evaporate fully, it is likely residue of impurities in the acetone or hydrocarbons, which where cracked inside the wall film during the combustion. There could also be traces of the silicone oil used as PIV seeding, though a test run without seeding exhibited a similar footprint.

Noteworthy is the inner area, where the true color image reveals thin-film interference effects. Here, the immediate spray impact seems to have cleared the piston surface from any residue and other soiling. The interference effects accompanied by the height measurements indicate sub-micron thin films, possibly as a remainder of the acetone wall film vaporization. Different dimensions of the footprint were found for different OPs. A manual measurement for OP A showed a smaller outer diameter of approximately 18 mm, which might be related to the later injection timing compared to OP C (see Table 7.2).

Another topic of interest regarding the fuel film is its vaporization regime. At atmospheric pressures, the boiling point of acetone is 56 °C, while the *Leidenfrost* temperature is reached between 135 and 185 °C [14]. In this regime, a vapor layer insulates the fluid from the hot wall, which greatly reduces heat transfer rates. However, surface properties play an important role, as surface contaminants and roughness increase the Leidenfrost temperature. Obviously, atmospheric pressures are only encountered during the intake phase. Late in the compression, in-cylinder pressures are in the range of 5 bar to 12 bar at ignition timing (OP A and C). Under these conditions, the boiling point of acetone is at 112 and 153 °C, respectively, as calculated by Preusche [196] with Refprop [100]. This range is below the piston glass temperatures presented in Chapter 5, which increase from 225 to 300 °C in the first 50 fired cycles. To the author's knowledge, no data on the pressure dependency of the Leidenfrost temperature exists for acetone.

However, Stanglmaier, Roberts, and Moses [229] investigated vaporization of isooctane and other model fuels at higher pressures and found that the shift in boiling point and Leidenfrost temperature with pressure is similar. Most importantly, they showed that at

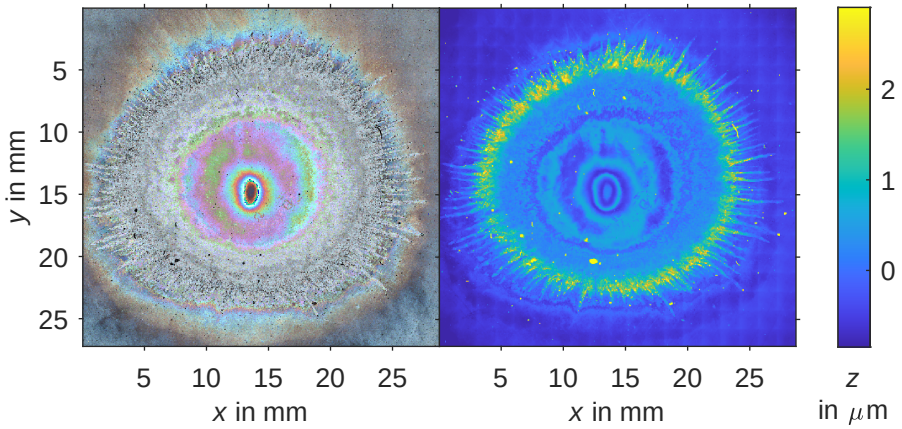


Figure 7.17: Confocal 3-D microscopy measurement of the spray footprint and residue of OP C. True color image of the surface texture (left) and height map (right). Arbitrary coordinate system, which does not conform to the engine coordinate system.

4.4 bar the Leidenfrost effect on isooctane and other model fuels is strongly reduced, as the vapor layer is increasingly compressed. As a result, vaporization rates of fuel wall films on warm engine surfaces may experience a minimum during the intake phase, due to the Leidenfrost effect, and again increasing rates at higher pressure during compression. Indications of the Leidenfrost effect on fuel wall films in a metallic spark-ignition engine were found by [99]. They injected different fuels onto the piston under fired operation and found that the emission of unburnt hydrocarbons increased when the piston temperature was more than 50 K higher than the respective fuel boiling point. Other effects, such as changes in the mixing field, could also be responsible for the increased emissions. Ding et al. [43] and He et al. [94] measured fuel films of gasoline and ethanol using *refractive index matching* on a rough piston glass. Their results speak against vaporization in the Leidenfrost regime, because a vapor layer would prevent the liquid from filling the surface roughness and negate their used measurement technique. For a concrete comparison, the wall temperatures would have to be available. Furthermore, the artificial surface roughness likely increases the Leidenfrost temperature significantly.

Regarding the current work, it is questionable whether vaporization in the Leidenfrost regime would lead to the observed, regular residue and spatial stability of the film. All in all, the exact regime of acetone vaporization in the present investigation cannot be determined with certainty. However, it can be assumed that vaporization rates are significantly higher than for pure evaporation, due to (film) boiling and convection.

### 7.3.2 Pool Fire - Flame or Pyrolysis?

Fuel wall films and their influence on combustion and pollutant production have been the subject of several studies (e.g. [31, 33, 127, 140, 208, 222, 231]). However, the processes behind the phenomenon commonly referred to as *pool fire*, are not yet comprehensively understood. Early studies in optically accessible engines reported luminous regions of

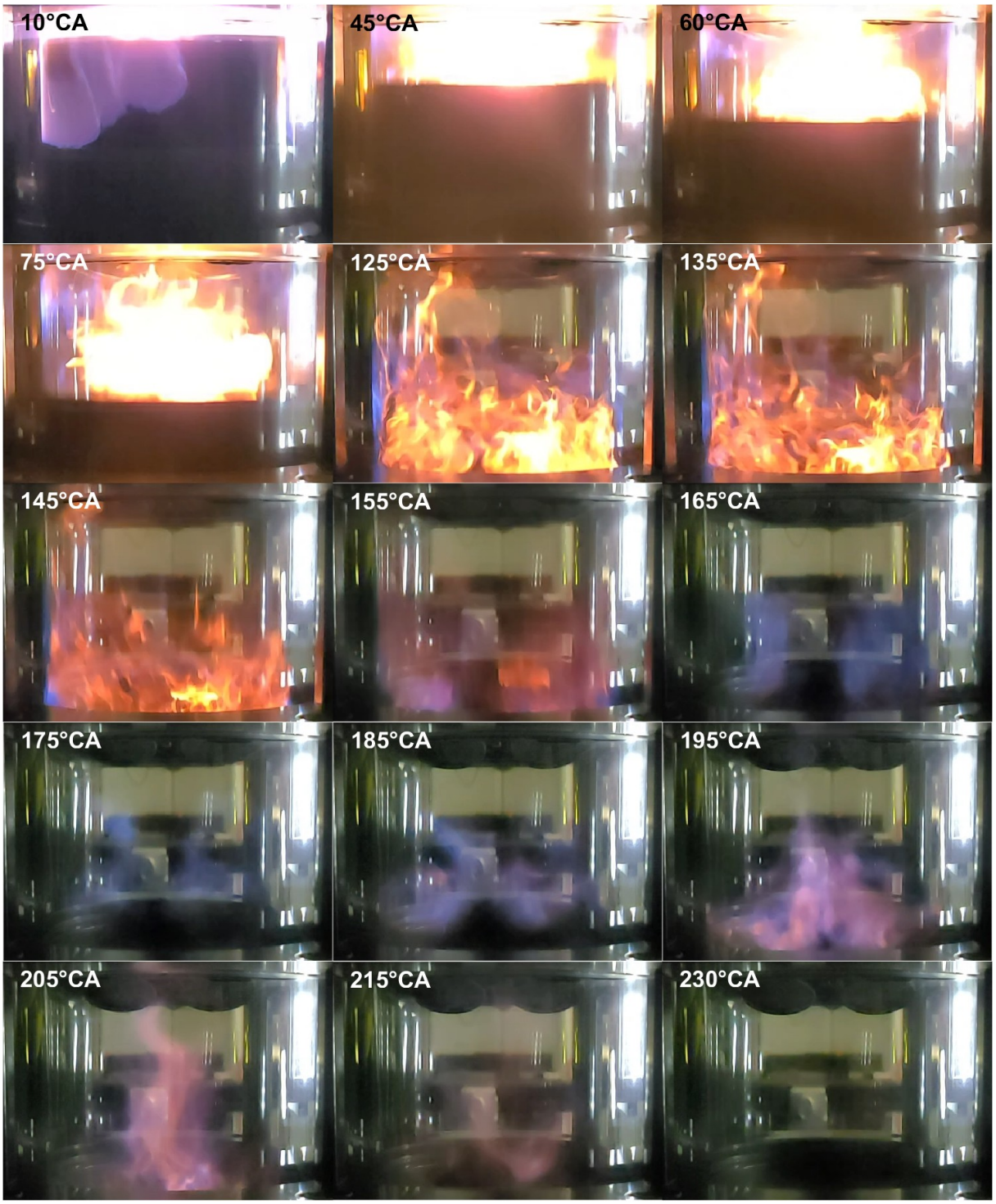


Figure 7.18: Visualization of the expansion and exhaust stroke of OP A with poolfire and crevice gas burning using a high-speed color camera.

orange color, which were characterized as diffusion flames above the evaporating wall film, leading to this naming [33, 140, 231, 263]. On the other hand, Ketterer and Cheng [126] concluded that the luminosity in their setup stemmed from temperature radiation of incandescent soot, which forms after high temperature pyrolysis in fuel rich regions during and after the combustion. This was supported by experiments at fuel-rich conditions, where a diffusion flame would not have enough oxygen to develop. Furthermore, in a variation of equivalence ratios, only the measured soot particle number changed, while the particle size distribution remained constant. This indicates that the pathway for soot production stayed similar regardless of equivalence ratio [127]. Other authors who reported OH-LIF signal, which would commonly be interpreted as a reaction zone marker, inside pool fires [207, 263] attribute this to background chemiluminescence of OH*, either as a product of hydrocarbon pyrolysis [261] or combustion.

The following section aims to find evidence for one of these interpretations. Figure 7.18 shows a visualization of the expansion and exhaust stroke, as acquired by a high-speed color camera (Samsung Galaxy S20 FE at 960 fps) from the sideview position (see Fig. 7.8). At 10 °CA the main combustion is still in progress and appears blue-white. One can see how the flame is pushed into the crevice. Typically, pool fire emission starts to appear at this crank angle. Continuing with 45 °CA, a bright emission originates from the piston top, which is clearly identifiable as orange-yellow pool fire between 60 and 140 °CA. Additionally, outgasing and combusting mixture from the expanding crevice gases can be seen as faint blue flames. Pool fire intensities decrease, mostly due to the expansion in volume[32]. Around 105 °CA, the exhaust valves open, though it takes until 130 °CA at a cylinder pressure of 4 bar, until the slope of the pressure trace changes. The pressure between cylinder and exhaust manifolds equalizes around 165 °CA at 1 bar. At this CAD, the pool fire can be seen to accelerate towards the cylinder roof, while the intensity diminishes. Only a faint, premixed flame from the crevice gases remains at BDC. Interestingly, pressure oscillations in the exhaust pipe lead to a backflow and subsequent increase in cylinder pressure to 1.3 bar at 215 °CA as well as a reduction in flow velocities and stretch, which stabilizes remaining crevice flames. Sometimes, an orange signal (re)appears, which could be either incandescence of heated up soot from previous pool fire regions or emissions from water vapor (Balmer $H_\alpha$-line at 656 nm [211]).

This analysis points towards a correlation of the pool fire luminosity with the in-cylinder temperature. Fired 1-D simulations in GT-Power (Gamma Technologies) predict a gas temperature of above 1000 K until the exhaust valves open [23]. This temperature would be sufficient to sustain pyrolysis reactions, which in the case of acetone begin at around 800 K [168], and lies above the *Draper point*[33] [49], such that visible soot glow is conceivable. Soot production, on the other hand, is said to start only above 1400 to 1500 K [20, 241] and is therefore assumed to slow down after about 50 °CA.

[32] less so because of the piston moving outside the FoV, as another, more angled view showed bright intensities above the piston surface even at BDC

[33] The Draper point is the temperature at which objects begin to emit enough light in the visible spectrum to be percieved by humans.

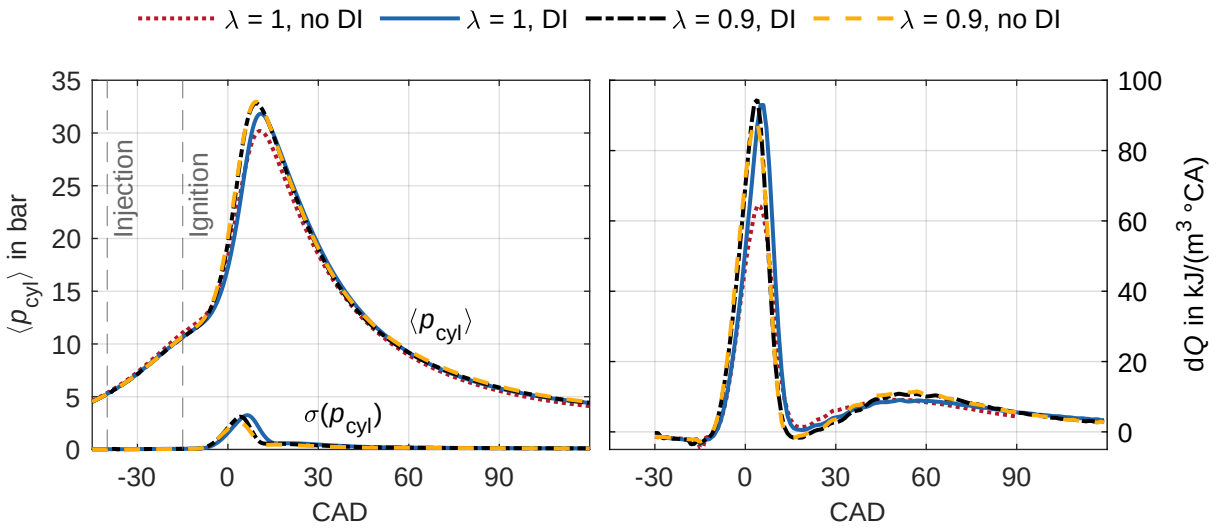


Figure 7.19: Phase averaged pressure traces (left) and calculated heat release (right) for fired operation with and without acetone DI.

To find further evidence for either hypothesis, the engine was operated at different equivalence ratios with and without DI. Figure 7.19 shows in-cylinder pressure traces and heat release rates for four different conditions: stoichiometric and globally rich, once with and once without DI, respectively, whereby in all cases premixed, homogeneous PFI was used. The estimated heat release rates are calculated by the software IndiCom (AVL) and are based on the pressure trace and the first law of thermodynamics[34] using a polytropic coefficient of 1.30.

The phase-averaged pressure traces share similar characteristics: a relatively modest increase in pressure due to the compression followed by a strong increase after ignition. Peak pressures are higher for the rich conditions, owing to a higher flame speed, and 2 bar lower for the $\lambda = 1$ case without DI, which was recorded in a different investigation, so the difference could be due to minor variations in boundary conditions or blow-by along the piston rings. In particular, the curves converge on a line during expansion. The same applies for the estimated heat release rates, where the combustion of crevice gases manifests in a second heat release peak[35]. The important observation here is that the pool fire phenomenon, which takes place from 10 to 150 °CA in cases with DI, does not alter the heat release rate to any measurable amount during expansion.

Another finding is that in the case of $\lambda = 0.9$ with DI, where the homogeneous PFI alone achieves stoichiometric conditions, pool fire appears in the usual manner. It is unlikely that enough oxygen is left in very rich, non-combusted regions to sustain a diffusion flame during expansion. In summary, the presented pool fire phenomenon is deemed

[34]Heat release estimated as $Q_i = \frac{1}{\kappa-1}\left[\kappa p_i\left(V_{i+n} - V_{i-n}\right) + V_i\left(p_{i+n} - p_{i-n}\right)\right]$, with the interval $n$, cylinder pressures $p$, cylinder volume $V$ and the polytropic coefficient $\kappa$

[35]The relative volume change of the cylinder and thereby the amount of outgassing from the crevice is maximum at 30 °CA. Since the crevice gas needs time for heat conduction and ignition, the second heat release peak follows a bit later. In addition, the pressure change affected by heat losses needs to be taken into account, by which one arrives at the presented heat release equation.

to be soot incandescence without the presence of a flame. The soot is formed partly in fuel-rich regions along the vaporizing wall film by incomplete combustion and partly by pyrolysis of fuel (acetone) in the hot in-cylinder gases with subsequent soot growth, aggregation and incandescence. The term *pool fire* - albeit potentially misleading - will continue to be used to follow popular convention and refers to visible soot formation above a wall film.

### 7.3.3 Multi-Parameter Comparison

After this introductory overview and the classification of pool fire, the multi-parameter data are analyzed.

Figure 7.20(a) shows the same cycle as Fig. 7.14 from the low-speed sideview camera. It is clear that the previously shown $x$-$y$-extent is coupled with an even greater $z$-extent. To further analyze this, Fig. 7.20(b) presents the probability of pool fire along the $z$-axis for all cycles and OPs. OP A, A lean and C exhibit approximately normal distributions centered in the tumble plane, with only rare events beyond $z = \pm 20\,\text{mm}$. Surprisingly OP B differs, in that the distribution is shifted, with a peak at $z = -8.3\,\text{mm}$. The reasons for this have not yet been identified clearly. OP B features the smallest injected fuel mass, with the longest time between end of injection and ignition, therefore evaporation and convection have a larger influence compared to the other OPs. There is no known systematic asymmetry in the $z$-velocity of this engine, based on measurements in a limited horizontal plane [41, p. 97], however the spark plug electrodes are oriented such that the gaps opens towards the $+z$-direction, which could induce asymmetries in the 3-D flow. Furthermore, as will be shown later, OP B exhibits far less pool fire than the other OPs. All these factors might contribute to the skewed distribution in $z$.

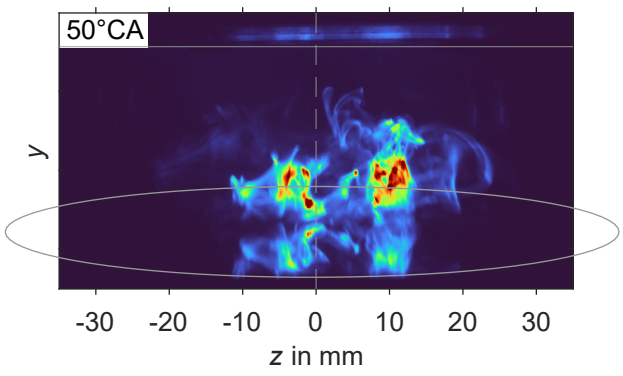


(a) False color sideview visualization of pool fire in the same cycle as shown in Fig. 7.14 for the PIV camera. The cylinder head and piston geometry are indicated by gray lines.

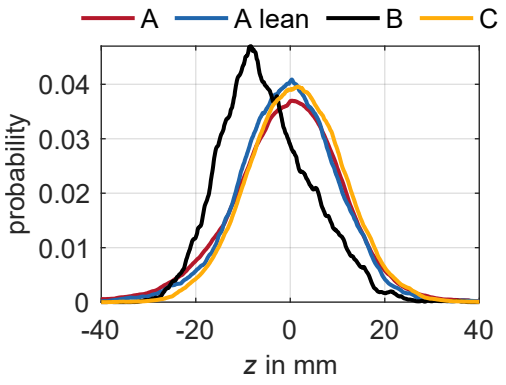


(b) Probability density function (PDF) of pool fire occurrence along the z-axis for all recorded cycles.

Figure 7.20: Sideview pool fire visualization.

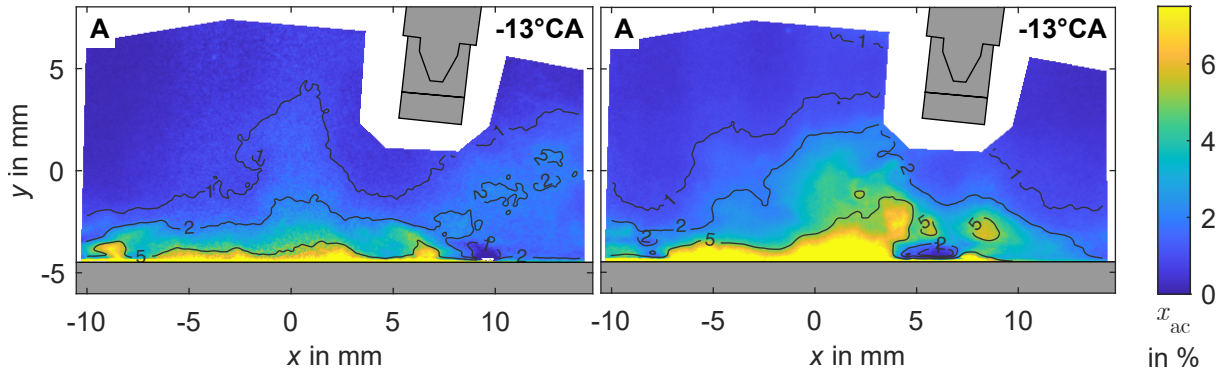


Figure 7.21: Instantaneous acetone mole fraction of OP A (−13 °CA). Shown are exemplary, randomly selected cycles (fired cycle 9 and ten of two different runs). The contour lines were derived from data filtered with a 2-D gauss and a standard deviation of 2.

**Mixture Field** A determining factor in the combustion and subsequent pool fire might be the mixture field. Instantaneous LIF results of two randomly selected measurement runs of OP A are shown in Fig. 7.21. Acetone mole fractions in the bulk flow are below 0.5 %. Plumes of acetone vapor can be seen to rise above the wall film. Close to the wall, acetone mole fractions above 5 % are measured, which marks the transition from stoichiometric to rich conditions if acetone were the only fuel present. Adding the homogeneously mixed isooctane with a mole fraction of approximately 1.5 %, a combined equivalence ratio Φ of more than 1.9 is reached. To assess the flammability limits of an isooctane-acetone mixture at room temperature and pressure, Le Chatelier's law is used [15]. In a fuel mixture with mole fractions of 8 % acetone and 92 % isooctane, the upper flammability limit is estimated to be 11.5 %[36]. However, this limit is expected to increase at the elevated pressures and temperatures inside the engine [15, 197]. In conclusion, the LIF measurements suggest that only a millimeter-thick region above the wall film is rich enough to extinguish the flame, though plumes extend up to the spark plug with a mixture richer than stoichiometry, which is a potential source of unburnt hydrocarbons and soot.

After these exemplary cycles, Figure 7.22 shows phase-averaged acetone mole fractions for all four OP. The characteristics from Fig. 7.21 apply: most of the FoV shows low average acetone mole fractions below 1 %, with values increasing towards the wall film. There is a slight tendency towards higher values on the right, especially for OP C, which is likely due to the strong spray-induced rightwards velocity still present, as discussed with Fig. 7.16.

Obviously, the wall temperature has a major influence on the film evaporation. Figure 7.23 compares histograms of the acetone mole fraction in the full FoV from the first fired cycles 1-20 (blue) and later fired cycles 49-69 (red). There is a clear trend towards lower acetone mole fractions during later fired cycles, as the peak of the mole fraction distribution moves by 0.18 percentage points for OP A, A lean and B, and by 0.06 percentage

[36]With 7 % and 13 % as upper flammability limits for isooctane and acetone, respectively [55].

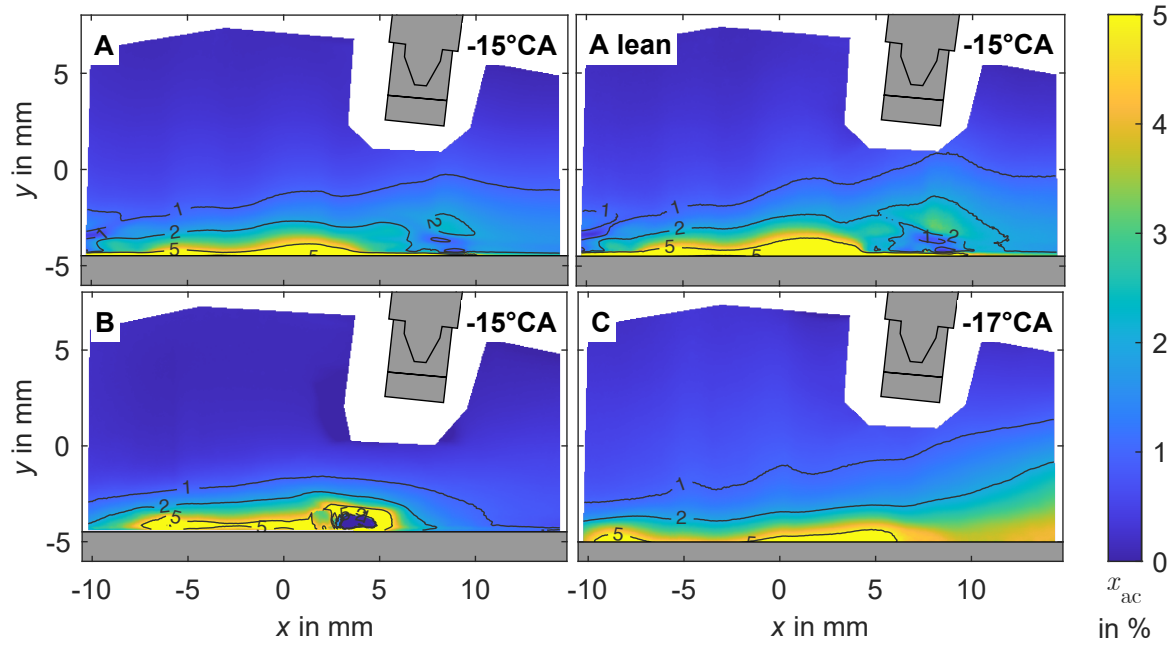


Figure 7.22: Average acetone mole fraction as measured by LIF.

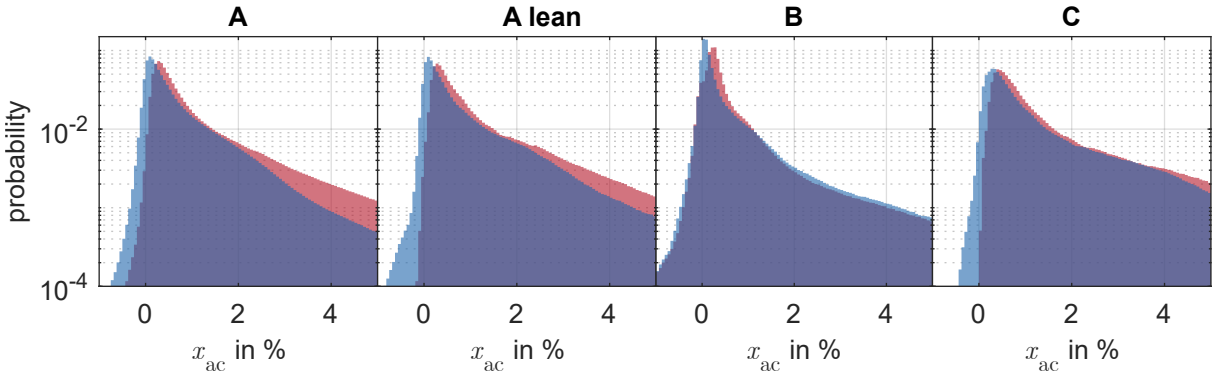


Figure 7.23: Histograms of the acetone mole fraction for fired cycles 1-20 (red) and 49-69 (blue).

points for OP C to the left. This indicates higher vaporization rates and subsequently more time for mixing as a consequence of rising wall temperatures, as discussed in Chapter 5 (see Fig. 5.16), where the temperature at the piston surface was found to increase from 480 to 575 K during the first 50 fired cycles. Interestingly, for OP B, the proportion of mole fractions above 1 % stays fairly constant and at a lower level. Thereby, it resembles the distributions of later fired cycles of the other OPs. Reasons for this could be the lower injected fuel mass and longer time from injection to ignition (and LIF acquisition), which could lead to a more homogeneous mixture of the *primary* vapor originating from atomized spray droplets. The *secondary* vaporization of the film is likely slower and resulting mixture inhomogenieties may be more confined to the near-wall region. This interpretation is supported by the mixture field shown in Fig. 7.22. Lastly, the lower heating rates of the piston surface in OP B due to the lower engine load (440 to 500 K in the first 50 fired cycles) result in less change in vaporization rates between cycles. As previously

mentioned, the distributions partly extend to negative mole fractions. This is due to imperfect background subtractions, as the soiling of cylinder walls and buildup of residue on the piston are dynamic processes, which increase the uncertainty and cannot always be fully corrected.

**Pool Fire** After this description of the mixture field, the pool fire phenomenon will be analyzed further. Looking at the $x$-$y$ pool fire probability maps of the first ten fired cycles of OP A in Fig. 7.24, the pool fire is centered between $x = -5$ to 10 mm, which is not surprising, since there the spray impingement and deflection was observed in Fig. 7.15. An interesting detail not resolved in this map is that the pool fire appears only at distances larger than 0.5 mm above the piston surface, most likely because of the temperature boundary layer above the colder wall where in addition endothermic vaporization takes place. This suggests that in this layer soot particles are either not formed or not hot enough to glow in the spectrum detected by the cameras.

To analyze the impact of the transient wall temperature on the pool fire, Fig. 7.25 shows the area of binarized pool fire as seen from the sideview camera with respect to the cycle number. Again, OP A, A lean and C exhibit similar trends, with relatively widespread pool fire occurrence in the beginning and a following decline, until around cycle 50 for OP A, where pool fire ceases to appear. The occurrence is more constant for OP B, where pool fire is rare and small in extent from the beginning, which is in line with the mentioned, comparably long time available for vaporization and mixing and the comparatively homogeneous mixing field in Fig. 7.22. Furthermore, combustion in OP B is the slowest, which decreases peak pressures and temperatures and could further reduce pool fire.

Another finding is the high variance, that is, high cycle-to-cycle fluctuations of the pool fire area. It was observed that in cycles with a small pool fire area (SPF), the pool fire tends to be swept away from the center and towards the piston surface. Figure 7.26 shows two exemplary cycles, once with a small and once with a large pool fire area (LPF). In the SPF cycle, the initial flame kernel first develops towards the right, which is mostly induced by the velocity field. Pool fire can be detected at 1 °CA. After the flame progresses

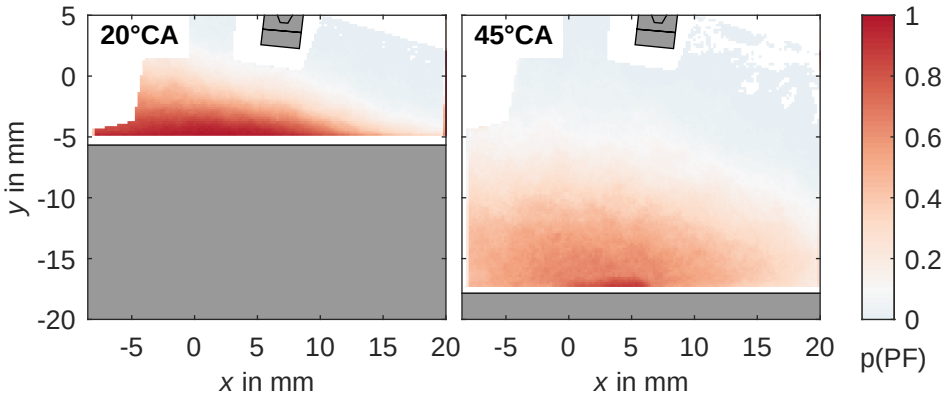


Figure 7.24: Pool fire probability maps of OP A cycle 2-10. The blank region in the top left is masked out due to reflections.

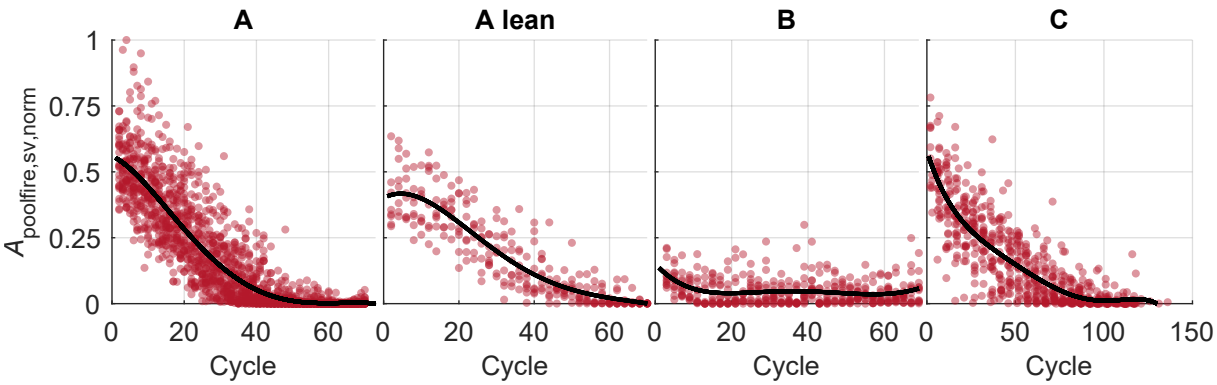


Figure 7.25: Pool fire occurrence. Binarized pool fire area (sideview) with respect to the fired cycle number. Fitted average shown in black.

to the cylinder center and the remaining fraction of the fuel combusts, the pool fire is convected to the right and pressed against the piston surface. This sudden acceleration could be a result of asymmetric combustion, in which the combustion rate and therefore the temperature expansion of the surrounding gas is not symmetric in all directions of the cylinder. In contrast, cycles with LPF tend to burn faster towards the center. Afterwards, the pool fire is observed to lift from the piston surface and then spread in a larger region, sometimes with higher overall intensities. The hypothesis is that convection of fuel rich regions towards and along the piston surface decreases the temperature experienced by the hydrocarbons and inhibits pyrolysis and soot formation and thereby minimizes the pool fire luminosity. To further analyze the relationships between the mixture and velocity field, flame development, and pool fire, the next sections will cover conditioned statistics and correlations.

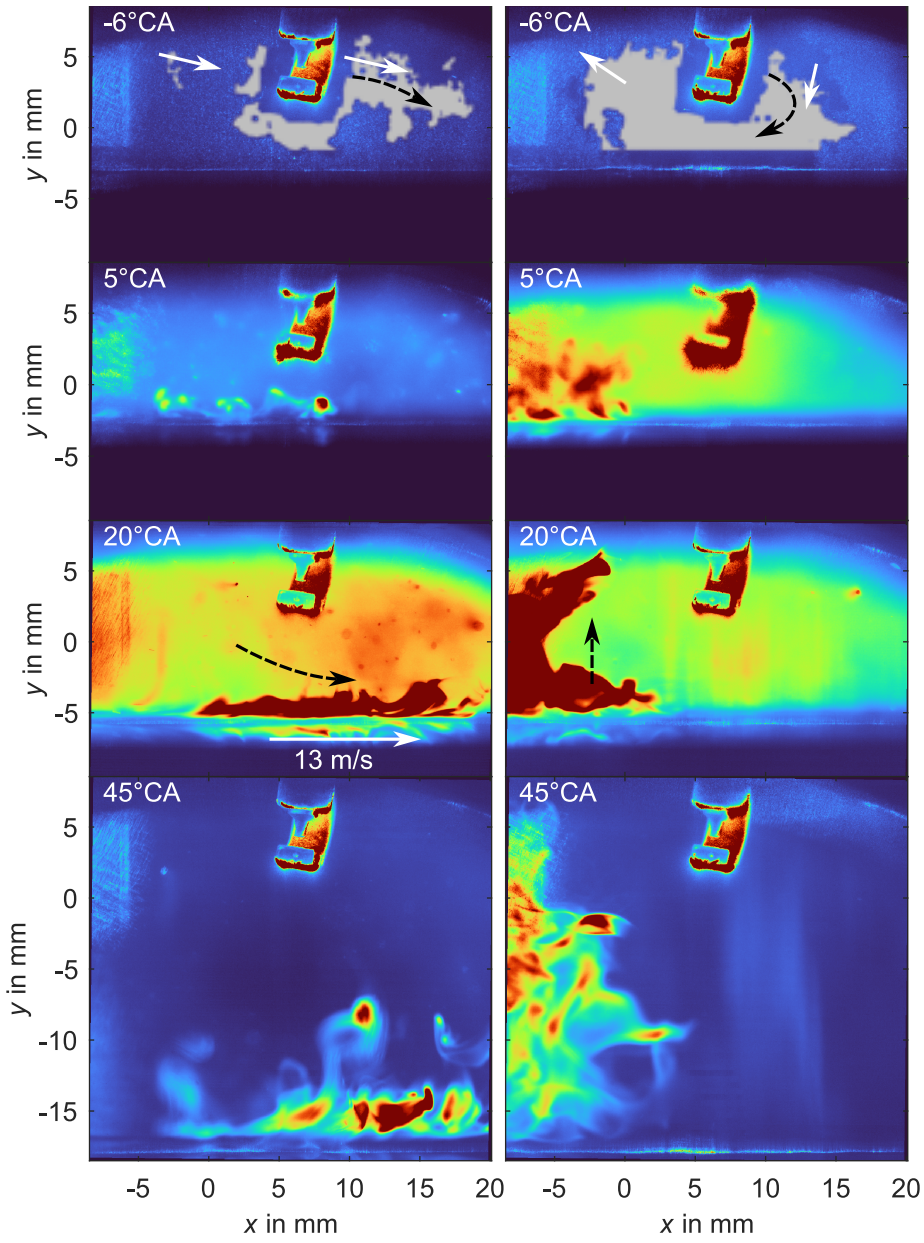


Figure 7.26: Conceptual comparison of two cycles with small (SPF, left) and large (LPF, right) pool fire (OP A, from cycles 1-10). False color images come from the PIV camera. Main velocity directions prior to ignition are indicated with white arrows at −6 °CA, while the black arrows shows the initial development of the flame (overlayed in gray). At 20 °CA, the movement of pool fire is indicated with black arrows.

### 7.3.4 Conditioned Statistics

Based on Fig. 7.25, samples (i.e. instantaneous cycles) were classified according to their pool fire area recorded by the sideview camera. After subtracting the polynomial fit representing a moving "average", samples from the first 10 fired cycles, with an area below the 0.15- and above the 0.85-quantile were selected and averaged[37, 38]. With this method, the fired cycle number (early or late) is not biased between the two groups. Figure 7.27 shows these conditioned phase-averages of OP A, with the small pool fire area subset (SPF) on the left and the large pool fire area subset (LPF) on the right. The sample size of both groups is 33 cycles.

Focusing on the velocity fields at ignition first, a clear difference can be observed between LPF and SPF cycles, whereby the latter exhibits a predominantly rightwards velocity around the spark plug and low magnitudes above the piston. In this region, LPF cycles feature a distinctively left-upwards flow. The acetone mixture field can be seen to change accordingly: rich regions extend farther away from the piston surface, as evaporating fuel is carried away. Furthermore, to the right of the spark plug, higher acetone mole fractions might stem from spray originally deflected towards the right and outside the FoV, which is now transported back. Still, the differences in the average mixture field appear to be comparatively minor.

A greater change can be observed for the development of the initial flame, which differs in both spatial extent and direction (Fig. 7.27): SPF flames in this plane are on average smaller, while LPF flames extend further to the left, towards the center of the combustion chamber. When quantifying the flame area growth, SPF cycles are delayed by 1 °CA compared to LPF cycles. This trend clearly correlates with the velocity field, as the spark plasma channel and initial flame kernel is convected in more or less favorable directions - or out of the measuring plane. Influencing variables on the combustion speed are the distance to the cylinder walls and spark plug geometry, which affects heat loss, as well as the local turbulence and equivalence ratio conditions. Thereby, the slightly richer mixtures found around the spark plug of LPF cycles could positively affect the flame growth, as the laminar flame speed typically peaks at fuel-air equivalence ratios above one [97, 191]. The susceptibility of the overall cycle performance to the early flame development has been documented in previous studies: Hanuschkin et al. [E89] found that the leftmost point of the flame in the tumble plane of OP C was sufficient to predict cycle performance in form of maximum cylinder pressure above chance using machine learning models. Therefore, the maximum cylinder pressure of both conditioned sets was analyzed. Due to the transient thermal conditions of the engine, the pressure was corrected by subtracting a moving average: $\Delta p_{\mathrm{cyl,max}} = p_{\mathrm{cyl,max}} - \mathrm{MovAvg}(p_{\mathrm{cyl,max}})$. However, the corresponding means and medians of the pressure deltas do not differ in a statistically significant level, as tested with a Two-Sample $t$-test[39], indicating that combustion speed

[37] Conditioned statistics were also calculated for cycles 35-45 and 65-85 for OP A and C, respectively. The trends were similar to the ones for cycle 1-10, such that only one group is presented here.

[38] The sideview camera only captures a 2D projection of 3D phenomena, but features the most complete FoV. Its pool fire area values are strongly correlated to ones from the PIV camera (OP A: Pearson's $r = 0.8$). The remaining spread between both systems is assumed to be from the smaller FoV of the PIV camera.

[39] At a significance level of $\alpha = 0.05$, calculated p-value $p = 0.059$.

and pool fires are not strongly correlated. In terms of time for mixing in the gas phase, the observed difference in combustion phasing is unlikely to have a significant impact.

In studies that measured evaporating gasoline-ethanol fuel films with refractive index matching on a piston glass, the films had a half life of 40 to 80 °CA [43, 44]. However, evaporation rates are highly dependent on wall temperatures (see e.g. [94, 118, 222]) and fuel volatility [222]. To investigate the evaporation characteristics, the LIF timing of OP C was varied (Fig. 7.28). Over the course of 4 °CA, the acetone mole fraction in the bulk flow and right-below the spark plug decreased slightly. The mole fraction peak in the histogram shifts by −0.2 %, while the acetone mole fraction in the near-wall region directly above the wall film is basically unchanged. All in all, it is concluded that the

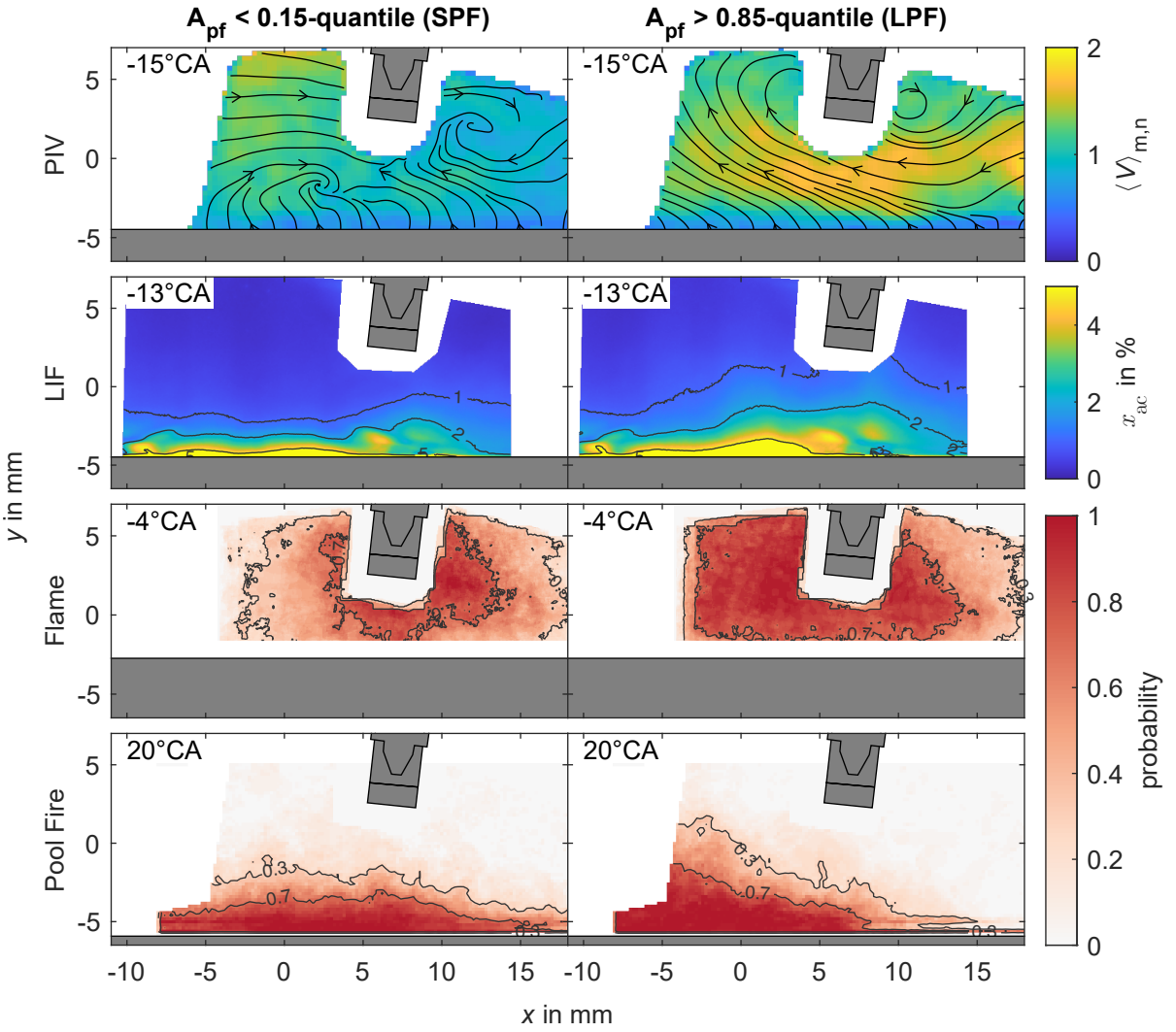


Figure 7.27: Conditioned phase-averages of different parameters of OP A, based on small (left) and large (right) pool fire area (sideview) in cycles 1-10. The velocity magnitude is normalized by the mean piston speed. Furthermore the acetone mole fraction and flame as well as pool fire probability maps are shown. Regions with $x \leq -5$ mm are partially masked out due to reflections.

1 °CA delay in combustion phasing for SPF compared to LPF cycles is unlikely to have a significant effect on the amount of acetone evaporated from the film and subsequent pool fire. Later fired cycles at higher wall temperatures are likely to be more sensitive, as the reduction in pool fire indicates more rapid and possibly complete evaporation of the film before spark ignition. For a more thorough analysis, additional measurements of the film footprint are needed.

Finally, the last panel of Fig. 7.27 shows pool fire probability maps acquired by the PIV camera. As a reminder: the data were conditioned to the pool fire area captured in a bigger FoV by the sideview camera. Pool fire of LPF cycles extends farther away from the piston surface and is located more towards the cylinder center, which is in line with the leftwards velocity at ignition.

The question remains as to what is causing the substantial increase (> 100 %, see Fig. 7.25) in (projected) pool fire area for LPF in comparison to SPF cycles at identical wall temperature levels. Soot production can be expected in regions with sufficiently high equivalence ratio and temperature. Studies report soot production for equivalence ratios of $\Phi \gtrsim 1.8$ with isooctane as fuel, which corresponds to a local acetone mole fraction of $x_{ac} \gtrsim 5\,\%$ in the current work, and temperatures >1500 K, [122] (see also Section 2.1.5). The LIF results show that such equivalence ratios are only reached in a thin layer above the wall film prior to combustion. In the burnt gas, temperatures are high enough to sustain pyrolysis and soot formation processes, though this is not the case inside the thermal boundary layer. In that sense, the conditioned data confirm the observation made for the two exemplary cycles in Fig. 7.26. In the derived hypothesis and conceptual model, pool fire is enhanced if a fuel rich mixture is transported by a stronger, turbulent flow into the bulk region. Since such a flow is accompanied with a stronger tumble, that is leftwards flow, a more symmetric combustion throughout the cylinder is achieved in the investigated engine and the remaining rich mixture experiences burnt-gas regions of sufficiently high temperatures. On the other hand, if low velocities are observed above the piston, distribution of acetone-rich mixture is less pronounced. Most importantly, resulting flames then typically develop dominantly to the right, leading to an asymmetric expansion of gases late in the combustion, which convects rich mixture to the right along and in the direction of the piston surface. Thereby, lower temperatures are encountered, which inhibit soot formation processes and/or visible soot incandescence, which ultimately decreases the (projected) pool fire area observed by the sideview camera. In

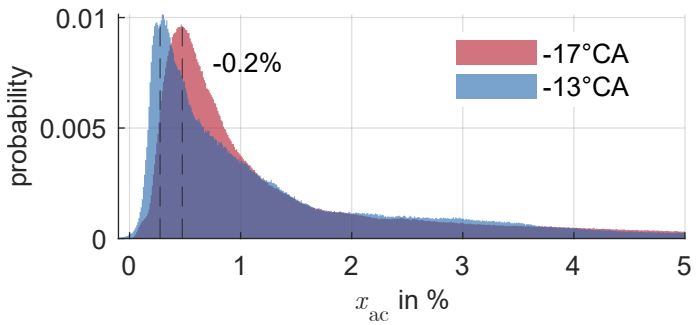


Figure 7.28: Acetone mole fraction of OP C at different CAD.

consequence, the emission of UHC should increase, which could be investigated in future measurements.

To finalize the discussion of conditioned data, in Fig. 7.29, conditioned averages of OP C are shown. The flow of LPF cycles is stronger leftwards oriented, which is similar to the results from OP A. Since the downwards component at $x = 0\,\text{mm}$ of SPF cycles is missing in LPF cycles, $x_{ac}$ seems to be increased at this position. Furthermore, mole fractions are significantly increased close to the piston around $x = 12\,\text{mm}$. The flame development seems to be similarly influenced by the flow: LPF cycles show a distinctively more leftwards progressed flame with a higher overall flame area. Compared to OP A, variations in flame size are more pronounced. This reflects in a statistically significant

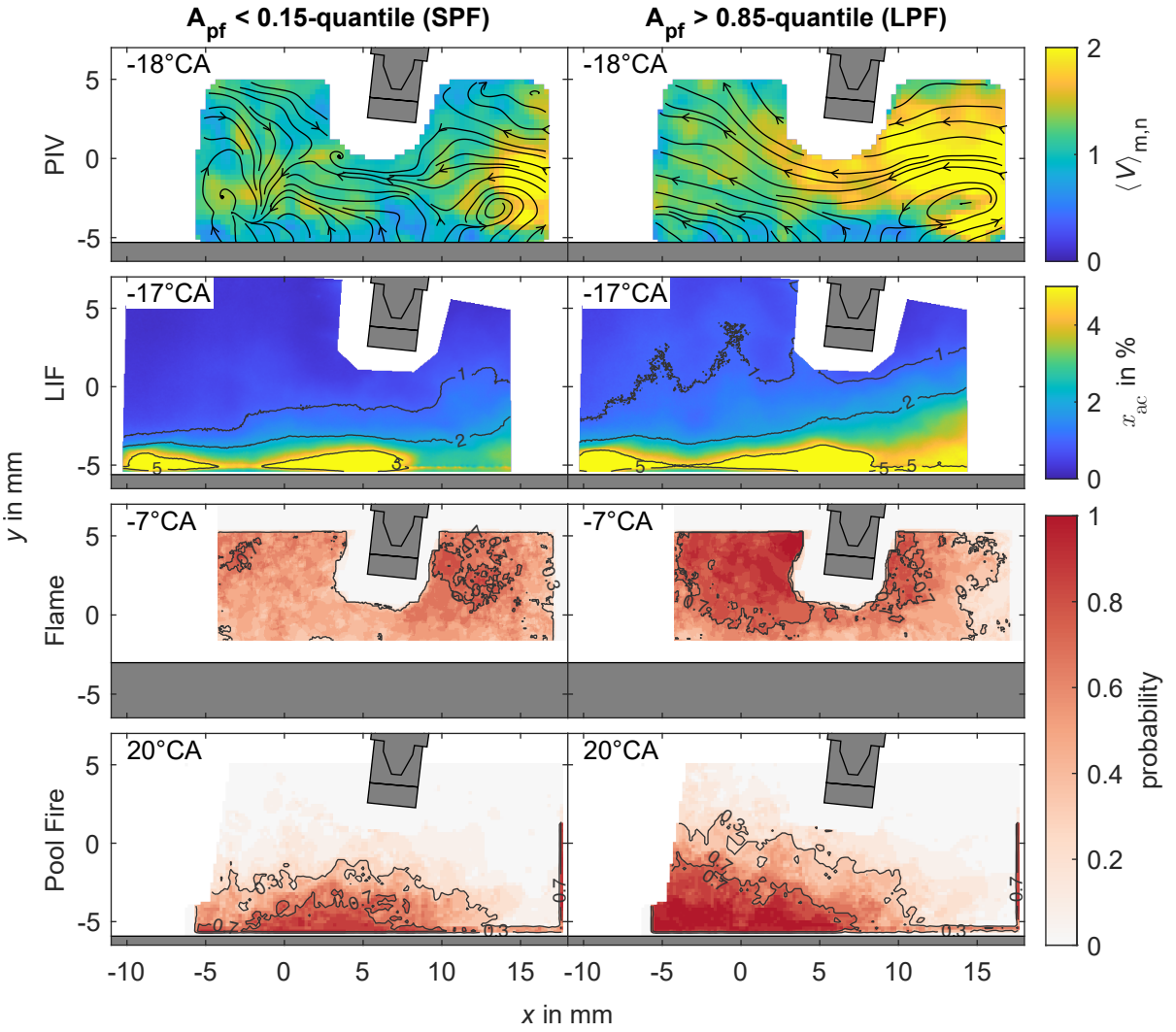


Figure 7.29: Conditioned phase-averages of different parameters of OP C, based on small (left) and large (right) pool fire area (sideview) in cycles 1-20. The velocity magnitude is normalized by the mean piston speed. Furthermore the acetone mole fraction (LIF) and flame as well as pool fire probability maps (PIV camera) are shown.

difference in the maximum cylinder pressure (not shown), as tested with a Two-Sample $t$-test[40]. The pool fire PDF itself shows trends similar to OP A, in that its peak is moved in LPF cycles towards the cylinder center and pool fire extends further away from the piston surface. It is noticeable that the higher mole fractions to the right of the FoV in LPF cycles do not correlate with a higher pool fire probability in that region, pointing towards the significance of the higher convection in the LPF set.

## 7.4 Correlations

Further insight might be gained by analyzing (linear) correlations between variables by means of Pearson's correlation coefficient $r_{ij}$. As shown in Fig. 7.30, the 2D data were divided in six stationary regions around the spark plug. Then, for each region, spatial averages of the selected variables were calculated and correlation coefficients between variables derived, once for fired cycles 1-20 (*first*) and once for cycles 50-70 (*last*). These region-wise averaged variables carry the superscript $^{\square}$. Table 7.3 gives an overview of the variables used.

Figure 7.31 shows heat maps of correlation coefficients for all four OP and different variable combinations. To obtain these values, non-significant correlations ($p \geq 0.05$) were removed and then absolute values of the correlation coefficients were averaged over regions and crank angles. The selected crank angles were from $-60\,°$CA to ignition for the velocity and for the flame area beginning with early flame development until burnt gas covers the field of view in most of the cycles. By taking the magnitude, significant correlations with different signs do not cancel each other out. An example is $V_x$, which typically correlates positively with the flame area to the right of the spark plug (positive velocities convect the flame to the right) and negatively to the left of the spark plug (negative velocities for a convection to the left and high flame areas there). The lower

[40]Significance level $\alpha = 0.05$, calculated p-value $p = 0.026$

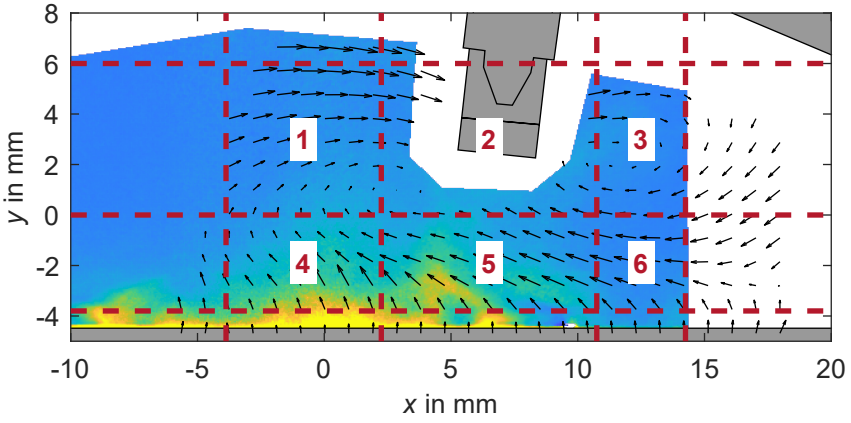


Figure 7.30: Definition of regions for correlation analysis. Exemplary LIF image (colormap) and velocity field (every third vector shown) of OP A.

Table 7.3: Variables used in the correlation analysis.

| Variable | Description | Measurement System | Global |
|---|---|---|---|
| $x_{ac}^{\square}$ | Acetone mole fraction | LIF | no |
| $A_{poolfire}^{\square}$ | Binarized pool fire area (small FoV) | PIV camera | no |
| $A_{flame}^{\square}$ | Binarized flame area | PIV camera | no |
| $p_{cyl,max}$ | Max. cylinder pressure per cycle | Indicating system | yes |
| $p_{cyl,max,rel}$ | Max. cylinder pressure per cycle, relative to moving average (global FoV) | Indicating system | yes |
| $\theta_{pcyl,max}$ | CAD of maximum cylinder pressure | Indicating system | yes |
| $A'_{poolfire,sv}$ | Binarized poolfire area, relative to moving average | Sideview camera | yes |
| $V_x^{\square}$ | $x$-component of velocity | PIV | no |
| $V_y^{\square}$ | $y$-component of velocity | PIV | no |

diagonal matrices show correlations of fired cycles 1-20 (*first*), the upper diagonal matrix of cycles 50-70 (*last*).

Several plausible correlations can be observed. First, both velocity components consistently correlate with the acetone mole fraction $x_{ac}^{\square}$ at values of $r \approx 0.4$. This fits previous observations, as the homogeneity of the mixture field is directly driven by the flow and for example large $V_y$ components transport acetone vapor away from the piston surface. In particular, the acetone mole fraction in far-wall regions 1-3 contribute to this correlation (not shown). No differences between *first* and *last* cycles exist. Second, higher correlations are found for the flame area $A_{flame}^{\square}$ and variables related to the cylinder pressure. This is not surprising, since a fast combustion will lead to earlier and higher pressure peaks in the cylinder.

Focusing on the (local) acetone mole fraction, correlations with the local flame area $A_{flame}^{\square}$ are rather weak, especially for OP A and B. In contrast, late cycles of OP A lean show values of up to 0.5. This is probably due to the higher sensitivity of the flame speed to the acetone concentration in the globally lean case. Intermediate correlations are found for the acetone mole fraction with the local pool fire area captured by the PIV camera $A_{poolfire}^{\square}$. In comparison, correlations with the sideview pool fire area $A'_{poolfire,sv}$ are consistently higher, since it captures the full in-cylinder volume. Again, no consistent difference between *first* and *last* cycles exist.

Another prominent, but spurious correlation exists between the moving-average-corrected pool fire area captured by the sideview camera $A'_{poolfire,sv}$ and the maximum cylinder pressure for OP B, reaching values of up to 0.66. In OP B, lower flame speeds due to the higher exhaust gas content[41] increase the variability of the combustion and lead to a greater coefficient of variation. Sometimes, combustion phasing is delayed by so much that the maximum cylinder pressure is reached due to the compression and combustion only adds a second peak in the expansion. This creates a spurious correlation.

[41]EGR is increased at part-load OPs due to backflow into the intake manifold.

Interestingly, $A'_{\text{poolfire,sv}}$ and the flame area show only intermediate correlations, with 0.31 and 0.39 for OP A and C, respectively. The pool fire area was used to define the groups of the conditional averages in the previous section, where a clear relationship between the flame and pool fire area was apparent (Fig. 7.27). To analyze this, Fig. 7.32 shows scatterplots of these two variables. Indeed, the relationship between both cannot be described by a linear equation. For both cases, the largest part of the data is seemingly uncorrelated and groups around a relative pool fire area of zero. The cycles selected for the SPF and LPF groups are highlighted by black borders. In these pool fire extremes, a more distinct pattern emerges: Large pool fire area cycles exhibit a faster combus-

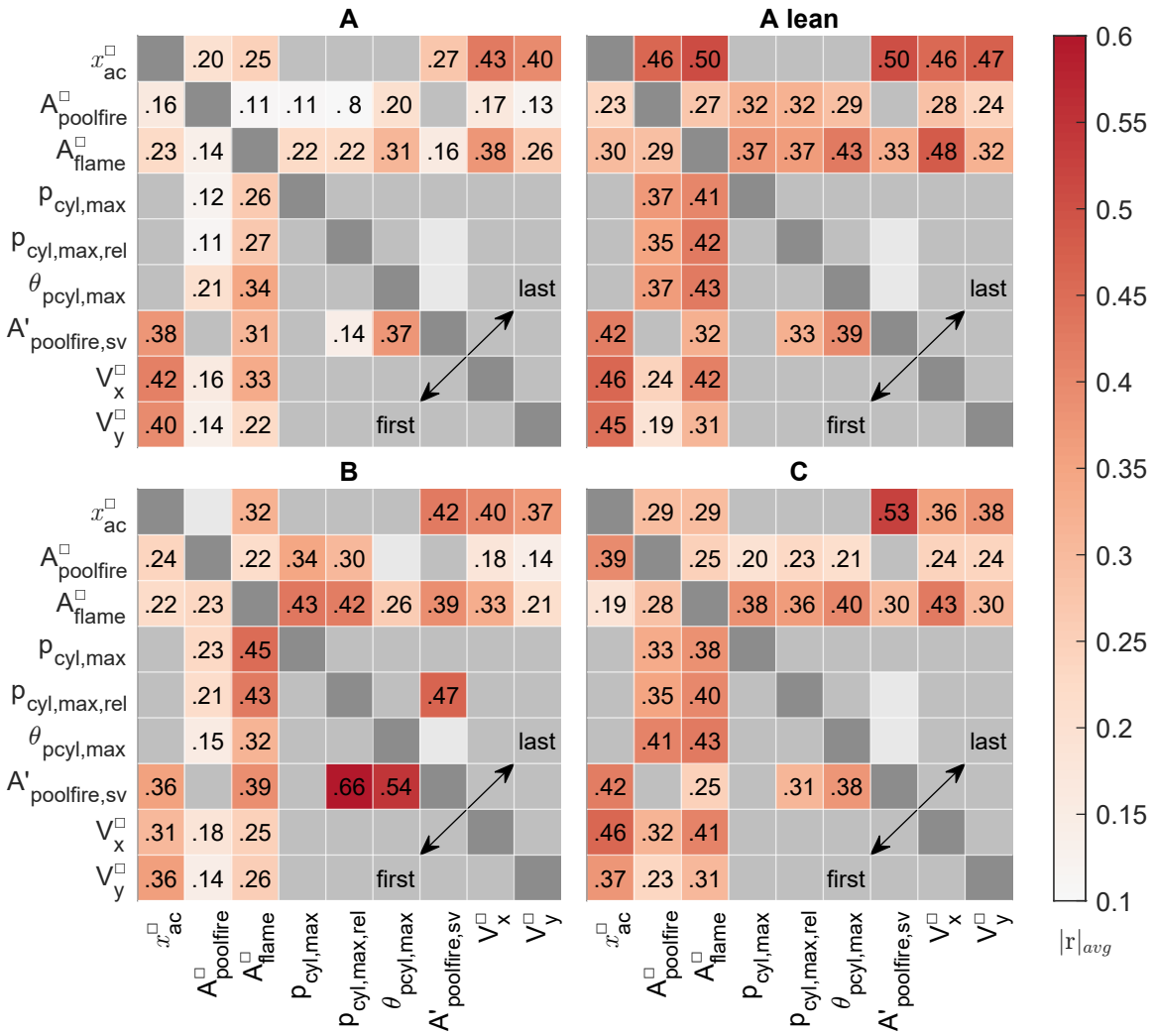


Figure 7.31: Pool fire correlation heat map. After taking the magnitude and removing non-significant correlations ($p \geq 0.05$), Pearson's correlation coefficients have been averaged over crank angles and the six regions. The lower diagonal matrix show correlations of fired cycles 1-20 (first), the upper diagonal matrix of cycles 50-70 (last). Values along the diagonal ($r = 1$) removed (dark gray), not-calculated values in intermediate gray, and values without a single significant correlation in light gray.

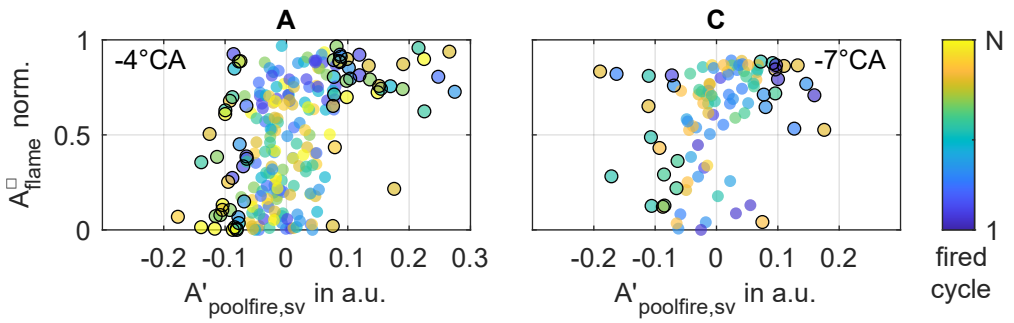


Figure 7.32: Relationship between flame area and relative pool fire area (sideview) for OP A and C. The flame area is evaluated in region 1 (Fig. 7.30) at the CAD shown in the corner. Cycles selected for the conditioned data are highlighted with black borders. Fired cycle number is indicated with the colormap (N = 10 and 20 for OP A and C, respectively).

tion with mostly large flame areas, while the small pool fire area cycles are distributed more homogeneously. This explains why the conditioned data show a distinct difference between the groups, which is significantly damped if the full dataset is included. It is obvious that linear correlations alone are not sufficient for a comprehensive description of a non-linear and multi-dimensional system. Conditioned statistics can therefore help to reveal further relationships between physical quantities.

### 7.4.1 Correlation Maps

Having found significant correlations for regionally-averaged variables, this section will cover spatially resolved correlation maps focusing on the comparison of OP A and A lean. Figure 7.33 shows the correlation of the local acetone mole fraction $x_{ac}(x,y)$ (at −13 °CA) with the flame area $A_{flame}$ (at −3 °CA), which here is a *global* value derived from the full, but still limited FoV of the PIV camera. There are extensive, positive correlations around the spark plug and towards the cylinder center. The correlations are higher for the lean case, with the difference increasing for *last* cycles compared to *first* cycles. This can be interpreted as evidence of the importance of the local equivalence ratio, as the flame speed in the lean regime is more sensitive to this ratio. To visualize the variables in the scatter plot of Fig. 7.33, the acetone mole fraction was averaged in a small region below the spark plug (dashed rectangle). As already indicated by the correlation map, the relationship between the two variables is more pronounced in the lean case. The flame tends to cover most of the FoV during the *last* cycles of OP A, which is visible in the asymptotically converging scatter plot. However, the presented results are insensitive to the crank angle of the flame area, indicating a minor effect of this FoV limit on the correlation.

Figure 7.34 shows the correlation of the mole fraction and the global pool fire area in the top panel. Correlations of similar spatial extent and value as between mole fraction and flame area are observed. The values are again higher for OP A lean, which likely implies a stronger influence of the local mixture on the flame speed. However, in the conditioned

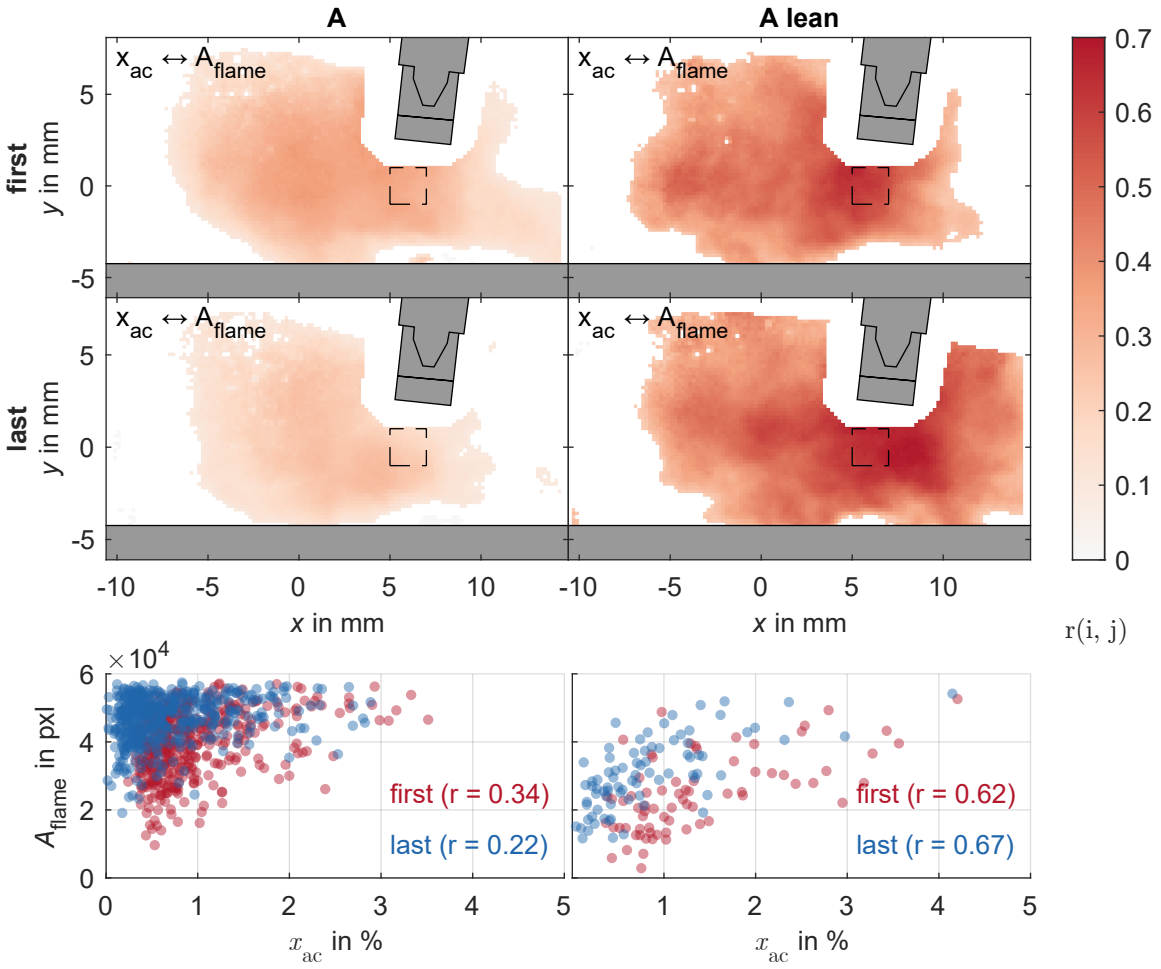


Figure 7.33: Spatially resolved correlation between the *global* flame area $A_{\text{flame}}$ at −3 °CA and the local acetone mole fraction $x_{\text{ac}}(x, y)$ at −13 °CA for *first* cycles 1-20 (top) and *last* cycles 50-69 (middle) of OP A and A lean. The RoI for the scatter plot in the bottom panel is marked with a dashed rectangle.

data presented in Section 7.3.4, it was hypothesized that in the cause-and-effect chain, the acetone mole fraction, flame, and pool fire are connected primarily indirectly through the velocity field. Thereby, stronger left-upwards velocities would both distribute acetone farther away from the piston and convect the flame into the cylinder center, which was found to favor pool fire. Even with the average velocity field being identical for OP A and A lean, the higher correlations for A lean do not prove a causal relationship between the local acetone mole fraction and pool fire. Instead, it could indicate a higher sensitivity of the combustion and subsequent pool fire processes to the flow field and convection, which in turn affects the mixture field. Likely, both the flow and local mixture play a role in flame development and pool fire. Another factor influencing the sensitivity of A lean with regard to pool fire is the higher relative oxygen content, which increases the proportion of complete combustion and inhibits soot production. Following this argument, more acetone will oxidize under lean operating conditions and a certain stratification of acetone-rich layers is needed to result in soot production and pool fire. Finally, the bot-

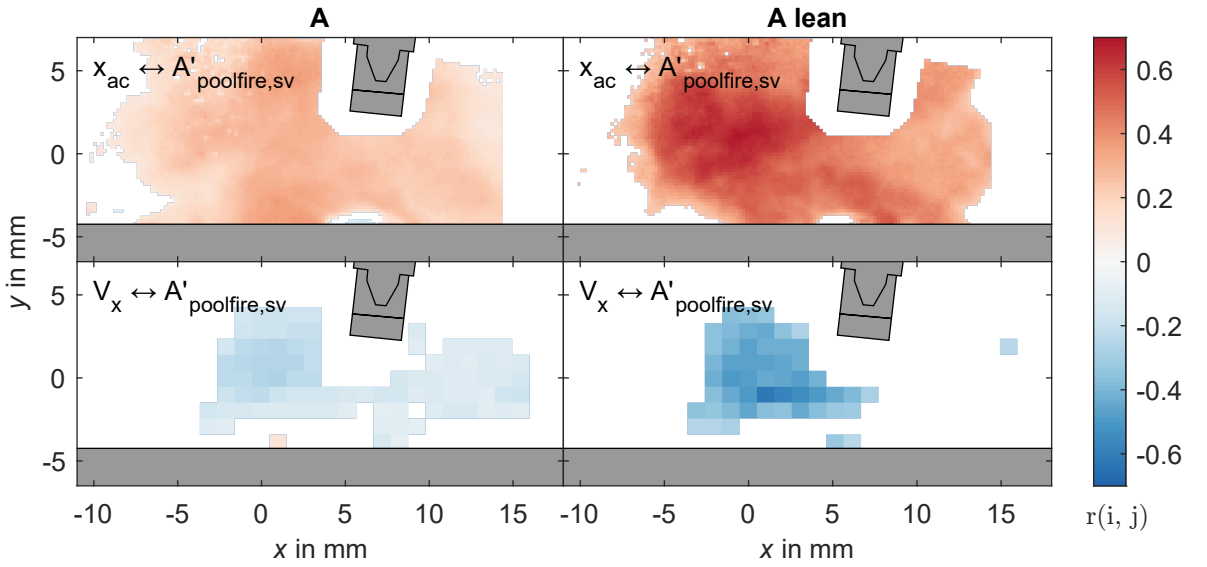


Figure 7.34: Spatially resolved and significant correlations of the acetone mole fraction $x_{ac}(x,y)$ (top) and $V_x$ (bottom), both at −13 °CA, with the global pool fire area $A'_{poolfire,sv}$ (sideview, moving-average subtracted). OP A and A lean are shown for cycles 50-69.

tom panel of Fig. 7.34 shows the correlation of the pool fire area with the velocity in the $x$-direction. Fitting to previous observations from the conditioned data, a leftwards flow correlates with a larger pool fire area in the full FoV. For OP A lean, higher correlation values are likewise observed.

**Multi-parameter correlation** Instead of pairwise analysis, a multidimensional comparison could help in analyzing the cause-and-effect chain. Figure 7.35 combines the velocity information, pool fire area, and acetone mole fraction of OP A and A lean in a polar scatter plot in order to show their underlying relationship. First, the global pool fire area relative to the moving average $A^{\square}_{poolfire}$ is shown on the radial axis, with the black circle signifying the average. Data inside the circle exhibit below average pool fires and vice versa. Second, the acetone mole fraction $x^{\square}_{ac}$ at −13 °CA in region 4 (Fig. 7.30) is represented by the colormap. Third, the piston-relative velocity $\vec{V}'^{\square}$ at −13 °CA in region 4 is given in two dimensions: The direction, that is, the angle with respect to the engine's $x$-axis is represented along the angular axis. As an example, a purely wall-parallel (piston-relative) velocity to the right appears at 0°, while a wall-perpendicular flow appears at 90°. Finally, the size (area) of each dot scales with the velocity magnitude.

There is a clear relationship between the velocity direction and the acetone mole fraction: The highest mole fractions are found when the flow is going to the left (≈ 180°). These cases also exhibit strong pool fire, which is also observed in the bottom panel of Fig. 7.34 by the negative correlation of $V_x$ with the poolfire area. On the other hand, a flow towards the right is associated with lower mole fractions and below average pool fire areas. This trend intensifies for later cycles and for OP A lean, where a rightwards flow leads exclusively to low pool fire areas and moderately low mole fractions. Interestingly,

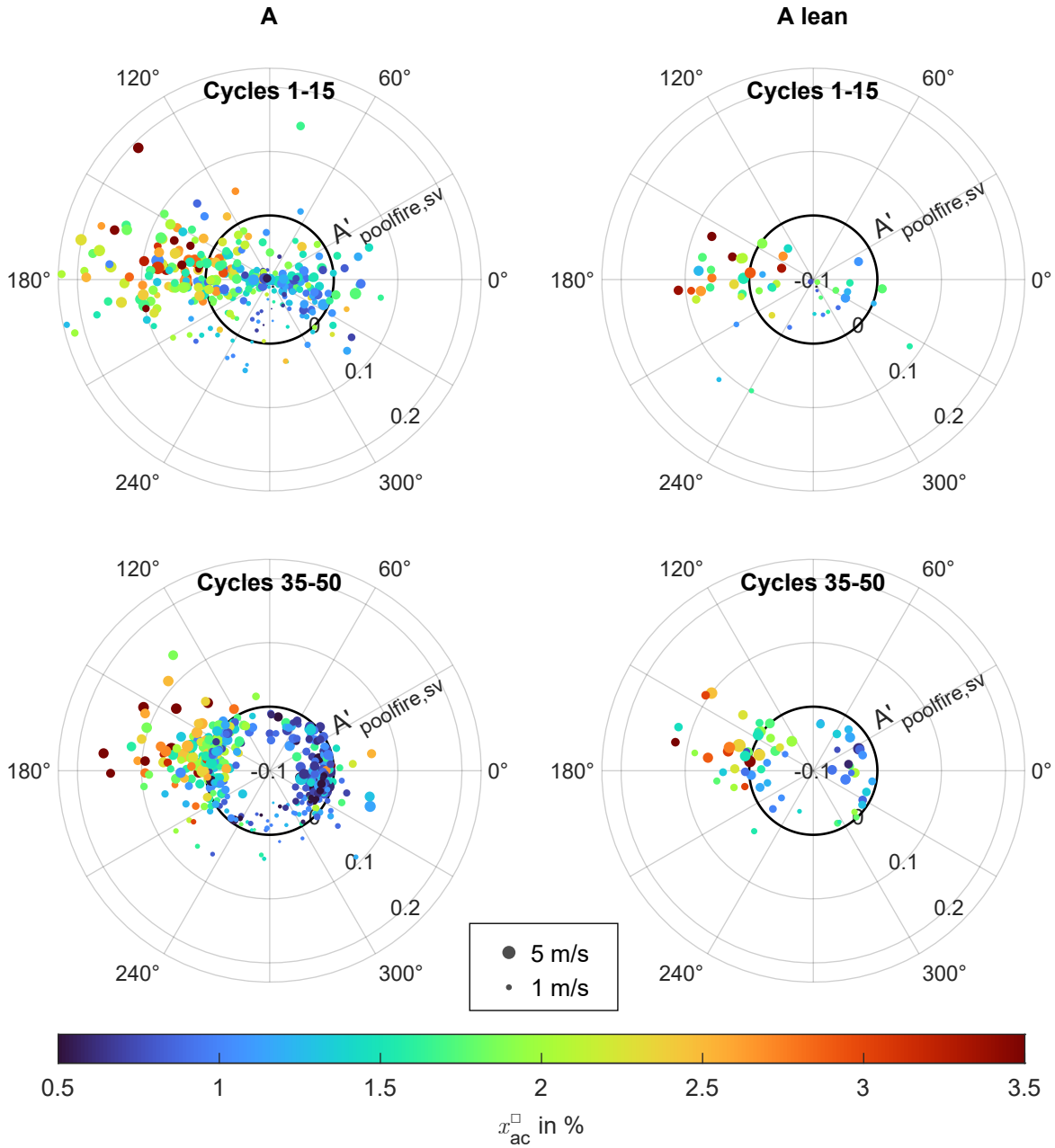


Figure 7.35: Polar scatter plot of the velocity, pool fire area, and acetone mole fraction. The relative global pool fire area $A'_{\text{poolfire,sv}}$ is shown on the radial axis, with the black circle signifying the value of the moving average ($\stackrel{\text{def}}{=} 0$; a value of $+0.1$ correspond to a pool fire area that is $+10\,\%$ of the FoV's area higher than the moving average). The colormap shows the acetone mole fraction $x_{\text{ac}}^{\square}$ in region 4 at $-13\,°\text{CA}$. The piston-relative velocity $\vec{V}'^{\square}$ in region 4 at $-13\,°\text{CA}$ is given with the direction (angle to the engine $x$-axis) represented along the angular axis, while the area of each dot scales with the velocity magnitude. OP A and A lean are shown for *first* (here 1-15) and *last* (here 35-50) cycles.

in later cycles, the velocity direction favoring pool fire shifts slightly upwards, away from the piston. The velocity magnitude seems to play a minor role, as the dot size is scattered quite homogeneously, besides the tendency that velocities towards the piston are weaker. Even though two variables in this analysis, namely velocity and acetone mole fraction, are evaluated in just a small region, there is a considerable degree of correlation.

In conclusion, the cause-and-effect chain between velocity, acetone mole fraction, and pool fire cannot be further differentiated with certainty. However, the relevance of the acetone mole fraction above the wall for later pool fire processes can be assessed with a comparison of OP A with A lean. In the latter case, both combustion and soot formation are more sensitive to the local equivalence ratio. However, the polar scatter plots show a similar relationship between the analyzed variables. Based on the similarity of the results for OP A and A lean it is hypothesized that the flow field is the primary factor in pool fire development. Thereby, the mixture field is influenced by the flow in the same way and thus only indirectly coupled to pool fire. This interpretation is consistent with the findings from the conditional averages and the formulated conceptual model, which emphasized the influence of the flow field on the flame development and the subsequent convection of soot precursors.

### 7.4.2 Summary

This chapter presented an investigation on fuel wall films and the development of *pool fire* during fired engine operation. Acetone was used as fuel and tracer for a single-hole direct injection during the late compression stroke, while most of the fuel was homogeneously supplied by PFI of isooctane. The near-wall mixture field was measured by employing acetone LIF with a single-line excitation at 315 nm, which was selected for its low temperature sensitivity based on results from a heated jet. Simultaneous HS PIV captured the velocity field in the tumble plane. Additionally, the flame and pool fire were visualized, the latter from two perspectives.

A basic characterization of the single-hole spray with its narrow plume was performed. The spray impinged on the piston, where a footprint was formed. It is assumed that this residue with a thickness of a few µm consists of cracked hydrocarbons. No definitive statement could be made about the regime of evaporation, though measured wall temperatures from Chapter 5 are above the Leidenfrost temperature. The effect of the DI on the velocity field was shown, as the flow above the piston is slowed down due to the spray momentum. Remaining flows from entrained air and shear layers were strongest for OP C, due to less time between the end of injection and spark ignition.

During the expansion stroke, orange pool fires emerged above the piston surface. These emissions originate from incandescent soot. A variation of the equivalence ratio and analysis of the heat release revealed that this soot is not formed in diffusion flames ([33, 140, 231]) but due to pyrolysis processes in fuel-rich zones of the (partially) burnt gas, which confirms the interpretation of Ketterer [126, 127]. Estimated in-cylinder temperatures during expansion were found to be high enough to warrant a visible soot glow.

Furthermore, the influence of wall temperatures was discussed, which increase from cycle to cycle during fired operation. As a consequence, vaporization rates increase, allowing more time for mixing with the bulk flow. In addition, the measured acetone mole fraction near the piston surface decreases, as the volume of the film shrinks. It was shown that pool fires cease to appear at sufficiently high wall temperatures, which was the case after 40-50 cycles for OP A and 70-80 cycles for OP C. Acetone mole fractions in the bulk flow were on average below 2 %, while higher mole fractions were typically only found in a region of up to 2 to 3 mm above the wall. In the current investigation, the minimum acetone mole fraction needed for the onset of soot formation is about 5 %, which limits the origin of pool fires to a small region above the wall film. Though the soot origin may be confined, pool fires were found to spread throughout the cylinder due to convection and ongoing gas expansion during combustion. This behavior was also found in more generic wind tunnel experiments [119].

Even at identical wall temperatures, the pool fire area was subject to strong CCV. Conditional averages based on the pool fire area revealed two distinct modes: A leftwards directed flow was accompanied by a slightly faster combustion, which was more centered in the cylinder. Additionally, more acetone was transported in the far-wall region. Pool fire was found to spread more vertically in this mode and expanded to larger than average areas. In comparison, a weaker flow reduced mixing and the speed of combustion. It was found that the early flame burnt to the right due to a rightwards directed flow at the spark plug. The following combustion was not centered in the cylinder and the asymmetric distribution of expanding gases led to a strong flow, which convected pool fire nests along the piston and into the colder temperature boundary layer. It is hypothesized that this inhibits soot formation processes and is the reason for the reduced pool fire intensity and area in this mode. Consequently, the emission of UHC should increase, which could be verified in future measurements.

In addition, linear correlations were analyzed. The velocity correlated strongly with the acetone mole fraction and flame area, at values of up to 0.48. Furthermore, the early flame development proved to be a good predictor for the peak cylinder pressure. Correlations were more pronounced for lean conditions and late fired cycles, since the film decreases in volume and the sensitivity of combustion to the flow and local equivalence ratio increases. In a spatially resolved analysis, significant correlations of the acetone mole fraction, flame and pool fire area, and velocity were found for an extensive region around the spark plug. These individual correlations were further supported by a multidimensional analysis.

# Chapter 8

# Summary and Outlook

## 8.1 Summary

Within the scope of this work, extensive experimental investigations were carried out using laser diagnostics in an optically accessible direct-injection spark-ignition engine. The focus was on near-processes, motivated by their influence on efficiency and pollutant formation as well as their complexity in accurate numerical modeling. In three campaigns, wall temperatures, the velocity boundary layer, and the formation of so-called *pool fires* were measured and analyzed. Aspects of particular novelty in this work are the characterization of flame-wall interactions inside the crevice, the resolution of the velocity boundary layer at technically relevant engine speeds and an analysis of their temporal-spatial variations, and a comprehensive description of mixing field, flow, combustion, and soot formation interactions. The main findings are summarized in the following paragraphs.

In Chapter 5, thermographic phosphors were applied to the cylinder head, piston top, and in the crevice. Wall temperatures in motored operation were found to be steady over cycles, with an increase of 5 to 10 K during compression and subsequent cooling back to its prior state. On the piston glass, temperatures of approximately 380 K exceeded the conditioning temperature by 50 K. Cylinder head and crevice temperatures were lower, at approximately 340 to 360 K, whereby the piston side temperature varied with vertical position. During fired operation, temperatures increased steadily, since the engine is not in thermal equilibrium. The greatest rise occurred during the first 50 cycles, with temperatures of 625 and 550 K being reached on the piston top for full- and part-load operation, respectively. During combustion, the flame was pushed into the crevice by expanding cylinder gases. Flame propagation itself was found to be limited in extent, as extinction occurred quickly. At a crevice depth of 55 mm, cycle-to-cycle variations (CCV) in the circumferential flame position led to cycle-intermittent wall temperature increases due to flame-wall interactions. Using the time-resolved temperature evolution, heat fluxes were estimated by assuming one-dimensional heat conduction. Peak heat fluxes in the crevice during motored operation were in the order of 0.1 and 1 $\mathrm{MW\,m^{-2}}$ for the cylinder glass and metallic piston side, respectively. During fired operation, up to 9 and 15 $\mathrm{MW\,m^{-2}}$ were measured on the metallic piston side for 800 and 1500 rpm, respectively, and approximately 1 $\mathrm{MW\,m^{-2}}$ on the piston and cylinder glass.

Using high-resolution particle tracking velocimetry (PTV), the phase-averaged velocity boundary layers during the late compression stroke at 2500 rpm were resolved down to the viscous sublayer (Chapter 6). For scaling in wall and semi-local units, wall temperatures from Chapter 5 were used. At 2500 rpm and 0.95 bar intake pressure, the viscous sublayer ($y^+ = 5$) was as thin as 30 µm. There was a strong overlap of the inner layer with the small outer layer, with the bulk flow starting at wall-scaled $y^+ = 30$-$90$. In an extension of previous studies, boundary layers at bulk Reynolds numbers of up to 100 000 showed no logarithmic layer, deviating from canonical channel flows but resembling those of impinging wall jets. This was shown in profiles of the velocity magnitude and fluctuations, which represent components of the Reynolds stress tensor. Due to a large number of acquired cycles, conditional averages could be evaluated. These revealed the influence of different flow modes, with strong acceleration and deceleration observed even in wall-parallel flows, and the horizontal position and temporal evolution determining the adherence to the law of the wall. For impinging flow modes, the degree of boundary layer development increased with the distance from the stagnation point, which is in notable similarity to classical channel flows.

In Chapter 7, a combination of optical diagnostics was applied to analyze processes in the presence of fuel wall films. During the compression phase, a wall film was deliberately created by injecting acetone with a single-hole injector, while most of the fuel was supplied homogeneously by port fuel injection (PFI) of isooctane. The near-wall mixture field was measured by single-line excitation laser-induced flourescence (LIF) at 315 nm, since the emission of acetone at this excitation wavelength has been shown to be sufficiently insensitive to temperature. Furthermore, simultaneous high-speed particle image velocimetry (PIV) was used to capture the velocity field and visualize the flame. Soot was visualized by natural luminosity imaging from two perspectives. To begin with, a characterization of the single-hole spray plume and the residue footprint was presented. The spray's momentum was shown to affect the velocity field by a slowing of the tumble and the appearance of recirculation zones. During the expansion stroke, the orange luminosity of pool fires was recorded. A variation of the equivalence ratio and analysis of the heat release revealed that this soot did not form in diffusion flames but due to pyrolysis processes in fuel-rich zones above the wall film. In the following, the term pool fire is still retained following popular convention and for consistency.

It was found that the pool fire's intensity decreased with increasing wall temperatures and consequently increasing evaporation rates during continuous fired operation. Similarly, the acetone mole fractions measured at spark timing above the film decreased. Due to the high volatility of acetone and strong increase of wall temperatures detailed in Chapter 5, pool fires ceased to appear after about 45 cycles for OP A and 75 cycles for OP C. Overall, measured acetone mole fractions in the bulk flow were below 2 % on average, with higher mole fractions of 5 to 10 % appearing only in the direct vicinity of the wall. Based on typical fuel-air equivalence ratios needed for soot production, pool fire formation is therefore limited to these near-wall regions. During the expansion stroke, however, soot is distributed throughout the cylinder due to the piston movement.

Significant CCV in the pool fire area at identical wall temperature were observed. Conditional averages based on the pool fire area revealed two modes: A flow towards the

cylinder center was accompanied by a slightly faster and more centered combustion. Pool fire was stronger in this case and spread more vertically throughout the expansion stroke. In contrast, the flame was burning preferentially to the right with weaker, rightwards-directed flows around the spark plug. Due to the non-centered combustion, an asymmetric expansion of in-cylinder gases followed, which led to a strong flow and convected pool fire nests along the piston. It was hypothesized that the reduced pool fire area in this mode is due to the prolonged contact with the colder temperature boundary layer, which in return, would reduce particle emissions but increase unburnt hydrocarbon (UHC) emissions.

An analysis of linear correlations revealed a strong relationship between the velocity field and the local acetone mole fraction as well as flame area. Correlations between the pool fire area, velocity, and acetone mole fraction were more pronounced for lean conditions, where the sensitivity of combustion to the flow and local equivalence ratio increases, and for higher wall temperatures, where the film vaporizes faster. Due to the complexity of the processes involved, no clear cause-and-effect chain could be derived, but it was hypothesized that in the investigated context, the flow field is the determining factor in soot formation processes. Thereby, the mixing field in the bulk flow is of lesser relevance than flame development and the overall combustion, which affects the temperature exposure of fuel-rich zones.

## 8.2 Technical Relevance

As outlined in Chapter 1, a number of technical improvements are necessary to meet future goals on reducing pollutant and greenhouse gas (GHG) emissions. These include higher compression ratios, downsizing, reduction of particle emissions, and advanced exhaust gas treatment. Thereby, detailed experiments and numerical simulations are complementary methods to improve the understanding of underlying physics and to aid the technical design. Wall temperatures are an important boundary condition not just for simulations, which typically have to reduce the system's complexity, for example by disregarding conjugate heat transfer. They are also key parameters for a number of processes such as film vaporization, flame quenching, and heat losses.

One technology currently being investigated to minimize heat losses is thermal barrier and thermal swing coatings [245]. However, their benefit in terms of thermodynamic efficiency has often been disappointing compared to theoretical expectations. Uchida [245] concluded that a detailed understanding and prediction of local and instantaneous transport and heat transfer processes is needed in order to optimize these technologies. As discussed in Chapter 5, boundary layers in engines do not adhere to wall laws derived from canonical flows, which limits the applicability of corresponding models. Therefore, efforts are needed to develop new models that capture non-equilibrium effects using physics- and data-informed approaches, as shown recently by Li et al. [149] and Bolla et al. [21].

Near-wall mixing and heat-transfer processes are important in the context of fuel wall films, as they dictate film vaporization and emission formation. The results presented in

Chapter 7 illustrate the complexity involved in these processes. Since future regulations will impose significantly stricter limits on the particle number in the exhaust, managing wall films and resulting emissions is particularly important in cold start conditions. The most effective approach in reducing particle emissions is to avoid wall wetting altogether, for example, through multi-hole sprays with high injection pressure and staggered injection schemes. However, preventing wall films will not always be possible. Next to the influence of the wall temperature, fuel properties are important in the spray formation and subsequent wall wetting and film vaporization. Therefore, additional research is needed for new low-carbon or carbon-neutral fuels such as biofuels and synthetic fuels. Additional complexity is added when the deposits on surfaces are considered. These introduce additional surface roughness, affecting the liquid contact angle and vaporization regime. An impact on the flow is also possible: Surface roughness was found to introduce secondary flows in the velocity boundary layer, a phenomenon called Prandtl's secondary flows of the second kind. This has previously been demonstrated only for generic channel flows, but in a study not presented here, Deyn et al. [E38] have shown that secondary flows also occur in the velocity boundary layer above artificial surface structures inside the engine. However, it is still an open question whether there is a noticeable effect on the macroscopic scales, such as on mixing rates and heat transfer. Another layer of complexity is added if thermal-swing coatings are considered. These lead to increased wall temperatures, which is advantageous for film vaporization, but also have a lower heat capacity than the metallic engine surface, which would affect vaporization-induced cooling of the wall. Furthermore, they may have a porous surface, which could act as a storage of liquid. Here, a detailed understanding of the underlying processes is necessary for technology development and application.

## 8.3 Outlook

Based on this first characterization of purposefully-placed wall films and subsequent processes, a number of follow-up investigations are of interest. In future work, measurements of the liquid spray footprint would be invaluable in assessing vaporization rates and the wall film's extent. Suitable optical diagnostics include measurements with refractive index matching [41, 93], LIF [77, 118], absorption [224], and thermographic phosphors [47]. In addition, fuels with different volatility could be investigated to allow generalization to multi-component fuels. Another aspect concerns the wall temperatures, which were shown to have a major effect on vaporization rates. Therefore, a metal piston with lower wall temperatures than the quartz piston window could be used. Finally, endoscopic measurements in a configuration with metallic cylinder liner would bridge the gap to realistic engine configurations. Furthermore, the external exhaust gas recirculation (EGR) could be varied to investigate the effect of lower oxygen concentrations and lower combustion temperatures, which was shown in a study by Koegl et al. [141] to either increase or reduce soot formation, depending on the fuel. These measurements could also be combined with a characterization of UHC and particle emissions, ideally time-resolved in the exhaust system or in-situ above the piston, for example, with laser absorption spectroscopy [39, 247]. To characterize pyrolysis processes and their influ-

ence on soot formation, PAH-LIF could be combined with LII [119]. This could verify the formulated hypothesis regarding the high variations in pool fire.

The deep crevice is a special feature of this optically accessible engine. Nevertheless, the crevice heat flux measurements in Chapter 5 indicated different penetration depths of the flame for different operating points. Further high-speed visualizations at different operating points would therefore allow a sensitivity study of flame extinction to the in-cylinder conditions.

Regarding macro- and microscopic flow phenomena, PIV measurements in a $z-y$-plane (vertical and perpendicular to the tumble plane) or $x-z$-plane (horizontal plane) could be used to detect the degeneration of the tumble flow into two separate swirl vortices, as it was predicted in a numerical study by Ding [45]. In an extension of boundary layer characterizations, PTV measurements further off-center than shown in this work could be attempted, to describe the influence of more extreme pressure gradients and flow separations. Furthermore, artificial roughness could be applied to analyze the influence of different surface finishes or deposits.

# Appendix A

## A.1 Permissions

### A.1.1 Elsevier - Proceedings of the Combustion Institute

Permission to use reuse content from [E214], which was used in Chapter 6:

# High-speed measurements and conditional analysis of boundary-layer flows at engine speeds up to 2500 rpm in a motored IC engine

Author: M. Schmidt,C. Welch,L. Illmann,A. Dreizler,B. Böhm

Publication: Proceedings of the Combustion Institute

Publisher: Elsevier

Date: Available online 24 September 2022

# DECLARATION ON THE CONTRIBUTION TO THE SCIENTIFIC PUBLICATION
## Erklärung zum Eigenanteil der wissenschaftlichen Veröffentlichung

Marius Schmidt, M.Sc.

### PAPER

**M. Schmidt**, C. Welch, L. Illmann, A. Dreizler, B. Böhm: High-speed measurements and conditional analysis of boundary-layer flows at engine speeds up to 2500 rpm in a motored IC engine. *Proceedings of the Combustion Institute*, 2022, https://doi.org/10.1016/j.proci.2022.07.199.

### CO-AUTHORS

Cooper Welch
Lars Illmann
Andreas Dreizler, Prof. Dr. habil.
Benjamin Böhm, Dr.-Ing.

### INDIVIDUAL CONTRIBUTIONS

- **Marius Schmidt**
  - Planned and lead the preparation of the experimental setup
  - Jointly conducted experiments with Lars Illmann and Cooper Welch
  - Developed code for processing and conducted analysis of the data
  - Main author of the paper: performed literature research, generated figures, wrote the initial manuscript, and wrote and managed the review process.
- **Cooper Welch and Lars Illmann**
  - Jointly conducted experiments with Marius Schmidt
  - Supported the interpretation and discussion of the results and the proofreading of the manuscript
- **Andreas Dreizler, and Benjamin Böhm**
  Provided resources for the conduction of the experiment. Supported in the planning, interpretation and discussion of the results and the proofreading of the manuscript.

### OVERALL CONTRIBUTION OF MARIUS SCHMIDT

A leading role in the conduction of the experiments. Code development, data analysis and interpretation, and writing of the manuscript.

This publication is not the subject of another ongoing or completed dissertation.

Marius Schmidt

Lars Illmann

Cooper Welch

Andreas Dreizler

Benjamin Böhm

# References


[1] C. Abram, B. Fond, and F. Beyrau. "Temperature measurement techniques for gas and liquid flows using thermographic phosphor tracer particles." In: *Progress in Energy and Combustion Science* 64 (2018), pp. 93–156. ISSN: 03601285. DOI: 10.1016/j.pecs.2017.09.001.

[2] R. J. Adrian and J. Westerweel. *Particle image velocimetry*. Vol. 30. Cambridge aerospace series. Cambridge: Cambridge Univ. Press, 2011. ISBN: 978-0521440080.

[3] M. Aldén, A. Omrane, M. Richter, and G. Särner. "Thermographic phosphors for thermometry: A survey of combustion applications." In: *Progress in Energy and Combustion Science* 37.4 (2011), pp. 422–461. ISSN: 03601285. DOI: 10.1016/j.pecs.2010.07.001.

[4] A. Y. Alharbi and V. Sick. "Investigation of boundary layers in internal combustion engines using a hybrid algorithm of high speed micro-PIV and PTV." In: *Experiments in Fluids* 49.4 (2010), pp. 949–959. ISSN: 0723-4864. DOI: 10.1007/s00348-010-0870-8.

[5] A. C. Alkidas. "Heat Transfer Characteristics of a Spark-Ignition Engine." In: *Journal of Heat Transfer* 102.2 (1980), pp. 189–193. ISSN: 0022-1481. DOI: 10.1115/1.3244258.

[6] A. C. Alkidas. "Combustion-chamber crevices: the major source of engine-out hydrocarbon emissions under fully warmed conditions." In: *Progress in Energy and Combustion Science* 25.3 (1999), pp. 253–273. ISSN: 03601285. DOI: 10.1016/S0360-1285(98)00026-4.

[7] S. W. Allison and G. T. Gillies. "Remote thermometry with thermographic phosphors: Instrumentation and applications." In: *The Review of scientific instruments* 68.7 (1997), pp. 2615–2650. ISSN: 0034-6748. DOI: 10.1063/1.1148174.

[8] M. K. Alzuabi, A. Wu, and V. Sick. "Experimental and numerical investigation of temperature fluctuations in the near-wall region of an optical reciprocating engine." In: *Proceedings of the Combustion Institute* 38.4 (2021), pp. 5879–5887. ISSN: 15407489. DOI: 10.1016/j.proci.2020.08.062.

[9] R. A. Antonia, M. Teitel, J. Kim, and L. W. B. Browne. "Low-Reynolds-number effects in a fully developed turbulent channel flow." In: *Journal of Fluid Mechanics* 236 (1992), pp. 579–605. ISSN: 0022-1120. DOI: 10.1017/s002211209200154x.

[10] E. Baum, B. Peterson, B. Böhm, and A. Dreizler. "On The Validation of LES Applied to Internal Combustion Engine Flows: Part 1: Comprehensive Experimental Database." In: *Flow, Turbulence and Combustion* 92.1-2 (2014), pp. 269–297. ISSN: 1386-6184. DOI: 10.1007/s10494-013-9468-6.

[11] E. Baum, B. Peterson, C. Surmann, D. Michaelis, B. Böhm, and A. Dreizler. "Investigation of the 3D flow field in an IC engine using tomographic PIV." In: *Proceedings of the Combustion Institute* 34.2 (2013), pp. 2903–2910. ISSN: 15407489. DOI: 10.1016/j.proci.2012.06.123.

[12] N. J. Beavis, W. Malalasekera, and S. S. Ibrahim. "A numerical study of intake valve jet flapping in a gasoline direct injection engine." In: *International Journal of Powertrains* 7.1/2/3 (2018), p. 38. ISSN: 1742-4267. DOI: 10.1504/IJPT.2018.10011445.

[13] T. Benzler. "Photo-physical characterization of aromatic compounds for laser-induced fluorescence based diagnostics of fuel concentration, temperature, and equivalence

ratio in practical combustion processes." PhD thesis. DuEPublico: Duisburg-Essen Publications online, University of Duisburg-Essen, Germany, 2019. DOI: 10.17185/DUEPUBLICO/70230.

[14] J. D. Bernardin and I. Mudawar. "The Leidenfrost Point: Experimental Study and Assessment of Existing Models." In: *Journal of Heat Transfer* 121.4 (1999), pp. 894–903. ISSN: 0022-1481. DOI: 10.1115/1.2826080.

[15] D. Bjerketvedt, J. R. Bakke, and K. van Wingerden. "Gas explosion handbook." In: *Journal of Hazardous Materials* 52.1 (1997), pp. 1–150. ISSN: 03043894. DOI: 10.1016/S0304-3894(97)81620-2.

[16] G. Blasse and B. C. Grabmaier. *Luminescent materials*. Berlin, Germany: Springer-Verlag, 1994. ISBN: 9783642790171. URL: https://ebookcentral.proquest.com/lib/kxp/detail.action?docID=3095698.

[17] G. Blasse, B. C. Grabmaier, and M. Ostertag. "The afterglow mechanism of chromium-doped gadolinium gallium garnet." In: *Journal of Alloys and Compounds* 200.1-2 (1993), pp. 17–18. ISSN: 09258388. DOI: 10.1016/0925-8388(93)90464-X.

[18] T. Blotevogel, M. Hartmann, H. Rottengruber, and A. Leipertz. "Tracer-based laser-induced fluorescence measurement technique for quantitative fuel/air-ratio measurements in a hydrogen internal combustion engine." In: *Applied Optics* 47.35 (2008), pp. 6488–6496. ISSN: 1559-128X. DOI: 10.1364/AO.47.006488.

[19] P. von Böckh and T. Wetzel, eds. *Wärmeübertragung*. Berlin, Heidelberg: Springer Berlin Heidelberg, 2014. ISBN: 978-3-642-37730-3. DOI: 10.1007/978-3-642-37731-0.

[20] H. Böhm, D. Hesse, H. Jander, B. Lüers, J. Pietscher, H. Wagner, and M. Weiss. "The influence of pressure and temperature on soot formation in premixed flames." In: *Symposium (International) on Combustion* 22.1 (1989), pp. 403–411. ISSN: 00820784. DOI: 10.1016/s0082-0784(89)80047-5.

[21] M. Bolla, M. Impagnatiello, K. Keskinen, G. Giannakopoulos, C. E. Frouzakis, Y. M. Wright, and K. Boulouchos. "Development of an algebraic wall heat transfer model for LES in IC engines using DNS data." In: *Proceedings of the Combustion Institute* 38.4 (2021), pp. 5811–5819. ISSN: 15407489. DOI: 10.1016/j.proci.2020.06.273.

[22] J. Borée and P. C. Miles. "In-Cylinder Flow." In: *Encyclopedia of Automotive Engineering*. John Wiley & Sons, Ltd, 2014. ISBN: 9781118354179. DOI: 10.1002/9781118354179.auto119.

[23] A. Brenner, T. Eichenlaub, P. Gehringer, J. Müller, V. Rezanov, and N. Schmidt-Rose. "Anwendung und Vergleich von 0D- und 1D-Simulationen an einem optisch zugänglichen Ottomotor." Advanced Research Project. Darmstadt: Technical University of Darmstadt, 2016.

[24] J. Brübach, C. Pflitsch, A. Dreizler, and B. Atakan. "On surface temperature measurements with thermographic phosphors: A review." In: *Progress in Energy and Combustion Science* 39.1 (2013), pp. 37–60. ISSN: 03601285. DOI: 10.1016/j.pecs.2012.06.001.

[25] S. Buhl, D. Hain, F. Hartmann, and C. Hasse. "A comparative study of intake and exhaust port modeling strategies for scale-resolving engine simulations." In: *International Journal of Engine Research* 19.3 (2018), pp. 282–292. ISSN: 1468-0874. DOI: 10.1177/1468087417707452.

[26] S. Bürkle, L. Biondo, C.-P. Ding, R. Honza, V. Ebert, B. Böhm, and S. Wagner. "In-Cylinder Temperature Measurements in a Motored IC Engine using TDLAS." In: *Flow, Turbulence and Combustion* (2018). ISSN: 1386-6184. DOI: 10.1007/s10494-017-9886-y.

[27] S. Campbell, E. Clasen, C. Chang, and K. T. Rhee. “Flames and Liquid Fuel in an SI Engine Cylinder During Cold Start.” In: *International Fuels & Lubricants Meeting & Exposition*. SAE International, 1996. DOI: 10.4271/961153.

[28] M. D. Chambers and D. R. Clarke. “Doped Oxides for High-Temperature Luminescence and Lifetime Thermometry.” In: *Annual Review of Materials Research* 39.1 (2009), pp. 325–359. ISSN: 1531-7331. DOI: 10.1146/annurev-matsci-112408-125237.

[29] B. H. Cheung. “Laser-Induced Fluorescence Diagnostics: Quantitative Photophysics and Time-Resolved Imaging.” PhD-Thesis. Stanford University, 2011. URL: https://stacks.stanford.edu/file/druid:mk228rf5946/Submission-augmented.pdf.

[30] B. H. Cheung and R. K. Hanson. “3-pentanone fluorescence yield measurements and modeling at elevated temperatures and pressures.” In: *Applied Physics B* 106.3 (2012), pp. 755–768. ISSN: 1432-0649. DOI: 10.1007/s00340-012-4901-4.

[31] V. S. Costanzo. “Effect of in-cylinder liquid fuel films on engine-out unburned hydrocarbon emissions for SI engines.” PhD thesis. Massachusetts: Massachusetts Institute of Technology, 2011. URL: http://hdl.handle.net/1721.1/65276.

[32] Council of the European Union. *‘Fit for 55’: Council adopts regulation on CO2 emissions for new cars and vans*. 28.03.2023. URL: https://www.consilium.europa.eu/en/press/press-releases/2023/03/28/fit-for-55-council-adopts-regulation-on-co2-emissions-for-new-cars-and-vans/.

[33] P. Dahlander, R. Babayev, S. Ravi Kumar, S. Etikyala, and L. Koopmans. “Particulates in a GDI Engine and Their Relation to Wall-Film and Mixing Quality.” In: *SAE Technical Paper Series*. SAE Technical Paper Series. SAE International400 Commonwealth Drive, Warrendale, PA, United States, 2022. DOI: 10.4271/2022-01-0430.

[34] M. Davy, P. Williams, D. Han, and R. Steeper. “Evaporation characteristics of the 3-pentanone–isooctane binary system.” In: *Experiments in Fluids* 35.1 (2003), pp. 92–99. ISSN: 0723-4864. DOI: 10.1007/s00348-003-0639-4.

[35] K. Dejima and O. Nakabeppu. “Local instantaneous heat flux measurements in an internal combustion engine using a MEMS sensor.” In: *Applied Thermal Engineering* 201 (2022), p. 117747. ISSN: 13594311. DOI: 10.1016/j.applthermaleng.2021.117747.

[36] K. Dejima, O. Nakabeppu, Y. Nakamura, T. Tsuchiya, and K. Nagasaka. “Three-point MEMS heat flux sensor for turbulent heat transfer measurement in internal combustion engines.” In: *International Journal of Engine Research* 20.7 (2019), pp. 696–705. ISSN: 1468-0874. DOI: 10.1177/1468087418770308.

[37] W. Demtröder. *Atome, Moleküle und Festkörper*. 5., neu bearbeitete und aktualisierte Auflage. Vol. 3. Springer-Lehrbuch. Berlin and Heidelberg: Springer Spektrum, 2016. ISBN: 978-3-662-49093-8. DOI: 10.1007/978-3-662-49094-5.

[39] O. Diemel, R. Honza, C.-P. Ding, B. Böhm, and S. Wagner. “In situ sensor for cycle-resolved measurement of temperature and mole fractions in IC engine exhaust gases.” In: *Proceedings of the Combustion Institute* 37.2 (2019), pp. 1453–1460. ISSN: 15407489. DOI: 10.1016/j.proci.2018.06.182.

[41] C.-P. Ding. *Wandnahe Interaktion von Strömung und Flamme in einem Ottomotor*. Norderstedt: Books on Demand, 2018. ISBN: 978-3-7481-2855-7.

[42] C.-P. Ding, R. Honza, B. Böhm, and A. Dreizler. ““Simultaneous measurement of flame impingement and piston surface temperatures in an optically accessible spark ignition engine”.” In: *Applied Physics B* 123.4 (2017), p. 110. ISSN: 1432-0649. DOI: 10.1007/s00340-017-6694-y. URL: http://dx.doi.org/10.1007/s00340-017-6694-y.

[43] C.-P. Ding, M. Sjöberg, D. Vuilleumier, D. L. Reuss, X. He, and B. Böhm. “Fuel film thickness measurements using refractive index matching in a stratified-charge SI en-

gine operated on E30 and alkylate fuels." In: *Experiments in Fluids* 59.3 (2018), p. 133. ISSN: 0723-4864. DOI: 10.1007/s00348-018-2512-5.

[44] C.-P. Ding, D. Vuilleumier, N. Kim, D. L. Reuss, M. Sjöberg, and B. Böhm. "Effect of engine conditions and injection timing on piston-top fuel films for stratified direct-injection spark-ignition operation using E30." In: *International Journal of Engine Research* 21.2 (2020), pp. 302–318. ISSN: 1468-0874. DOI: 10.1177/1468087419869785.

[45] Z. Ding. "Large-eddy simulation and spatio-temporal analysis of internal engine aerodynamics." PhD. Thesis. Université d'Orléans, 2022. URL: https://theses.hal.science/tel-03966527.

[47] P. Dragomirov, A. Mendieta, C. Abram, B. Fond, and F. Beyrau. "Planar measurements of spray-induced wall cooling using phosphor thermometry." In: *Experiments in Fluids* 59.3 (2018). ISSN: 0723-4864. DOI: 10.1007/s00348-017-2480-1.

[48] M. C. Drake, T. D. Fansler, A. S. Solomon, and G. A. Szekely. "Piston Fuel Films as a Source of Smoke and Hydrocarbon Emissions from a Wall-Controlled Spark-Ignited Direct-Injection Engine." In: *SAE Technical Paper Series*. SAE Technical Paper Series. SAE International400 Commonwealth Drive, Warrendale, PA, United States, 2003. DOI: 10.4271/2003-01-0547.

[49] J. W. Draper. "LIV. On the production of light by heat." In: *The London, Edinburgh, and Dublin Philosophical Magazine and Journal of Science* 30.202 (1847), pp. 345–360. ISSN: 1941-5982. DOI: 10.1080/14786444708647190.

[51] S. Einecke, C. Schulz, and V. Sick. "Measurement of temperature, fuel concentration and equivalence ratio fields using tracer LIF in IC engine combustion." In: *Applied Physics B* 71.5 (2000), pp. 717–723. ISSN: 1432-0649. DOI: 10.1007/s003400000383.

[52] M. Elstner. *Physikalische Chemie II: Quantenmechanik und Spektroskopie*. Berlin, Heidelberg: Springer Berlin Heidelberg, 2021. ISBN: 978-3-662-61461-7. DOI: 10.1007/978-3-662-61462-4.

[54] Engine Combustion Network. *Engine Combustion Network*. 22.04.2023. URL: https://ecn.sandia.gov/.

[55] Engineering ToolBox. *Gases - Explosion and Flammability Concentration Limits*. URL: https://www.engineeringtoolbox.com/explosive-concentration-limits-d_423.html.

[56] D. Escofet-Martin, A. O. Ojo, N. T. Mecker, M. A. Linne, and B. Peterson. "Simultaneous 1D hybrid fs/ps rotational CARS, phosphor thermometry, and CH* imaging to study transient near-wall heat transfer processes." In: *Proceedings of the Combustion Institute* 38.1 (2021), pp. 1579–1587. ISSN: 15407489. DOI: 10.1016/j.proci.2020.06.097.

[57] European Comission. *Proposal for Euro 7*. 10.11.2022.

[58] M. A. Everest and D. B. Atkinson. "Discrete sums for the rapid determination of exponential decay constants." In: *The Review of scientific instruments* 79.2 Pt 1 (2008), p. 023108. ISSN: 0034-6748. DOI: 10.1063/1.2839918.

[59] C. Fach, N. Rödel, J. Schorr, C. Krüger, A. Dreizler, and B. Böhm. "Multi-parameter imaging of in-cylinder processes during transient engine operation for the investigation of soot formation." In: *International Journal of Engine Research* 23.9 (2022), pp. 1573–1585. ISSN: 1468-0874. DOI: 10.1177/14680874211019976.

[60] C. Fach, N. Rödel, J. Schorr, C. Krüger, A. Dreizler, and B. Böhm. "Investigation of in-cylinder soot formation in a DISI engine during transient operation by simultaneous endoscopic PIV and flame imaging." In: *International Journal of Engine Research* 24.3 (2023), pp. 1175–1189. ISSN: 1468-0874. DOI: 10.1177/14680874221079764.

[61] S. Faust, T. Dreier, and C. Schulz. “Photo-physical properties of anisole: temperature, pressure, and bath gas composition dependence of fluorescence spectra and lifetimes.” In: *Applied Physics B* 112.2 (2013), pp. 203–213. ISSN: 1432-0649. DOI: 10.1007/s00340-013-5420-7.

[62] S. Faust, M. Goschütz, S. A. Kaiser, T. Dreier, and C. Schulz. “A comparison of selected organic tracers for quantitative scalar imaging in the gas phase via laser-induced fluorescence.” In: *Applied Physics B* 117.1 (2014), pp. 183–194. ISSN: 1432-0649. DOI: 10.1007/s00340-014-5818-x.

[63] B. Fond, C. Abram, A. L. Heyes, A. M. Kempf, and F. Beyrau. “Simultaneous temperature, mixture fraction and velocity imaging in turbulent flows using thermographic phosphor tracer particles.” In: *Optics express* 20.20 (2012), pp. 22118–22133. DOI: 10.1364/OE.20.022118.

[64] D. E. Foster and P. O. Witze. “Velocity Measurements in the Wall Boundary Layer of a Spark-Ignited Research Engine.” In: *SAE Technical Paper Series*. SAE Technical Paper Series. SAE International400 Commonwealth Drive, Warrendale, PA, United States, 1987. DOI: 10.4271/872105.

[65] D. Freudenhammer, B. Peterson, C.-P. Ding, B. Boehm, and S. Grundmann. “The Influence of Cylinder Head Geometry Variations on the Volumetric Intake Flow Captured by Magnetic Resonance Velocimetry.” In: *SAE International Journal of Engines* 8.4 (2015). ISSN: 1946-3944. DOI: 10.4271/2015-01-1697.

[66] D. Frieden, V. Sick, J. Gronki, and C. Schulz. “Quantitative oxygen imaging in an engine.” In: *Applied Physics B* 75.1 (2002), pp. 137–141. ISSN: 1432-0649. DOI: 10.1007/s00340-002-0992-7.

[67] R. Friedman and W. C. Johnston. “The Wall–Quenching of Laminar Propane Flames as a Function of Pressure, Temperature, and Air–Fuel Ratio.” In: *Journal of Applied Physics* 21.8 (1950), pp. 791–795. ISSN: 0021-8979. DOI: 10.1063/1.1699760.

[68] W. Friedrich, R. Grzeszik, and M. Wensing. “Mixture Formation in a CNG-DI Engine in Stratified Operation.” In: *SAE Technical Paper Series*. SAE Technical Paper Series. SAE International400 Commonwealth Drive, Warrendale, PA, United States, 2015. DOI: 10.4271/2015-24-2474.

[69] A. P. Fröba, F. Rabenstein, K.-U. Münch, and A. Leipertz. “Mixture of triethylamine (TEA) and benzene as a new seeding material for the quantitative two-dimensional laser-induced exciplex fluorescence imaging of vapor and liquid fuel inside SI engines.” In: *Combustion and Flame* 112.1-2 (1998), pp. 199–209. ISSN: 00102180. DOI: 10.1016/S0010-2180(97)81768-3.

[70] N. Fuhrmann, J. Brübach, and A. Dreizler. “Phosphor thermometry: A comparison of the luminescence lifetime and the intensity ratio approach.” In: *Proceedings of the Combustion Institute* 34.2 (2013), pp. 3611–3618. ISSN: 15407489. DOI: 10.1016/j.proci.2012.06.084.

[71] N. Fuhrmann, J. Brübach, and A. Dreizler. “On the mono-exponential fitting of phosphorescence decays.” In: *Applied Physics B* 116.2 (2014), pp. 359–369. ISSN: 1432-0649. DOI: 10.1007/s00340-013-5700-2.

[72] N. Fuhrmann, T. Kissel, A. Dreizler, and J. Brübach. “Gd 3 Ga 5 O 12: Cr—a phosphor for two-dimensional thermometry in internal combustion engines.” In: *Measurement Science and Technology* 22.4 (2011), p. 45301. ISSN: 0957-0233. DOI: 10.1088/0957-0233/22/4/045301.

[73] N. Fuhrmann, C. Litterscheid, C.-P. Ding, J. Brübach, B. Albert, and A. Dreizler. “Cylinder head temperature determination using high-speed phosphor thermometry in a

fired internal combustion engine." In: *Applied Physics B* 116.2 (2014), pp. 293–303. ISSN: 1432-0649. DOI: 10.1007/s00340-013-5690-0.

[74] N. Fuhrmann, M. Schild, D. Bensing, S. A. Kaiser, C. Schulz, J. Brübach, and A. Dreizler. "Two-dimensional cycle-resolved exhaust valve temperature measurements in an optically accessible internal combustion engine using thermographic phosphors." In: *Applied Physics B* 106.4 (2012), pp. 945–951. ISSN: 0946-2171. DOI: 10.1007/s00340-011-4819-2.

[75] N. Fuhrmann, M. Schneider, C.-P. Ding, J. Brübach, and A. Dreizler. "Two-dimensional surface temperature diagnostics in a full-metal engine using thermographic phosphors." In: *Measurement Science and Technology* 24.9 (2013), p. 95203. ISSN: 0957-0233. DOI: 10.1088/0957-0233/24/9/095203.

[76] N. Fuhrmann. *Phosphor Thermometrie zur Bestimmung von Oberflächentemperaturen in Verbrennungsmotoren: Zugl.: Darmstadt, Techn. Univ., Diss., 2013*. Messtechnik und Sensorik. Aachen: Shaker, 2013. ISBN: 978-3-8440-1975-9.

[77] J. N. Geiler, R. Grzeszik, S. Quaing, A. Manz, and S. A. Kaiser. "Development of laser-induced fluorescence to quantify in-cylinder fuel wall films." In: *International Journal of Engine Research* 19.1 (2018), pp. 134–147. ISSN: 1468-0874. DOI: 10.1177/1468087417733865.

[79] G. K. Giannakopoulos, K. Keskinen, J. Koch, C. E. Frouzakis, Y. M. Wright, and K. Boulouchos. "Characterizing the Evolution of Boundary Layers in IC Engines by Combined Direct Numerical and Large-Eddy Simulations." In: *Flow, Turbulence and Combustion* (2022). ISSN: 1386-6184. DOI: 10.1007/s10494-022-00383-1.

[80] M. Greene. "Momentum Near-wall Region Characterization in a Reciprocating Internal-combustion Engine." Dissertation. Michigan: University of Michigan, 2017. URL: https://deepblue.lib.umich.edu/handle/2027.42/136962.

[81] M. L. Greene. "Momentum Near-wall Region Characterization in a Reciprocating Internal-combustion Engine." Dissertation. Michigan: University of Michigan, 2017. URL: https://deepblue.lib.umich.edu/handle/2027.42/140984.

[82] M. Greifenstein. "Experimental investigations of flame-cooling air interaction in an effusion cooled pressurized single sector model gas turbine combustor." PhD thesis. UNSPECIFIED, 2021. DOI: 10.26083/TUPRINTS-00019205.

[83] M. Greifenstein. *Yet Another Siemens Star Evaluation Script (YASSES)*. 2022. URL: https://github.com/tudarsm/yasses.

[84] F. Grossmann, P. B. Monkhouse, M. Ridder, V. Sick, and J. Wolfrum. "Temperature and pressure dependences of the laser-induced fluorescence of gas-phase acetone and 3-pentanone." In: *Applied Physics B* 62.3 (1996), pp. 249–253. ISSN: 1432-0649. DOI: 10.1007/BF01080952.

[85] M. J. Hall, F. V. Bracco, and D. A. Santavicca. "Cycle-Resolved Velocity and Turbulence Measurements in an IC Engine With Combustion." In: *SAE Technical Paper Series*. SAE Technical Paper Series. SAE International400 Commonwealth Drive, Warrendale, PA, United States, 1986. DOI: 10.4271/860320.

[86] D. Han and R. R. Steeper. "An LIF equivalence ratio imaging technique for multicomponent fuels in an IC engine." In: *Proceedings of the Combustion Institute* 29.1 (2002), pp. 727–734. ISSN: 15407489. DOI: 10.1016/S1540-7489(02)80093-1.

[87] D. A. Hansen and E. K. C. Lee. "Radiative and nonradiative transitions in the first excited singlet state of simple linear aldehydes." In: *The Journal of Chemical Physics* 63.8 (1975), pp. 3272–3277. ISSN: 0021-9606. DOI: 10.1063/1.431802.

[88] R. K. Hanson, R. M. Spearrin, and C. S. Goldenstein. *Spectroscopy and Optical Diagnostics for Gases*. Cham: Springer International Publishing, 2016. ISBN: 978-3-319-23251-5. DOI: 10.1007/978-3-319-23252-2.

[90] J. Hartwig, G. Mittal, K. Kumar, and C.-J. Sung. "System Validation Experiments for Obtaining Tracer Laser-Induced Fluorescence Data at Elevated Pressure and Temperature." In: *Applied spectroscopy* 72.4 (2018), pp. 618–626. DOI: 10.1177/0003702817746409.

[91] H. Hattori and Y. Nagano. "Direct numerical simulation of turbulent heat transfer in plane impinging jet." In: *International Journal of Heat and Fluid Flow* 25.5 (2004), pp. 749–758. ISSN: 0142727X. DOI: 10.1016/j.ijheatfluidflow.2004.05.004.

[93] X. He, Y. Li, M. Sjöberg, D. Vuilleumier, C.-P. Ding, F. Liu, and X. Li. "Impact of coolant temperature on piston wall-wetting and smoke generation in a stratified-charge DISI engine operated on E30 fuel." In: *Proceedings of the Combustion Institute* 37.4 (2019), pp. 4955–4963. ISSN: 15407489. DOI: 10.1016/j.proci.2018.07.073.

[94] X. He, Y. Zhou, Z. Liu, Q. Yang, M. Sjöberg, D. Vuilleumier, C.-P. Ding, and F. Liu. "Impact of coolant temperature on the combustion characteristics and emissions of a stratified-charge direct-injection spark-ignition engine fueled with E30." In: *Fuel* 309 (2022), p. 121913. ISSN: 00162361. DOI: 10.1016/j.fuel.2021.121913.

[95] Heraeus. *Properties of fused silica*. 24.02.2023.

[96] R. Hessel, Z. Yue, R. Reitz, M. Musculus, and J. O'Connor. "Guidelines for Interpreting Soot Luminosity Imaging." In: *SAE International Journal of Engines* 10.3 (2017), pp. 1174–1192. ISSN: 1946-3944. DOI: 10.4271/2017-01-0716.

[97] J. Heywood. *Internal Combustion Engine Fundamentals 2E*. 2nd edition. New York, N.Y.: McGraw-Hill Education and McGraw Hill, 2019. ISBN: 9781260116113. URL: https://www.accessengineeringlibrary.com/content/book/9781260116106.

[98] H. Hu and M. Koochesfahani. "A novel method for instantaneous, quantitative measurement of molecular mixing in gaseous flows." In: *Experiments in Fluids* 33.1 (2002), pp. 202–209. ISSN: 0723-4864. DOI: 10.1007/s00348-002-0452-5.

[99] Y. Huang, T. Alger, R. D. Matthews, and J. Ellzey. "The Effects of Fuel Volatility and Structure on HC Emissions from Piston Wetting in DISI Engines." In: *SAE Technical Paper Series*. SAE Technical Paper Series. SAE International400 Commonwealth Drive, Warrendale, PA, United States, 2001. DOI: 10.4271/2001-01-1205.

[100] M. Huber, A. Harvey, E. Lemmon, G. Hardin, I. Bell, and M. McLinden. *NIST Reference Fluid Thermodynamic and Transport Properties Database (REFPROP) Version 10 - SRD 23*. 2018. DOI: 10.18434/T4/1502528.

[101] IEA. *Global CO2 emissions from transport by subsector*. Ed. by IEA. Paris, 2022. URL: https://www.iea.org/data-and-statistics/charts/global-co2-emissions-from-transport-by-subsector-2000-2030.

[102] IEA. *CO2 Emissions in 2022*. Ed. by IEA. Paris, 2023. URL: https://www.iea.org/reports/co2-emissions-in-2022.

[103] IEA. *Global EV Outlook 2023*. Ed. by IEA. Paris, 2023. URL: https://www.iea.org/reports/global-ev-outlook-2023.

[104] Institut für Arbeitsschutz der Deutschen Gesetzlichen Unfallversicherung. *GESTIS Stoffdatenbank*. Ed. by IFA. 2023. URL: https://gestis.dguv.de/.

[105] IPCC. *Climate Change 2021: The Physical Science Basis. Contribution of Working Group I to the Sixth Assessment Report of the Intergovernmental Panel on Climate Change*. Cambridge University Press, 2021. DOI: 10.1017/9781009157896.

[106] IPCC. *Climate Change 2022: Mitigation of Climate Change. Working Group III Contribution to the IPCC Sixth Assessment Report*. Cambridge University Press, 2022. DOI: 10.1017/9781009157926.

[107] IPCC. *AR6 Synthesis Report: Climate Change 2023*. Ed. by IPCC. 2023. URL: https://www.ipcc.ch/report/ar6/syr/.

[108] W. Ipp. "Analyse der Kraftstoffverteilung bei der Benzindirekteinspritzung (BDE) mit laseroptischen Meßverfahren." Dissertation. Universität Erlangen-Nürnberg, 2004.

[109] S. Ishizawa. "An experimental study on quenching crevice widths in the combustion chamber of a spark-ignition engine." In: *Symposium (International) on Combustion* 26.2 (1996), pp. 2605–2611. ISSN: 00820784. DOI: 10.1016/S0082-0784(96)80094-4.

[110] T. Itoh, A. Kakuho, H. Hishinuma, T. Urushiahara, Y. Takagi, K. Horie, M. Asano, E. Ogata, and T. Yamasita. "Development of a New Compound Fuel and Fluorescent Tracer Combination for Use with Laser Induced Fluorescence." In: *SAE Technical Paper Series*. SAE Technical Paper Series. SAE International400 Commonwealth Drive, Warrendale, PA, United States, 1995. DOI: 10.4271/952465.

[111] C. Jainski, L. Lu, A. Dreizler, and V. Sick. "High-speed micro particle image velocimetry studies of boundary-layer flows in a direct-injection engine." In: *International Journal of Engine Research* 14.3 (2013), pp. 247–259. ISSN: 1468-0874. DOI: 10.1177/1468087412455746.

[112] S. Jakirlić and K. Hanjalić. "A new approach to modelling near-wall turbulence energy and stress dissipation." In: *Journal of Fluid Mechanics* 459 (2002), pp. 139–166. ISSN: 0022-1120. DOI: 10.1017/S0022112002007905.

[113] P. Janas, M. D. Ribeiro, A. Kempf, M. Schild, and S. A. Kaiser. "Penetration of the Flame Into the Top-Land Crevice - Large-Eddy Simulation and Experimental High-Speed Visualization." In: *SAE Technical Paper Series*. SAE Technical Paper Series. SAE International400 Commonwealth Drive, Warrendale, PA, United States, 2015. DOI: 10.4271/2015-01-1907.

[114] L. S. Johansson. "Characterisation of Particle Emissions from Small-Scale Biomass Combustion." Dissertation. Goeteborg: Chalmers Univ. of Technology, 2002. URL: https://www.osti.gov/etdeweb/biblio/20437694.

[115] A. Joshi. "Review of Vehicle Engine Efficiency and Emissions." In: *SAE International Journal of Advances and Current Practices in Mobility* 4.5 (2022), pp. 1704–1733. ISSN: 2641-9645. DOI: 10.4271/2022-01-0540.

[116] A. Joshi. "Year in Review: Progress towards Decarbonizing Transport and Near-Zero Emissions." In: *SAE Technical Paper Series*. Ed. by A. Joshi. SAE Technical Paper Series. SAE International400 Commonwealth Drive, Warrendale, PA, United States, 2023. DOI: 10.4271/2023-01-0396.

[117] G. Jovicic, L. Zigan, S. Will, and A. Leipertz. "Phosphor thermometry in turbulent hot gas flows applying Dy:YAG and Dy:Er:YAG particles." In: *Measurement Science and Technology* 26.1 (2015), p. 015204. ISSN: 0957-0233. DOI: 10.1088/0957-0233/26/1/015204.

[118] N. Jüngst, N. Frapolli, Y. M. Wright, K. Boulouchos, and S. A. Kaiser. "Experimental and numerical investigation of evaporating fuel films in combustion." In: *Applications in Energy and Combustion Science* 7 (2021), p. 100033. ISSN: 2666352X. DOI: 10.1016/j.jaecs.2021.100033.

[119] N. Jüngst and S. A. Kaiser. "Visualization of soot formation from evaporating fuel films by laser-induced fluorescence and incandescence." In: *Proceedings of the Combustion*

*Institute* 38.1 (2021), pp. 1089–1097. ISSN: 15407489. DOI: 10.1016/j.proci.2020.06.076.

[120] C. J. Kähler, S. Scharnowski, and C. Cierpka. "On the uncertainty of digital PIV and PTV near walls." In: *Experiments in Fluids* 52.6 (2012), pp. 1641–1656. ISSN: 0723-4864. DOI: 10.1007/s00348-012-1307-3.

[121] S. A. Kaiser, M. Schild, and C. Schulz. "Thermal stratification in an internal combustion engine due to wall heat transfer measured by laser-induced fluorescence." In: *Proceedings of the Combustion Institute* 34.2 (2013), pp. 2911–2919. ISSN: 15407489. DOI: 10.1016/j.proci.2012.05.059.

[122] T. Kamimoto and M. Bae. "High Combustion Temperature for the Reduction of Particulate in Diesel Engines." In: *SAE transactions* 97 (1988), pp. 692–701. DOI: 10.4271/880423.

[123] W. M. Kays. "Turbulent Prandtl Number—Where Are We?" In: *Journal of Heat Transfer* 116.2 (1994), pp. 284–295. ISSN: 0022-1481. DOI: 10.1115/1.2911398.

[124] K. Keskinen and G. Giannakopoulos. *Boundary layer data from a wall-resolved LES of OP E in the Darmstadt Engine: Personal Communication*. 2021.

[125] K. Keskinen, G. Giannakopoulos, M. Bolla, J. Koch, Y. M. Wright, C. Frouzakis, K. Boulouchos, M. Schmidt, B. Böhm, and A. Dreizler. "Novel Insight into Engine Near-Wall Flows and Wall Heat Transfer Using Direct Numerical Simulations and High-Fidelity Experiments." In: *21. Internationales Stuttgarter Symposium*. Ed. by M. Bargende, H.-C. Reuss, and A. Wagner. Proceedings. Wiesbaden: Springer Fachmedien Wiesbaden, 2021, pp. 377–394. ISBN: 978-3-658-33520-5. DOI: 10.1007/978-3-658-33521-2{\textunderscore}26.

[126] J. E. Ketterer and W. K. Cheng. "On the Nature of Particulate Emissions from DISI Engines at Cold-Fast-Idle." In: *SAE International Journal of Engines* 7.2 (2014), pp. 986–994. ISSN: 1946-3944. DOI: 10.4271/2014-01-1368.

[127] J. E. Ketterer. "Soot formation in direct injection spark ignition engines under cold-idle operating conditions." Dissertation. Massachusetts: Massachusetts Institute of Technology, 2013. URL: https://dspace.mit.edu/handle/1721.1/85538.

[128] A. H. Khalid and K. Kontis. "Thermographic Phosphors for High Temperature Measurements: Principles, Current State of the Art and Recent Applications." In: *Sensors (Basel, Switzerland)* 8.9 (2008), pp. 5673–5744. DOI: 10.3390/s8095673.

[129] V. Khamaganov, R. Karunanandan, A. Rodriguez, and J. N. Crowley. "Photolysis of CH3C(O)CH3 (248 nm, 266 nm), CH3C(O)C2H5 (248 nm) and CH3C(O)Br (248 nm): pressure dependent quantum yields of CH3 formation." In: *Physical chemistry chemical physics : PCCP* 9.31 (2007), pp. 4098–4113. ISSN: 1463-9076. DOI: 10.1039/b701382e.

[130] M. Kim, H. Cho, Y. Cho, and K. Min. "Computational and Optical Investigation of Liquid Fuel Film on the Cylinder Wall of an SI Engine." In: *SAE Technical Paper Series*. SAE Technical Paper Series. SAE International400 Commonwealth Drive, Warrendale, PA, United States, 2003. DOI: 10.4271/2003-01-1113.

[131] G. F. King, R. P. Lucht, and J. C. Dutton. "Quantitative dual-tracer planar laser-induced fluorescence measurements of molecular mixing." In: *Optics letters* 22.9 (1997), pp. 633–635. ISSN: 1539-4794. DOI: 10.1364/ol.22.000633.

[132] T. Kitamura, T. Ito, J. Senda, and H. Fujimoto. "Mechanism of smokeless diesel combustion with oxygenated fuels based on the dependence of the equivalence ration and temperature on soot particle formation." In: *International Journal of Engine Research* 3.4 (2002), pp. 223–248. ISSN: 1468-0874. DOI: 10.1243/146808702762230923.

[133] C. Knappe, M. Algotsson, P. Andersson, M. Richter, M. Tunér, B. Johansson, and M. Aldén. “Thickness dependent variations in surface phosphor thermometry during transient combustion in an HCCI engine.” In: *Combustion and Flame* 160.8 (2013), pp. 1466–1475. ISSN: 00102180. DOI: 10.1016/j.combustflame.2013.02.023.

[134] W. Koban, J. D. Koch, R. K. Hanson, and C. Schulz. “Oxygen quenching of toluene fluorescence at elevated temperatures.” In: *Applied Physics B* 80.6 (2005), pp. 777–784. ISSN: 1432-0649. DOI: 10.1007/s00340-005-1769-6.

[135] W. Koban. “Photophysical characterization of toluene and 3 pentanone for quantitative imaging of fuel/air ratio and temperature in combustion systems.” PhD thesis. Heidelberg University Library, 2005. DOI: 10.11588/HEIDOK.00005846.

[136] W. Koban, J. D. Koch, R. K. Hanson, and C. Schulz. “Absorption and fluorescence of toluene vapor at elevated temperatures.” In: *Physical Chemistry Chemical Physics* 6.11 (2004), pp. 2940–2945. ISSN: 1463-9084. DOI: 10.1039/B400997E. URL: https://pubs.rsc.org/en/content/articlepdf/2004/cp/b400997e.

[137] J. D. Koch and R. K. Hanson. “Temperature and excitation wavelength dependencies of 3-pentanone absorption and fluorescence for PLIF applications.” In: *Applied Physics B* 76.3 (2003), pp. 319–324. ISSN: 1432-0649. DOI: 10.1007/s00340-002-1084-4.

[138] J. D. Koch. “Fuel tracer photophysics for quantitative planar laser-induced fluorescence.” Dissertation. Stanford University, 2005.

[139] P. Koch, M. G. Löffler, M. Wensing, and A. Leipertz. “Study of the mixture formation processes inside a modern direct-injection gasoline engine.” In: *International Journal of Engine Research* 11.6 (2010), pp. 455–471. ISSN: 1468-0874. DOI: 10.1243/14680874JER606.

[140] M. Koegl, B. Hofbeck, S. Will, and L. Zigan. “Investigation of soot formation and oxidation of ethanol and butanol fuel blends in a DISI engine at different exhaust gas recirculation rates.” In: *Applied Energy* 209 (2018), pp. 426–434. ISSN: 03062619. DOI: 10.1016/j.apenergy.2017.11.034.

[141] M. Koegl, B. Hofbeck, S. Will, and L. Zigan. “Influence of EGR and ethanol blending on soot formation in a DISI engine.” In: *Proceedings of the Combustion Institute* 37.4 (2019), pp. 4965–4972. ISSN: 15407489. DOI: 10.1016/j.proci.2018.07.103.

[142] P. Kranz. “Imaging of mixing processes in spark-ignition engines via quantitative laser-induced fluorescence.” Dissertation. Duisburg: Universität Duisburg-Essen, 2020. URL: https://doi.org/10.17185/duepublico/72672.

[143] P. Kranz, D. Fuhrmann, M. Goschütz, S. Kaiser, S. Bauke, K. Golibrzuch, H. Wackerbarth, P. Kawelke, J. Luciani, L. Beckmann, J. Zachow, M. Schuette, O. Thiele, and T. Berg. “In-Cylinder LIF Imaging, IR-Absorption Point Measurements, and a CFD Simulation to Evaluate Mixture Formation in a CNG-Fueled Engine.” In: *SAE International Journal of Engines* 11.6 (2018), pp. 1221–1238. ISSN: 1946-3944. DOI: 10.4271/2018-01-0633.

[144] J. Laichter and S. A. Kaiser. “Optical Investigation of the Influence of In-cylinder Flow and Mixture Inhomogeneity on Cyclic Variability in a Direct-Injection Spark Ignition Engine.” In: *Flow, Turbulence and Combustion* (2022). ISSN: 1386-6184. DOI: 10.1007/s10494-022-00344-8.

[145] J. R. Lakowicz. *Principles of Fluorescence Spectroscopy*. Boston, MA: Springer US, 2006. ISBN: 978-0-387-31278-1. DOI: 10.1007/978-0-387-46312-4.

[146] C. Lav, R. D. Sandberg, K. Tanimoto, and K. Terakado. “Momentum boundary-layer characterisation from a pulsed impinging jet.” In: *International Journal of Heat and*

*Fluid Flow* 94 (2022), p. 108918. ISSN: 0142727X. DOI: 10.1016/j.ijheatfluidflow.2021.108918.

[147] B. Lawton. "Effect of Compression and Expansion on Instantaneous Heat Transfer in Reciprocating Internal Combustion Engines." In: *Proceedings of the Institution of Mechanical Engineers, Part A: Power and Process Engineering* 201.3 (1987), pp. 175–186. ISSN: 0263-7138. DOI: 10.1243/PIME{\textunderscore}PROC{\textunderscore}1987{\textunderscore}201{\textunderscore}022{\textunderscore}02.

[148] T. Lefeuvre, P. S. Myers, and O. A. Uyehara. "Experimental Instantaneous Heat Fluxes in a Diesel Engine and Their Correlation." In: *SAE Technical Paper Series*. SAE Technical Paper Series. SAE International400 Commonwealth Drive, Warrendale, PA, United States, 1969. DOI: 10.4271/690464.

[149] Y. Li, F. Ries, W. Leudesdorff, K. Nishad, A. Pati, C. Hasse, J. Janicka, S. Jakirlić, and A. Sadiki. "Non-equilibrium wall functions for large Eddy simulations of complex turbulent flows and heat transfer." In: *International Journal of Heat and Fluid Flow* 88 (2021), p. 108758. ISSN: 0142727X. DOI: 10.1016/j.ijheatfluidflow.2020.108758.

[150] S. Lind, J. Trost, L. Zigan, A. Leipertz, and S. Will. "Application of the tracer combination TEA/acetone for multi-parameter laser-induced fluorescence measurements in IC engines with exhaust gas recirculation." In: *Proceedings of the Combustion Institute* 35.3 (2015), pp. 3783–3791. ISSN: 15407489. DOI: 10.1016/j.proci.2014.06.144.

[151] S. Lind, L. Zigan, J. Trost, A. Leipertz, and S. Will. "Simultaneous two-dimensional measurement of fuel–air ratio and temperature in a direct-injection spark-ignition engine using a new tracer-pair laser-induced fluorescence technique." In: *International Journal of Engine Research* 17.1 (2016), pp. 120–128. ISSN: 1468-0874. DOI: 10.1177/1468087415613938.

[152] P. Linstrom. *NIST Chemistry WebBook, NIST Standard Reference Database 69*. 1997. DOI: 10.18434/T4D303.

[153] M. Löffler, K. Kröckel, P. Koch, F. Beyrau, A. Leipertz, S. Grasreiner, and A. Heinisch. "Simultaneous Quantitative Measurements of Temperature and Residual Gas Fields Inside a Fired SI-Engine Using Acetone Laser-Induced Fluorescence." In: *SAE Technical Paper Series*. SAE Technical Paper Series. SAE International400 Commonwealth Drive, Warrendale, PA, United States, 2009. DOI: 10.4271/2009-01-0656.

[154] M. Löffler, F. Beyrau, and A. Leipertz. "Acetone laser-induced fluorescence behavior for the simultaneous quantification of temperature and residual gas distribution in fired spark-ignition engines." In: *Applied Optics* 49.1 (2010), pp. 37–49. ISSN: 1559-128X. DOI: 10.1364/AO.49.000037.

[155] M. G. Löffler. *Entwicklung einer planaren Lasermesstechnik zur simultanen Temperatur- und Konzentrationsmessung bei Gemischbildungsprozessen im Ottomotor: Zugl.: Erlangen-Nürnberg, Univ., Diss., 2011*. Als Ms. gedr. Vol. 2011,5. Berichte zur Energie- und Verfahrenstechnik. Erlangen: ESYTEC Energie- und Systemtechnik GmbH, 2011. ISBN: 3931901769.

[156] A. Lozano, B. Yip, and R. K. Hanson. "Acetone: a tracer for concentration measurements in gaseous flows by planar laser-induced fluorescence." In: *Experiments in Fluids* 13.6 (1992), pp. 369–376. ISSN: 0723-4864. DOI: 10.1007/BF00223244.

[157] M. Luong, W. Koban, and C. Schulz. "Novel strategies for imaging temperature distribution using Toluene LIF." In: *Journal of Physics: Conference Series* 45 (2006), pp. 133–139. ISSN: 1742-6588. DOI: 10.1088/1742-6596/45/1/017.

[158] M. Luong, R. Zhang, C. Schulz, and V. Sick. “Toluene laser-induced fluorescence for in-cylinder temperature imaging in internal combustion engines.” In: *Applied Physics B* 91.3-4 (2008), pp. 669–675. ISSN: 1432-0649. DOI: 10.1007/s00340-008-2995-5.

[159] P. C. Ma, T. Ewan, C. Jainski, L. Lu, A. Dreizler, V. Sick, and M. Ihme. “Development and Analysis of Wall Models for Internal Combustion Engine Simulations Using High-speed Micro-PIV Measurements.” In: *Flow, Turbulence and Combustion* 98.1 (2017), pp. 283–309. ISSN: 1386-6184. DOI: 10.1007/s10494-016-9734-5.

[160] P. C. Ma, M. Greene, V. Sick, and M. Ihme. “Non-equilibrium wall-modeling for internal combustion engine simulations with wall heat transfer.” In: *International Journal of Engine Research* 18.1-2 (2017), pp. 15–25. ISSN: 1468-0874. DOI: 10.1177/1468087416686699.

[161] J. R. MacDonald, C. M. Fajardo, M. Greene, D. Reuss, and V. Sick. “Two-Point Spatial Velocity Correlations in the Near-Wall Region of a Reciprocating Internal Combustion Engine.” In: *SAE Technical Paper Series*. SAE Technical Paper Series. SAE International400 Commonwealth Drive, Warrendale, PA, United States, 2017. DOI: 10.4271/2017-01-0613.

[162] M. J. MacDonald and J. M. Roscoe. “The photolysis of acetone at 308 nm.” In: *Journal of Photochemistry and Photobiology A: Chemistry* 57.1-3 (1991), pp. 441–451. ISSN: 10106030. DOI: 10.1016/1010-6030(91)85036-G.

[163] L. P. Maguire, S. Szilagyi, and R. E. Scholten. “High performance laser shutter using a hard disk drive voice-coil actuator.” In: *The Review of scientific instruments* 75.9 (2004), pp. 3077–3079. ISSN: 0034-6748. DOI: 10.1063/1.1786331.

[164] Z. A. Mansurov. “Soot Formation in Combustion Processes (Review).” In: *Combustion, Explosion, and Shock Waves* 41.6 (2005), pp. 727–744. ISSN: 0010-5082. DOI: 10.1007/s10573-005-0083-2.

[165] MATLAB. Natick, Massachusetts, 2022.

[166] T. Mederer, W. Friedrich, J. Trost, L. Zigan, and M. Wensing. “Simultaneous spatially resolved visualization of fuel/air ratio and residual gas distribution in an optically accessible SI engine.” In: *14. Internationales Stuttgarter Symposium*. Ed. by M. Bargende, H.-C. Reuss, and J. Wiedemann. Proceedings. Wiesbaden: Springer Fachmedien Wiesbaden, 2014, pp. 349–372. ISBN: 978-3-658-05129-7. DOI: 10.1007/978-3-658-05130-3{\textunderscore}25.

[167] C. Meißner, H. Schneider, E. Sidiropoulos, J. I. Hölzer, T. Heckmann, B. Böhm, A. Dreizler, and T. Seeger. “Investigation on wall and gas temperatures inside a swirled oxy-fuel combustion chamber using thermographic phosphors, O2 rotational and vibrational CARS.” In: *Fuel* 289 (2021), p. 119787. ISSN: 00162361. DOI: 10.1016/j.fuel.2020.119787.

[168] I. Meziane, Y. Fenard, N. Delort, O. Herbinet, J. Bourgalais, A. Ramalingam, K. A. Heufer, and F. Battin-Leclerc. “Experimental and modeling study of acetone combustion.” In: *Combustion and Flame* (2022), p. 112416. ISSN: 00102180. DOI: 10.1016/j.combustflame.2022.112416.

[169] H. A. Michelsen, M. B. Colket, P.-E. Bengtsson, A. D’Anna, P. Desgroux, B. S. Haynes, J. H. Miller, G. J. Nathan, H. Pitsch, and H. Wang. “A Review of Terminology Used to Describe Soot Formation and Evolution under Combustion and Pyrolytic Conditions.” In: *ACS nano* 14.10 (2020), pp. 12470–12490. DOI: 10.1021/acsnano.0c06226.

[170] V. Modica, C. Morin, and P. Guibert. “3-Pentanone LIF at elevated temperatures and pressures: measurements and modeling.” In: *Applied Physics B* 87.1 (2007), pp. 193–204. ISSN: 1432-0649. DOI: 10.1007/s00340-006-2548-8.

[171] A. Montanaro, L. Allocca, and M. Lazzaro. “Iso-Octane Spray from a GDI Multi-Hole Injector under Non- and Flash Boiling Conditions.” In: *SAE Technical Paper Series*. SAE Technical Paper Series. SAE International400 Commonwealth Drive, Warrendale, PA, United States, 2017. DOI: 10.4271/2017-01-2319.

[172] J. P. Monty, Z. Harun, and I. Marusic. “A parametric study of adverse pressure gradient turbulent boundary layers.” In: *International Journal of Heat and Fluid Flow* 32.3 (2011), pp. 575–585. ISSN: 0142727X. DOI: 10.1016/j.ijheatfluidflow.2011.03.004.

[173] M. M. Moser, C. H. Onder, and L. Guzzella. “Using exhaust pressure pulsations to detect deteriorations of oxygen sensor dynamics.” In: *Sensors and Actuators B: Chemical* 191 (2014), pp. 384–395. ISSN: 09254005. DOI: 10.1016/j.snb.2013.10.015.

[174] National Center for Biotechnology Information. *PubChem*. Ed. by NIH. 2023. URL: https://pubchem.ncbi.nlm.nih.gov.

[175] C. Neto, D. R. Evans, E. Bonaccurso, H.-J. Butt, and V. S. J. Craig. “Boundary slip in Newtonian liquids: a review of experimental studies.” In: *Reports on Progress in Physics* 68.12 (2005), pp. 2859–2897. ISSN: 0034-4885. DOI: 10.1088/0034-4885/68/12/R05.

[176] D. J. O. Nijeweme, J. B. W. Kok, C. R. Stone, and L. Wyszynski. “Unsteady in-cylinder heat transfer in a spark ignition engine: Experiments and modelling.” In: *Proceedings of the Institution of Mechanical Engineers, Part D: Journal of Automobile Engineering* 215.6 (2001), pp. 747–760. ISSN: 0954-4070. DOI: 10.1243/0954407011528329.

[177] S. W. North, D. A. Blank, J. D. Gezelter, C. A. Longfellow, and Y. T. Lee. “Evidence for stepwise dissociation dynamics in acetone at 248 and 193 nm.” In: *The Journal of Chemical Physics* 102.11 (1995), pp. 4447–4460. ISSN: 0021-9606. DOI: 10.1063/1.469493.

[178] A. O. Ojo, D. Escofet-Martin, C. Abram, B. Fond, and B. Peterson. “Precise surface temperature measurements at kHz-rates using phosphor thermometry to study flame-wall interactions in narrow passages.” In: *Combustion and Flame* 240 (2022), p. 111984. ISSN: 00102180. DOI: 10.1016/j.combustflame.2022.111984.

[179] A. O. Ojo, D. Escofet-Martin, J. Collins, G. Falconetti, and B. Peterson. “Experimental investigation of thermal boundary layers and associated heat loss for transient engine-relevant processes using HRCARS and phosphor thermometry.” In: *Combustion and Flame* 233 (2021), p. 111567. ISSN: 00102180. DOI: 10.1016/j.combustflame.2021.111567.

[180] A. O. Ojo, D. Escofet-Martin, and B. Peterson. “High-precision 2D surface phosphor thermometry at kHz-rates during flame-wall interaction in narrow passages.” In: *Proceedings of the Combustion Institute* (2022). ISSN: 15407489. DOI: 10.1016/j.proci.2022.09.048.

[181] C. H. Onder and H. P. Geering. “Measurement of the Wall-Wetting Dynamics of a Sequential Injection Spark Ignition Engine.” In: *SAE Technical Paper Series*. SAE Technical Paper Series. SAE International400 Commonwealth Drive, Warrendale, PA, United States, 1994. DOI: 10.4271/940447.

[182] J. Parks, J. Armfield, J. Storey, T. Barber, and E. Wachter. “In Situ Measurement of Fuel Absorption into the Cylinder Wall Oil Film During Engine Cold Start.” In: *SAE Technical Paper Series*. SAE Technical Paper Series. SAE International400 Commonwealth Drive, Warrendale, PA, United States, 1998. DOI: 10.4271/981054.

[183] A. Pati. “Numerical investigation of the in-cylinder flow-spray-wall interactions in direct injection engines.” PhD thesis. Technical University of Darmstadt, 2022. DOI: 10.26083/tuprints-00022861.

[185] R. Payri, F. J. Salvador, P. Martí-Aldaraví, and D. Vaquerizo. "ECN Spray G external spray visualization and spray collapse description through penetration and morphology analysis." In: *Applied Thermal Engineering* 112 (2017), pp. 304–316. ISSN: 13594311. DOI: 10.1016/j.applthermaleng.2016.10.023.

[186] F. Persson, S. Hemdal, and M. Andersson. "Fluorobenzene and Fluorotoluene with Triethylamine as Exciplex Tracers for Two-Phase Visualization in Gasoline-like Fuel Sprays." In: *Proc. 20th Annual Conference on Liquid Atomization and Spray Systems (ILASS Europe 2005)*. 2005. URL: https://www.ilasseurope.org/iclass/ilass2005/papers/measurements%20techniques/p69-74[measurtech]hemdal.pdf.

[187] B. R. Petersen, J. B. Ghandhi, and J. D. Koch. "Fluorescence saturation measurements of 3-pentanone." In: *Applied Physics B* 93.2-3 (2008), pp. 639–644. ISSN: 1432-0649. DOI: 10.1007/s00340-008-3189-x.

[188] B. Peterson, E. Baum, B. Böhm, and A. Dreizler. "Early flame propagation in a spark-ignition engine measured with quasi 4D-diagnostics." In: *Proceedings of the Combustion Institute* 35.3 (2015), pp. 3829–3837. ISSN: 15407489. DOI: 10.1016/j.proci.2014.05.131.

[189] B. Peterson and V. Sick. "Simultaneous flow field and fuel concentration imaging at 4.8 kHz in an operating engine." In: *Applied Physics B* 97.4 (2009), pp. 887–895. ISSN: 1432-0649. DOI: 10.1007/s00340-009-3620-y.

[190] B. Peterson, E. Baum, B. Böhm, V. Sick, and A. Dreizler. "Evaluation of toluene LIF thermometry detection strategies applied in an internal combustion engine." In: *Applied Physics B* 117.1 (2014), pp. 151–175. ISSN: 0946-2171. DOI: 10.1007/s00340-014-5815-0.

[191] S. PICHON, G. BLACK, N. CHAUMEIX, M. YAHYAOUI, J. SIMMIE, H. CURRAN, and R. DONOHUE. "The combustion chemistry of a fuel tracer: Measured flame speeds and ignition delays and a detailed chemical kinetic model for the oxidation of acetone." In: *Combustion and Flame* 156.2 (2009), pp. 494–504. ISSN: 00102180. DOI: 10.1016/j.combustflame.2008.10.001.

[192] P. H. Pierce, J. B. Ghandhi, and J. K. Martin. "Near-Wall Velocity Characteristics in Valved and Ported Motored Engines." In: *SAE Technical Paper Series*. SAE Technical Paper Series. SAE International400 Commonwealth Drive, Warrendale, PA, United States, 1992. DOI: 10.4271/920152.

[193] C. Plengsaard and C. Rutland. "Improved Engine Wall Models for Large Eddy Simulation (LES)." In: *SAE Technical Paper Series*. SAE Technical Paper Series. SAE International400 Commonwealth Drive, Warrendale, PA, United States, 2013. DOI: 10.4271/2013-01-1097.

[194] S. B. Pope. *Turbulent flows*. 10. print. Cambridge: Cambridge Univ. Press, 2013. ISBN: 9780521598866.

[195] L. Prandtl. "7. Bericht über Untersuchungen zur ausgebildeten Turbulenz." In: *ZAMM - Journal of Applied Mathematics and Mechanics / Zeitschrift für Angewandte Mathematik und Mechanik* 5.2 (1925), pp. 136–139. ISSN: 00442267. DOI: 10.1002/zamm.19250050212.

[196] A. Preusche. "Non-invasive thermometry and wake mixture fraction determination of evaporating droplets at elevated pressures using laser spectroscopy." PhD thesis. Darmstadt: Technical University of Darmstadt, 2021. DOI: 10.26083/TUPRINTS-00019515.

[197] C. Qi, X. Yan, Y. Wang, Y. Ning, X. Yu, Y. Hou, X. Lv, J. Ding, E. Shi, and J. Yu. "Flammability Limits of Combustible Gases at Elevated Temperatures and Pressures: Recent Ad-

vances and Future Perspectives." In: *Energy & Fuels* 36.21 (2022), pp. 12896–12916. ISSN: 0887-0624. DOI: 10.1021/acs.energyfuels.2c02567.

[198] M. Raffel, C. E. Willert, F. Scarano, C. J. Kähler, S. T. Wereley, and J. Kompenhans. *Particle Image Velocimetry: A Practical Guide*. 3rd Edition. Cham: Springer, 2018. ISBN: 9783319688510.

[199] M. Raffel, C. E. Willert, S. T. Wereley, and J. Kompenhans. *Particle Image Velocimetry*. Berlin, Heidelberg: Springer Berlin Heidelberg, 2007. ISBN: 978-3-540-72307-3. DOI: 10.1007/978-3-540-72308-0.

[200] C. D. Rakopoulos, G. M. Kosmadakis, and E. G. Pariotis. "Critical evaluation of current heat transfer models used in CFD in-cylinder engine simulations and establishment of a comprehensive wall-function formulation." In: *Applied Energy* 87.5 (2010), pp. 1612–1630. ISSN: 03062619. DOI: 10.1016/j.apenergy.2009.09.029.

[201] B. S. Reddy and B. N. Chatterji. "An FFT-based technique for translation, rotation, and scale-invariant image registration." In: *IEEE transactions on image processing : a publication of the IEEE Signal Processing Society* 5.8 (1996), pp. 1266–1271. ISSN: 1057-7149. DOI: 10.1109/83.506761.

[202] M. Reeves. "Particle image velocimetry applied to internal combustion engine in-cylinder flows." In: (2010). URL: https://repository.lboro.ac.uk/articles/thesis/Particle_image_velocimetry_applied_to_internal_combustion_engine_in-cylinder_flows/9519014.

[203] Y. Ren, Z. Huang, H. Miao, Y. Di, D. Jiang, K. Zeng, B. Liu, and X. Wang. "Combustion and emissions of a DI diesel engine fuelled with diesel-oxygenate blends." In: *Fuel* 87.12 (2008), pp. 2691–2697. ISSN: 00162361. DOI: 10.1016/j.fuel.2008.02.017.

[204] A. Renaud, C.-P. Ding, S. Jakirlic, A. Dreizler, and B. Böhm. "Experimental characterization of the velocity boundary layer in a motored IC engine." In: *International Journal of Heat and Fluid Flow* 71 (2018), pp. 366–377. ISSN: 0142727X. DOI: 10.1016/j.ijheatfluidflow.2018.04.014.

[205] H. Richter and J. Howard. "Formation of polycyclic aromatic hydrocarbons and their growth to soot—a review of chemical reaction pathways." In: *Progress in Energy and Combustion Science* 26.4-6 (2000), pp. 565–608. ISSN: 03601285. DOI: 10.1016/S0360-1285(00)00009-5.

[206] A. Rohatgi. *Webplotdigitzer: Version 4.6*. 2022. URL: https://automeris.io/WebPlotDigitizer.

[207] A. Roque, F. Foucher, W. Imoehl, and J. Helie. "Generation and Oxidation of Soot due to Fuel Films Utilizing High Speed Visualization Techniques." In: *SAE Technical Paper Series*. SAE Technical Paper Series. SAE International400 Commonwealth Drive, Warrendale, PA, United States, 2019. DOI: 10.4271/2019-01-0251.

[208] A. Roque, F. Foucher, Q. Lamiel, B. Imoehl, N. Lamarque, and J. Helie. "Impact of gasoline direct injection fuel films on exhaust soot production in a model experiment." In: *International Journal of Engine Research* 21.2 (2020), pp. 367–390. ISSN: 1468-0874. DOI: 10.1177/1468087419879851.

[209] C. J. Rutland. "Large-eddy simulations for internal combustion engines – a review." In: *International Journal of Engine Research* 12.5 (2011), pp. 421–451. ISSN: 1468-0874. DOI: 10.1177/1468087411407248.

[210] V. M. Salazar and S. A. Kaiser. "An Optical Study of Mixture Preparation in a Hydrogen-fueled Engine with Direct Injection Using Different Nozzle Designs." In: *SAE International Journal of Engines* 2.2 (2009), pp. 119–131. ISSN: 1946-3944. DOI: 10.4271/2009-01-2682.

[211] J. Sansonetti. *Handbook of Basic Atomic Spectroscopic Data, NIST Standard Reference Database 108*. 2003. DOI: 10.18434/T4FW23.

[212] F. Scarano, S. Ghaemi, G. C. A. Caridi, J. Bosbach, U. Dierksheide, and A. Sciacchitano. "On the use of helium-filled soap bubbles for large-scale tomographic PIV in wind tunnel experiments." In: *Experiments in Fluids* 56.2 (2015). ISSN: 0723-4864. DOI: 10.1007/s00348-015-1909-7.

[213] H. Schlichting and K. Gersten. *Boundary-Layer Theory*. Berlin, Heidelberg: Springer Berlin Heidelberg, 2017. ISBN: 978-3-662-52917-1. DOI: 10.1007/978-3-662-52919-5.

[216] M. Schmitt, C. E. Frouzakis, Y. M. Wright, A. G. Tomboulides, and K. Boulouchos. "Direct numerical simulation of the compression stroke under engine-relevant conditions: Evolution of the velocity and thermal boundary layers." In: *International Journal of Heat and Mass Transfer* 91 (2015), pp. 948–960. ISSN: 00179310. DOI: 10.1016/j.ijheatmasstransfer.2015.08.031.

[217] M. Schmitt, C. E. Frouzakis, Y. M. Wright, A. G. Tomboulides, and K. Boulouchos. "Investigation of wall heat transfer and thermal stratification under engine-relevant conditions using DNS." In: *International Journal of Engine Research* 17.1 (2016), pp. 63–75. ISSN: 1468-0874. DOI: 10.1177/1468087415588710.

[218] R. E. Scholten. "Enhanced laser shutter using a hard disk drive rotary voice-coil actuator." In: *The Review of scientific instruments* 78.2 (2007), p. 026101. ISSN: 0034-6748. DOI: 10.1063/1.2437199.

[219] C. Schulz and V. Sick. "Tracer-LIF diagnostics: quantitative measurement of fuel concentration, temperature and fuel/air ratio in practical combustion systems." In: *Progress in Energy and Combustion Science* 31.1 (2005), pp. 75–121. ISSN: 03601285. DOI: 10.1016/j.pecs.2004.08.002.

[220] F. Schulz and F. Beyrau. "Comparison of the Spray and the Spray/Wall Interaction of Two Gasoline Injectors." In: *International Journal of Automotive Technology* 19.4 (2018), pp. 615–622. ISSN: 1229-9138. DOI: 10.1007/s12239-018-0058-4.

[221] M. A. Shahbaz, S. Jahangir, and S. A. Kaiser. "Imaging of flame propagation and temperature distribution in an all-metal gasoline engine with endoscopic access via anisole-LIF." In: *SAE Technical Paper Series*. SAE Technical Paper Series. SAE International400 Commonwealth Drive, Warrendale, PA, United States, 2023.

[222] M. A. Shahbaz, N. Jüngst, R. Grzeszik, and S. A. Kaiser. "Endoscopic fuel film, chemiluminescence, and soot incandescence imaging in a direct-injection spark-ignition engine." In: *Proceedings of the Combustion Institute* 38.4 (2021), pp. 5869–5877. ISSN: 15407489. DOI: 10.1016/j.proci.2020.09.004.

[223] M. Shimura, S. Yoshida, K. Osawa, Y. Minamoto, T. Yokomori, K. Iwamoto, M. Tanahashi, and H. Kosaka. "Micro particle image velocimetry investigation of near-wall behaviors of tumble enhanced flow in an internal combustion engine." In: *International Journal of Engine Research* (2018), p. 146808741877471. ISSN: 1468-0874. DOI: 10.1177/1468087418774710.

[224] K. Shway, N. Jüngst, M. Bardi, G. Bruneaux, and S. A. Kaiser. "A multispectral UV–vis absorption technique for quantitative high-speed field-sequential imaging of fuel films and soot in combustion." In: *Proceedings of the Combustion Institute* (2022). ISSN: 15407489. DOI: 10.1016/j.proci.2022.08.099.

[225] J. D. Smith and V. Sick. "Quantitative, dynamic fuel distribution measurements in combustion-related devices using laser-induced fluorescence imaging of biacetyl in iso-

octane." In: *Proceedings of the Combustion Institute* 31.1 (2007), pp. 747–755. ISSN: 1540-7489. DOI: 10.1016/j.proci.2006.07.049.

[226] S. Someya, M. Uchida, K. Tominaga, H. Terunuma, Y. Li, and K. Okamoto. "Lifetime-based phosphor thermometry of an optical engine using a high-speed CMOS camera." In: *International Journal of Heat and Mass Transfer* 54.17-18 (2011), pp. 3927–3932. ISSN: 00179310. DOI: 10.1016/j.ijheatmasstransfer.2011.04.032. URL: https://www.sciencedirect.com/science/article/pii/S0017931011002511.

[227] K. Song, E. Clasen, C. Chang, S. Campbell, and K. T. Rhee. "Post-Flame Oxidation and Unburned Hydrocarbon in a Spark-Ignition Engine." In: *1995 SAE International Fall Fuels and Lubricants Meeting and Exhibition*. SAE International, 1995. DOI: 10.4271/952543.

[228] P. R. Spalart. "Numerical study of sink-flow boundary layers." In: *Journal of Fluid Mechanics* 172.-1 (1986), p. 307. ISSN: 0022-1120. DOI: 10.1017/S0022112086001751.

[229] R. H. Stanglmaier, C. E. Roberts, and C. A. Moses. "Vaporization of Individual Fuel Drops on a Heated Surface: A Study of Fuel-Wall Interactions within Direct-Injected Gasoline (DIG) Engines." In: *SAE Technical Paper Series*. SAE Technical Paper Series. SAE International400 Commonwealth Drive, Warrendale, PA, United States, 2002. DOI: 10.4271/2002-01-0838.

[230] P. Stephan. "B1 Wärme und verschiedene Arten der Wärmeübertragung." In: *VDI-Wärmeatlas*. Berlin, Heidelberg: Springer Berlin Heidelberg, 2013, pp. 19–22. ISBN: 978-3-642-19980-6. DOI: 10.1007/978-3-642-19981-3{\textunderscore}3.

[231] E. Stevens and R. Steeper. "Piston Wetting in an Optical DISI Engine: Fuel Films, Pool Fires, and Soot Generation." In: *SAE Technical Paper Series*. SAE Technical Paper Series. SAE International400 Commonwealth Drive, Warrendale, PA, United States, 2001. DOI: 10.4271/2001-01-1203.

[232] B. D. Stojkovic, T. D. Fansler, M. C. Drake, and V. Sick. "High-speed imaging of OH* and soot temperature and concentration in a stratified-charge direct-injection gasoline engine." In: *Proceedings of the Combustion Institute* 30.2 (2005), pp. 2657–2665. ISSN: 15407489. DOI: 10.1016/j.proci.2004.08.021. URL: https://www.sciencedirect.com/science/article/pii/S0082078404000736.

[233] M. Stripf, A. Schulz, and H.-J. Bauer. "Modeling of Rough-Wall Boundary Layer Transition and Heat Transfer on Turbine Airfoils." In: *Journal of Turbomachinery* 130.2 (2008). ISSN: 0889-504X. DOI: 10.1115/1.2750675.

[234] W. Sutherland. "LII. The viscosity of gases and molecular force." In: *The London, Edinburgh, and Dublin Philosophical Magazine and Journal of Science* 36.223 (1893), pp. 507–531. ISSN: 1941-5982. DOI: 10.1080/14786449308620508.

[235] J. Taler. *Solving Direct and Inverse Heat Conduction Problems*. Berlin, Heidelberg: Springer Berlin / Heidelberg, 2006. ISBN: 9783540334712. URL: https://ebookcentral.proquest.com/lib/kxp/detail.action?docID=571829.

[236] S. Thoduka. *Fourier-Mellin transform*. 20.03.2021. URL: https://sthoduka.github.io/imreg_fmt/docs/fourier-mellin-transform/.

[237] M. C. Thurber, F. Grisch, B. J. Kirby, M. Votsmeier, and R. K. Hanson. "Measurements and modeling of acetone laser-induced fluorescence with implications for temperature-imaging diagnostics." In: *Applied Optics* 37.21 (1998), pp. 4963–4978. ISSN: 1559-128X. DOI: 10.1364/ao.37.004963.

[238] M. C. Thurber and R. K. Hanson. "Simultaneous imaging of temperature and mole fraction using acetone planar laser-induced fluorescence." In: *Experiments in Fluids* 30.1 (2001), pp. 93–101. ISSN: 0723-4864. DOI: 10.1007/S003480000142.

[239] K. H. Tran, P. Guibert, C. Morin, J. Bonnety, S. Pounkin, and G. Legros. “Temperature measurements in a rapid compression machine using anisole planar laser-induced fluorescence.” In: *Combustion and Flame* 162.10 (2015), pp. 3960–3970. ISSN: 00102180. DOI: 10.1016/j.combustflame.2015.07.033.

[240] K. H. Tran, C. Morin, M. Kühni, and P. Guibert. “Fluorescence spectroscopy of anisole at elevated temperatures and pressures.” In: *Applied Physics B* 115.4 (2014), pp. 461–470. ISSN: 1432-0649. DOI: 10.1007/s00340-013-5626-8.

[241] D. R. Tree and K. I. Svensson. “Soot processes in compression ignition engines.” In: *Progress in Energy and Combustion Science* 33.3 (2007), pp. 272–309. ISSN: 03601285. DOI: 10.1016/j.pecs.2006.03.002.

[242] C. Tropea, J. F. Foss, and A. L. Yarin, eds. *Springer Handbook of Experimental fluid mechanics*. [Online-Ausg.] Berlin: Springer Science+Business Media, 2007. ISBN: 9783540251415. DOI: 10.1007/978-3-540-30299-5. URL: http://www.springerlink.de/content/w3732k/?p=0441a71f1c0544c497419a185495a8a3&pi=0.

[243] J. Trost, L. Zigan, and A. Leipertz. “Quantitative vapor temperature imaging in DISI-sprays at elevated pressures and temperatures using two-line excitation laser-induced fluorescence.” In: *Proceedings of the Combustion Institute* 34.2 (2013), pp. 3645–3652. ISSN: 15407489. DOI: 10.1016/j.proci.2012.05.093.

[244] J. Trost, M. Löffler, L. Zigan, and A. Leipertz. “Simultaneous quantitative Acetone-PLIF measurements for determination of temperature and gas composition fields in an IC-engine.” In: *Physics Procedia* 5 (2010), pp. 689–696. ISSN: 18753892. DOI: 10.1016/j.phpro.2010.08.100.

[245] N. Uchida. “A review of thermal barrier coatings for improvement in thermal efficiency of both gasoline and diesel reciprocating engines.” In: *International Journal of Engine Research* 23.1 (2022), pp. 3–19. ISSN: 1468-0874. DOI: 10.1177/1468087420978016.

[246] F. Uyma. “Untersuchungen auf dem Gebiet der Al-Mg-Si- und Al/Mg2Si-in-situ Legierungen.” Dissertation. Freiberg: Technische Universität Bergakademie Freiberg, 2007. URL: https://nbn-resolving.org/urn:nbn:de:bsz:105-366350.

[247] S. Wagner, L. Biondo, H. Gerken, T. Steinhaus, L. Illmann, and C. Beidl. “Portable and Compact TDLAS Measurement System for Exhaust Gas Diagnostics at Real Driving Conditions.” In: *OSA Optical Sensors and Sensing Congress 2021 (AIS, FTS, HISE, SENSORS, ES)*. Washington, D.C.: Optica Publishing Group, 2021, ETh1A.1. ISBN: 978-1-943580-90-3. DOI: 10.1364/ES.2021.ETh1A.1.

[248] Q. Wang, Y. Zhang, L. Jiang, and D. Zhao. “Quantitative gaseous temperature and mole concentration measurements in spray generated mixture by p-xylene-PLIF imaging.” In: *Combustion Science and Technology* 190.6 (2018), pp. 949–966. ISSN: 0010-2202. DOI: 10.1080/00102202.2017.1416359.

[249] Q. Wang, Y. Zhang, L. Jiang, D. Zhao, P. Guibert, and S. Yang. “Fluorescence and absorption characteristics of p-xylene: applicability for temperature measurements.” In: *Applied Physics B* 123.9 (2017). ISSN: 1432-0649. DOI: 10.1007/s00340-017-6817-5.

[250] T. Wei and W. W. Willmarth. “Reynolds-number effects on the structure of a turbulent channel flow.” In: *Journal of Fluid Mechanics* 204.-1 (1989), p. 57. ISSN: 0022-1120. DOI: 10.1017/S0022112089001667.

[251] J. Weinkauff, P. Trunk, J. H. Frank, M. J. Dunn, A. Dreizler, and B. Böhm. “Investigation of flame propagation in a partially premixed jet by high-speed-Stereo-PIV and acetone-PLIF.” In: *Proceedings of the Combustion Institute* 35.3 (2015), pp. 3773–3781. ISSN: 15407489. DOI: 10.1016/j.proci.2014.05.022.

[256] N. Wermuth and V. Sick. "Absorption and Fluorescence Data of Acetone, 3-Pentanone, Biacetyl, and Toluene at Engine-Specific Combinations of Temperature and Pressure." In: *SAE Technical Paper Series*. SAE Technical Paper Series. SAE International400 Commonwealth Drive, Warrendale, PA, United States, 2005. DOI: 10.4271/2005-01-2090.

[257] J. Westerweel and F. Scarano. "Universal outlier detection for PIV data." In: *Experiments in Fluids* 39.6 (2005), pp. 1096–1100. ISSN: 0723-4864. DOI: 10.1007/s00348-005-0016-6.

[258] B. Williams, P. Ewart, X. Wang, R. Stone, H. Ma, H. Walmsley, R. Cracknell, R. Stevens, D. Richardson, H. Fu, and S. Wallace. "Quantitative planar laser-induced fluorescence imaging of multi-component fuel/air mixing in a firing gasoline-direct-injection engine: Effects of residual exhaust gas on quantitative PLIF." In: *Combustion and Flame* 157.10 (2010), pp. 1866–1878. ISSN: 00102180. DOI: 10.1016/j.combustflame.2010.06.004.

[259] P. O. Witze and R. M. Green. "LIF and Flame-Emission Imaging of Liquid Fuel Films and Pool Fires in an SI Engine During a Simulated Cold Start." In: *SAE Technical Paper Series*. SAE Technical Paper Series. SAE International400 Commonwealth Drive, Warrendale, PA, United States, 1997. DOI: 10.4271/970866.

[260] E. Yokoyama, M. Shimura, M. Kamata, O. Nakabeppu, T. Yokomori, and M. Tanahashi. "Simultaneous High-speed and High-resolution PIV and Heat Flux Measurements near Piston Top under Tumble Enhanced Condition." In: *Flow, Turbulence and Combustion* (2022). ISSN: 1386-6184. DOI: 10.1007/s10494-022-00360-8.

[261] D. P. Zaleski, R. Sivaramakrishnan, H. R. Weller, N. A. Seifert, D. H. Bross, B. Ruscic, K. B. Moore, S. N. Elliott, A. V. Copan, L. B. Harding, S. J. Klippenstein, R. W. Field, and K. Prozument. "Substitution Reactions in the Pyrolysis of Acetone Revealed through a Modeling, Experiment, Theory Paradigm." In: *Journal of the American Chemical Society* 143.8 (2021), pp. 3124–3142. DOI: 10.1021/jacs.0c11677.

[262] F. Zentgraf. "Investigation of Reaction and Transport Phenomena during Flame-Wall Interaction Using Laser Diagnostics." Dissertation. Technical University of Darmstadt, 2022. DOI: 10.26083/tuprints-00021314.

[263] H. Zhang, X. Liang, Y. Wang, S. Zhu, and Z. Liu. "Experimental study of turbulent flame propagation under wall film conditions." In: *Fuel* 330 (2022), p. 125509. ISSN: 00162361. DOI: 10.1016/j.fuel.2022.125509.

[264] R. Zhang and V. Sick. "Multi-Component Fuel Imaging in a Spray-Guided Spark-Ignition Direct-Injection Engine." In: *SAE Technical Paper Series*. SAE Technical Paper Series. SAE International400 Commonwealth Drive, Warrendale, PA, United States, 2007. DOI: 10.4271/2007-01-1826.

[265] L. Zigan. "Imaging Techniques for Multi-Parameter Determination in Mixture Formation and Combustion Processes." Habilitation. 2020. DOI: 10.25593/OPUS4-FAU-14844.

[266] L. Zigan, J. Trost, and A. Leipertz. "Simultaneous imaging of fuel vapor mass fraction and gas-phase temperature inside gasoline sprays using two-line excitation tracer planar laser-induced fluorescence." In: *Applied Optics* 55.6 (2016), pp. 1453–1460. ISSN: 1559-128X. DOI: 10.1364/AO.55.001453.

# List of Publications


[E38] L. H. von Deyn, M. Schmidt, R. Örlü, A. Stroh, J. Kriegseis, B. Böhm, and B. Frohnapfel. "Ridge-type roughness: from turbulent channel flow to internal combustion engine." In: *Experiments in Fluids* 63.1 (2022). ISSN: 0723-4864. DOI: 10.1007/s00348-021-03353-x.

[E40] C.-P. Ding, B. Peterson, M. Schmidt, A. Dreizler, and B. Böhm. "Flame/flow dynamics at the piston surface of an IC engine measured by high-speed PLIF and PTV." In: *Proceedings of the Combustion Institute* (2018). ISSN: 15407489. DOI: 10.1016/j.proci.2018.06.215.

[E46] Z. Ding, K. Truffin, S. Jay, M. Schmidt, F. Foucher, and J. Borée. "On the Use of LES and 3D Empirical Mode Decomposition for Analyzing Cycle-to-Cycle Variations of In-Cylinder Tumbling Flow." In: *Flow, Turbulence and Combustion* (2023). ISSN: 1386-6184. DOI: 10.1007/s10494-023-00405-6.

[E50] D. Dreher, M. Schmidt, C. Welch, S. Ourza, S. Zündorf, J. Maucher, S. Peters, A. Dreizler, B. Böhm, and A. Hanuschkin. "Deep feature learning of in-cylinder flow fields to analyze cycle-to-cycle variations in an SI engine." In: *International Journal of Engine Research* 22.11 (2021), pp. 3263–3285. ISSN: 1468-0874. DOI: 10.1177/1468087420974148.

[E53] L. Engelmann, C. Welch, M. Schmidt, D. Meller, P. Wollny, B. Böhm, A. Dreizler, and A. Kempf. "A temporal fluid-parcel backwards-tracing method for Direct-Numerical and Large-Eddy Simulation employing Lagrangian particles." In: *Applied Energy* 342 (2023), p. 121094. ISSN: 03062619. DOI: 10.1016/j.apenergy.2023.121094.

[E78] C. Geschwindner, P. Kranz, C. Welch, M. Schmidt, B. Böhm, S. A. Kaiser, and J. de La Morena. "Analysis of the interaction of Spray G and in-cylinder flow in two optical engines for late gasoline direct injection." In: *International Journal of Engine Research* (2019), p. 146808741988153. ISSN: 1468-0874. DOI: 10.1177/1468087419881535.

[E89] A. Hanuschkin, S. Zündorf, M. Schmidt, C. Welch, J. Schorr, S. Peters, A. Dreizler, and B. Böhm. "Investigation of cycle-to-cycle variations in a spark-ignition engine based on a machine learning analysis of the early flame kernel." In: *Proceedings of the Combustion Institute* 38.4 (2021), pp. 5751–5759. ISSN: 15407489. DOI: 10.1016/j.proci.2020.05.030.

[E92] M. Haussmann, F. Ries, J. B. Jeppener-Haltenhoff, Y. Li, M. Schmidt, C. Welch, L. Illmann, B. Böhm, H. Nirschl, M. J. Krause, and A. Sadiki. "Evaluation of a Near-Wall-Modeled Large Eddy Lattice Boltzmann Method for the Analysis of Complex Flows Relevant to IC Engines." In: *Computation* 8.2 (2020), p. 43. DOI: 10.3390/computation8020043.

[E184] A. Pati, D. Paredi, C. Welch, M. Schmidt, C. Geschwindner, B. Böhm, T. Lucchini, G. D'Errico, and C. Hasse. "Numerical and experimental investigations of the early injection process of Spray G in a constant volume chamber and an optically accessible DISI engine." In: *International Journal of Engine Research* 107.1 (2021), p. 146808742110394. ISSN: 1468-0874. DOI: 10.1177/14680874211039422.

[E214] M. Schmidt, C. Welch, L. Illmann, A. Dreizler, and B. Böhm. “High-speed measurements and conditional analysis of boundary-layer flows at engine speeds up to 2500 rpm in a motored IC engine.” In: *Proceedings of the Combustion Institute* (2022). ISSN: 15407489. DOI: 10.1016/j.proci.2022.07.199.

[E215] M. Schmidt, C.-P. Ding, B. Peterson, A. Dreizler, and B. Böhm. “Near-Wall Flame and Flow Measurements in an Optically Accessible SI Engine.” In: *Flow, Turbulence and Combustion* 106.2 (2021), pp. 597–611. ISSN: 1386-6184. DOI: 10.1007/s10494-020-00147-9.

[E252] C. Welch, L. Illmann, M. Schmidt, and B. Böhm. “Experimental characterization of the turbulent intake jet in an engine flow bench.” In: *Experiments in Fluids* 64.5 (2023). ISSN: 0723-4864. DOI: 10.1007/s00348-023-03640-9.

[E253] C. Welch, M. Schmidt, C. Geschwindner, S. Wu, M. S. Wooldridge, and B. Böhm. “The influence of in-cylinder flows and bulk gas density on early Spray G injection in an optical research engine.” In: *International Journal of Engine Research* (2021), p. 146808742110423. ISSN: 1468-0874. DOI: 10.1177/14680874211042320.

[E254] C. Welch, M. Schmidt, L. Illmann, A. Dreizler, and B. Böhm. “The Influence of Flow on Cycle-to-Cycle Variations in a Spark-Ignition Engine: A Parametric Investigation of Increasing Exhaust Gas Recirculation Levels.” In: *Flow, Turbulence and Combustion* 110.1 (2023), pp. 185–208. ISSN: 1386-6184. DOI: 10.1007/s10494-022-00347-5.

[E255] C. Welch, M. Schmidt, K. Keskinen, G. Giannakopoulos, K. Boulouchos, A. Dreizler, and B. Boehm. “The Effects of Intake Pressure on In-Cylinder Gas Velocities in an Optically Accessible Single-Cylinder Research Engine.” In: *SAE Technical Paper Series*. SAE Technical Paper Series. SAE International400 Commonwealth Drive, Warrendale, PA, United States, 2020. DOI: 10.4271/2020-01-0792.